Droplet control in aqueous and hydrocarbon fluids: Long, end-associative polymers dictate fluid behavior under elongational flows

Thesis by
Robert Whitson Learsch

In Partial Fulfillment of the Requirements for the
Degree of
Doctor of Philosophy in Materials Science

CALIFORNIA INSTITUTE OF TECHNOLOGY
Pasadena, California

2023
Defended October 20, 2022

Robert Whitson Learsch
ORCID: 0000-0001-6329-5879

ACKNOWLEDGEMENTS

Looking over this document, I'm struck by how removed my doctoral dissertation is from the process by which I created it. In writing it, I worked very hard to connect the dots in a linear, coherent order; if I was successful, reading it will give you the impression that my work was conducted in a single, continuous, fluid motion.

There are many trajectories which could possibly describe the reality of conducting this research, and none of them are "a fluid motion." My path was full of false starts, pivots, reversals, and re-investigations.[i] And from my experience, most PhDs follow similar non-linear paths. Fortunately, I had an abundance of help while charting this course.

Thank you to Lealia Xiong, my wife, my buddy, and my best friend. I literally would not be here without your unconditional love and support. I could easily write a second dissertation on how lucky I am that we found one another, but this is not the place. 我爱你宝bae.

Thank you to Red, Hojin, Priya, Andy, Ben, Rachel, Tiziana, Paresh, Jin, Dennis, Jacque, Rohit, and Sasha, my current and former group mates for interrupting the long days and frustrating experiments with moments of connection, joy, and laughter. Thank you to Pedro, Fernando, Valère, Amy, Andrew, Max, Cullen, Sean, Sarah, Edward, Holly, Jorge, Hayley, Keisuke, Juan, Hannah, Paige, my friends inside and outside of Caltech, for bringing their perspective on what is reasonable and what is possible.

Thank you to my parents, Bob and Suzanne, for helping me so much from 3000 miles away.

Thank you to Professor Julie Kornfield for taking a chance on me after witnessing my disastrous first candidacy exam. Working with you has absolutely made me a better scientist, a better communicator, and a better educator. I hope to retain a fraction of your skepticism and all of your enthusiasm.

Thank you to Abigail McCann, Christine Jary, and Therese Bagsit, the Kornfield group administrative staff. The research group would literally disintegrate your scheduling wizardry and attention to detail.

[i] Searching things again, as in, re-search?

Thank you to Professor Troian, Professor Faber, and Dr. Chris Nelson, my other committee members. Donating your time and expertise has shored up my scientific foundation, bolstered my academic rigor, and vastly improved both my doctoral dissertation and my PhD experience.

Thank you to Professor Justin Bois for hosting the Introduction to Programming for the Biological Sciences Bootcamp and for your passionate hatred of bar graphs. Spending those countless hours on Zoom with you in the summer of 2020 enabled much of the work in my thesis and encouraged me to think more deeply about statistics.

Thank you to Jennifer and Christy, APhMS and EAS administrators for your cheerful attitudes. Your combined support, wisdom, and experience are valuable resources for any student lucky enough to cross paths with you.

Thank you to the other mentors in my life for encouraging and motivating me to reach the finish line: Dr. Mishra, Dr. Walsh, Dr. Vargas-Gonzalez, Dr. Grindy, Professor Holten-Andresen, Professor Griffith, Professor Olivetti, Professor Yee, Professor Tertuliano, Professor Portela, Professor Sun, Professor Miyake, Professor Bowman, Professor Greer, Professor Wang, Professor Goddard, Professor Robb, and Professor Fultz.

Thank you to the staff at the Caltech Library TechLab. You 3D printed countless parts for me which are still in use to this day, and which I hope will continue to be used for years to come. I was able to build the DoSER instrument and actually conduct the measurements which compose my thesis because of you.

Thank you to the National Science Foundation's Graduate Research Fellowship and the Dow University Partnership Initiative; without either of these programs, my PhD would have been stopped in its tracks. In addition to the funding, the Dow University Partnership Initiative freely gave hours of time with experts across Dow who have wide expertise and led to critical insights.

Finally, thank you for reading my thesis. Even if you take nothing else from reading this tome, please remember to wash your produce.

ABSTRACT

Modifying elongational flows, seen in sprayed mists, turbulent flows, and droplet spreading and retraction following impact, is of interest in diverse industries, including agriculture and aviation. Long flexible polymers (with fully extended lengths 1 to 10 μm) modify the elongational flow behavior of a fluid to which they are added. At low concentrations (1 to 10% of their overlap concentrations), their effect is mild under shear flow (shear viscosity increases < 50%), but dramatic under elongational flows (extensional viscosity increases $\geq$ 300).

These long polymers are not widely used in practice because they degrade under strong flows, such as passing through pumps and filters, that typically precede spray. Pairwise end-associative polymers can overcome this limitation. Pulling apart non-covalent associative bonds under such strong flow conditions relieves the tension along the polymer backbone. The pairwise end-associative polymers that are effective in mist control and drag reduction are individually short enough to avoid chain scission in flows that would break long covalent polymers, yet long enough that 6 to 8 associative polymers connected end-to-end create supermolecules that are as effective as their long covalent counterparts.

This thesis systematically compares the effect of long covalent and long end-associative polymers on the fluid's extensional flow properties and the polymers' performance in controlling droplet impact and spray breakup. To measure the elongational flow properties, I implemented and enhanced the Dripping onto Substrate Extensional Rheometry (DoSER) technique (Chapter 2) and applied it to long covalent polymers (Chapter 3) and to end-to-end associative polymers (Chapter 4). Preparing solutions in which the polymers negligibly affect the interfacial tension (< 10%) allows us to explore the relationship between extensional flow properties and droplet impact (Chapter 5) and spray (Chapter 6).

By combining the quantitative measurements of extensional viscosity and extensional relaxation time with the corresponding behavior in impact and spray, I correlate the structure of polymers to the solution behavior in droplet rebound and spray breakup. This work has the potential to reduce pesticide contamination of soil, water, and air from agricultural sprays and fire hazard associated with hydrocarbon lubricants.

TABLE OF CONTENTS

LIST OF ILLUSTRATIONS

Number *Page*

LIST OF TABLES

Number *Page*

LIST OF SYMBOLS AND ABBREVIATIONS

β	A measure of K_{eq} for ligand metal complexes: $\beta = \log_{10}(K_1 \quad K_2)$
$\Delta\rho$	The density difference between a fluid and air
ΔG	The change in Gibbs free energy: $\Delta G = \Delta H \quad - T\Delta S$
ΔH	The change in enthalpy
ΔS	The change in entropy
$\dot{\epsilon}$	Strain rate: $\dot{\epsilon} = d\epsilon/dt$
ϵ	Strain
η	The viscosity of the fluid, without specifying the type of flow
η_0	The shear viscosity of the pure solvent of a solution
η_E	The elongational viscosity of the fluid, the viscosity under elongational flow
$\eta_E^{\dagger}$	The estimated plateau elongational viscosity, calculated from $\eta_E(t)$
η_E^{∞}	The plateau elongational viscosity, found from the plateau in the graph of $\eta_E(\epsilon)$ in a DoSER experiment
η_S	The shear viscosity of the fluid, the viscosity under shear flow
λ_E	The elongational relaxation time of the fluid
ν	The Flory exponent
$\overrightarrow{R}$	The end to end distance of a polymer chain
ϕ_i	The zenith bond angle of between the i^{th} and $i-1^{th}$ monomeric repeat units
ρ	The fluid's density
σ	The surface tension of the fluid
θ_c	The contact angle between a fluid and its substrate
θ_i	The azimuth bond angle of between the i^{th} and $i-1^{th}$ monomeric repeat units
A	A constant that characterizes the substrate-fluid interactions in droplet impact experiments
c	The concentration of a solute in solution

c^* The critical overlap concentration: The concentration at which polymers in their solvent begin to interact with one another

C_i Coefficents C_1, C_2 and C_3, used in solving a third order polynomial

D The diameter of a droplet of fluid

$D(t)$ The minimum diameter of the liquid bridge in the DoSER experiment

$D(t_c)$ The minimum diameter of the liquid bridge in the DoSER experiment at the critical time

D_0 The outer diameter of the needle used in the DoSER technique

d_m The maximum diameter a droplet spreads to during impact

$D_{EC}(t)$ The predicted minimum diameter of the liquid bridge during elastocapillary behavior in the DoSER experiment

$D_{IC}(t)$ The predicted minimum diameter of the liquid bridge during inerto-capillary behavior in the DoSER experiment

D_{inner} The inner diameter of the needle used in the DoSER technique

D_{pred} The diameter of a droplet predicted from its density, surface tension, and the inner diameter of the orifice

$Diss_{b-c}$ The energy dissipated between moments b and c in droplet impact

E_b The energy at moment b in the droplet impact: the moment of maximum expansion

E_c The energy at moment c in the droplet impact: the moment of maximum rebound

E_r The energy at the hypothetical moment r in the droplet impact: where a sphere of fluid has 0 velocity and is just separated from the substrate

E_{ERE} The “excess rebound energy" of a droplet, introduced in Mao, Kuhn, and Tran [11]

F The applied force

g The acceleration due to gravity, on Earth g = 9.8 m/s/s

G_E The extensional elastic modulus

g_i The i^{th} mode of a polymer’s relaxation spectrum

H The gap height, the distance between the needle and substrate in the DoSER technique

h_m The maximum height a rebounding droplet reaches after impact

J Joules

K Kelvin (Temperature)

K_1 The equilibrium constant of the association of an empty ligand with a metal ion

K_2 The equilibrium constant of the association of an mono-ligand metal complex with an additional ligand

k_B Boltzmann's constant: $k_B = 1.38x10^{-23}$ J/K

K_{eq} The equilibrium constant of the overall formation of an associative complex

KE The kinetic energy of a falling droplet: $KE = mv^2/2$

l The length of a monomeric repeat unit

$L(x)$ The Langevin function: $L(x) = \coth(x) - 1/x$

$L^{-1}(x)$ The inverse Langevin function

m The degree of supramolecular polymerization: the number of polymeric repeat units in a megasupramolecule

m The mass of a droplet of fluid

M_n Number average molecular weight: $M_n = \frac{\sum_i M_i N_i}{\sum_i N_i}$

M_w Weight average molecular weight: $M_w = \frac{\sum_i M_i^2 N_i}{\sum_i M_i N_i}$

ms Milliseconds

N The degree of polymerization of a polymer: the number of repeat units in a polymer chain

n The number of technical replicates in an experiment

Oh The Ohnessorge number, with unspecificed viscosity: $Oh = \eta/(\sqrt{\sigma}\rho D)$

Oh_E The Ohnessorge number, with elongational viscosity: $Oh_E = \eta_E/(\sqrt{\sigma}\rho D)$

Oh_S The Ohnessorge number, with shear viscosity: $Oh_S = \eta_S/(\sqrt{\sigma}\rho D)$

P The persistance length of a polymer chain: at distances beyond the persistence length the polymer segments are uncorrelated from one another

PE The potential energy of a falling droplet: $PE = mgH$

R The universal gas constant: $R = 8.314$ J/mol/K

Re The Reynold number, with unspecificed viscosity: $Re = vD\rho/\eta$

Re_E The Reynold number, with elongational viscosity: $Re_E = vD\rho/\eta_E$

Re_S The Reynold number, with shear viscosity: $Re_S = vD\rho/\eta_S$

s Seconds

T Temperature

t Time

t_c The critical time: the moment of transition to elastocapillary behavior in a DoSER experiment

Tr Trouton's ratio: $Tr = \eta_E/\eta_S$

v The velocity of a falling droplet

We The Weber number: $We = \rho v^2 D/\sigma$

Z The partition function

H_2O Water

Đ The dispersity of a polymer: Đ = M_w/M_n

Đ† The dispersity of a mixture of polymers, calculated assuming the starting materials are uniform in molecular weight

CB[6] Cucurbit[6]uril

Co Cobalt

Cu Copper

DA Diacid-ended poly(cyclooctadiene)

DB Dibase-ended poly(cyclooctadiene)

DoSER Dripping onto substrate extensional rheometry

EC Elastocapillary: A regime of fluids where elastic and capillary forces dominate the behavior; viscosity is neglected

Fe Iron

IC Inerto-capillary: A regime of fluids where momentum and capillary forces dominate the behavior; viscosity is neglected

kg Kilograms

L Ligand, a generic ligand used in a ligand-metal association reaction

M Metal ion, a generic metal ion used in a ligand-metal association reaction

Mg Megagrams

mg Milligrams

mol Moles

MW Molecular weight, unspecified average

Ni Nickle

PAA Poly(acrylic acid)

PAM Poly(acrylamide)

PAO Poly(alphaolefin)

PCOD Poly(cyclooctadiene)

PEO Poly(ethylene oxide)

T-PAM Terpyridine ended poly(acrylamide)

VC Viscocapillary: A regime of fluids where viscous and capillary forces dominate the behavior; momentum is neglected

Weight % Weight percent: The mass of solute divided by the mass of the solution

Chapter 1

POLYMER ADDITIVES FOR FLUID PROPERTY MODIFICATION

1.1 Benefits of controlling extensional behavior of fluids

This work is focused on extensional flow, which is encountered in situations such as filming bowing, fluid spraying from an opening, and turbulent fluid flows. Spray creates a mist of droplets with a range of diameters and velocities, and changing the extensional fluid properties can improve the performance of these sprays in two very different contexts.

Agriculture

The bulk of this work is with poly(acrylamide) (PAM), a water soluble polymer, and motivated by the agriculture industry. Presently, agricultural water is treated with fertilizers, pesticides, herbicides, fungicides, and other additives to aid in the cultivation of food. Fertilizers and the water itself are effective whether they ultimately wind up on the plant or in the soil, while pesticides are only effective if they deposit onto the plants' leaves. In practice, crops retain only about 20% to 50% of the pesticides added to the water, and the other 80% can be found in streams, wells, and aquifers.[1] This should be alarming. The agricultural industry is spending energy and raw materials to create pesticides that are ultimately wasted. In fact, we are actively poisoning our water supply by allowing so much pesticide to go off-target.

As the droplets are created by spraying liquid through a nozzle, the small droplets drift off-target through the air, while the largest droplets rebound or splash off the leaves that they impact. Polymeric additives are attractive for solving this problem because they modify both the drop size distribution and the behavior of the droplets themselves.

Fire suppression

Poly(cyclooctadiene) (PCOD) is soluble in hydrocarbon fluids like organic solvents, gasoline, and other carbon-based oils, and holds great interest to the aviation industry where safety is paramount and failure can be catastrophic. In an engine, fuel is sprayed to produce small and uniform droplets to undergo complete and rapid com-

bustion.[2] However, in the event of a failure such as a damaged or disconnected line, the accidental release of small droplets evaporate to form a dangerous flammable mist.[3–6] The presence of these mists increases the danger of failures in the aviation industry, and in the event of ignition, severely increase the consequences.

1.2 Fundamental polymer science

Essential polymer chemistry

Polymers are a special type of molecule that consist of many repeating parts connected by covalent chemical bonds. The repeating parts (*monomers*) can individually consist of many different elements: carbon and hydrogen are common; monomers containing oxygen and nitrogen often lead to desirable properties; and more exotic elements such as silicon, fluorine, and chlorine can be used to create niche materials. Furthermore, polymers are unique in their statistical nature. Every molecule of a small-molecule chemical is identical. For example, acetylsalicylic acid (Aspirin, $C_9H_8O_4$) is the exact same number of atoms, connected in the exact same way, every time it is produced across the world. In contrast, no two poly(styrene) (Styrofoam) products are chemically identical. Each synthesis produces a unique distribution of polymer molecular weights.[i] The polymer distributions are characterized by their dispersity, Đ:

$$Đ = \frac{M_w}{M_n} = \frac{\sum_i M_i^2 N_i}{\sum_i N_i}, \tag{1.1}$$

where M_w is the weight-average molecular weight, M_n is the number-average molecular weight, and in the summations, M_i and N_i are the mass and number of the i^{th} species.

Because the fundamental feature of all polymers is their repeating nature, polymers are a class of materials with a broad spectrum of possibilities. They can be solid or liquid under ambient conditions, hard, soft, tough, brittle, hydrophobic, hydrophilic, *etc*., *etc*. This vast array of possible properties is accessible by changing the identity of the repeating units and the architecture by which they are connected. Long polymers in solution, even at minuscule concentrations, radically change the behavior of the fluids under certain fluid flow conditions.

[i] Nature, of course, can produce and reproduce chemically identical proteins with almost 100% success, e.g., DNA.

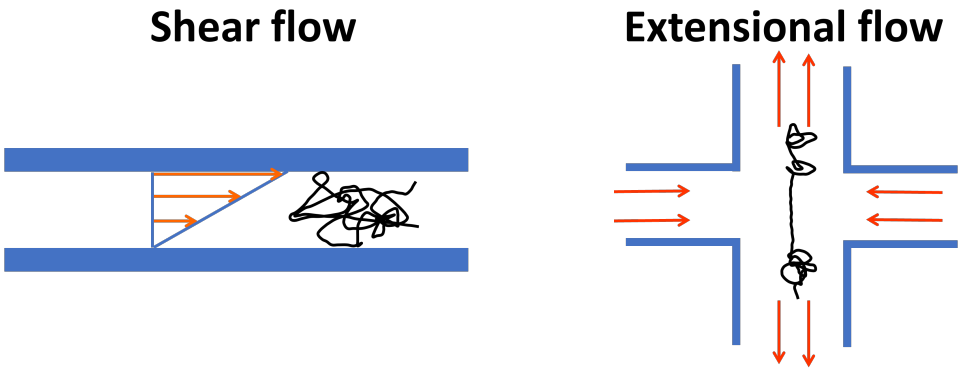

Figure 1.1: (left): A polymer under shear flow produced by a conventional parallel plate rheometer. (right): A polymer under elongational flow in cross-slot flow geometry. Figure modified from an unpublished original by Dr. Red Lhota and used with permission.

Shear and elongational flow

Any fluid flow can be decomposed into a shear and an elongational component.[7] Shear flow is categorized by perpendicular directions of the applied stress and velocity gradient of the fluid (Figure 1.1, left). Elongational flows require the applied stress and velocity gradient in the fluid to be parallel, which results in the stretching of the fluid elements. In the lab, most commercial rheometers produce a state of shear flow, for example in a parallel plate type geometry, where one plate is fixed, creating a no-slip boundary condition, and the other moves, applying a stress. Elongational flows can be produced by, for example, a cross slot flow geometry (Figure 1.1, right).

At rest, polymers take a coiled configuration which minimizes their free energy. The exact size and shape of the coil depends on the length of the polymer, temperature, the polymer-solvent interactions. The root-mean-square of the end to end distance is defined as:

$$\sqrt{<\overrightarrow{R}^2>} = N^{\nu} l, \tag{1.2}$$

where N is the number of repeat units, ν is the Flory exponent which captures the polymer-solvent interactions including the temperature, and l is the length of a single repeat unit. ν takes values from $\sim 1/3$ to $\sim 3/5$, and N can be 10^3, 10^4, or beyond. The coiled polymer will always be much smaller than its fully extended state, which has $R_{max} = Nl$. For example, a coiled polymer with $N = 10000$ will have $\sqrt{<\overrightarrow{R}^2>} \approx 0.01 R_{max}$. In absolute terms, $l \sim 0.15$ nm, yielding $\sqrt{<\overrightarrow{R}^2>} \approx 15$ nm and $R_{max} \sim 1500$ nm.

Under mild shear flows, the polymers retain the coiled configuration that they assume at thermodynamic equilibrium. Instead of uncoiling, they prefer to rotate, which only mildly increases η_S. Under higher intensity shear flows or elongational flows, the fluid deformation forces the polymers to uncoil. Although no chemical bonds are broken, the transition from the coiled to fully stretched state costs an immense amount of energy in the form entropy. As the polymer elongates, there are fewer and fewer accessible microstates for the chain to explore while maintaining the end to end distance in that moment. The fewer microstates there are for a given configuration, the lower the entropy of that configuration is and the more energy it costs to inhabit.[8,9] The fluid must pay the entropic cost associated with forcing the polymers into an unfavorable configuration, and this gives rise to the increased η_E observed in polymer solutions.

Measurement of elongational properties

The distinction between η_S and η_E is paramount in polymer solutions. Due to the unique coil-stretch transition that polymers undergo, it is impossible to predict η_E by measuring η_S. Many other types of solutions maintain Trouton's ratio, $Tr = \frac{\eta_E}{\eta_S}$ of 3.[10] For polymers solutions, Tr is commonly 100 to 10000 and η_E must be measured directly.

The common methods to measure η_E are capillary breakup extensional rheometry (CaBER), Rayleigh-Ohnesorge jetting extensional rheometer (ROJER), and dripping-onto-substrate extensional rheometry (DoSER).[11–22] Each of these techniques force the fluid into a state of elongational flow by producing a filament of fluid. The filament is observed over its lifetime with high-speed video and the change in the filament's diameter over time is analyzed to measure η_E and other properties of the fluid.

The key difference between the different techniques is how the filaments are produced. In CaBER, the fluid is placed in contact with two parallel plates close together. The experiment begins by applying a step strain to the plates, moving them apart rapidly and observing the filament of fluid formed as the fluid bridges the two plates (Figure 1.2a). In ROJER, the fluid is pushed through a nozzle to create a jet. The jet of fluid undergoes break up and the gives rise to many droplets. Prior to the complete separation of a single droplet, a filament forms connecting it to the original jet, and these filaments are analyzed to determine η_E (Figure 1.2b).[ii]

[ii] ROJER is sometimes referred to as a "flying CaBER" which I think is extremely accurate and also hilarious.[11,24,25]

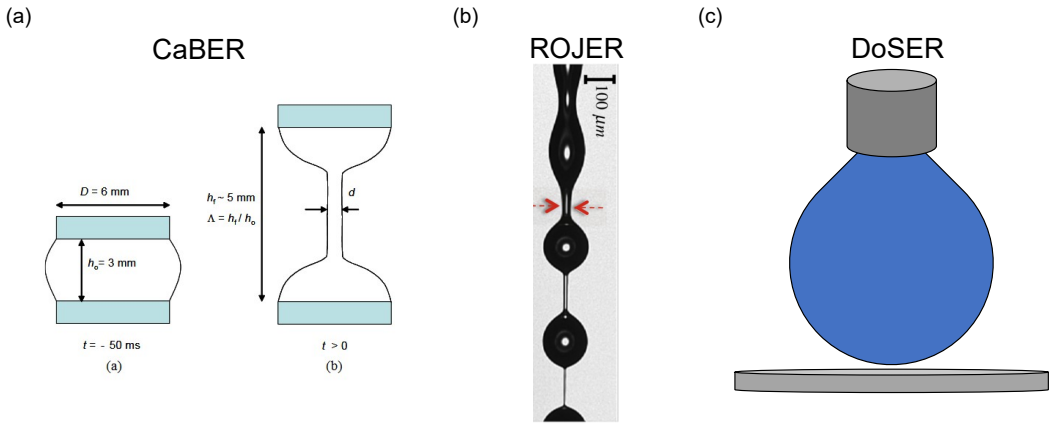

Figure 1.2: Methods of measuring elongatinoal viscosity (η_E) by producing a controlled elongational flow in the lab. In each technique, a filament of fluid is produced and the evolution of its diameter in time is observed. (a): Schematic illustration of the capillary breakup extensional rheometry (CaBER) test. A droplet of fluid is placed between two parallel plates, and the plates are moved apart from one another with a rapidly applied step-strain. Image originally from Rodd et al. [23], licensed under CC BY-NC-ND 3.0. (b): Snapshot of a Rayleigh-Ohnesorge jetting extensional rheometer (ROJER) experiment: A jet of fluid is produced and as it gives way to droplets, many filaments are produced. Image originally from Keshavarz et al. [11], reproduced with permission. (c): Schematic illustration of dripping-onto-substrate extensional rheometry (DoSER): A droplet of fluid is produced through a needle and slowly makes contact with the substrate underneath. As the fluid transfers to the substrate, the filament is produced.

Finally, DoSER creates the filament in a much more gentle way. Instead of applying a step-strain, a droplet of fluid is produced from a needle and slowly brought into contact with a substrate (Figure 1.2c). As it transfers from the needle to the substrate, it forms a filament similar to what is seen in CaBER.

Of the three, the CaBER technique is the most developed. It is the only commercialized instrument used to measure fluid properties under elongational flow.[26] However, CaBER struggles with low viscosity (commonly due to low polymer concentration) solutions. The analysis assumes that the step strain which creates the filament is applied instantaneously to the fluid. In practice, the application of the strain, although it is applied very fast, takes a finite amount of time. In low η_E solutions, the breakup can begin before the plates reach their final separation distance.[17,19,26]

Because of this limitation, and in discussions with subject matter experts, I chose to build a DoSER instrument for the measurement of η_E on our polymer solutions. Furthermore, I knew I would need to do droplet impact experiments, and the

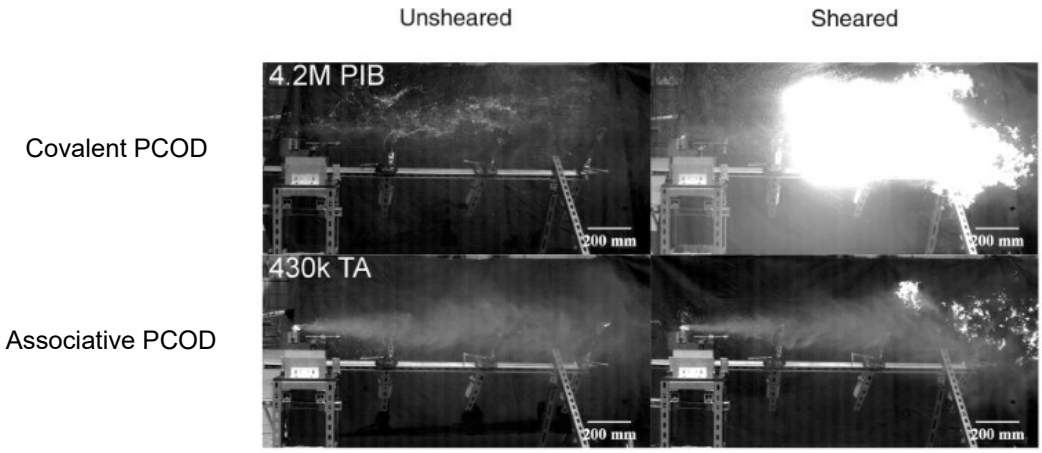

Figure 1.3: Testing of jet fuel mists in the presence of ignition sources with 4.2 Mg/mol covalent (top row) and 430 kg/mol associative (bottom row) poly(cyclooctadiene) (PCOD) added at 0.3 weight %. In the unsheared (left) jet fuel, both covalent and associative PCOD prevents the mist from igniting. After passing the fuel through a pump ("sheared," right), only the associative PCOD prevents ignition. Image from Wei et al. [4]. Reprinted and modified with permission from AAAS.

observation of droplet impacts and DoSER both make use of similar hardware.

Associative polymers in jet fuel

Previous work in the Kornfield group developed PCOD based polymers which suppressed the formation of flammable mists when added to jet fuel. To test this, a live fire test was performed under the supervision of the local fire department in which jet fuel was sprayed in a style that could be caused by an airplane crash. Even in the presence of an ignition source, the polymer treated jet fuel did not combust (Figure 1.3). The polymer dissolved in jet fuel, near 0.3 weight %, substantially modified the rheological properties and spray behavior of the fluid. Notably, the presence of the polymer additive did not impact the performance of the engine: it generated the same amount of power, particulate matter, and NOx compounds from combustion of the treated and untreated fuels. Long polymers dissolved in fluid will create a spray pattern with higher average diameter.[11,27–31] For example, polymers increase the diameter of the spray distribution by resisting droplet breakup.

Individual droplets are formed by perturbations to the stream of fluid, these perturbations create additional surface area exposed to the surrounding atmosphere, and at a critical amplitude, the surface tension drives pinch-off and forms droplets.[32,33] Prior to pinch-off, the fluid forms narrow ligaments and these ligaments amplify the

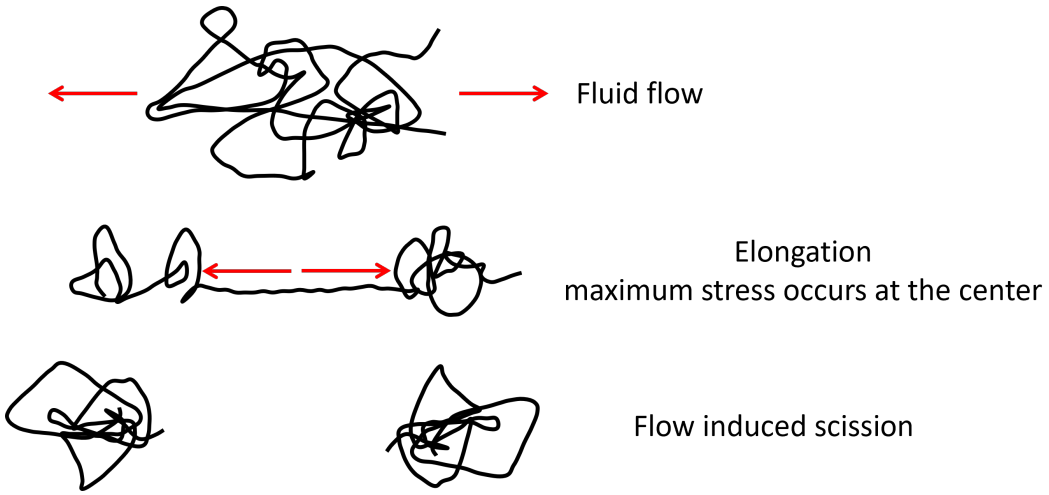

Figure 1.4: The degradation of polymers under intense elongational flow. The tension along the polymer chain is maximum at the center, eventually overcoming the strength of the covalent chemical bond. Figure originally found in Lhota [44], reproduced with permission.

effect of the polymers. The fluid flow in the ligaments forces the polymers to uncoil and this uncoiling motion resists and delays the formation of droplets, leading to larger droplets.[34,35]

The uncoiling of the polymer chains creates larger droplets in sprays and also gives rise to the difficulty in deploying long polymers for use in practical applications.[36–43] As the polymer chain uncoils, it experiences high tension at its center. Eventually, under intense flow conditions that combine high strain rates and high strains, the tension along the polymer chain will be sufficient to overcome the strength of a single chemical bond along the backbone, degrading the polymer and reducing its efficacy (Figure 1.4).

To overcome this limitation, linear end-associative polymers were developed.[4,43] These polymers have end groups which participate in non-covalent, associative bonding with one another and form megasupramolecules in solution. Individual polymers of moderate length associate with one another *via* their end groups to form ultra-long new polymers, where the repeat unit now is itself a polymer chain (Figure 1.6). In megasupramolecules, the associative sites at the end of the repeat units act as sacrificial bonds, relieving the tension along the polymer chain that leads to degradation under intense flow, and re-associating into megasupramolcules afterwards.

1.3 Applying linear-end associative megasupramolecules to other chemical systems

In this dissertation, I set out to demonstrate that the long, end-associative polymers first seen in Wei et al. [4] can be applied to other systems. To accomplish that, the first step is to understand *how* the associative PCODs contribute to fire suppression.

In Wei et al. [4], the droplet diameter distribution from sprayed solutions was not measured directly. The only reported fluid property was the Specific Viscosity, η_{sp}. η_{sp} compares the shear viscosity (η_S) of a polymer solution to that of its solvent (η_0) and is defined as $\eta_{sp} = \frac{\eta_S - \eta_0}{\eta_0}$. All polymer solutions, including the degraded covalent controls, had $2 > \eta_{sp} > 0$, meaning they increased η_S of the solvent, but not very substantially.

The effect of long polymers in solution is much more prominent under elongational flow rather than shear flow. Although these long polymers increased η_S by $\sim 3x$, the increase in elongational or extensional viscosity, η_E, could be $100x$ or greater than pure solvent. This is due to the coil-stretch transition the polymer chains undergo during elongational flow.

Associative chemistry for use in water

The megasupramolecules in jet fuel are associated by end groups which readily participate in hydrogen bonding with one another. Hydrogen bonding works well in this context because the polymer backbone and fuel itself have no atoms which can participate in hydrogen bonding (O, F, N). Water (H_2O) eagerly participates in hydrogen bonding, but water in jet fuel is not a common occurrence.[iii]

To use these end-associative linear polymers in H_2O, a different type of associative chemistry would have to be used. Fortunately, there is a wide array of non-covalent bonding schemes that are compatible with H_2O.[45] The types of associative chemistries fall broadly into the categories of metal-ligand complexes, host-guest interactions, and ionic interactions.

The strength of associative interactions is quantified by their equilibrium constant K_{eq}. K_{eq} is a measure of how many associations are formed at equilibrium. The formation of an associative complex, AB, from individual species A and B, is represented as $\mathrm{A} + \mathrm{B} \underset{\mathrm{k}_b}{\overset{\mathrm{k}_a}{\rightleftharpoons}} \mathrm{AB}$ where k_a is the rate of association and k_b is the rate

[iii] or you have bigger problems!

of disassociation. The overall rate constant,

$$K_{eq} = \frac{k_a}{k_b} = \frac{[\mathrm{AB}]}{[\mathrm{A}][\mathrm{B}]}, \tag{1.3}$$

is related to the Gibbs energy of formation by:

$$\Delta G = -2.3RT \log_{10}(K_{eq}), \tag{1.4}$$

where T is the temperature, R is the universal gas constant, and ΔG is the change in free energy of association. From Equations 1.3 and 1.4, the total number of associated complexes depends exponentially on the bonding strength of their association. Due to the differences in electronic and steric effects, K_{eq} takes on a range of values for the different types of associative chemistries: $10^2 < K_{eq} < 10^{40}$. Metal-ligand interactions generally have the highest values of K_{eq} ($K_{eq} > 10^{15}$) and guest-host interactions have lower values: $10^2 < K_{eq} < 10^{15}$.[45–50] Even the weakest host-guest interaction is stronger than a single hydrogen bond (Table 1.1).[51]

Types of associative bonding

Host-guest interactions provide the most intuitive picture of associative chemistry. For example, β-cyclodextrin (β-CD) and adamantane ($(CH)_4(CH_2)_6$) will spontaneously associate in aqueous solution (Figure 1.5). β-CD forms a hydrophobic pocket inside its core, which adamantane will be drawn towards to minimize its exposure to H_2O.

Metal-ligand interactions behave similarly, except a multi-valent metal ion (M) coordinates with multiple of the same ligands (L).[53–58] These associations occur in multiple steps: $\mathrm{M} + 2\,\mathrm{L} \overset{\mathrm{K_1}}{\rightleftharpoons} \mathrm{LM} + \mathrm{L} \overset{\mathrm{K_2}}{\rightleftharpoons} \mathrm{LML}$ (Figure 1.6). The overall K_{eq} is the product of K_1 and K_2,

$$\mathrm{M} + 2\,\mathrm{L} \overset{\mathrm{K_1\,K_2}}{\rightleftharpoons} \mathrm{LML},$$

and is often reported as β.

$$\beta = \log_{10} K_1 + \log_{10} K_2 = \log_{10} K_{eq} \tag{1.5}$$

The strength of the metal-ligand interaction depends not only on the identity of the ligand, but also the identity of the metal (Table 1.1).

The ionic type of associations use charged repeat unit at the end (or throughout) of a neutrally charged polymer chain. Polymer segments with oppositely charged repeat units attract one another and create transient linkages between the polymers (Figure

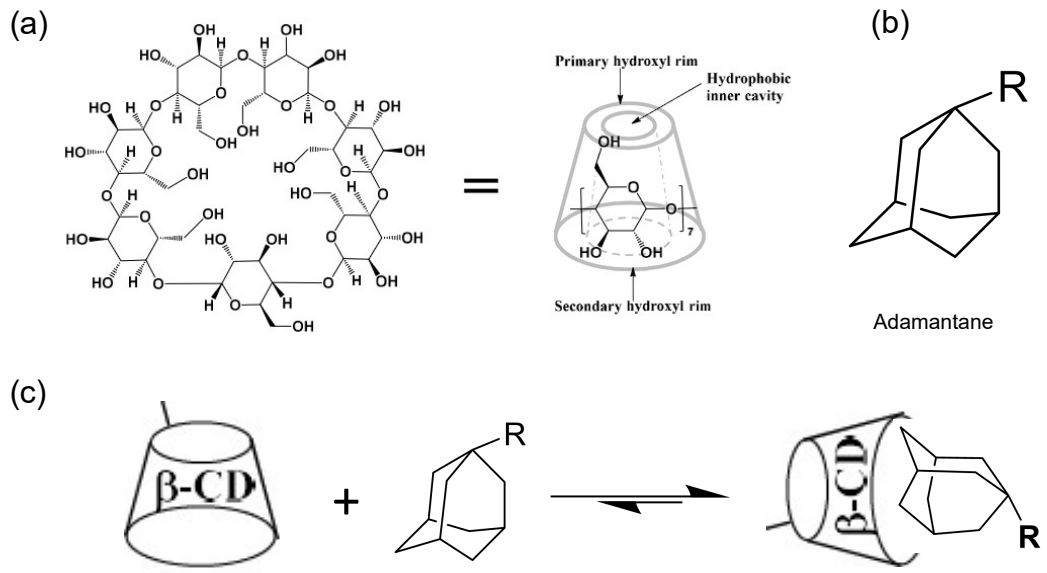

Figure 1.5: An example of host-guest association. (a): β-cyclodextrin (β-CD) forms a tapered cylinder with a hydrophobic pocket inside. Originally from Kim [52], reproduced with permission. (b): Molecular structure of adamantane, which is a hydrophobic molecule and attracted to the interior pocket of β-CD. (c): The spontaneous association of β-CD (host) and adamantane (guest) in solution.

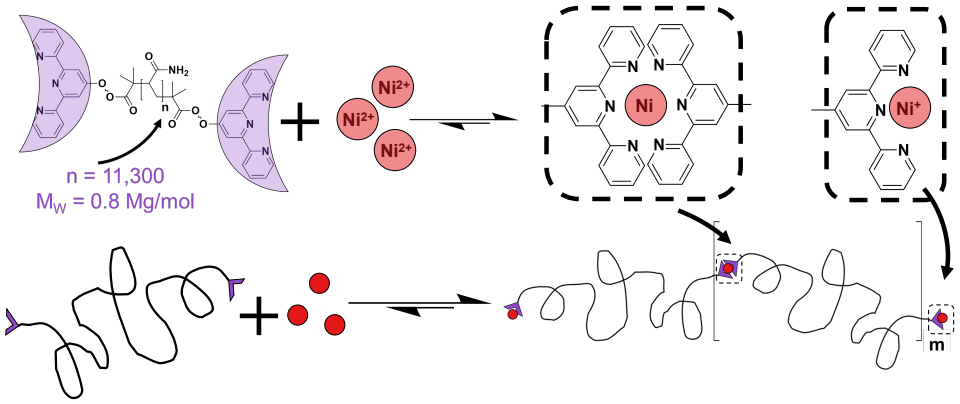

Figure 1.6: The formation of megasupramolecules from PAM with terpyridine ligands as end groups and Ni(II) ions.

Table 1.1: Equilibrium constant of selected associative chemical motifs. Values from Lewis et al. [43], Appel et al. [45], and Xu, Han, and Yan [51].

Chemistry	Association type	$\log_{10} K_1$	$\log_{10} K_2$	$\log_{10} K_{eq}$
Terpyridine + Ni	Metal-ligand	10.7	11.1	21.8
Terpyridine + Fe	Metal-ligand	7.1	13.8	20.9
Terpyridine + Cu	Metal-ligand	12.3	6.8	19.1
Spermine + CB[6]	Guest-host	-	-	11.5
Adamantane + β-CD	Guest-host	-	-	5.5
H-bond	Hydrogen bond	-	-	0.7

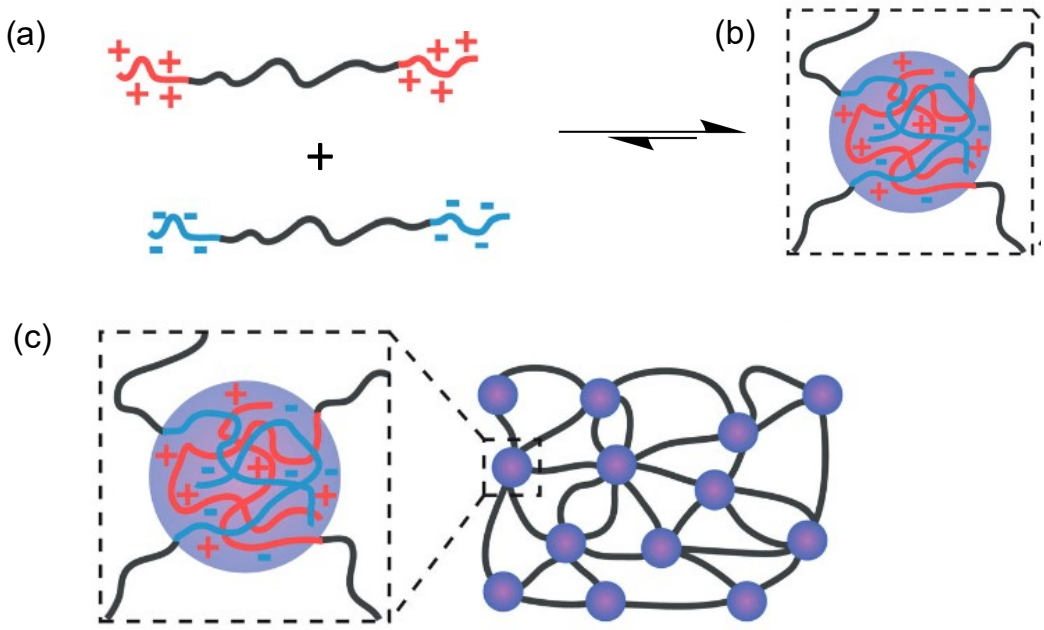

Figure 1.7: Cartoon schematic of ionic end-group associations. (a): Block copolymers with oppositely charged end groups. (b) A crosslink made from 4 unique polymer chains associated with one another via ionic interactions. (c): A polymer network or gel is formed from these crosslinks which connect > 2 polymer chains. Images modified from Appel et al. [45], reproduced with permission.

1.7). A single charged group will not strongly connect two polymer chains, so a single end group will consist of many repeat units with the same polarity in a row. The association strength depends on the number of charged repeat units in contact with one another. In contrast to the other types of associative bonds, a solution of di-functional, oppositely charged ionic polymers will form a gel instead of long linear polymers. Because of the many charged repeat units on a single polymer end, each end group can interact with more than one chain. By creating nodes which connect more than two polymers, the resulting network resembles a gel rather than a viscous liquid. Because of this possibility, my work focuses on guest-host and metal-ligand interactions.

Thermodynamics of associations

The equilibrium constants in Table 1.1 and thermodynamics in Equation 1.4 are based on solutions of the reacting species alone, prior to their integration into the polymer chain. The full energy balance for associations in polymers must also include the entropic cost of linking the polymer chains together. In the formation of linear megasupramolecules, that penalty is low: the reduced freedom of

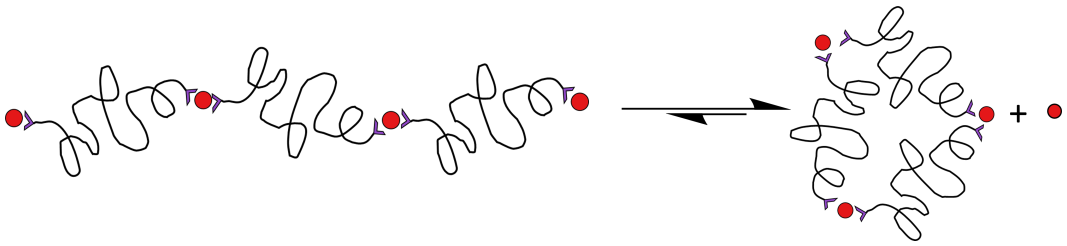

Figure 1.8: Cartoon schematic of the formation of ring-shaped megasupramolecules from metal-ligand based associations. The ligands on the ends come together and form a bis-complex, ejecting one metal ion.

motion only costs $3k_BT$ per association.[iv] The overall energy balance for linear megasupramolecules is

$$\Delta G = k_BT\left(-(m-1)\ln\left(K_{eq}\right) + 3(m-1)\right),$$

where m is the number of polymer repeat units in the megasupramolecule. Equivalently in $\log_{10}$:

$$\Delta G = k_BT\left(-2.3(m-1)\log_{10}\left(K_{eq}\right) + 3(m-1)\right). \tag{1.6}$$

In the case of metal-ligand interactions, the terminal end groups can also bind with metal ions from solution, although this does not increase the length of the megasupramolecule, it reduces ΔG by an additional $2.3 * \log_{10} K_1$ per ligand, so if enough metal ions are present in solution, those sites will also be occupied.

The associative end groups are also capable of forming ring-shaped, in addition to linear, supramolecules (Figure 1.8). The energetic cost of forming rings is

$$\Delta G = k_BT\left(-2.3 * \log_{10} K_{eq} + \frac{3}{2}\ln\left(m * N\right)\right), \tag{1.7}$$

where N is the number of repeat units in a single polymer and m is the number of polymers in the ring. In metal-ligand interactions, if a metal ion is ejected in this process, K_{eq} is replaced with K_2/K_1 to correctly model the change in ΔG. The formation of rings is highly discouraged by entropy, but for combinations of high K_{eq} and low $(m * N)$, it is a possibility. If

$$\log_{10} K_{eq} > 0.65\ln\left(m * N\right), \tag{1.8}$$

then the formation of rings has a negative ΔG. For $N = 10000$, which is equivalent to a PAM M_w of 800 kg/mol, the spontaneous formation of 1 and 2 membered rings is possible with terpyridine-Fe(II) interactions.

[iv] The change in entropy of the associating species is accounted for in K_{eq}, so we only need to add the change in entropy of the growing polymer chain.

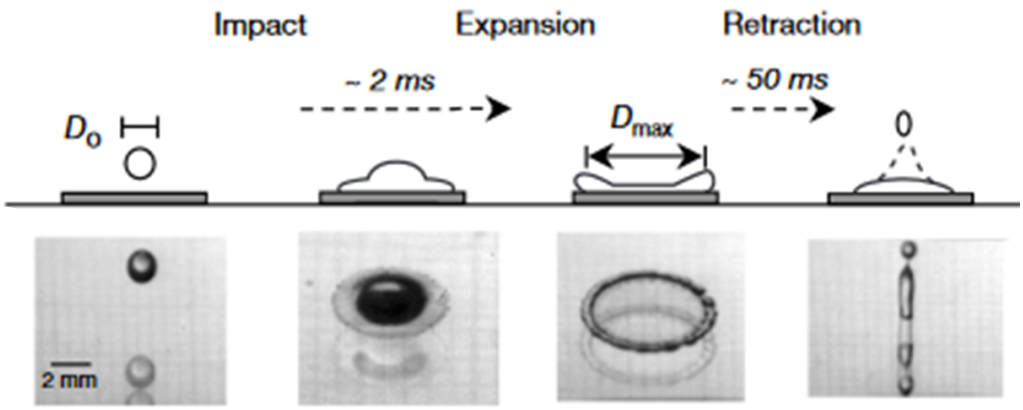

Figure 1.9: The phases of a droplet impact illustrated with a water droplet onto a hydrophobic substrate. Immediately after impact, the droplet enters the expansion phase until it reaches its maximum diameter, D_{max}. After which, it reverses direction and begins retraction. With enough energy, the droplet will rebound off the substrate after retraction phase. Images modified from Bergeron et al. [36]. Reprinted with permission.

1.4 Objective of this work

The overall objective of this work is to correlate the structure (molecular weight, concentration, and associative strength) of associative polymer solutions, their fluid properties (shear viscosity, η_S, and elongational viscosity, η_E), and the performance metrics of droplet rebound suppression in agriculture and mist suppression in aviation. The fluid properties can be measured in the lab more easily and precisely than performance in the targeted application, and thus the fluid properties can inform further development of the polymer solution structure.

Agriculture

In the targeted application of linear end associative polymers to improve droplet retention for agricultural sprays, the polymer additive serves an additional purpose.[59] Not only can it increase the droplet diameters sprayed from the nozzle to reduce drift, but it will also simultaneously reduce the rebound and splashing of the larger droplets it produces.

The droplet impact process comprises two main phases: expansion and retraction. They are marked by key moments: impact and maximum expansion (Figure 1.9). Regardless of the outcome, all droplets follow the same pattern. Starting from a spherical droplet falling towards the substrate, impact begins when the droplet makes contact with the target and begins expansion.[36,60–64] In the expansion phase, the momentum the droplet brings with impact causes the fluid to disrupt its spherical

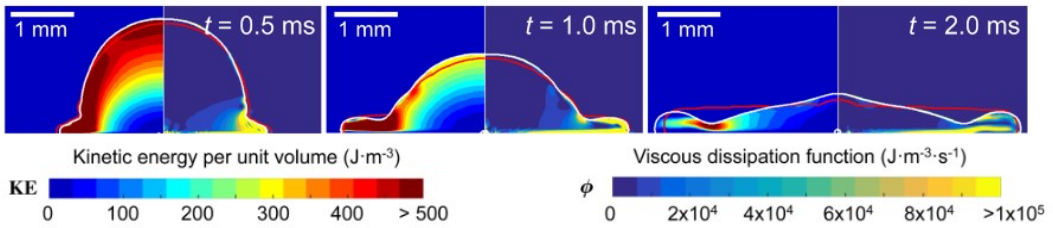

Figure 1.10: Numerical simulation of the time evolution of droplet impact for water droplets with velocity v = 1.0 m/s onto a steel surface. The contour map on the left depicts kinetic energy per unit volume, and on the right shows viscous dissipation per unit volume. Images and results from Lee et al. [65], reproduced with permission.

shape and flatten into a disc-like shape.[v] After some time, the droplet reaches its moment of maximum expansion where it momentarily has a velocity (v) and kinetic energy (KE) of 0 as it reverses direction. The retraction phase follows maximum expansion and is driven by surface tension. The fluid seeks to reduce the energy of its configuration by reducing the surface area exposed to both the atmosphere and the substrate and eventually reaches equilibrium.

There are velocity gradients parallel and perpendicular to the substrate, and both elongational and shear flow occurs substantially throughout the droplet's expansion and retraction (Figure 1.10). Thus, the increased η_E of polymer solutions will dissipate the kinetic energy of the droplet as it expands and retracts, resulting in lower velocity and increased deposition.

Fire suppression in aviation

In addition to fuel, there are other flammable fluids in an engine that can lead to uncontrolled fire in the event of an accident. The oils used for lubrication and thermal control in the engine (poly(α-olefins) (PAO)) are similarly dangerous to the fuel itself: they can create highly flammable mists if sprayed through an opening with sufficient pressure.[2,66]

The lubrication system is ideally a closed loop. In contrast to fuel in a combustion system, where the additives are intended to be consumed in the combustion process, additives to PAO are expected to persist until the oil is changed or a catastrophic event occurs. From a practical standpoint, the lubrication system is a much better target for designer, difficult-to-make, polymer additives. You derive the safety benefit for the entire lifetime of the PAO, which is much longer than the lifetime of the

[v] Sometimes this moment will have a large gradient in the thickness, where the outer rim is the thickest part of the droplet and the inner volume is a very thin layer.

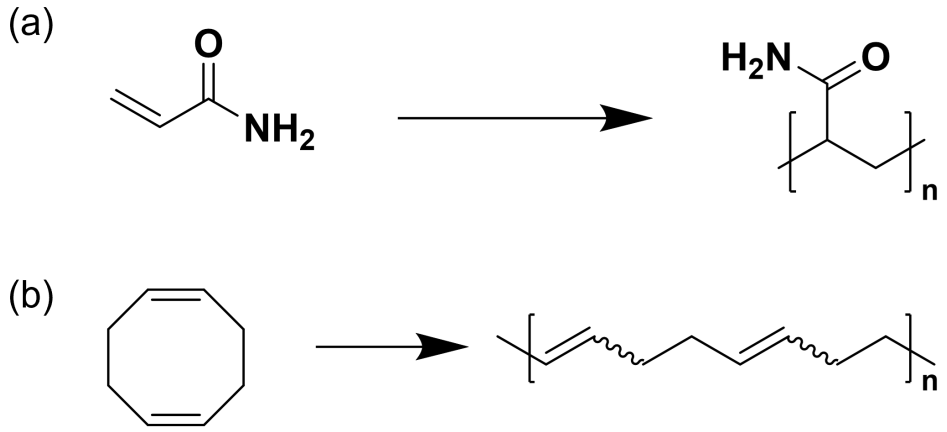

Figure 1.11: (a): The acrylamide monomer and its polymer, poly(acrylamide) (PAM). (b): 1,5 cyclooctadiene (COD) monomer and its polymer, poly(cyclooctadiene) (PCOD).

same volume of fuel. Consequently, the total mass of polymer additive required to improve PAO safety for a month of flights is dramatically less than the amount of fuel additive required for the same time span.

1.5 Scope of work performed

Structure: Types of polymers investigated in this work

In my thesis, I focus on two long, linear polymers ($> 10,000$ repeat units) with simple repeat units of acrylamide and octadiene (Figure 1.11). The polymers are similar in their length (long) and architecture (linear), but the different backbones imbue them with different solubility. PAM is soluble in H_2O due to its amide pendant groups interacting favorably with H_2O, and poly(cyclooctadiene) (PCOD) is soluble in organic liquids like jet fuel and engine oil. Because the PCOD backbone is entirely hydrocarbon based, it is insoluble in H_2O.

Both PAM and PCOD can be synthesized to high M_w and with low Đ. Because of their shared length and architecture, they affect their solvents in similar ways. The targeted applications of reducing rebound in droplet impact and reducing the formation of mists in fluid sprays are hypothesized to benefit from high η_E. As other processes such as pumping and mixing produce predominantly shear flows, a low η_S is desirable to preserve the practicality of these polymer solutions. To best meet this competing constraints, solutions with low polymer concentration are of interest. With sufficiently long polymers, even a small concentration can severely increase η_E which is accompanied by a relatively modest increase in η_S.

Therefore, I predominately test solutions with low concentrations of long, linear polymers, in both H_2O and PAO. Between terpyridine-metal, host-guest, and hydrogen bonding interactions, I tested associations with equilibrium constants from $10^{5.5}$ to 10^{22}. My experiments were restricted to polymers with $M_w > 0.8$ Mg/mol and solutions with concentrations < 2 weight %.

Properties: Improvements to the DoSER measurement technique

The DoSER instrument measures the minimum diameter of a filament of fluid as it evolves in time. In general, the evolution and shape of the filament depends on the balance of inertial forces (due to the density of the fluid), viscous forces (due to the shear viscosity of the fluid), and elastic forces (due to the polymers in solution) against capillary forces (due to the surface tension of the fluid). In practice, the fluids' behavior can be estimated as a single balance at any given time: either inerto-capillary (inertial balanced by capillary, IC), viscocapillary (viscous balanced by capillary, VC), or elastocapillary (elastic balanced by capillary, EC).

For example, to assume the fluid behavior is in the IC regime, the Ohnessorge number (Oh) is calculated:

$$Oh = \frac{\eta_S}{\sqrt{\sigma D \rho}}, \tag{1.9}$$

where η_S is the shear viscosity, σ is the surface tension, D is the diameter of the fluid droplet, and ρ is the fluid's density. If $Oh \ll 1$, then the contribution from η_S can be neglected in and capillary and inertial forces dominate.

In verifying and improving the DoSER technique, I used samples of pure solvent: H_2O and PAO. For both of these fluids, $Oh \ll 1$, and their behavior falls in the IC regime. I also studied solutions of pure solvent and polymer; filaments of these fluids first behaves according to the IC regime, but then as the experiment proceeds, the elastic forces eclipse those of inertia and the filament is better modeled by EC behavior. Critically, no fluids which demonstrate VC behavior are tested or analyzed in this work.

Performance: Droplet impact and mist suppression

To test the performance of aqueous solutions in droplet impact applications, I recorded single droplets produced *via* syringe pump as they impact onto parafilm substrates arriving normal to the surface with velocities between 0.5 and 4.8 m/s. With this method, I tested pure H_2O, solutions of water and glycerol, and aqueous solutions of traditional and associative PAM. Although the ultimate behavior

depends on the surface tension as well as the other fluid properties, I did not intentionally vary the surface tension outside of adding either glycerol or PAM to modify the solutions' viscosity.

To test the effect of PCOD in PAO for the aviation industry, mist suppression studies were done by Dr. Jacob Temme at the Army Research Laboratory (ARL). Solutions of pure PAO were compared to PAO with traditional and associative PCOD. Similarly to the droplet impact experiments, the surface tension was not intentionally varied, although we expect it to change the fluid's capacity to form mists.

References

[1] M. Damak, M. N. Hyder, and K. K. Varanasi. "Enhancing Droplet Deposition through In-Situ Precipitation". In: *Nature Communications* 7.1 (Nov. 25, 2016), p. 12560. ISSN: 2041-1723. DOI: 10.1038/ncomms12560. URL: http://www.nature.com/articles/ncomms12560 (visited on 02/05/2021).

[2] R. Horrocks and I. of Mechanical Engineers, eds. *Fuel Systems for IC Engines: 14 - 15 March 2012, IMechE, London ; [Papers from the IMechE's Fuel Systems for IC Engines Conference, the Latest in This Successful Series on Fuel Injection Systems for Internal Combustion Engines]*. IMechE C 1342. Oxford: WP, Woodhead Publ, 2012. 335 pp. ISBN: 978-0-85709-604-3 978-0-85709-210-6.

[3] S. Peng and R. Landel. "Rheological Behavior of FM-9 Solutions and Correlation with Flammability Test Results and Interpretations". In: *Journal of Non-Newtonian Fluid Mechanics* 12.1 (Jan. 1983), pp. 95–111. ISSN: 03770257. DOI: 10.1016/0377-0257(83)80007-X. URL: https://linkinghub.elsevier.com/retrieve/pii/037702578380007X (visited on 10/05/2022).

[4] M. H. Wei et al. "Megasupramolecules for Safer, Cleaner Fuel by End Association of Long Telechelic Polymers". In: *Science* 350.6256 (2015), pp. 72–75. ISSN: 10959203. DOI: 10.1126/science.aab0642.

[5] G. H. McKinley and T. Sridhar. "Filament-Stretching Rheometry of Complex Fluids". In: *Annual Review of Fluid Mechanics* 34.1 (2002), pp. 375–415. URL: http://www.annualreviews.org/doi/abs/10.1146/annurev.fluid.34.083001.125207 (visited on 03/23/2016).

[6] N. R. C. (U.S.) and N. R. C. (U.S.), eds. *Aviation Fuels with Improved Fire Safety: A Proceedings*. Washington, D.C: National Academy Press, 1997. 141 pp. ISBN: 978-0-309-05833-9.

[7] C. Clasen et al. "How Dilute Are Dilute Solutions in Extensional Flows?" In: *Journal of Rheology* 50.6 (Nov. 2006), pp. 849–881. ISSN: 0148-6055, 1520-8516. DOI: 10.1122/1.2357595. URL: http://sor.scitation.org/doi/10.1122/1.2357595 (visited on 05/14/2021).

[8] M. Rubinstein and R. H. Colby. *Polymer Physics*. Oxford ; New York: Oxford University Press, 2003. 440 pp. ISBN: 978-0-19-852059-7.

[9] "Über Die Mechanische Bedeutung Des Zweiten Hauptsatzes Der Wärmetheorie". In: L. Boltzmann. *Wissenschaftliche Abhandlungen*. Ed. by F. Hasenöhrl. 1st ed. Cambridge University Press, Aug. 23, 2012, pp. 9–33. ISBN: 978-1-108-05279-5 978-1-139-38142-0. DOI: 10.1017/CBO9781139381420.003. URL: https://www.cambridge.org/core/product/identifier/CBO9781139381420A008/type/book_part (visited on 10/04/2022).

[10] C. J. Petrie. "One Hundred Years of Extensional Flow". In: *Journal of Non-Newtonian Fluid Mechanics* 137.1-3 (Aug. 2006), pp. 1–14. ISSN: 03770257. DOI: 10.1016/j.jnnfm.2006.01.010. URL: https://linkinghub.elsevier.com/retrieve/pii/S037702570600036X (visited on 05/06/2020).

[11] B. Keshavarz et al. "Studying the Effects of Elongational Properties on Atomization of Weakly Viscoelastic Solutions Using Rayleigh Ohnesorge Jetting Extensional Rheometry (ROJER)". In: *Journal of Non-Newtonian Fluid Mechanics* 222 (Aug. 2015), pp. 171–189. ISSN: 03770257. DOI: 10.1016/j.jnnfm.2014.11.004. URL: https://linkinghub.elsevier.com/retrieve/pii/S0377025714002055 (visited on 02/12/2020).

[12] L. N. Jimenez et al. "Extensional Relaxation Time, Pinch-Off Dynamics, and Printability of Semidilute Polyelectrolyte Solutions". In: *Macromolecules* 51.14 (July 24, 2018), pp. 5191–5208. ISSN: 0024-9297, 1520-5835. DOI: 10.1021/acs.macromol.8b00148. URL: https://pubs.acs.org/doi/10.1021/acs.macromol.8b00148 (visited on 05/10/2021).

[13] K.-W. Hsiao et al. "Passive Non-Linear Microrheology for Determining Extensional Viscosity". In: *Physics of Fluids* 29.12 (Dec. 2017), p. 121603. ISSN: 1070-6631, 1089-7666. DOI: 10.1063/1.4993736. URL: http://aip.scitation.org/doi/10.1063/1.4993736 (visited on 05/10/2021).

[14] B. P. Robertson and M. A. Calabrese. *Volatile Dripping onto Substrate (vDoS) Extensional Rheology of Viscoelastic Polymer Solutions*. preprint. In Review, Nov. 8, 2021. DOI: 10.21203/rs.3.rs-964629/v1. URL: https://www.researchsquare.com/article/rs-964629/v1 (visited on 02/28/2022).

[15] W. Mathues et al. "CaBER vs ROJER—Different Time Scales for the Thinning of a Weakly Elastic Jet". In: *Journal of Rheology* 62.5 (Sept. 2018), pp. 1135–1153. ISSN: 0148-6055, 1520-8516. DOI: 10.1122/1.5021834. URL: http://sor.scitation.org/doi/10.1122/1.5021834 (visited on 03/24/2021).

[16] S. Kheirandish, I. Gubaydullin, and N. Willenbacher. "Shear and Elongational Flow Behavior of Acrylic Thickener Solutions. Part II: Effect of Gel Content". In: *Rheologica Acta* 48.4 (May 2009), pp. 397–407. ISSN: 0035-4511, 1435-1528. DOI: 10.1007/s00397-008-0324-x. URL: http://link.springer.com/10.1007/s00397-008-0324-x (visited on 05/05/2021).

[17] J. Dinic, L. N. Jimenez, and V. Sharma. "Pinch-off Dynamics and Dripping-onto-Substrate (DoS) Rheometry of Complex Fluids". In: *Lab on a Chip* 17.3 (2017), pp. 460–473. ISSN: 1473-0197, 1473-0189. DOI: 10.1039/C6LC01155A. URL: http://xlink.rsc.org/?DOI=C6LC01155A (visited on 01/08/2020).

[18] A. Zell et al. “Is There a Relationship between the Elongational Viscosity and the First Normal Stress Difference in Polymer Solutions?” Sept. 14, 2009. arXiv: 0909.2506 [cond-mat, physics:physics]. URL: http://arxiv.org/abs/0909.2506 (visited on 08/04/2020).

[19] J. Dinic et al. “Extensional Relaxation Times of Dilute, Aqueous Polymer Solutions”. In: *ACS Macro Letters* 4.7 (July 21, 2015), pp. 804–808. ISSN: 2161-1653, 2161-1653. DOI: 10.1021/acsmacrolett.5b00393. URL: https://pubs.acs.org/doi/10.1021/acsmacrolett.5b00393 (visited on 01/08/2020).

[20] M. Rosello et al. “Dripping-onto-Substrate Capillary Breakup Extensional Rheometry of Low-Viscosity Printing Inks”. In: *Journal of Non-Newtonian Fluid Mechanics* 266 (Apr. 2019), pp. 160–170. ISSN: 03770257. DOI: 10.1016/j.jnnfm.2019.03.006. URL: https://linkinghub.elsevier.com/retrieve/pii/S0377025718302994 (visited on 03/05/2020).

[21] K. T. Lauser, A. L. Rueter, and M. A. Calabrese. “Small-Volume Extensional Rheology of Concentrated Protein and Protein-Excipient Solutions”. In: *Soft Matter* 17.42 (2021), pp. 9624–9635. ISSN: 1744-683X, 1744-6848. DOI: 10.1039/D1SM01253C. URL: http://xlink.rsc.org/?DOI=D1SM01253C (visited on 07/12/2022).

[22] L. N. Jimenez, C. D. V. Martínez Narváez, and V. Sharma. “Capillary Breakup and Extensional Rheology Response of Food Thickener Cellulose Gum (NaCMC) in Salt-Free and Excess Salt Solutions”. In: *Physics of Fluids* 32.1 (Jan. 1, 2020), p. 012113. ISSN: 1070-6631, 1089-7666. DOI: 10.1063/1.5128254. URL: http://aip.scitation.org/doi/10.1063/1.5128254 (visited on 11/19/2020).

[23] L. E. Rodd et al. “Capillary Break-up Rheometry of Low-Viscosity Elastic Fluids”. In: *Applied Rheology* 15.1 (Feb. 1, 2005), pp. 12–27. ISSN: 1617-8106. DOI: 10.1515/arh-2005-0001. URL: https://www.degruyter.com/document/doi/10.1515/arh-2005-0001/html (visited on 08/04/2022).

[24] C. Tirel et al. “Multi-Scale Analysis of a Viscoelastic Liquid Jet”. In: *Journal of Non-Newtonian Fluid Mechanics* 245 (July 2017), pp. 1–10. ISSN: 03770257. DOI: 10.1016/j.jnnfm.2017.05.001. URL: https://linkinghub.elsevier.com/retrieve/pii/S0377025716303305 (visited on 10/28/2022).

[25] B. Keshavarz and G. H. McKinley. “Micro-Scale Extensional Rheometry Using Hyperbolic Converging/Diverging Channels and Jet Breakup”. In: *Biomicrofluidics* 10.4 (July 2016), p. 043502. ISSN: 1932-1058. DOI: 10.1063/1.4948235. URL: http://aip.scitation.org/doi/10.1063/1.4948235 (visited on 10/28/2022).

[26] E. Miller, C. Clasen, and J. P. Rothstein. "The Effect of Step-Stretch Parameters on Capillary Breakup Extensional Rheology (CaBER) Measurements". In: *Rheologica Acta* 48.6 (July 2009), pp. 625–639. ISSN: 0035-4511, 1435-1528. DOI: 10.1007/s00397-009-0357-9. URL: http://link.springer.com/10.1007/s00397-009-0357-9 (visited on 10/05/2022).

[27] R. S. Marano et al. "Polymer Additives as Mist Suppressants in Metalworking Fluids Part I: Laboratory and Plant Studies - Straight Mineral Oil Fluids". In: *S.A.E. Transactions* 104 (Section 5 1995), pp. 136–146.

[28] K. K. Chao et al. "Antimisting Action of Polymeric Additives in Jet Fuels". In: *AIChE Journal* 30.1 (Jan. 1984), pp. 111–120. ISSN: 0001-1541, 1547-5905. DOI: 10.1002/aic.690300116. URL: http://doi.wiley.com/10.1002/aic.690300116 (visited on 03/23/2016).

[29] R. W. Lewis et al. "Polymeric Drift Control Adjuvants for Agricultural Spraying". In: *Macromolecular Chemistry and Physics* 217.20 (Oct. 2016), pp. 2223–2242. ISSN: 10221352. DOI: 10.1002/macp.201600139. URL: https://onlinelibrary.wiley.com/doi/10.1002/macp.201600139 (visited on 03/23/2022).

[30] E. Hilz. "Spray Drift Review: The Extent to Which a Formulation Can Contribute to Spray Drift Reduction". In: *Crop Protection* (2013), p. 9.

[31] S. Kooij et al. "What Determines the Drop Size in Sprays?" In: *Physical Review X* 8.3 (July 20, 2018). ISSN: 2160-3308. DOI: 10.1103/PhysRevX.8.031019. URL: https://link.aps.org/doi/10.1103/PhysRevX.8.031019 (visited on 06/11/2020).

[32] V. Tirtaatmadja, G. H. McKinley, and J. J. Cooper-White. "Drop Formation and Breakup of Low Viscosity Elastic Fluids: Effects of Molecular Weight and Concentration". In: *Physics of Fluids* 18.4 (Apr. 2006), p. 043101. ISSN: 1070-6631, 1089-7666. DOI: 10.1063/1.2190469. URL: http://aip.scitation.org/doi/10.1063/1.2190469 (visited on 02/12/2020).

[33] B. Keshavarz et al. "Ligament Mediated Fragmentation of Viscoelastic Liquids". In: *Physical Review Letters* 117.15 (Oct. 7, 2016), p. 154502. ISSN: 0031-9007, 1079-7114. DOI: 10.1103/PhysRevLett.117.154502. URL: https://link.aps.org/doi/10.1103/PhysRevLett.117.154502 (visited on 02/12/2020).

[34] R. P. Mun, J. A. Byars, and D. V. Boger. "The Effects of Polymer Concentration and Molecular Weight on the Breakup of Laminar Capillary Jets". In: (1998), p. 13. DOI: 10.1016/S0377-0257(97)00074-8.

[35] A. N. Rozhkov. "Dynamics and Breakup of Viscoelastic Liquids (A Review)". In: *Fluid Dynamics* 40.6 (Nov. 2005), pp. 835–853. ISSN: 0015-4628, 1573-8507. DOI: 10.1007/s10697-006-0001-7. URL: http://link.springer.com/10.1007/s10697-006-0001-7 (visited on 09/30/2022).

[36] V. Bergeron et al. “Controlling Droplet Deposition with Polymer Additives”. In: *Nature* 405.6788 (June 2000), pp. 772–775. ISSN: 0028-0836, 1476-4687. DOI: 10.1038/35015525. URL: http://www.nature.com/articles/35015525 (visited on 08/05/2020).

[37] E. J. Soares. “Review of Mechanical Degradation and De-Aggregation of Drag Reducing Polymers in Turbulent Flows”. In: *Journal of Non-Newtonian Fluid Mechanics* 276 (Feb. 2020), p. 104225. ISSN: 03770257. DOI: 10.1016/j.jnnfm.2019.104225. URL: https://linkinghub.elsevier.com/retrieve/pii/S0377025719304197 (visited on 11/19/2020).

[38] S. Jouenne et al. “Degradation (or Lack Thereof) and Drag Reduction of HPAM Solutions During Transport in Turbulent Flow in Pipelines”. In: *Oil and Gas Facilities* 4.01 (Feb. 12, 2015), pp. 80–92. ISSN: 2224-4514. DOI: 10.2118/169699-PA. URL: https://onepetro.org/OGF/article/4/01/80/207287/Degradation-or-Lack-Thereof-and-Drag-Reduction-of (visited on 03/24/2022).

[39] P. Nghe, P. Tabeling, and A. Ajdari. “Flow-Induced Polymer Degradation Probed by a High Throughput Microfluidic Set-Up”. In: *Journal of Non-Newtonian Fluid Mechanics* 165.7 (2010), pp. 313–322. URL: http://www.sciencedirect.com/science/article/pii/S037702571000008X (visited on 09/13/2016).

[40] L. M. Ver Vers. “Determination of Acrylamide Monomer in Polyacrylamide Degradation Studies by High-Performance Liquid Chromatography”. In: *Journal of Chromatographic Science* 37.12 (Dec. 1, 1999), pp. 486–494. ISSN: 0021-9665, 1945-239X. DOI: 10.1093/chromsci/37.12.486. URL: https://academic.oup.com/chromsci/article-lookup/doi/10.1093/chromsci/37.12.486 (visited on 03/30/2022).

[41] E. A. Smith, S. L. Prues, and F. W. Oehme. “Environmental Degradation of Polyacrylamides”. In: *Ecotoxicology and Environmental Safety* 37.1 (June 1997), pp. 76–91. ISSN: 01476513. DOI: 10.1006/eesa.1997.1527. URL: https://linkinghub.elsevier.com/retrieve/pii/S014765139791527X (visited on 03/30/2022).

[42] K. Brakstad and C. Rosenkilde. “Modelling Viscosity and Mechanical Degradation of Polyacrylamide Solutions in Porous Media”. In: *All Days*. SPE Improved Oil Recovery Conference. Tulsa, Oklahoma, USA: SPE, Apr. 11, 2016, SPE-179593–MS. DOI: 10.2118/179593-MS. URL: https://onepetro.org/SPEIOR/proceedings/16IOR/All-16IOR/Tulsa,%20Oklahoma,%20USA/187343 (visited on 03/23/2022).

[43] R. W. Lewis et al. “Ultra-High Molecular Weight Linear Coordination Polymers with Terpyridine Ligands”. In: *Chemical Science* 10.24 (2019), pp. 6174–6183. ISSN: 2041-6520, 2041-6539. DOI: 10.1039/C9SC01115C. URL: http://xlink.rsc.org/?DOI=C9SC01115C (visited on 08/25/2021).

[44] R. C. Lhota. "Rheological Characterization of Polymer Additives for Mist Control and Drag Reduction". California Institute of Technology, May 27, 2022. DOI: 10.7907/WAV1-4T47. URL: https://resolver.caltech.edu/CaltechTHESIS:05262022-231652129 (visited on 09/30/2022).

[45] E. A. Appel et al. "Supramolecular Polymeric Hydrogels". In: *Chemical Society Reviews* 41.18 (2012), p. 6195. ISSN: 0306-0012. DOI: 10.1039/c2cs35264h. URL: http://xlink.rsc.org/?DOI=c2cs35264h.

[46] M. V. Rekharsky and Y. Inoue. "Complexation Thermodynamics of Cyclodextrins". In: *Chemical Reviews* 98.5 (July 30, 1998), pp. 1875–1918. ISSN: 0009-2665, 1520-6890. DOI: 10.1021/cr970015o. URL: https://pubs.acs.org/doi/10.1021/cr970015o (visited on 09/09/2022).

[47] P. Ahmadi and J. B. Ghasemi. "3D-QSAR and Docking Studies of the Stability Constants of Different Guest Molecules with Beta-Cyclodextrin". In: *Journal of Inclusion Phenomena and Macrocyclic Chemistry* 79.3-4 (Aug. 2014), pp. 401–413. ISSN: 1388-3127, 1573-1111. DOI: 10.1007/s10847-013-0363-5. URL: http://link.springer.com/10.1007/s10847-013-0363-5 (visited on 09/09/2022).

[48] A. Harada, Y. Takashima, and M. Nakahata. "Supramolecular Polymeric Materials via Cyclodextrin–Guest Interactions". In: *Accounts of Chemical Research* 47.7 (July 15, 2014), pp. 2128–2140. ISSN: 0001-4842, 1520-4898. DOI: 10.1021/ar500109h. URL: https://pubs.acs.org/doi/10.1021/ar500109h (visited on 09/09/2022).

[49] S. Liu et al. "The Cucurbit[*n*]Uril Family: Prime Components for Self-Sorting Systems". In: *Journal of the American Chemical Society* 127.45 (Nov. 1, 2005), pp. 15959–15967. ISSN: 0002-7863, 1520-5126. DOI: 10.1021/ja055013x. URL: https://pubs.acs.org/doi/10.1021/ja055013x (visited on 10/05/2022).

[50] D. Taura et al. "Macromolecular Recognition of Cyclodextrin: Inversion of Selectivity of Beta-Cyclodextrin toward Adamantyl Groups Induced by Macromolecular Chains: Macromolecular Recognition of Cyclodextrin: Inversion of Selectivity of . . . " In: *Macromolecular Rapid Communications* 30.20 (Oct. 19, 2009), pp. 1741–1744. ISSN: 10221336. DOI: 10.1002/marc.200900283. URL: https://onlinelibrary.wiley.com/doi/10.1002/marc.200900283 (visited on 09/09/2022).

[51] Q. Xu, B. Han, and H. Yan. "Equilibrium Constant and Enthalpy for the Hydrogen Bonding of Acetic Acid with Tetrahydrofuran in Supercritical CO $_2$". In: *The Journal of Physical Chemistry A* 103.27 (July 1, 1999), pp. 5240–5245. ISSN: 1089-5639, 1520-5215. DOI: 10.1021/jp9900739. URL: https://pubs.acs.org/doi/10.1021/jp9900739 (visited on 10/05/2022).

[52] H. Kim. "New Long End-Associative Polymers for Mist Control in I. Aqueous Solutions and II. Hydrocarbon Solvents". California Institute of Technology, Aug. 26, 2022. DOI: 10.7907/RSX9-QT39. URL: https://resolver.caltech.edu/CaltechTHESIS:08252022-035254306 (visited on 09/30/2022).

[53] R. Shunmugam et al. "Metal-Ligand-Containing Polymers: Terpyridine as the Supramolecular Unit: Metal-Ligand-Containing Polymers: Terpyridine as . . . " In: *Macromolecular Rapid Communications* 31.9-10 (May 12, 2010), pp. 784–793. ISSN: 10221336. DOI: 10.1002/marc.200900869. URL: https://onlinelibrary.wiley.com/doi/10.1002/marc.200900869 (visited on 09/27/2021).

[54] L. Wang et al. "Introducing Seven Transition Metal Ions into Terpyridine-Based Supramolecules: Self-Assembly and Dynamic Ligand Exchange Study". In: *Journal of the American Chemical Society* 142.4 (Jan. 29, 2020), pp. 1811–1821. ISSN: 0002-7863, 1520-5126. DOI: 10.1021/jacs.9b09497. URL: https://pubs.acs.org/doi/10.1021/jacs.9b09497 (visited on 02/25/2022).

[55] Yan et al. "Linear and Nonlinear Dynamic Behavior of Polymer Micellar Assemblies Connected by Metallo-Supramolecular Interactions". In: *Polymers* 11.10 (Sept. 20, 2019), p. 1532. ISSN: 2073-4360. DOI: 10.3390/polym11101532. URL: https://www.mdpi.com/2073-4360/11/10/1532 (visited on 05/05/2021).

[56] S. C. Grindy et al. "Control of Hierarchical Polymer Mechanics with Bioinspired Metal-Coordination Dynamics". In: *Nature Materials* 14.12 (Dec. 2015), pp. 1210–1216. ISSN: 14764660. DOI: 10.1038/nmat4401. URL: http://www.nature.com/articles/nmat4401.

[57] Q. Li et al. "Controlling Hydrogel Mechanics via Bio-Inspired Polymer-Nanoparticle Bond Dynamics". In: *ACS Nano* 10.1 (Jan. 2016), pp. 1317–1324. ISSN: 1936086X. DOI: 10.1021/acsnano.5b06692. URL: http://pubs.acs.org/doi/10.1021/acsnano.5b06692.

[58] N. Holten-Andersen et al. "pH-induced Metal-Ligand Cross-Links Inspired by Mussel Yield Self-Healing Polymer Networks with near-Covalent Elastic Moduli". In: *Proceedings of the National Academy of Sciences of the United States of America* 108.7 (2011), pp. 2651–2655. ISSN: 00278424. DOI: 10.1073/pnas.1015862108.

[59] M. Xu et al. "Quantifying the Effect of Extensional Rheology on the Retention of Agricultural Sprays". In: *Physics of Fluids* 33.3 (Mar. 1, 2021), p. 032107. ISSN: 1070-6631, 1089-7666. DOI: 10.1063/5.0038391. URL: https://aip.scitation.org/doi/10.1063/5.0038391 (visited on 03/15/2021).

[60] B. V. Orme et al. “Droplet Retention and Shedding on Slippery Substrates”. In: *Langmuir* 35.28 (July 16, 2019), pp. 9146–9151. ISSN: 0743-7463, 1520-5827. DOI: 10.1021/acs.langmuir.9b00931. URL: https://pubs.acs.org/doi/10.1021/acs.langmuir.9b00931 (visited on 10/15/2020).

[61] E. Villermaux. “Fragmentation versus Cohesion”. In: *Journal of Fluid Mechanics* 898 (Sept. 10, 2020), P1. ISSN: 0022-1120, 1469-7645. DOI: 10.1017/jfm.2020.366. URL: https://www.cambridge.org/core/product/identifier/S0022112020003663/type/journal_article (visited on 03/24/2021).

[62] Y. Song et al. “The Use of Folate/Zinc Supramolecular Hydrogels to Increase Droplet Deposition on *Chenopodium Album* L. Leaves”. In: *ACS Sustainable Chemistry & Engineering* 8.34 (Aug. 31, 2020), pp. 12911–12919. ISSN: 2168-0485, 2168-0485. DOI: 10.1021/acssuschemeng.0c03396. URL: https://pubs.acs.org/doi/10.1021/acssuschemeng.0c03396 (visited on 09/17/2020).

[63] G. J. Dorr et al. “Spray Retention on Whole Plants: Modelling, Simulations and Experiments”. In: *Crop Protection* 88 (Oct. 2016), pp. 118–130. ISSN: 02612194. DOI: 10.1016/j.cropro.2016.06.003. URL: https://linkinghub.elsevier.com/retrieve/pii/S026121941630134X (visited on 03/25/2021).

[64] M. Qin et al. “On the Role of Liquid Viscosity in Affecting Droplet Spreading on a Smooth Solid Surface”. In: *International Journal of Multiphase Flow* 117 (Aug. 2019), pp. 53–63. ISSN: 03019322. DOI: 10.1016/j.ijmultiphaseflow.2019.05.002. URL: https://linkinghub.elsevier.com/retrieve/pii/S0301932218308772 (visited on 06/07/2022).

[65] J. B. Lee et al. “Energy Budget of Liquid Drop Impact at Maximum Spreading: Numerical Simulations and Experiments”. In: *Langmuir* 32.5 (Feb. 9, 2016), pp. 1279–1288. ISSN: 0743-7463, 1520-5827. DOI: 10.1021/acs.langmuir.5b03848. URL: https://pubs.acs.org/doi/10.1021/acs.langmuir.5b03848 (visited on 12/16/2020).

[66] Department of Defense. *Performance Specification Coolant Fluid, Hydrolytically Stable, Dielectric*. MIL-PRF-87252E. Department of Defense, Mar. 21, 2018. DOI: 10.1520/MNL10848M. URL: http://www.astm.org/doiLink.cgi?MNL10848M (visited on 08/01/2022).

Chapter 2

MINIMIZING VARIANCE AND BIAS IN DRIPPING-ONTO-SUBSTRATE RHEOMETRY (DOSER) BY OPTIMIZING GAP DISTANCE AND AUTOMATING IMAGE ANALYSIS

The work in this chapter is in preparation for submission as an invited manuscript to Physics of Fluids . *The experiments were conceived by RWL, Dr. Red Lhota, and Professor Julie Kornfield. The experiments were executed by RWL. The image and data analysis software package and workflow was designed and implemented by RWL and Dr. Lhota. The PAM was synthesized by Dr. Hojin Kim. The manuscript was prepared by RWL, Dr. Lhota, and Professor Kornfield.*

Dripping onto substrate extensional rheometry (DoSER) is a valuable method to measure extensional properties, expands the range of fluids that can be characterized to include solutions with elongational relaxation times (λ_E) $<$ 1 ms, and uses a simple apparatus with three key components: a needle, a substrate, and a video camera. Two obstacles to adoption of the method are insufficient guidance regarding the configuration (e.g., needle diameter, needle-substrate gap height, substrate) for a fluid of interest and the subjective decisions that are involved in current data analysis procedures. Here, we describe the relationship of fluid properties and the optimal gap height to minimize variability in droplet behavior and an algorithm that eliminates subjectivity from the determination of the critical time. Implementing these guidelines and data processing techniques reduces experimental variance and accelerates the research pipeline because the processing is fully automated. These protocols enable new DoSER users to begin generating high quality data more quickly and previously unexplored fluids to be tested on DoSER more easily.

2.1 Dripping onto substrate elongational rheometry (DoSER)

Elongational flow is prevalent in myriad industrial processes such as spraying, printing, and fuel injection.[1–4] In polymeric solutions, the elongational viscosity (η_E) can be orders of magnitudes higher than the shear viscosity (η) and dictate the overall behavior of the process. Furthermore, in polymeric solutions, η_E cannot be estimated from η and must be measured independently.[5,6] To measure it, scientists induce a controlled elongational flow field and measure the fluid's response.[7]

Commercially available elongational rheometers (e.g., capillary breakup extensional rheometer) cannot be used to measure dilute polymer solutions due to the strain being applied in a step-like manner.[8,9] When the solution's relaxation time is on the order of the milliseconds, the fluid filament will break before the instrument has finished applying the strain.[10,11] To address this deficiency, Dinic et al developed the dripping onto substrate elongational rheometry (DoSER) which excels at measuring an array of fluids, including low concentration polymer solutions.[9,12,13] Furthermore, solutions with low η present an additional practical challenge: the samples cannot be easily loaded onto the plates of the CaBER instrument. Briefly, the DoSER technique works as follows: a small (10 to 20 uL) volume of fluid is dispensed from a needle and brought into contact with a substrate underneath (Figure 2.1 (a)). The fluid transfers from the needle to the substrate by forming a liquid bridge between the two. This process occurs on the order of milliseconds and is filmed with a high-speed video camera (Figure 2.1 (b)). From the high speed video, the shape of the liquid bridge and the minimum diameter at each frame is extracted to find the diameter at each time, normalized by the outer-diameter of the needle $\frac{D(t)}{D_0}$. There are myriad excellent references on establishing the DoSER technique which go into greater detail.[4,9,12–15] The other DoSER instruments constructed in a similar way do not exactly replicate the hardware used by Dinic et. al.[7,13] The associated data analysis can be similarly unique.

For example, the critical time (t_c) marks the transition to fluid behavior in the elasto-capillary (EC) regime. Preceding t_c, the fluid exhibits either inertio-capillary (IC) or viscocapillary (VC) behavior depending on its η, density (ρ), surface tension (σ), and the outer diameter of the needle (D_0) arranged into the dimensionless Ohnessorge number ($Oh = \frac{\eta}{\sqrt{D_0 \rho \sigma}}$).[13] If $Oh \ll 1$, the fluid follows IC behavior; when $Oh \gtrsim 1$ the fluid exhibits VC behavior. In prior literature, t_c is identified manually by eye.[7,9,13,16]

We address the variation in hardware by systematically testing DoSER configurations and providing guidelines for the initial conditions for the data collection phase of the experiment. We also developed methods to consistently process high speed videos and objectively identify the t_c. To ensure our results will generalize to the array of fluids which can be tested using DoSER, we investigated low concentration, aqueous solutions of poly(acrylamide), its solvent (H_2O, $Oh = 0.002$), and a chemically distinct solvent: poly(alpha olefin) (BRAYCO 889 MIC) (PAO, $Oh = 0.01$). Both H_2O and PAO behave according to the IC behavior.Aqueous PAM demonstrates EC

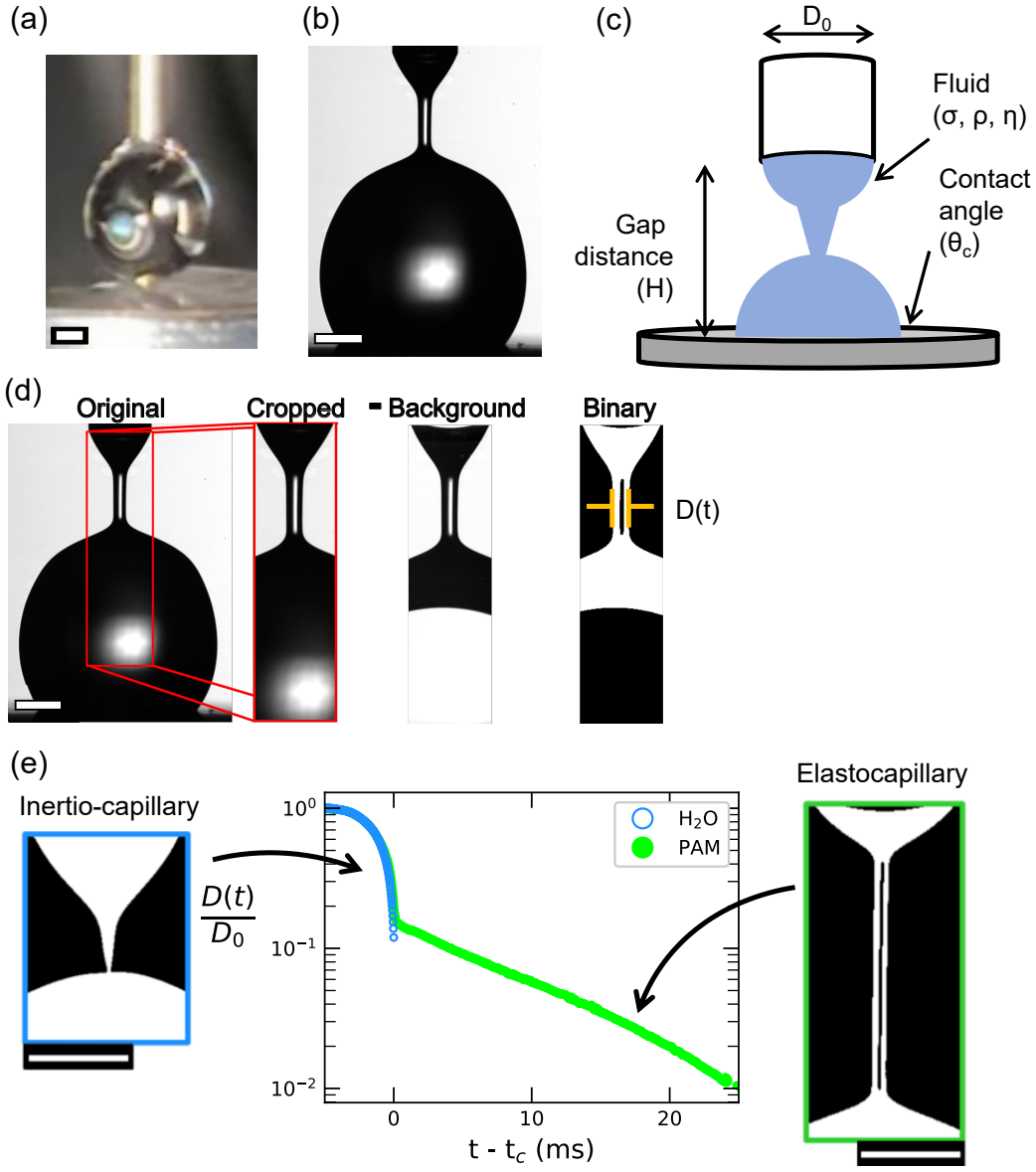

Figure 2.1: (a) Photograph showing a droplet of water suspended from the needle, about to make contact with the substrate. (b) A single image from the video camera of a DoSER experiment with an elasto-capillary fluid. (c) Schematic representation of the DoSER experiment, with relevant parameters labeled. (d) Example of the image processing pipeline. The binarized image is analyzed to determine the minimum diameter of each frame, $D(t)$. (e) Example DoSER traces for interio-capillary behavior (H_2O) and elastocapillary behavior (PAM solution). The scale bars represent 0.5 mm throughout.

behavior and we determine the elongational relaxation time (λ_E) and elongation viscosity (η_E) of the PAM solutions.

We present contributions to the DoSER procedure at each stage: the mechanical setup of the experiment and its initial conditions (Figure 2.1 (c)); the image processing pipeline to create a numerical dataset (Figure 2.1 (d)); and the analysis of the EC dataset. At each step in this process, we aim to reduce experimental variation and opportunity for a researcher's bias to corrupt the analysis. We achieve this by delegating as many decisions as possible to the fluid and its dataset. For the experimental set up, we let other measurable characteristics of the fluid, such as σ and ρ, dictate the initial conditions of gap distance and substrate selection. In image analysis, we rely on the images themselves to dictate the binarization threshold using the Otsu binarization algorithm;[17] in data analysis, we use signatures within the dataset to tell us where the EC behavior begins.

2.2 Initial conditions and experimental setup

Gap distance H effects on inertio-capillary fluids

To understand the effect of the gap distance (H) on DOSER measurements, we systematically varied H for different fluids (Table A.2), with three different size needles (Table A.1). All of the combinations of fluids and needle diameters satisfy the criterion for intertio-capillary (rather than visco-capillary) behavior: $Oh = \eta/(D_0\rho\sigma)^{1/2} \ll 1$. In inertio-capillary (IC) fluids, the balance of inertial and capillary fluids dictate the evolution of the liquid bridge; the effect of viscosity can be neglected. Water (H_2O) is an excellent example of an IC fluid, as the surface tension is quite high and the viscosity is relatively low, leading to $Oh \ll 1$. Both H_2O and PAO exhibit similar failure modes when H takes extreme low or high values. When H is small, the fluid does not transfer to the substrate but instead reaches an equilibrium spanning from the needle to the substrate, we call this "premature cessation." When H is large, the fluid separates from the needle before making contact with the substrate, forming a short lived free-falling droplet, which we call "premature separation" (Figure 2.2b). Premature cessation of flow occurs when the fluid makes contact with the substrate prior to reaching a volume sufficient to make a free drop. Premature separation occurs when there is enough vertical clearance to fit the free droplet of fluid as well as the necking region near the needle prior to making contact with the substrate. The size of a free droplet of fluid, therefore, plays a central role in the range of H in which DoSER measurements are feasible.

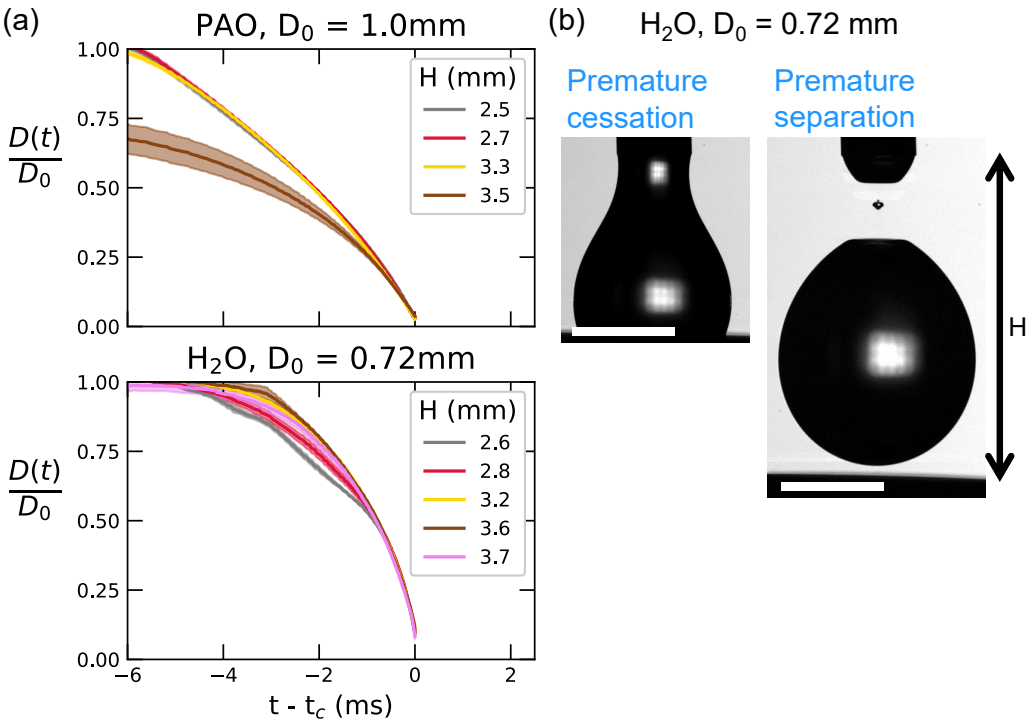

Figure 2.2: (a) Normalized minimum diameter ($D(t)/D_0$) for n = 5 replicated experiments (the shaded bands show ± one standard error) for selected values of gap height (H): (top) polyalphaolefin (PAO), (bottom) H_2O. (b) Failure of the experiment occurs when (left) H is so small that cessation of the flow occurs prior to pinch-off or (right) H is so large that a free falling droplet punches off prior to contact with the substrate. The scale bars represent 1 mm. Note that the values of H in part (b) are just outside of the range of H values for H_2O in part (a).

Beyond feasibility, the H used for DoSER experiments would ideally minimize experimental artifacts. Newtonian fluids that exhibit IC behavior ($Oh << 1$) are useful for detecting experimental artifacts because their behavior is well understood. In IC behavior, the moment the liquid bridge breaks is called the pinch-off time or the critical time (t_c). Increasing the quantity ($t_c - t$), i.e., going backwards in time, the diameter of the thinnest part of the liquid bridge increases in a predictable manner:[9,12]

$$\frac{D_{IC}(t)}{D_0} = \alpha \left(\frac{8\sigma}{\rho D_0^3} \right)^{\frac{1}{3}} (t_c - t)^{\frac{2}{3}}. \tag{2.1}$$

The leading coefficient α is a numerical prefactor, typically between 0.4 and 1.[18–21] Equation 2.1 provides an objective way to identify values of H that minimize the deviation between the observed $\frac{D(t)}{D_0}$ and the well-established IC behavior $\frac{D_{IC}(t)}{D_0}$. Therefore we calculate the residual for each frame $\left| \left(\frac{D(t)}{D_0} \right) - \left(\frac{D_{IC}(t)}{D_0} \right) \right|$ and calculate

an average residual:

$$\text{Average Residual} = \frac{1}{f_2 - f_1} \sum_{f=f_1}^{f_2} \left| \frac{D(f)}{D_0} - \frac{D_{IC}(f)}{D_0} \right|, \tag{2.2}$$

where f refers to a specific frame, f_1 is the frame in which $\frac{D(t)}{D_0}$ is closest to $\frac{1}{2}$, and f_2 is the first frame where $\frac{D(t)}{D_0} = 0$.

Literature guidance for selecting H is based on D_0, ranging from $1.4D_0$ to $3D_0$. In our experiments, $H = 1.4D_0$ is in the regime of premature cessation for all three cases, as is $H = 3D_0$ for one case, H_2O with $D_0 = 0.72$ mm (Figure 2.4, left). In each case, there are values of H for which the average residual is $< 1\%$; however, these values of H are not simply proportional to D_0.

Instead of D_0, we propose using the theoretical prediction for the diameter of a free drop (D_{pred}) as the characteristic length scale (Figure 2.3):

$$D_{pred} = \left(\frac{6 D_{inner} \sigma}{\Delta \rho g} \right)^{\frac{1}{3}}, \tag{2.3}$$

where D_{inner} is the inner diameter of the needle, σ is the fluid's surface tension, $\Delta\rho$ is the density difference between the fluid and air, and g is the acceleration due to gravity.[22–24]

For each pair of needle diameter and fluid, we present the Average Residual in two ways: as a function of the gap distance in absolute terms and in a dimensionless form, H/D_{pred} (Figure 2.4). When we consider only the dimensional height H (Figure 2.4, left), the lower bound ranges from 2.0 to 3.0 mm and the upper bound ranges from 3.9 to 5.6 mm. Viewing the results in terms of the free droplet size, H/D_{pred} (Figure 2.4, right), the bounds for premature cessation fall into a narrow range of $0.8 < H/D_{pred} < 0.9$ and the bounds for premature separation fall into a range between $1.5 < H/D_{pred} < 1.7$. Moreover, the H values that consistently provide low average residuals cluster near $H/D_{pred} \approx 1.2$ for all pairs of fluid and needle. It is interesting that the optimal values of H are dictated using a criterion that is independent of the substrate (in Table A.2 contact angles range from 19° to 71°). Our reasoning focuses on physics that is agnostic to the substrate: proximity of the substrate to a dangling drop or release of a free drop without contact with the substrate. We considered the consequences of contact angle on the subsequent fluid dynamics using the free droplet volume as a characteristic volume and using the contact angle to estimate h, the height of the spherical cap. For all of the

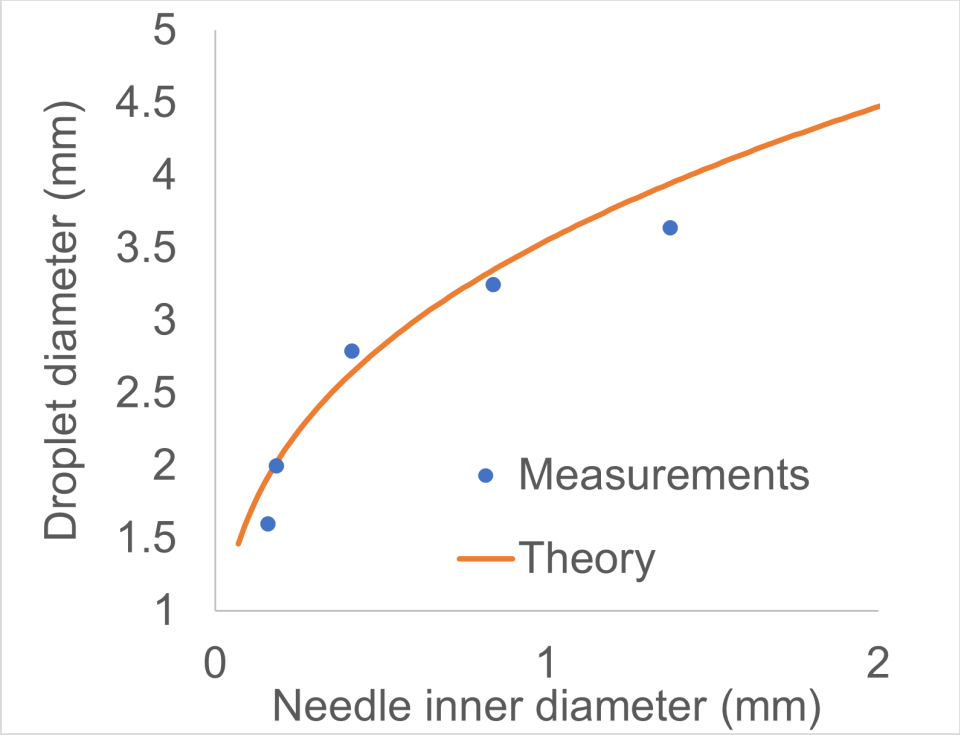

Figure 2.3: Measured diameter of water droplets from needles with a variety of inner diameters, shown with the diameter's predicted by Equation 2.3.

combinations of fluid and substrate we tested, h ranges from $0.2D_{pred}$ to $0.4D_{pred}$. Incorporating the height of the spherical cap, we can restate our guideline for gap distance: using $H - h \approx 0.9D_{pred}$ will render reproducible DoSER results which match the behavior predicted by the IC theory. From our perspective, $H = 1.2D_{pred}$ is a much more practical recommendation, and its success underscores the idea that the fluid properties dominate the physics, while the substrate contributes only a 20 to 30% effect on the ideal H.

Our guideline is based purely on the inner needle diameter which is provided by the manufacturer and properties of the fluid which can be measured independently from the DoSER technique. A researcher can setup a DoSER measurement on a new fluid with high confidence that the selected values of H will provide producible and accurate measurements *a priori*, without requiring a time consuming evaluation of the parameters. Consistently following the procedure also further enables fair comparison between fluids of different physical properties, such as polar and non-polar solvents.

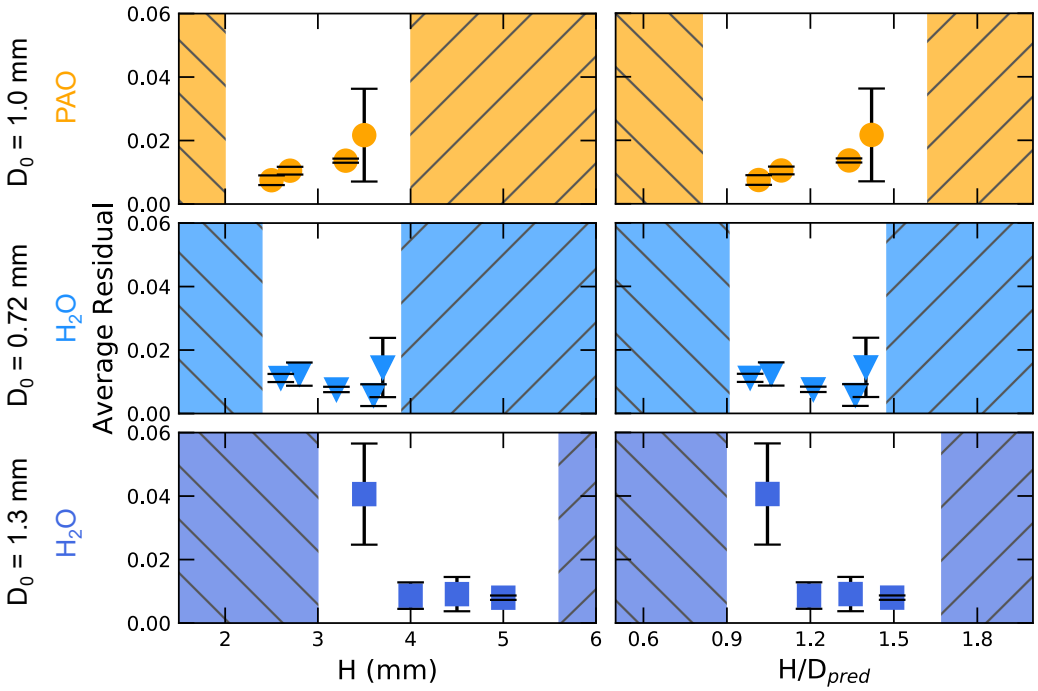

Figure 2.4: (left) Ranges of gap height (H) below the minimum imposed by cessation prior to pinch off (hashed \), H for which dripping onto aluminum substrate occurs (results shown for average residual defined in Equation 2.2), and H greater than the maximum imposed by free droplet formation prior to contact with the substrate (hashed /). (right) The same ranges presented in terms of dimensionless gap distance using the theoretical free droplet diameter D_{pred}. For D_0 = 1.0 mm, D_{pred}^{PAO} = 2.5 mm; for D_0 = 0.72 mm, $D_{pred}^{H_2O}$ = 2.6 mm; and for D_0 = 1.3 mm, $D_{pred}^{H_2O}$ = 3.3 mm, (Equation 2.3). Symbols show the average of n = 5 replicates; error bars show ± one standard deviation.

Substrate effects for inertio-capillary fluids

Using H values in the acceptable range determined from subsection 2.2 (PAO: H = 3.3 mm, H/D_{pred} = 1.3; H_2O: H = 3.5 mm, H/D_{pred} = 1.3), we subjected both PAO and H_2O to DoSER experiments on two substrates. We used aluminum, as insubsection 2.2, and clean glass substrates, which are commonly used in other literature employing the DoSER technique.[4,13,15] Additionally, we measured the contact angle (θ_c) between the fluid and the substrates using the same optical setup (Figure 2.5a).

PAO ($\sigma \approx 30$ mN/m)[25] had lower contact angles with both substrates and formed thin, wide puddles of fluid on both glass and aluminum (Figure 2.5a top). Dripping onto both substrates produced low residual, low variance DoSER traces (Figure 2.5c). H_2O ($\sigma \approx 73$ mN/m) behaved very differently on the two substrates. The

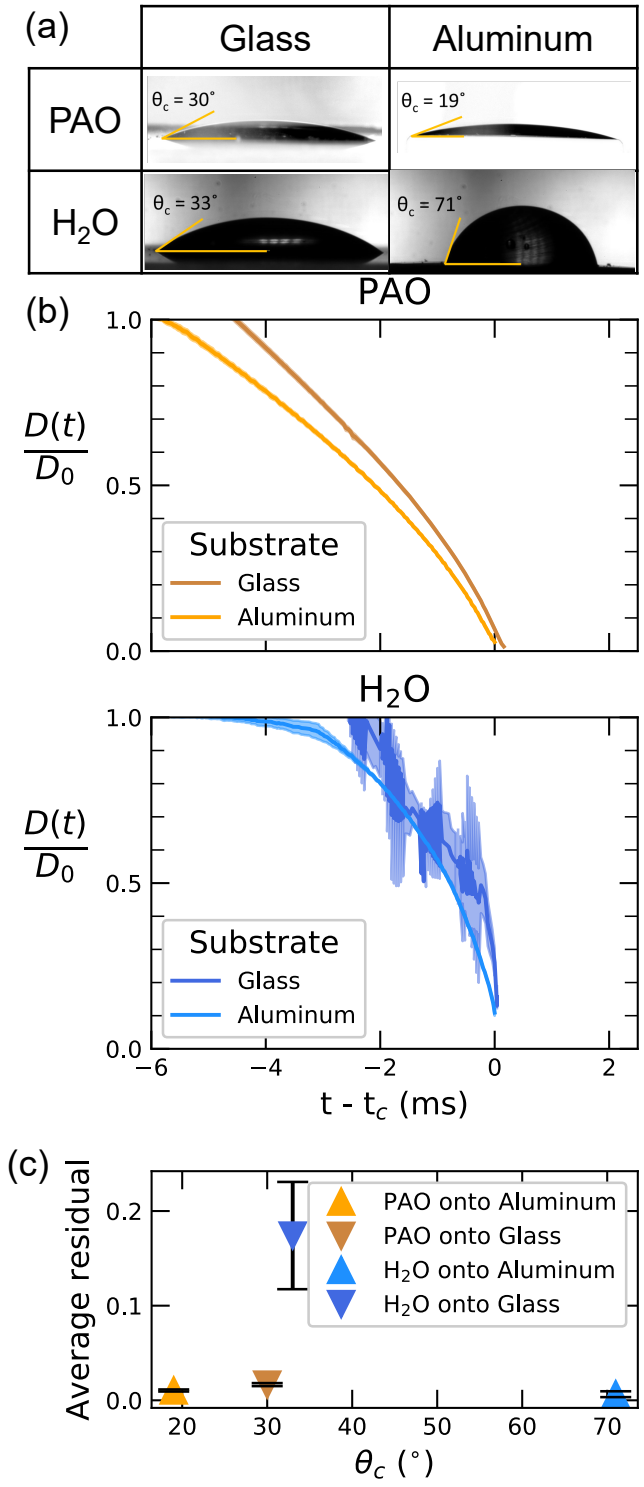

Figure 2.5: (a) Photos of sessile droplets of (top) PAO and (bottom) H_2O on (left) glass and (right) aluminum (contact angle, θ_c, indicated). Background subtraction was used on the PAO images. (b) Normalized minimum diameter ($D(t)/D_0$) for n = 5 replicated experiments (the shaded bands show ± one standard error) for the two different substrates: (top) PAO and (bottom) H_2O. (c) Average residual relative to theoretical inertio-capillary response (Equation 2.2) as a function of contact angle θ_c. The error bars show the standard deviation for each condition.

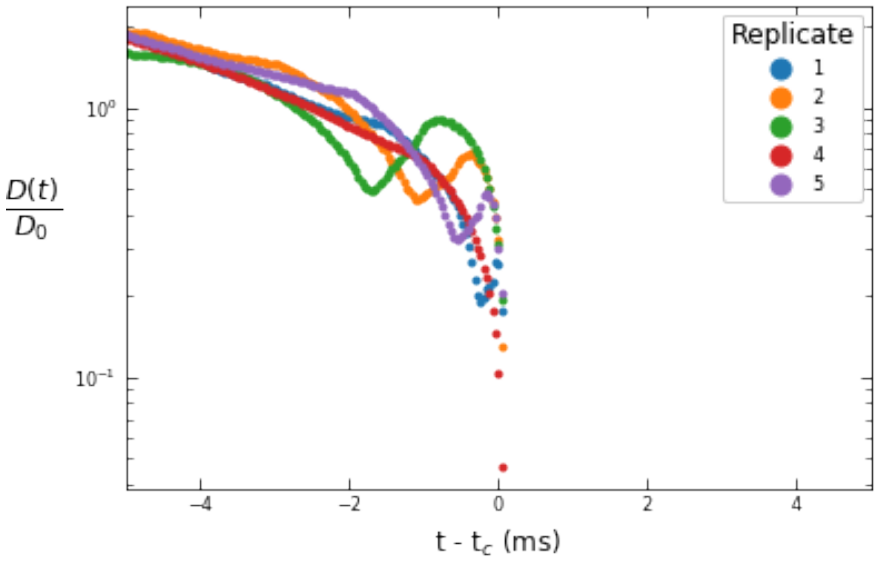

Figure 2.6: Normalized minimum diameter against time of 5 replicates of H_2O onto a glass substrate with H fixed (H = 3.5mm).

contact angles between H_2O and glass and aluminum are 33° and 71° respectively, and this difference yielded distinct behavior in DoSER experiments. H_2O matched the behavior predicted by IC behavior (Equation 2.1) when bridging onto aluminum substrates compared with glass. Additionally, we observe instability in evolution of the H_2O liquid bridge when dripping onto a glass substrate. Repeated experimental replicates produce distinct and unpredictable results (Figure 2.5b, bottom) and 3 of the 5 replicates do not exhibit monotonic decrease in $\frac{D(t)}{D_0}$ as t increases (Figures 2.6 and 2.8). When our results were analyzed using the average residual analysis (Equation 2.2), the H_2O onto glass case is a clear outlier (Figure 2.5 c). The results when dripping H_2O onto glass are intertwined with the low θ_c between H_2O and glass (Figure 2.7). H_2O eagerly spreads into a thin puddle and rapidly exposes surface area to the glass substrate. As this spreading happens on the timescale of the DoSER experiments, it creates extra flow drawing the fluid from the needle, increasing the strain rate. The increased spreading speed is most visible shortly after contact with the substrate. The diameter of wetted area on the substrate well exceeds D_0 within 1 ms of contact with the glass substrate (Figure 2.7 top, 0.68 ms). Additionally, the increased strain rate creates differences in the curvature of the H_2O droplet as the experiment progresses. When dripped onto glass, the H_2O takes on a geometry resembling a shelf (Figure 2.7 top, 0.32 ms): it has two regions

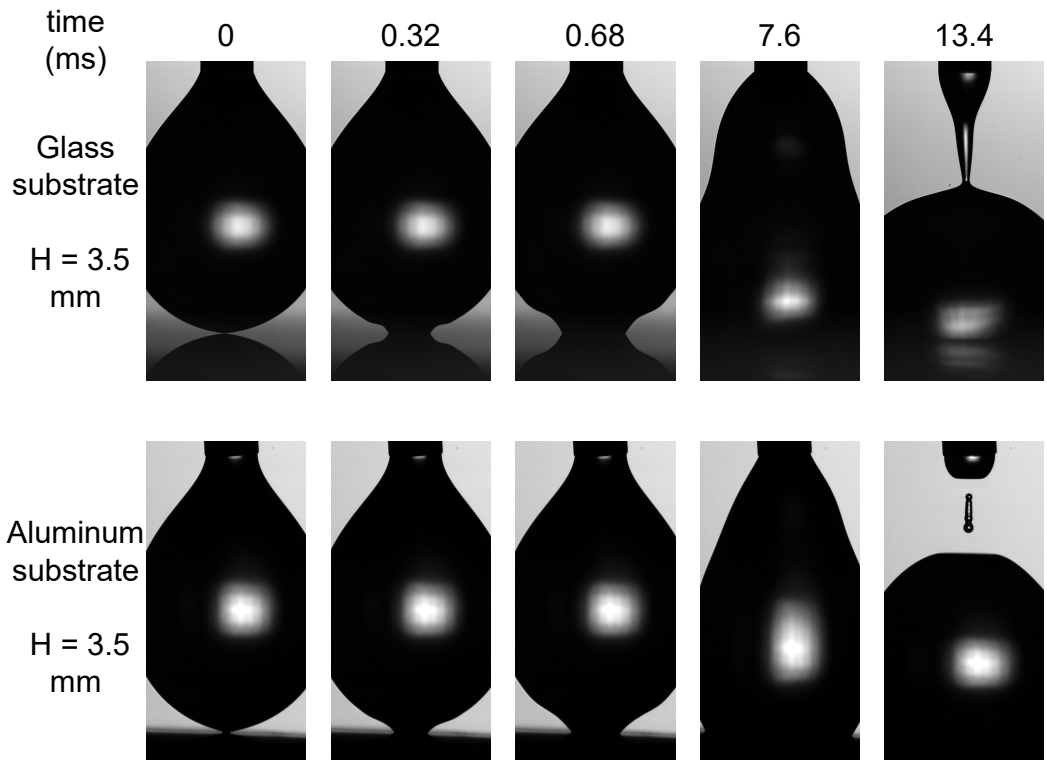

Figure 2.7: Select frames from DoSER experiments with pure H_2O onto glass (top) and aluminum (bottom). The images are synchronized by the setting $t = 0$ to the moment the fluid makes contact with the substrate.

of high curvatures, opposite in sign and close together in space. These regions signal an unstable geometric configuration of the droplet and ultimately manifests in the higher variability we observe between experimental replicates (Figures 2.5 and 2.8). In contrast, the H_2O dripped onto aluminum spreads more slowly, shows mild curvatures throughout the experiment, and produces low variance between replicates (Figure 2.9).

The PAO has a higher η (3 mPa s) than water (1 mPa s), and is more tolerant to changes in substrate in DOSER experiments.[25] We believe the combination of higher η and smaller $\Delta\theta_c$ damps the changes in initial conditions caused by changing substrates. Consequently, the impact of substrate choice depends not only on the interactions between the fluid and the substrate, but also on the fluid properties.

Effect of gap distance and contact angle for elasto-capillary fluids

As with the pure H_2O and PAO, experiments with varied gap distance revelead that aqueous solutions of PAM permit successful DoSER experiments in a limited range of H. The lower bound due to premature cessation of flow is unmodified by

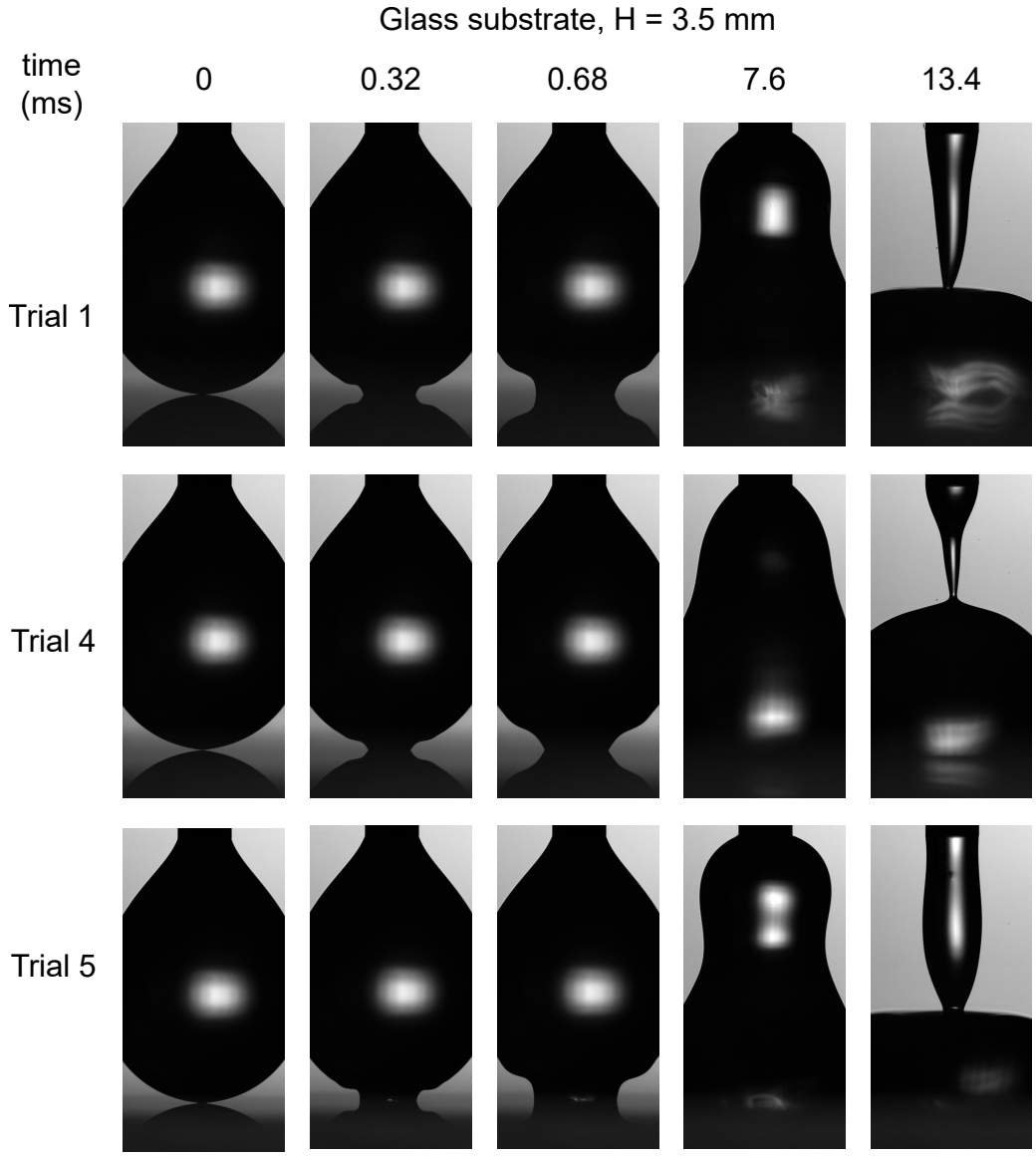

Figure 2.8: Selected still images from multiple trials of DoSER experiments with H_2O onto the glass substrate with the same initial conditions. The time is normalized to the moment of contact with the substrate.

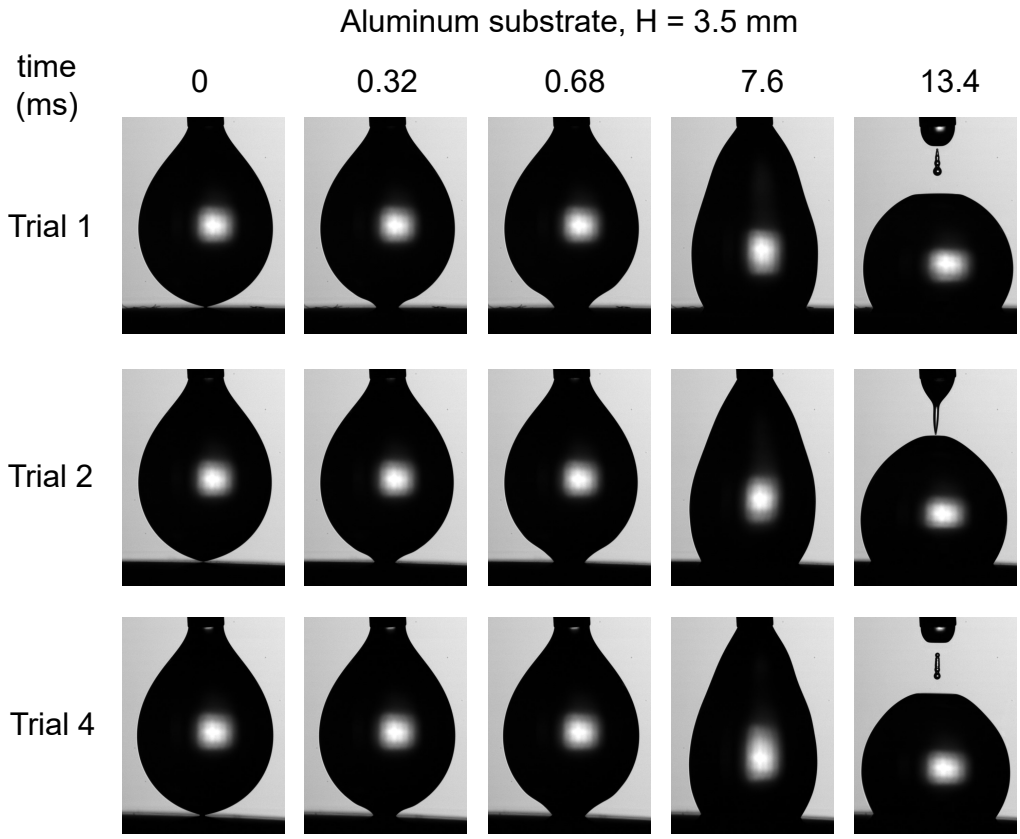

Figure 2.9: Selected still images from multiple trials of DoSER experiments with H_2O onto the aluminum substrate with the same initial conditions. The time is normalized to the moment of contact with the substrate.

PAM. Near the upper bound of feasible values of H, the polymer inhibits premature separation (experiments can go to completion for $H = 4.0$ mm, $H/D_{pred} = 1.5$, Figure 2.10). However, the data at $H = 4.0$ mm behave quantitatively differently from those in the range 2.9mm $< H <$ 3.5mm. They produce replicates with higher standard error, lower values for $D(t_c)$, and lower values of λ_E with higher standard deviation. The window of H values that provide low standard error for H_2O also provide low standard error for the aqueous PAM solutions. Therefore, the limits established by the pure solvent (Figure 2.4, $0.9 < H/D_{pred}^{solvent} < 1.5$) should be followed when investigating solutions of the solvent. Of the variables in Equation 2.3, σ can easily take the largest range of values. Adding PAM to H_2O at these concentrations does not appreciably change σ,[26,27] giving rise to the unchanged limits on H/D_{pred} we observe. However, we believe disrupting the surface tension with a different type of additive (e.g., surfactant) would require re-evaluation of the limits of H.

Table 2.1: Fluid properties with ± one standard deviation of PAM solution under the various conditions tested

Substrate	H (mm)	$D(t_c)/D_0$	λ_E (ms)	η_E^∞ (Pa s)	$\eta_E^\dagger$ (Pa s)
Al	2.9	0.27 ± .00	5.7 ± 0.3	45 ± 0.2	48.3 ± 0.3
Al	3.2	0.26 ± .00	5.5 ± 0.1	45 ± 0.1	47.6 ± 0.4
Al	3.5	0.25 ± .00	5.5 ± 0.1	49 ± 0.1	49.0 ± 0.4
Glass	3.5	0.35 ± .01	5.5 ± 0.1	67 ± 11.7	35.6 ± 0.3
Al	4.0	0.21 ± .01	4.9 ± 0.4	43 ± 2.2	52.1 ± 1.4

We also tested the PAM solution on glass and aluminum substrates using $H/D_{pred}^{H_2O} = 1.3$, which provided low residual for pure H_2O on aluminum (Figure 2.4b). Both substrates produce data similar in the EC region: they decay with the same slope, yielding the same value for λ_E (Table 2.1). The behavior preceding the EC region ($t < t_c$) reveals the differences between the substrates (Figure 2.10a, lower). In the absence of PAM, the liquid bridge of pure water would have broken after t_c of the elastocapillary fluid. The elastocapillary fluids form a thread at $t = t_c$, which connects the fluid attached to the needle with the droplet of fluid which has made contact with the substrate. The behavior of the lower droplet is quite different on aluminum than on glass. On glass, the lower droplet spreads more rapidly due to the greater outward radial force exerted at the contact line on glass ($\theta_c = 33°$) than on aluminum ($\theta_c = 71°$). Relative to the liquid thread, its lower attachment is rapidly displaced downward when the substrate is glass. There is a distinct region of behavior between t_c and the onset of unambiguous exponential decay, which signals the EC region. In this region, the DoSER trace consistently takes on a parabolic shape with a duration of 7 ms before giving way to EC behavior (Figure 2.11). We believe this parabolic region is the equilibration of the surface effects accelerating the fluid and the polymer chains uncoiling to resist that flow. When varying the substrate, the DoSER trace onto glass substrates are roughly 5 ms longer from contact to separation than the DoSER traces onto aluminum (Figure 2.10b). If we imagine the EC starting at the end of this distinct parabolic behavior, we recover an EC duration of 33 ms ($= 6\lambda_E$) for both substrates, and note that $D(t_c + 7\text{ms})_{glass} \approx D(t_c)_{Al}$.

Within a single substrate, $\eta_{E,Al}^\infty$ and $\eta_{E,Al}^\dagger$ are within 10% of one another when $H < 4$ mm ($H/D_{pred}^{solvent} < 1.5$). This reassures us that $\eta_E^\dagger$ can be used to approximate η_E^∞ under reliable experimental conditions. In contrast, $\eta_{E,glass}^\dagger \approx 0.5\eta_{E,glass}^\infty$, further indicating that glass is not a suitable substrate for DoSER with aqueous polymer

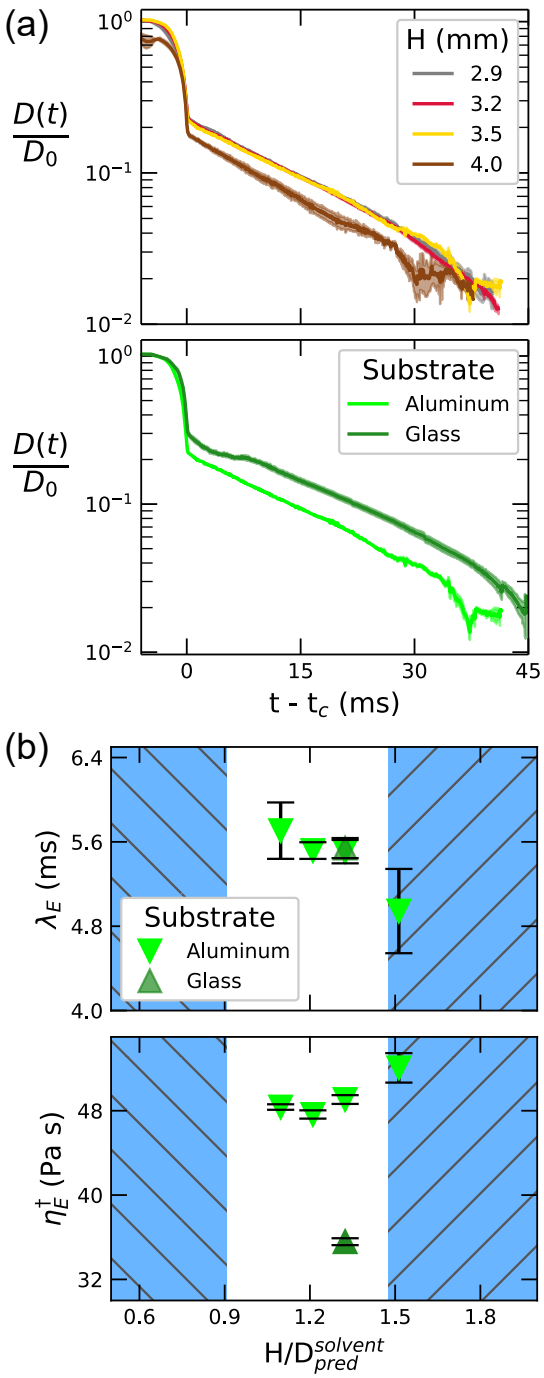

Figure 2.10: (a) Normalized minimum diameter ($D(t)/D_0$) for n = 5 replicated experiments (the shaded bands show ± one standard error) of 0.04 weight %, 6.7 Mg/mol PAM solution onto an aluminum substrate at (top) selected values of gap height (H) and (bottom) at H = 3.5 mm ($H/D_{pred}^{H_2O}$ = 1.3) onto glass and aluminum substrates. (b) Values of (top) elongational relaxation time (λ_E) and (bottom) estimated elongational viscosity ($\eta_E^\dagger$, Equation 2.10) as a function of contact normalized gap distance $H/D_{pred}^{solvent}$. For these experiments where D_0 = 0.72 mm, $D_{pred}^{solvent}$ = 2.6 mm (Equation 2.3). The error bars show the standard deviation for each condition.

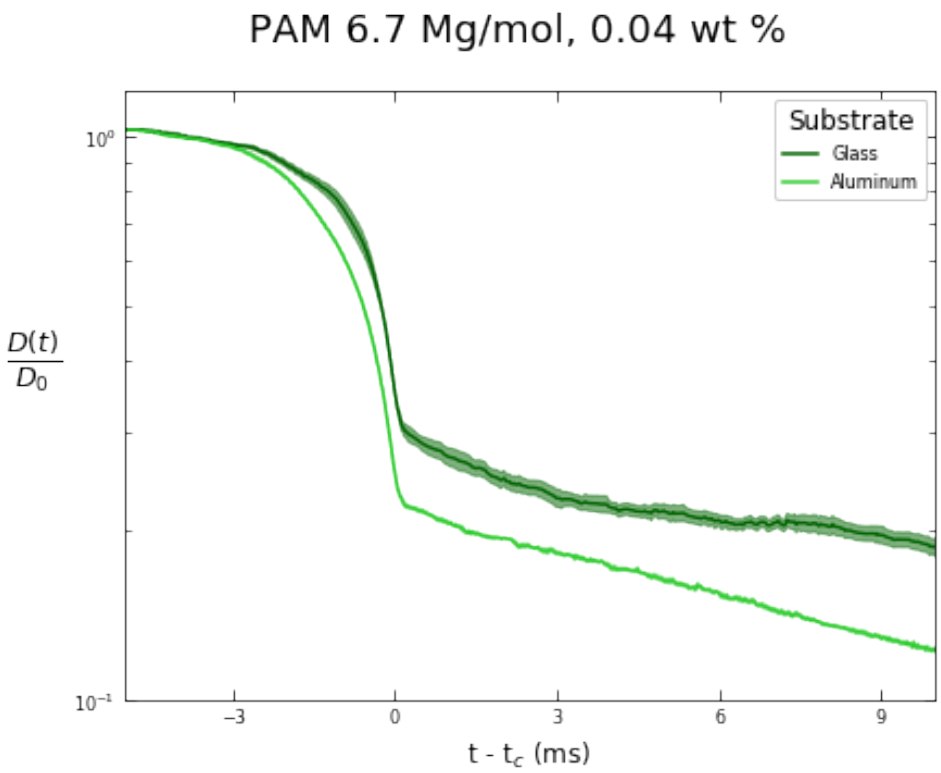

Figure 2.11: Normalized minimum diameter ($D(t)/D_0$) against time highlighting the critical time of transition (t_c) for PAM solution onto glass and aluminum. The onset of EC behavior is delayed ≈ 7 milliseconds after t_c in the glass experiments.

solutions. Across both substrates, the η_E and ϵ plots (Figures 2.12 and 2.13) are qualitatively similar. Because η_E is a property of the fluid, it should be independent of the substrate; however, there is a glaring disparity. The difference between $\eta^{\dagger}_{E,\,glass}$ and $\eta^{\dagger}_{E,\,Al}$ corresponds to the difference in $D(t_c)$ values: $D(t_c)_{glass}$ is erroneously $\frac{1}{0.7}D(t_c)_{Al}$. When that value is used in further calculations, the error propagates into the value of $\eta^{\dagger}_{E,\,glass}$, yielding $\eta^{\dagger}_{E,\,glass} = 0.7\eta^{\dagger}_{E,\,Al}$. Replacing $D(t_c)_{glass}$ with $D(t_c + 7ms)_{glass}$ ($\approx D(t_c)_{Al}$) recovers the value of $\eta^{\dagger}_{E,\,Al}$. Because the results for aqueous polymer solutions are susceptible to errors introduced by the extraneous flows that accompany a low θ_c substrate, we further favor using substrates with high values of θ_c for the fluid of choice. This produces droplets with large, stable spherical caps onto the substrate which lead to higher quality measurements.

2.3 Image analysis

Image collection

For each solution, DoSER was performed using the following procedure. An aliquot was slowly loaded into a syringe through the relevant blunt-tip needle. The syringe

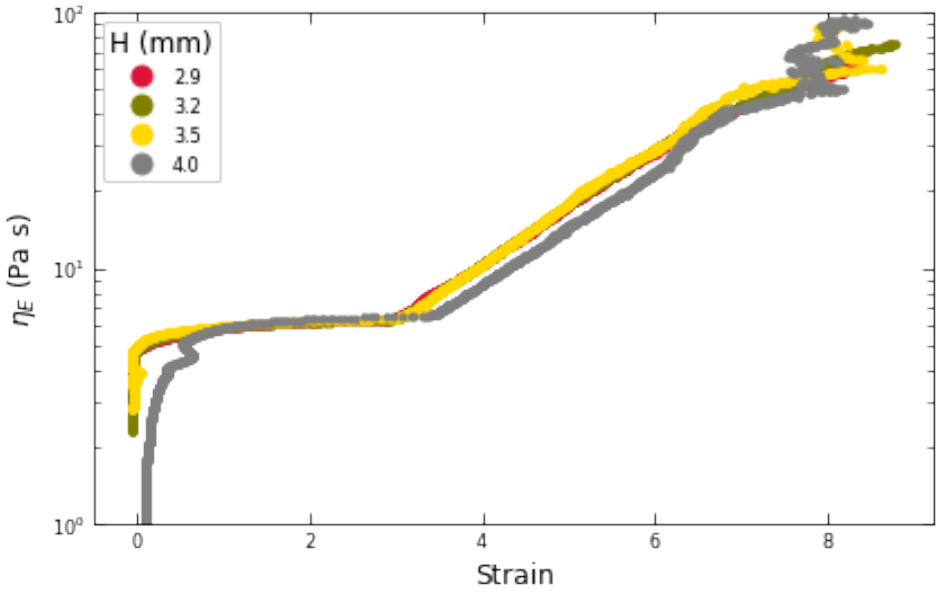

Figure 2.12: Elongational viscosity (η_E) against strain (ϵ) graph for PAM solution onto aluminum with different values of gap height (H). The plateau value of elongational viscosity (η_E^∞) is determined by identifying the plateau in η_E. Each point is the mean of 5 replicates, synchronized by $t - t_c$.

was attached to the syringe pump and the syringe pump was slowly advanced until solution was observed to drip from the needle, and then the needle tip was cleaned. A clean substrate was positioned below the needle tip. The light was turned on and the camera was focused and aligned with the needle tip. The substrate was then raised or lowered to the correct height (as describe above) relative to the needle tip. A background video with a droplet-free needle and substrate was acquired. A drop was dispensed from the needle tip by the syringe pump at a rate of 0.02 mL/min, until the drop was nearly touching the substrate. The syringe pump was stopped prior to droplet-substrate contact. The events of droplet contact through liquid bridge formation and pinchoff were recorded. A clean substrate was then placed below the needle tip. Dispensing drops onto a clean substrate was repeated until five total runs were recorded. The videos were analyzed using the *dosertools* Python package (Section 2.3) to obtain the normalized diameter as function of time after the critical time (time of transition between solvent behavior and elastocapillary response). The decay of the normalized diameter is used to evaluate the extensional relaxation time. In our experiments, run-to-run variation on the DoSER instrument was observed to be more significant than errors in fitting–errors in measured relaxation times are thus quantified using the run-to-run variation. Solutions with relaxation times of 0.05

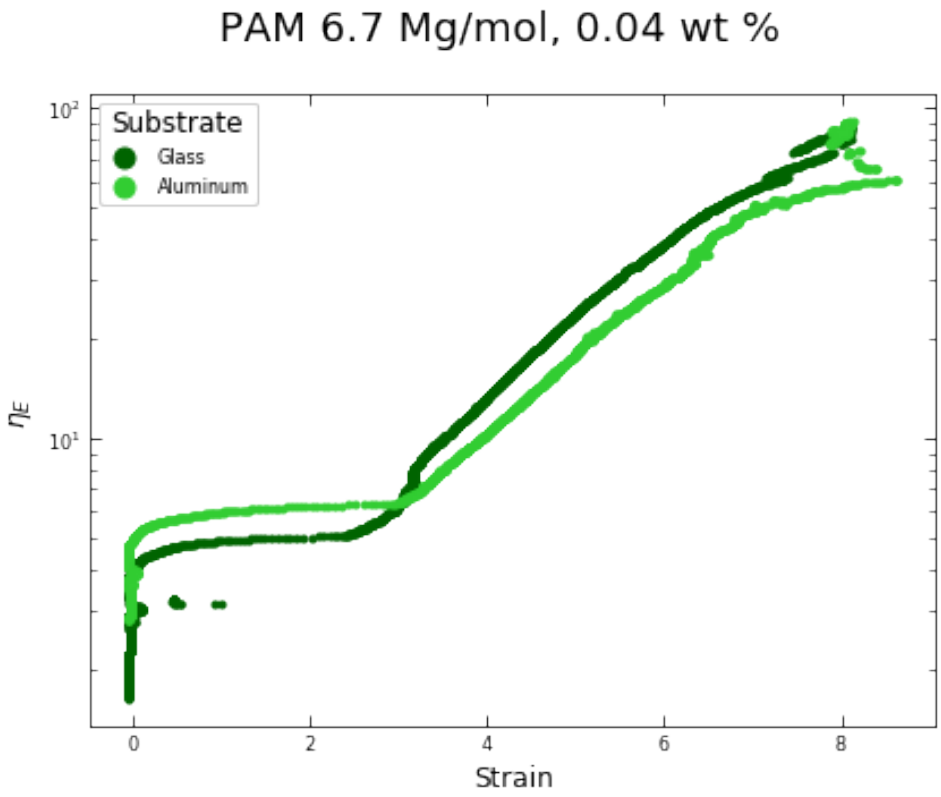

Figure 2.13: Elongational viscosity (η_E) against strain (ϵ) graph for PAM solution onto glass and aluminum. The plateau value of elongational viscosity (η_E^∞) is determined by identifying the plateau in η_E. Each point is the mean of 5 replicates, synchronized by $t - t_c$.

ms and lower were difficult to consistently characterize on our instrument. Ambient temperature was measured with each experiment and was in the range 15 ± 1 °C.

Setting the camera shutter speed

The shutter speed depends on the level of magnification, strength of the light, and frame rate. Our goal is to set it fast enough such that the fine details of the filaments near the end of the experiment can be resolved accurately. To accomplish this, we monitor the intensity of the background and increase the shutter speed until the intensity values of the background are just below the upper limit of the detector, eg, 200 on a detector with a maximum intensity of 255.

Image processing with *dosertools*

The following methods are included in the *dosertools* Python package. *dosertools* was used to process all the videos used in this study. It is hosted at https://github.com/rlearsch/dosertools,

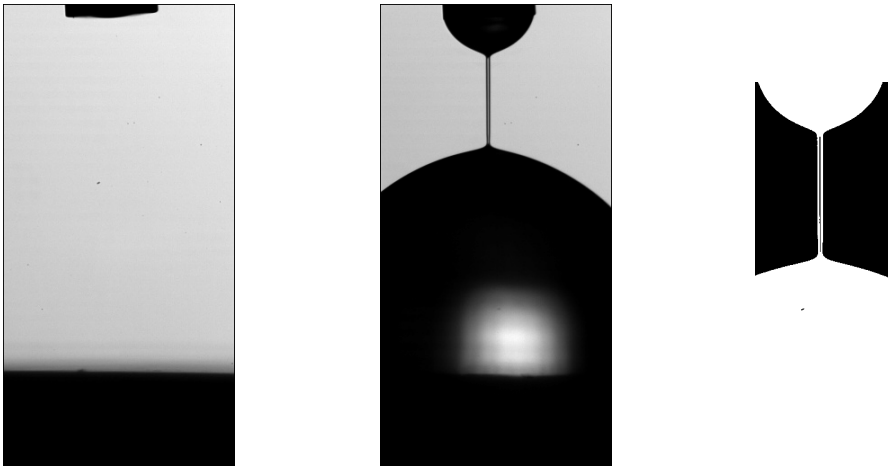

(a) Background (b) Experimental (c) Binary

Figure 2.14: Example (a) background, (b) experimental, and (c) binarized images for a 6M PEO, 0.0066 wt% in diionized water solution. Figure reproduced from Lhota [28] with permission.

along with documentation, and is installable via *pip install dosertools* for use with Python 3.8+.

Background subtraction and binarization

Because light sources and cameras are not always uniform in their ability to produce and observe (respectively) light, we use background subtraction to reduce the impact of noise and other features of a non-uniform background (such as particulates on a lens or a dead pixel) on our processed images and thus our diameter data. Our recommended best practice is to capture a 100 frame background video of the nozzle in its experimental position above a substrate with both a clean nozzle and substrate (Figure 2.14(a)). In our experiments, it was sufficient to capture a single background video for a group of 5 experimental runs; however, if the light source and/or camera varies on shorter time scales, we recommend a background paired with each experimental video (Figure 2.14(b)). To perform the background subtraction, we use the median of the background frames, crop both the image and the background, subtract the background median from the image, then rescale the pixel intensity of the resultant image based on the maximum intensity value. After background subtraction, the images are binarized using the Otsu algorithm.[17] Compared to the literature method, where an arbitrary cutoff value for binarization is chosen by the user,[9,12,13,21,29,30] the Otsu method does not require any input from the user. After binarization, pixels where either the fluid, the nozzle, or the substrate

are visible will be white, while the surrounding background will be black (Figure 2.14(c)).

Liquid bridge diameter

To process the binary images into normalized diameter data, the nozzle diameter (D_0) is determined from either the background or experimental video, depending on which video has an image of a clean nozzle. Then, we determine the diameter of the liquid bridge at all heights and determine if the liquid bridge has already pinched off by looking for rows where no white pixels are present. If the liquid bridge is still intact, the minimum diameter is then computed as the average diameter of all diameters within 2 pixels of the absolute minimum (e.g., if the minimum diameter of a given frame is 5 pixels, rows with diameters of 5, 6, and 7 pixels contribute to the average). This averaging alleviates observed problems with stair stepping in the diameter with time due to the finite size of a pixel. By taking the average with rows of similar diameters, we obtain a better estimate of the minimum diameter as it evolves in time. This minimum diameter ($D(t)$) is divided by the nozzle diameter (D_0) determined earlier to obtain the normalized minimum diameter ($D(t)/D_0$). The frames-per-second with which the video was filmed is used in conjunction with the frame number to determine the time (t) for each frame.

Determining the critical time

The moment of transition from either the inertio-capillary or the visco-capillary regime to the EC regime (t_c) is used to align the normalized diameter data. Prior literature determined the critical time by inspection.[9,12,21,29,30] We developed a method for detecting the critical time through finding the moment of maximum strain rate within the window of normalized diameter in which transition occurs; this is described in detail in the following subsection.

Intra-frame t_c calculation

The intra-frame adjustments to t_c are performed as follows: The replicate with the lowest value of $\frac{D(t_c)}{D_0}$, determined by the frame with maximum strain rate is fixed as the reference replicate. We select a subset of the reference dataset consisting of the $t = t_c$ and the 9 frames prior to $t = t_c$. One at a time, the other replicates are compared to this subset of the reference data. The comparison is made between a subset of the 10 frames preceding $t = t_c$, (where $t < t_c$, excluding $t = t_c$) from the

comparison datasets. To find the refined value of t_c, a constant is added to t_c which minimizes the euclidean distance (calculated with *scipy.spatial.distance.cdist*) between the $\frac{D(t)}{D_0}$ and $t - t_c$ pairs from the reference and replicate data. This unique value is determined by the iterative Broyden–Fletcher–Goldfarb–Shanno (BFGS) algorithm (implemented with *scipy.optimize.minimize*).[31–34] If the absolute value of the constant which minimizes the euclidean distance between these datasets is greater than 2/(frame rate), the constant is set to 2/(frame rate). The adjusted value (t_c from $\dot{\epsilon}$ plus the constant determined above) of t_c is propagated through the original time data and the relevant quantities (e.g., $D(t_c)$, η_E) are recalculated.

Extensional properties

The EC regime (Equation 3.3) consists of the data after the critical time and before the finite-extensibility regime. To determine the extensional relaxation time (λ_E), a linear regression is performed on data recast as $ln(D/D_0)$ versus $t - t_c$. The slope (m) obtained is thus used to calculate λ_E ($\lambda_E = \frac{-1}{3m}$).

Data analysis

In addition to the initial conditions dictated by the experimental set up such as the θ_c and H, there are additional opportunities for improvement in the data processing aspect of DoSER experiments. For example, quantifying the slope of the elasto-capillary (EC) regime to find the extensional relaxation time is fundamental to the DoSER technique. The behavior in the EC regime is described precisely by a balance between elastic (g_i and $\lambda_{E,i}$) and capillary (σ) forces:

$$\frac{D_{EC}(t)}{D_0} = \sum_i \left(\frac{g_i D_0}{4\sigma}\right)^{1/3} \exp(\frac{-t}{3\lambda_{E,i}}), \tag{2.4}$$

where g_i and $\lambda_{E,i}$ are the corresponding extensional modulus and relaxation time for the i^{th} mode. We adopt the hypothesis of Entov and Hinch:[12,35] the behavior of the EC regime can be approximated by using only the longest relaxation time of the system, yielding:

$$\frac{D_{EC}(t)}{D_0} \approx \left(\frac{G D_0}{4\sigma}\right)^{1/3} \exp(\frac{-t}{3\lambda_E}). \tag{2.5}$$

We modify the expression to include the critical time (t_c),

$$\frac{D_{EC}(t)}{D_0} \approx \left(\frac{G D_0}{4\sigma}\right)^{1/3} \exp(\frac{-(t - t_c)}{3\lambda_E}), \tag{2.6}$$

where t_c is the moment of transition from the preceding regime to the EC regime. Prior literature determined the critical time by visual inspection of the source videos

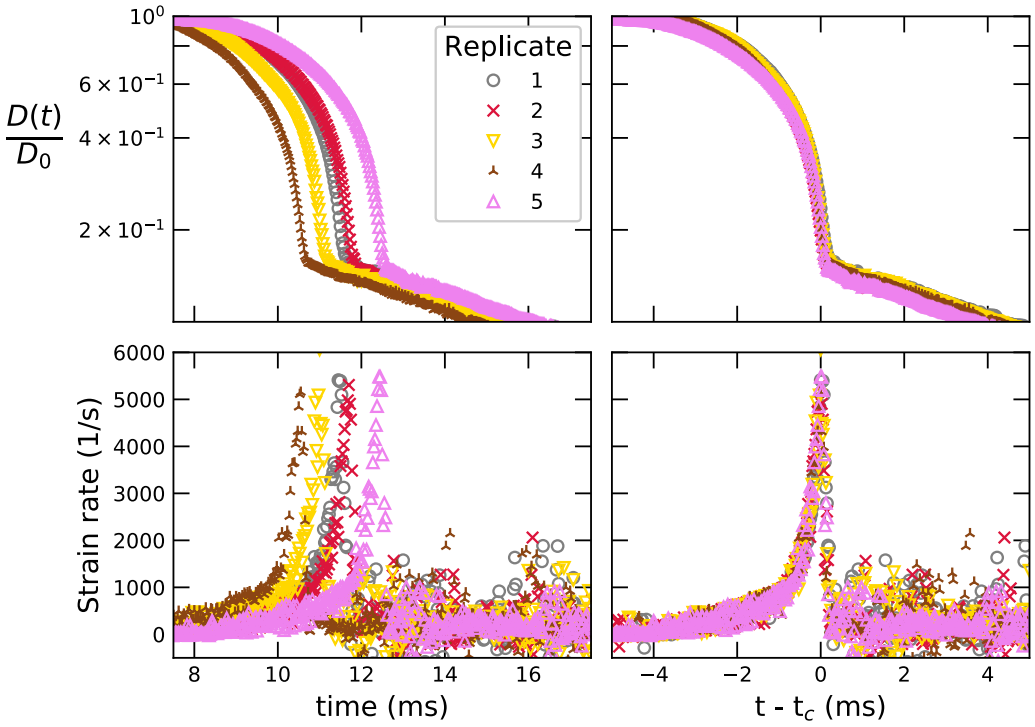

Figure 2.15: (top) Normalized minimum diameter ($D(t)/D_0$) and (bottom) strain rate for n = 5 replicate experiments for an aqueous solution of 0.15 weight % polyacrlyamide (PAM) with M_w = 4.8$x10^6$ g/mol measured using gap height (H) = 3.5 mm onto aluminum. (left) The moment of contact between the droplet and substrate is taken as t = 0; and (right) the frame with maximum strain rate is taken as t_c.

or the numerical datasets.[9,12,21,29,30] A reliable value of t_c is necessary to properly analyze multiple experimental replicates, which may have different relative start and end times depending on user choices of where to begin and end videos.

We developed a method for detecting the critical time using the fluid's strain rate. The true strain rate can be calculated from the time derivative of the diameter data:

$$\dot{\epsilon}(t) = -2\frac{\left(\frac{dD(t)/D_0}{dt}\right)}{D(t)/D_0} = -2\frac{dD(t)/dt}{D(t)}. \tag{2.7}$$

Because the data are discrete images from a video, we use a numerical derivative to calculate the instantaneous strain rate:

$$\dot{\epsilon}(f_i) = -2\left(\frac{D(f_{i+1}) - D(f_{i-1})}{2\Delta t D(f_i)}\right), \tag{2.8}$$

where f_i is the i^{th} frame and Δt = frame rate^{-1} is the time between frames. We calculate the strain rate from Equation 2.8 and use the frame with the maximum

strain rate in a reasonable range of values of $\frac{D(t)}{D_0}$. A typical range would be from $0.25 > \frac{D(t)}{D_0} > 0.05$, allowing $\frac{D(t_c)}{D_0}$ to take on a wide range of values. The bounding serves only to eliminate the noisy regions in the strain rate signal without being overly prescriptive. By finding the critical time systematically rather than by inspection, we significantly reduced variation in analyses which rely on the values of $\frac{D(t_c)}{D_0}$, such as calculating η_E (Figure 2.15). In addition to refining the determination of values for t_c and $\frac{D(t_c)}{D_0}$, automating a tedious and time consuming task, calculating t_c from the $D(t)$ data offers an additional experimental benefit. In contrast to a commonly used alternative method of taking the moment of contact between droplet and substrate as $t = 0$, the top of the substrate was required to be in the field of view as the video is taken. As our method of calculation does not rely on observing this contact, we magnify the region where filament thinning takes place when the video is collected. Magnifying this region allows us to capture meaningful images of the filament at thinner diameters and resolve finer changes in $D(t)$.

Our method consistently places t_c at a value *slightly* ($\approx$ 250us, with our hardware) before the unambiguous exponential decay that is characteristic of the EC region (Figure 2.16). Consequently, we believe our maximum strain rate method identifies the beginning of the transient transition to the EC region. Including this transient region in the analysis has no adverse effect on our ability to reproduce values of λ_E reported in literature; in solutions with $\lambda_E \geq 2$ ms, the transient represents 2% or less of the duration of the EC region.

Although the value of t_c changes depending on the arbitrary choice of beginning frame, the value $D(t_c)/D_0 = ((GD_0)/(4\sigma))^{1/3}$ is a property of the solution being tested and thus should be independent of the start time of the recording. Similarly, the strain rate at t_c is a property of the solution: the strain rate required to induce polymer chain stretching.[30] Determination of the maximum strain rate $\dot{\epsilon}(t_c)$ is frustrated by two inherent characteristics. First, the derivative of an experimental observable is very noisy. Second, the peak is very sharp and the moment of maximal $\dot{\epsilon}$ generally falls between frames of the highspeed video.

To elucidate the peak in $\dot{\epsilon}$, the determination of t_c can be further refined by allowing the value of critical time to take on values in the continuous range surrounding the value of t_c determined from the maximum strain rate (Section 2.3). By allowing the value of t_c to vary up to $\pm$ one exposure duration, we account for this limitation in the experimental technique and further refine the determination of these fluid properties (Figure 2.16).

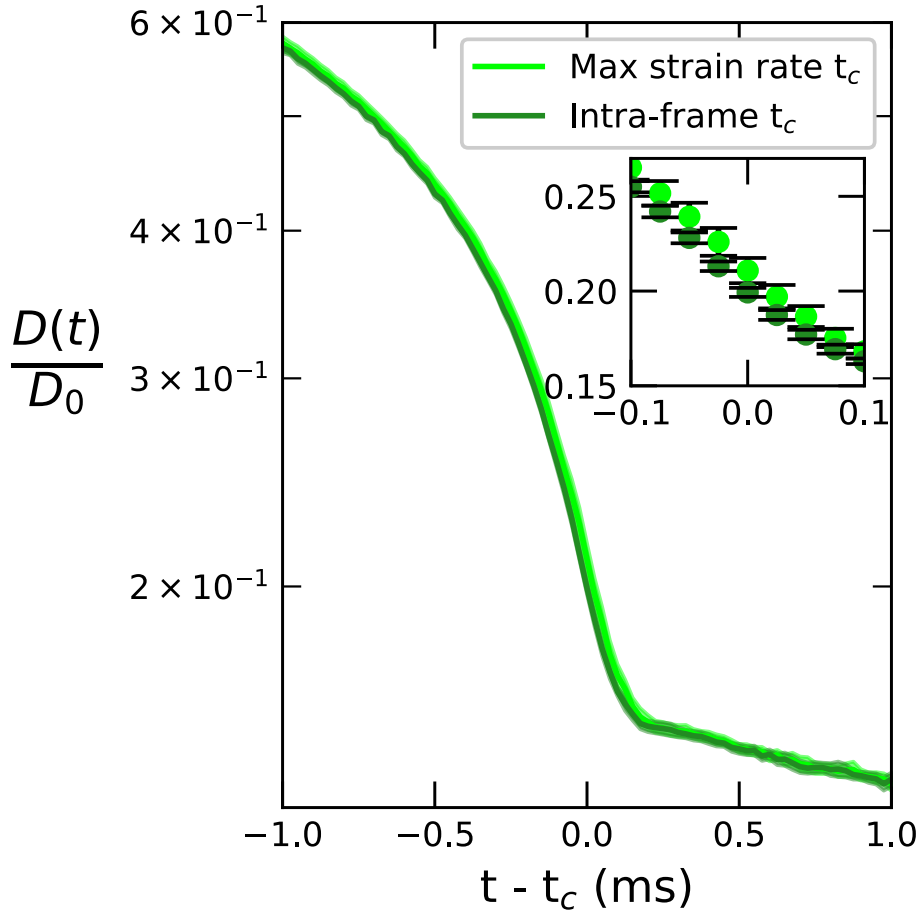

Figure 2.16: Normalized minimum diameter ($D(t)/D_0$) for n = 5 replicate experiments (shaded band shows ± one standard error) for two choices of t_c: either the frame having greatest strain rate (max strain rate t_c, highest $\dot{\epsilon}$ frame) or the interpolated time of maximum strain rate (intra-frame t_c, time of $\dot{\epsilon}_{max}$) which differs by less than (frame rate)$^{-1}$ relative to the highest $\dot{\epsilon}$ frame. Inset: Expanded view of the effect of fine-tuning t_c with the error bars (representing ± one standard error of n = 5 replicates) shown for individual frames.

Identifying t_c *via* $\dot{\epsilon}_{max}$ is most important for the transition to and analysis of the EC regime; however, it is also valuable for fluids with pure IC or VC behavior. Multiple replicates of the same fluid with IC behavior can be synchronized using $\dot{\epsilon}_{max}$ (e.g., Figures 2.2 and 2.5b), which makes comparison of their behaviors possible. Although we did not explicitly test this method on VC behavior, datasets in the literature show a maximum of $dD(t)/dt$ at the moment of pinch-off, indicating synchronization using $\dot{\epsilon}_{max}$ would be useful.[12,15,36]

Furthermore, systematically determining t_c and the corresponding value of $\frac{D(t_c)}{D_0}$ are essential to calculate the elongational viscosity from DoSER data. Manipulation of Equations 2.5 and 2.7 yields an analytical expression for the elongational viscosity in the EC regime:[5,12,37,38]

$$\eta_E = \frac{3\lambda_E \sigma}{D(t_c)\exp(\frac{-(t-t_c)}{3\lambda_E})}. \tag{2.9}$$

The results of this equation are often presented as a function of strain (ϵ): η_E increases as ϵ accumulates throughout the experiment and plateaus as the experiment progresses (Figure 2.13). The value at the plateau, called η_E^∞, is used to compare extensional viscosity across fluids.

Traditionally, η_E^∞ is estimated from the plot of η_E and ϵ; here we present an alternative method to determine it via calculation. Our calculations rely on the observation that the duration of the EC regime, Δt_{EC}, is consistently $6\lambda_E$.[21] The equation $\Delta t_{EC} = 6\lambda_E$ holds for both PEO and PAM solutions and is independent of the concentration and molecular weight. Because Equation 2.9 is derived from the governing equation for EC behavior (Equation 2.5), we use $t - t_c = 6\lambda_E$ to find the final moment that Equation 2.9 is valid. Evaluating Equation 2.9 at this moment yields a value for η_E^∞ without referring to the plot of η_E and ϵ. Our estimate, which we call $\eta_E^\dagger$,

$$\eta_E^\dagger = \frac{3\lambda_E \sigma}{D(t_c)\exp(-2)}, \tag{2.10}$$

relies on the values of λ_E, σ, and the precisely determined $D(t_c)$.

2.4 Conclusions and future work

Although DoSER is not yet widespread in the literature, it is proving to be a valuable complement to other elongational rheometry techniques. Our work to simplify the technical details of the experimental procedure and accelerate the transformation from video to solution properties, as well the work of other early adopters, will encourage more scientists to implement DoSER in their own research.

This contribution aims to support researchers who are implementing DoSER for research on relatively low viscosity fluids (here we examined polymer solutions that have concentrations so low that the shear viscosity is only slightly altered from that of the solvent, ranging from 1 mPa s for H_2O to 3 mPa s for the particular PAO lubricant we examined.) We focus on operating parameters (especially the height of the orifice above the substrate) and tools that reduce variability (especially bias) in the analysis of the images acquired during the dripping event.

We introduced several practical considerations for improving the consistency of both mechanical setup and analysis of DoSER experiments. For example, setting the gap distance based on the D_{pred} of the fluid enables fair comparison between fluids with a variety of surface tensions and densities. Additionally, our fully automated analysis pipeline takes raw video and deterministically produces numerical datasets and values of t_c, λ_E, etc. with no intervention from the researcher. We systematically removed opportunities for bias to seep into the analysis and allows for confident comparisons between fluids tested on different equipment, by different researchers, or simply on different days. These subjective inputs, such as manually identifying t_c and setting the binarization threshold, have the potential to alter the results and conclusions from the experiment. To encourage adoption of our techniques, the analysis software is available on github and pypi as the Python package *dosertools*.

The fluids we tested in this work have low vapor pressures and we assumed they were not evaporating substantially during experiments. For work on high vapor pressure fluids, see the modifications to DoSER by Robertson et al.[14] Furthermore, we consciously excluded fluids that exhibit visco-capillary (VC) behavior in this work. Numerically distinguishing IC and VC fluids can be quite challenging and presently we rely on the images themselves to make the distinction. VC fluids form a horizontally symmetric liquid bridge when transitioning from the needle to the substrate, while IC fluids do not exhibit this symmetry.[12] The *dosertools* package could plausibly be extended to include this distinction between IC and VC behavior but is beyond the scope of this section.

References

[1] R. P. Mun, J. A. Byars, and D. V. Boger. "The Effects of Polymer Concentration and Molecular Weight on the Breakup of Laminar Capillary Jets". In: (1998), p. 13. DOI: 10.1016/S0377-0257(97)00074-8.

[2] K. K. Chao et al. "Antimisting Action of Polymeric Additives in Jet Fuels". In: *AIChE Journal* 30.1 (Jan. 1984), pp. 111–120. ISSN: 0001-1541, 1547-5905. DOI: 10.1002/aic.690300116. URL: http://doi.wiley.com/10.1002/aic.690300116 (visited on 03/23/2016).

[3] D. J. Dijkstra et al. "The Relationship between Rheological Properties and Spraying Behavior of Polymer Dispersions". In: *Macromolecular Symposia* 249–250.1 (Apr. 2007), pp. 647–653. ISSN: 10221360, 15213900. DOI: 10.1002/masy.200750450. URL: http://doi.wiley.com/10.1002/masy.200750450 (visited on 05/07/2021).

[4] M. Rosello et al. "Dripping-onto-Substrate Capillary Breakup Extensional Rheometry of Low-Viscosity Printing Inks". In: *Journal of Non-Newtonian Fluid Mechanics* 266 (Apr. 2019), pp. 160–170. ISSN: 03770257. DOI: 10.1016/j.jnnfm.2019.03.006. URL: https://linkinghub.elsevier.com/retrieve/pii/S0377025718302994 (visited on 03/05/2020).

[5] G. H. McKinley and T. Sridhar. "Filament-Stretching Rheometry of Complex Fluids". In: *Annual Review of Fluid Mechanics* 34.1 (2002), pp. 375–415. URL: http://www.annualreviews.org/doi/abs/10.1146/annurev.fluid.34.083001.125207 (visited on 03/23/2016).

[6] G. H. McKinley. "Visco-Elasto-Capillary Thinning and Break-Up of Complex Fluids". In: (2005), p. 48.

[7] B. Keshavarz et al. "Studying the Effects of Elongational Properties on Atomization of Weakly Viscoelastic Solutions Using Rayleigh Ohnesorge Jetting Extensional Rheometry (ROJER)". In: *Journal of Non-Newtonian Fluid Mechanics* 222 (Aug. 2015), pp. 171–189. ISSN: 03770257. DOI: 10.1016/j.jnnfm.2014.11.004. URL: https://linkinghub.elsevier.com/retrieve/pii/S0377025714002055 (visited on 02/12/2020).

[8] P. Marmottant and E. Villermaux. "Fragmentation of Stretched Liquid Ligaments". In: *Physics of Fluids* 16.8 (Aug. 2004), pp. 2732–2741. ISSN: 1070-6631, 1089-7666. DOI: 10.1063/1.1756030. URL: http://aip.scitation.org/doi/10.1063/1.1756030 (visited on 05/28/2020).

[9] J. Dinic et al. "Extensional Relaxation Times of Dilute, Aqueous Polymer Solutions". In: *ACS Macro Letters* 4.7 (July 21, 2015), pp. 804–808. ISSN: 2161-1653, 2161-1653. DOI: 10.1021/acsmacrolett.5b00393. URL: https://pubs.acs.org/doi/10.1021/acsmacrolett.5b00393 (visited on 01/08/2020).

[10] L. E. Rodd et al. “Capillary Break-up Rheometry of Low-Viscosity Elastic Fluids”. In: *Applied Rheology* 15.1 (Feb. 1, 2005), pp. 12–27. ISSN: 1617-8106. DOI: 10.1515/arh-2005-0001. URL: https://www.degruyter.com/document/doi/10.1515/arh-2005-0001/html (visited on 08/04/2022).

[11] C. Clasen et al. “How Dilute Are Dilute Solutions in Extensional Flows?” In: *Journal of Rheology* 50.6 (Nov. 2006), pp. 849–881. ISSN: 0148-6055, 1520-8516. DOI: 10.1122/1.2357595. URL: http://sor.scitation.org/doi/10.1122/1.2357595 (visited on 05/14/2021).

[12] J. Dinic, L. N. Jimenez, and V. Sharma. “Pinch-off Dynamics and Dripping-onto-Substrate (DoS) Rheometry of Complex Fluids”. In: *Lab on a Chip* 17.3 (2017), pp. 460–473. ISSN: 1473-0197, 1473-0189. DOI: 10.1039/C6LC01155A. URL: http://xlink.rsc.org/?DOI=C6LC01155A (visited on 01/08/2020).

[13] K. T. Lauser, A. L. Rueter, and M. A. Calabrese. “Small-Volume Extensional Rheology of Concentrated Protein and Protein-Excipient Solutions”. In: *Soft Matter* 17.42 (2021), pp. 9624–9635. ISSN: 1744-683X, 1744-6848. DOI: 10.1039/D1SM01253C. URL: http://xlink.rsc.org/?DOI=D1SM01253C (visited on 07/12/2022).

[14] B. P. Robertson and M. A. Calabrese. *Volatile Dripping onto Substrate (vDoS) Extensional Rheology of Viscoelastic Polymer Solutions*. preprint. In Review, Nov. 8, 2021. DOI: 10.21203/rs.3.rs-964629/v1. URL: https://www.researchsquare.com/article/rs-964629/v1 (visited on 02/28/2022).

[15] J. Dinic and V. Sharma. “Power Laws Dominate Shear and Extensional Rheology Response and Capillarity-Driven Pinching Dynamics of Entangled Hydroxyethyl Cellulose (HEC) Solutions”. In: *Macromolecules* 53.9 (May 12, 2020), pp. 3424–3437. ISSN: 0024-9297, 1520-5835. DOI: 10.1021/acs.macromol.0c00077. URL: https://pubs.acs.org/doi/10.1021/acs.macromol.0c00077 (visited on 05/05/2021).

[16] L. N. Jimenez, C. D. V. Martínez Narváez, and V. Sharma. “Capillary Breakup and Extensional Rheology Response of Food Thickener Cellulose Gum (NaCMC) in Salt-Free and Excess Salt Solutions”. In: *Physics of Fluids* 32.1 (Jan. 1, 2020), p. 012113. ISSN: 1070-6631, 1089-7666. DOI: 10.1063/1.5128254. URL: http://aip.scitation.org/doi/10.1063/1.5128254 (visited on 11/19/2020).

[17] N. Otsu. “A Threshold Selection Method from Gray-Level Histograms”. In: *IEEE Transactions on Systems, Man, and Cybernetics* 9.1 (Jan. 1979), pp. 62–66. ISSN: 0018-9472, 2168-2909. DOI: 10.1109/TSMC.1979.4310076. URL: http://ieeexplore.ieee.org/document/4310076/ (visited on 07/28/2022).

[18] C. Wagner et al. “Droplet Detachment and Satellite Bead Formation in Viscoelastic Fluids”. In: *Physical Review Letters* 95.16 (Oct. 14, 2005), p. 164504. ISSN: 0031-9007, 1079-7114. DOI: 10.1103/PhysRevLett.95.164504. URL: https://link.aps.org/doi/10.1103/PhysRevLett.95.164504 (visited on 10/03/2022).

[19] A. Deblais et al. “Viscous Effects on Inertial Drop Formation”. In: *Physical Review Letters* 121.25 (Dec. 21, 2018), p. 254501. ISSN: 0031-9007, 1079-7114. DOI: 10.1103/PhysRevLett.121.254501. URL: https://link.aps.org/doi/10.1103/PhysRevLett.121.254501 (visited on 10/03/2022).

[20] J. Dinic and V. Sharma. “Computational Analysis of Self-Similar Capillary-Driven Thinning and Pinch-off Dynamics during Dripping Using the Volume-of-Fluid Method”. In: *Physics of Fluids* 31.2 (Feb. 2019), p. 021211. ISSN: 1070-6631, 1089-7666. DOI: 10.1063/1.5061715. URL: http://aip.scitation.org/doi/10.1063/1.5061715 (visited on 05/10/2021).

[21] J. Dinic and V. Sharma. “Macromolecular Relaxation, Strain, and Extensibility Determine Elastocapillary Thinning and Extensional Viscosity of Polymer Solutions”. In: *Proceedings of the National Academy of Sciences* 116.18 (Apr. 30, 2019), pp. 8766–8774. ISSN: 0027-8424, 1091-6490. DOI: 10.1073/pnas.1820277116. URL: http://www.pnas.org/lookup/doi/10.1073/pnas.1820277116 (visited on 05/05/2021).

[22] H. N. Oguz and A. Prosperetti. “Dynamics of Bubble Growth and Detachment from a Needle”. In: *Journal of Fluid Mechanics* 257 (-1 Dec. 1993), p. 111. ISSN: 0022-1120, 1469-7645. DOI: 10.1017/S0022112093003015. URL: http://www.journals.cambridge.org/abstract_S0022112093003015 (visited on 07/28/2022).

[23] R. Guigon et al. “Harvesting Raindrop Energy: Experimental Study”. In: *Smart Materials and Structures* 17.1 (Feb. 1, 2008), p. 015039. ISSN: 0964-1726, 1361-665X. DOI: 10.1088/0964-1726/17/01/015039. URL: https://iopscience.iop.org/article/10.1088/0964-1726/17/01/015039 (visited on 07/28/2022).

[24] J. D. Berry et al. “Measurement of Surface and Interfacial Tension Using Pendant Drop Tensiometry”. In: *Journal of Colloid and Interface Science* 454 (Sept. 2015), pp. 226–237. ISSN: 00219797. DOI: 10.1016/j.jcis.2015.05.012. URL: https://linkinghub.elsevier.com/retrieve/pii/S002197971500466X (visited on 01/13/2020).

[25] Department of Defense. *Performance Specification Coolant Fluid, Hydrolytically Stable, Dielectric*. MIL-PRF-87252E. Department of Defense, Mar. 21, 2018. DOI: 10.1520/MNL10848M. URL: http://www.astm.org/doiLink.cgi?MNL10848M (visited on 08/01/2022).

[26] J. Jung, J. Jang, and J. Ahn. “Characterization of a Polyacrylamide Solution Used for Remediation of Petroleum Contaminated Soils”. In: *Materials* 9.1 (Jan. 2, 2016), p. 16. ISSN: 1996-1944. DOI: 10.3390/ma9010016. URL: http://www.mdpi.com/1996-1944/9/1/16 (visited on 04/15/2022).

[27] M. Xu et al. “Quantifying the Effect of Extensional Rheology on the Retention of Agricultural Sprays”. In: *Physics of Fluids* 33.3 (Mar. 1, 2021), p. 032107. ISSN: 1070-6631, 1089-7666. DOI: 10.1063/5.0038391. URL: https://aip.scitation.org/doi/10.1063/5.0038391 (visited on 03/15/2021).

[28] R. C. Lhota. “Rheological Characterization of Polymer Additives for Mist Control and Drag Reduction”. California Institute of Technology, May 27, 2022. DOI: 10.7907/WAV1-4T47. URL: https://resolver.caltech.edu/CaltechTHESIS:05262022-231652129 (visited on 09/30/2022).

[29] J. Dinic, M. Biagioli, and V. Sharma. “Pinch-off Dynamics and Extensional Relaxation Times of Intrinsically Semi-Dilute Polymer Solutions Characterized by Dripping-onto-Substrate Rheometry”. In: *Journal of Polymer Science Part B: Polymer Physics* 55.22 (Nov. 15, 2017), pp. 1692–1704. ISSN: 08876266. DOI: 10.1002/polb.24388. URL: http://doi.wiley.com/10.1002/polb.24388 (visited on 01/08/2020).

[30] J. Dinic and V. Sharma. “Flexibility, Extensibility, and Ratio of Kuhn Length to Packing Length Govern the Pinching Dynamics, Coil-Stretch Transition, and Rheology of Polymer Solutions”. In: *Macromolecules* 53.12 (June 23, 2020), pp. 4821–4835. ISSN: 0024-9297, 1520-5835. DOI: 10.1021/acs.macromol.0c00076. URL: https://pubs.acs.org/doi/10.1021/acs.macromol.0c00076 (visited on 05/05/2021).

[31] C. G. Broyden. “The Convergence of a Class of Double-rank Minimization Algorithms 1. General Considerations”. In: *IMA Journal of Applied Mathematics* 6.1 (1970), pp. 76–90. ISSN: 0272-4960, 1464-3634. DOI: 10.1093/imamat/6.1.76. URL: https://academic.oup.com/imamat/article-lookup/doi/10.1093/imamat/6.1.76 (visited on 08/05/2022).

[32] R. Fletcher. “A New Approach to Variable Metric Algorithms”. In: *The Computer Journal* 13.3 (Mar. 1, 1970), pp. 317–322. ISSN: 0010-4620, 1460-2067. DOI: 10.1093/comjnl/13.3.317. URL: https://academic.oup.com/comjnl/article-lookup/doi/10.1093/comjnl/13.3.317 (visited on 08/05/2022).

[33] D. Goldfarb. “A Family of Variable-Metric Methods Derived by Variational Means”. In: *Mathematics of Computation* 24.109 (1970), pp. 23–26. ISSN: 0025-5718, 1088-6842. DOI: 10.1090/S0025-5718-1970-0258249-6. URL: https://www.ams.org/mcom/1970-24-109/S0025-5718-1970-0258249-6/ (visited on 08/05/2022).

[34] D. F. Shanno. “Conditioning of Quasi-Newton Methods for Function Minimization”. In: *Mathematics of Computation* 24.111 (1970), pp. 647–656. ISSN: 0025-5718, 1088-6842. DOI: 10.1090/S0025-5718-1970-0274029-X. URL: https://www.ams.org/mcom/1970-24-111/S0025-5718-1970-0274029-X/ (visited on 08/05/2022).

[35] V. Entov and E. Hinch. “Effect of a Spectrum of Relaxation Times on the Capillary Thinning of a Filament of Elastic Liquid”. In: *Journal of Non-Newtonian Fluid Mechanics* 72.1 (Sept. 1997), pp. 31–53. ISSN: 03770257. DOI: 10.1016/S0377-0257(97)00022-0. URL: https://linkinghub.elsevier.com/retrieve/pii/S0377025797000220 (visited on 04/02/2021).

[36] A. Brückner et al. “Evolutionary Assembly of Cooperating Cell Types in an Animal Chemical Defense System”. In: *Cell* 184.25 (Dec. 2021), 6138–6156.e28. ISSN: 00928674. DOI: 10.1016/j.cell.2021.11.014. URL: https://linkinghub.elsevier.com/retrieve/pii/S0092867421013295 (visited on 09/08/2022).

[37] D. F. James and T. Sridhar. “Molecular Conformation during Steady-state Measurements of Extensional Viscosity”. In: *Journal of Rheology* 39.4 (July 1995), pp. 713–724. ISSN: 0148-6055, 1520-8516. DOI: 10.1122/1.550653. URL: http://sor.scitation.org/doi/10.1122/1.550653 (visited on 09/02/2022).

[38] M. Stelter et al. “Investigation of the Elongational Behavior of Polymer Solutions by Means of an Elongational Rheometer”. In: *Journal of Rheology* 46.2 (Mar. 2002), pp. 507–527. ISSN: 0148-6055, 1520-8516. DOI: 10.1122/1.1445185. URL: http://sor.scitation.org/doi/10.1122/1.1445185 (visited on 09/02/2022).

Chapter 3

COVALENT POLY(ACRYLAMIDE): STRUCTURE-PROPERTY RELATIONSHIP

I would like to reiterate my gratitude for my fellow graduate students, without whom this research would not have been possible. The careful synthesis of covalent PAMs was performed by Dr. Hojin Kim.[1] Some GPC measurements used also performed by Dr. Hojin Kim, the rest were done by RWL. All shear rheometry was performed by Dr. Red Lhota.[2] All DoSER experiments and analysis were done by RWL.

The associative polymers used in jet fuel and oil consist of a hydrocarbon backbone and end groups rich with hydrogen bonding sites.[3] To implement similar behavior in H_2O , both the backbone and associating groups have to be redesigned.

We chose to use a poly(acrylamide) (PAM) backbone. PAM is one of a few common water soluble polymer backbones (the others being poly(ethylene oxide) (PEO) and poly(acrylic acid) (PAA)) and is commonly used in soil treatments.[4–7] Consequently, it is already approved for use in agricultural applications.[8] Additionally, PEO, a more commonly studied water soluble polymer, is notoriously unstable in solution, making PAM a more desirable choice for research.[9–13] Water's willingness to engage in hydrogen bonding means that we cannot rely on the polymers to reliably associate with one another to form long, end associated megasupramolecules through hydrogen bonding. Instead, the H_2O in solution would occupy the hydrogen bonding sites on the polymer ends. Therefore, the associative groups were redesigned as well.

This section will focus on the *covalent* or conventional PAM. It is necessary to characterize its behavior in solution as a baseline to make a comparison with the associative PAMs. My goal was to study a range of molecular weights and concentrations to establish the relationship between those quantities and the fluid properties of elongational relaxation time (λ_E) and viscosity (η_E). Because the fluid flow following a droplet impact is highly elongational, these are the relevant quantities to measure to predict the outcome of droplet impacts.[11,14–18]

All DoSER experiments in this chapter were performed with 22G (D_0 = 0.718 mm) needles, onto aluminum substrates with a gap height (H) of $\sim$ 3.2 mm (H/D_0 = 4.5, $H/D_{pred}^{solvent}$ = 1.2), and at temperatures ranging from 15 to 17 $^\circ$ C. The values of H

and identity of the substrate was chosen to optimize the experimental conditions per the experiments in Chapter 2.

Broadly, adding polymers to solution increases the λ_E and η_E of the solution without changing the η_S or σ. The fundamental reason for behavior is that the polymer chains respond differently to shear flow and elongational flow. At rest, the polymers are coiled randomly with a the root mean square of average end to end distance: $\sqrt{<\overrightarrow{R}^2>} = N^{\frac{1}{2}}l$, where N is the number of repeat units and l is the length of a single repeat unit.[i] Under mild shear flows, as η_S is measured, the coils do not change shape but instead they tumble or rotate; this motion contributes to a moderate increase in η_S. In shear flow, η_S changes behavior above and below a critical concentration, c^*.[19] c^* describes the overlap concentration for polymers in solution. At $c > c^*$, the coils begin to interact with one another as the fluid deforms and they rotate. These interactions compound and η_S increases sharply with c when $c > c^*$. When $c < c^*$, the polymer coils do not interact with one another and increasing the concentration only mildly increases η_S until $c = c^*$.[2]

However, under elongational flow, the polymer chains extend from their coiled state and sharply increase $\sqrt{<\overrightarrow{R}^2>}$. This forced uncoiling of the polymer chain is accompanied with a large entropic penalty: the number of available microstates decreases with the increase in $\sqrt{<\overrightarrow{R}^2>}$.[19,20] Forcing the polymer chain into a configuration with fewer available microstates costs energy and the energy required to pay this entropic penalty and elongate the polymer manifests as an increase in the measured values of η_E and λ_E. Because the shape and realized length of the polymers are changing throughout this process, the value of c^* determined from shear rheometry does not correctly capture the concentration at which polymer chains overlap under elongational flow. The elongational overlap concentration, c_E^*, is likely much lower.[21,22]

Furthermore, the η_E and λ_E of a polymer solution cannot be predicted from shear flow measurements. In extreme cases, a polymer solution can have $\frac{\eta_E}{\eta_S} = 1000$ or more. For simple fluids, $\frac{\eta_E}{\eta_S}$, known as Trouton's ratio or Tr, is 3.[23,24] If the mechanism of chain elongation increasing η_E is correct, then η_E should depend on the molecular weight (M_w) of the polymer in solution. For aqueous solutions,

[i] Although $\sqrt{<\overrightarrow{R}^2>} = N^{\frac{1}{2}}l$, the average itself $<\overrightarrow{R}>= 0$. A single measurement of end-to-end distance will have non-zero magnitude but the vector is equally likely to have any direction, resulting in an average of 0.

the academic community has measured λ_E and η_E of PEO solutions with different concentrations, but almost entirely at M_w = 1 Mg/mol. There are scattered data of PEO with M_w = 2 Mg/mol, and no results reported on PAM solutions. By measuring PAM solutions with different M_w and concentrations, I will discover the relationship between λ_E, η_E, M_w, and c. Additionally, I can test the effect of the side group. The PAM repeat unit is unique among PEO and PCOD in that it holds more mass in the side group (the amide: $CONH_2$, 44 g/mol) than the backbone (C_2H_3, 27 g/mol). In the current Rouse and Zimm models used to understand the effect of M_w on λ_E and η_E, the drag on a single repeat unit is assumed to be proportional to the length of the repeat unit, effectively ignoring the bulky side groups. Analysis of PAM solutions will elucidate the validity of that assumption and help to generalize the understanding of how different polymer structure affects the solution properties.

3.1 Elongational relaxation time measurement and scaling

By changing the molecular weight and concentration of PAM solutions, the corresponding changes in solution properties can be resolved with DoSER. Increasing the molecular weight and increasing the concentration of PAM both increase the elongational relaxation time (λ_E) and elongational viscosity (η_E). The increased elongational relaxation time manifests as a longer lived filament and a longer duration of elasto-capillay behavior (EC). The EC behavior is captured by the following balance between elastic (g_i and $\lambda_{E,i}$) and capillary (surface tension, σ) forces:

$$\frac{D_{EC}(t)}{D_0} = \sum_i \left(\frac{g_i D_0}{4\sigma}\right)^{1/3} \exp\left(\frac{-t}{3\lambda_{E,i}}\right), \tag{3.1}$$

where g_i and $\lambda_{E,i}$ are the corresponding extensional modulus and relaxation time for a mode i. I adopt the hypothesis of Entov and Hinch [25] and Dinic, Jimenez, and Sharma [26]: the behavior of the EC regime can be approximated by using only the longest relaxation time of the system, yielding:

$$\frac{D_{EC}(t)}{D_0} \approx \left(\frac{G D_0}{4\sigma}\right)^{1/3} \exp\left(\frac{-t}{3\lambda_E}\right). \tag{3.2}$$

We also include the critical time, t_c, which is the moment of transition from the preceding regime to the EC regime, to align the normalized diameter data. A reliable value of the critical time is necessary to fairly compare videos which may have different relative start and end times depending on user choices of where to begin and end videos. Prior literature determined the critical time by visual inspection of the source videos or the numerical datasets.[26–30] By definition, the

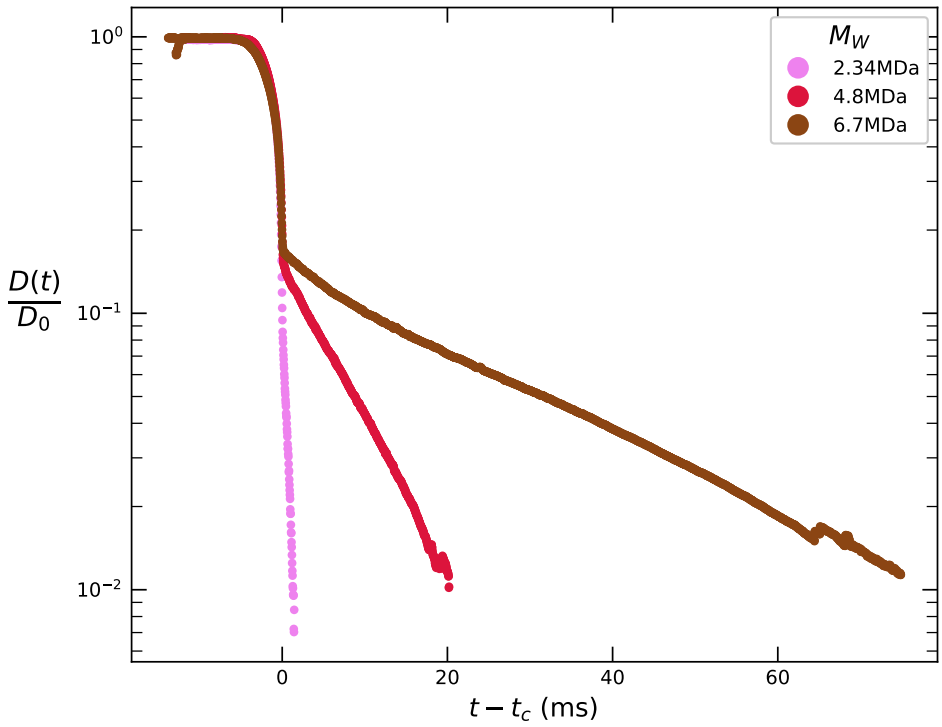

Figure 3.1: Minimum normalized diameter ($D(t)/D_0$) evolution in time (t) for PAM solutions with a concentration of 0.1 weight % and weight average molecular weight (M_w) of 2.34, 4.8, and 6.7 Mg/mol. At each M_w, every point is the average value $D(t)/D_0$ of 5 trials for a given $t - t_c$.

normalized diameter at the critical time is $\frac{D(t_c)}{D_0}$, and we substitute this value into Equation 3.2 for the leading coefficient. This substitution renders the final form of the equation describing EC behavior,

$$\frac{D_{EC}(t)}{D_0} = \frac{D(t_c)}{D_0} \exp\left(\frac{-(t - t_c)}{3\lambda_E}\right), \tag{3.3}$$

which I use for further calculations.

By fitting $\frac{D(t)}{D_0}$ to the exponential decay in Equation 3.3, I determined λ_E for PAM solutions with M_w = 2.3, 4.8, and 6.7 Mg/mol and a range of concentrations from 0.01 to 1 weight %. An example of this (Figure 3.1) shows the effect of increasing M_w at a constant concentration of 0.1 weight %. After $t = t_c$, the measured diameter decreases much faster in the low M_w solution (pink) than the high M_w solution (brown). For $t < t_c$, $D(t)/D_0$ is nearly identical for all three solutions tested, indicating the measurement cannot distinguish the difference in M_w prior to $t = t_c$. Each set of experiments in a single M_w shows a similar increase in λ_E as the concentration increases (Figure 3.2). Because these data are plotted on logarithmic

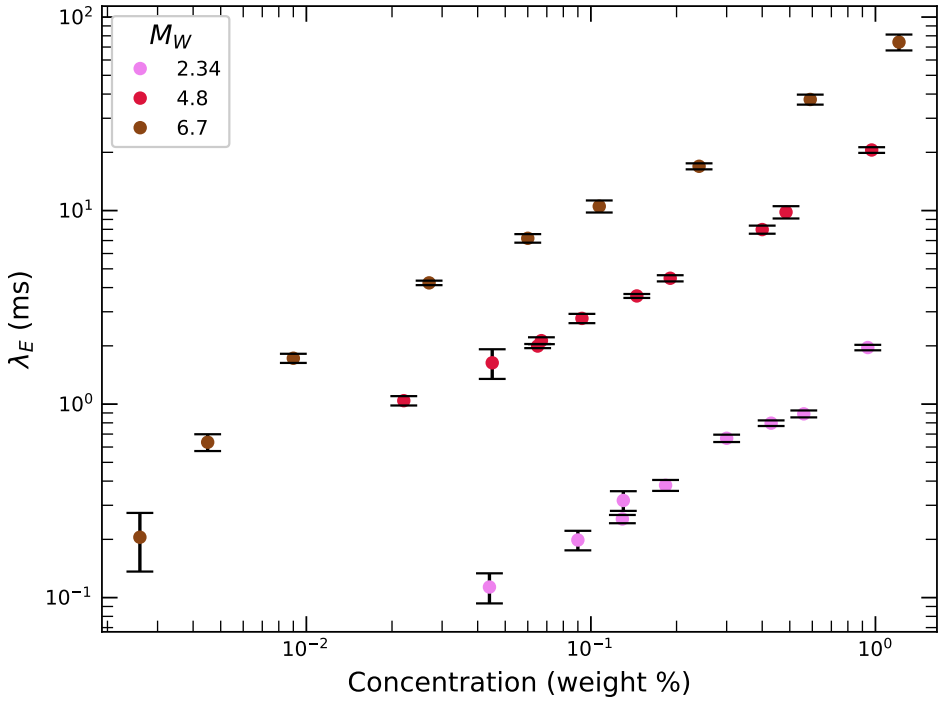

Figure 3.2: The elongational relaxation time (λ_E), a mean of n = 5 trials, measured by DoSER for covalent PAM with weight average molecular weight (M_w) from 2 Mg/mol to 7 Mg/mol and concentration from 0.01 weight % to 2 weight %. The error bars show ±1 standard deviation.

axes, these similar slopes represent a power law scaling. In this case, $\lambda_E \sim c^{0.77}$. Furthermore, for any given concentration, the measured λ_E is heavily influenced by the M_w of the PAM solution. As the polymer M_w increases, the λ_E always increases. I expanded the empirical fitting to include the M_w and found

$$\lambda_E \sim M_w^{3.6} c^{0.77}. \tag{3.4}$$

The exponents found in Equation 3.4 show that the λ_E depends much more on the M_w or length of the polymer chain than the number or concentration of polymer chains in solution. However, the observed M_w scaling ($M_w^{3.6}$) exceeds the exponent of 2 predicted by Rouse-Zimm theory.[2,19,29] There are no other reports of experimental results relating λ_E to changing M_w in aqueous solutions, so my experimentally observed scaling of 3.6 is plausible.[ii]

I attribute the discrepancy between the theory and experiment to the assumptions made in the Rouse model. This model is based on an entropic spring argument:

[ii]Data I collected on aqueous poly(ethylene oxide) solutions, which appears primarily in Section 2.3 of Lhota [2], yields $\lambda_E \sim M_w^{2.5} c^{0.9}$, again exceeding the exponent predicted by theory.

it treats the polymers as Gaussian chains and does predict the response to small deformations well. However, in DoSER experiments, the polymers are assumed to reach their finite extensibility limit, indicated by a sharp drop in $D(t)/D_0$, at the end of the EC regime.[21,25,29] This assumption means the polymer chains have extended well beyond the small deformations where the Rouse model, and the entropic spring approximation upon which it is based, is accurate. Therefore, the λ_E measured on DoSER is more accurately viewed as a combination of the result from the Rouse model and the statistical mechanics treatment for a polymer chain under a constant force.

In this model, the partition function is evaluated explicitly for every conformational state, where a single end-to-end vector is calculated as

$$R_z = \sum_{i=1}^{N} P \cos\theta_i, \tag{3.5}$$

where P is the polymer's persistence length in solution and θ_i is the bond angle between the i^{th} and $i-1^{th}$ persistence length. The partition function is the summation over all states and the energy associated with each one:

$$Z = \sum^{states} \exp\left(\frac{FR_z}{k_BT}\right) \tag{3.6}$$

where F is the applied force, k_B is Boltzman's constant, T is the temperature, and R_z is defined above.[19] Substituting Equation 3.5 into Equation 3.6 yields:

$$Z = \int \exp\left(\frac{FP}{k_BT}\sum_{i=1}^{N}\cos\theta_i\right)\prod_{i=1}^{N}\sin\theta_i d\theta_i d\phi_i,$$

which evaluates to:

$$Z = \left(\frac{4\pi \sinh FP/(k_BT)}{FP/(k_BT)}\right)^N. \tag{3.7}$$

The partition function is directly related to Gibb's free energy G by Boltzmann's relation:[31]

$$G(T,F,N) = -k_BT\ln Z = -k_BTN\left(\ln\left(4\pi\sinh\frac{FP}{(k_BT)}\right) - \ln\left(\frac{FP}{k_BT}\right)\right), \tag{3.8}$$

and can be used to calculate the change in energy between two systems under different applied forces. As this derivation is purely based on entropy, it assumes that no chemical bonds are formed or broken under the applied force; changes in enthalpy must be accounted for separately.

Finally the displacement can be calculated by the partial derivative of G with respect to the applied force F:

$$< R >= -\frac{\delta G}{\delta F} = NP\left(\coth\left(\frac{FP}{k_BT}\right) - \frac{k_BT}{FP}\right). \tag{3.9}$$

The expression $L(x) = \coth x - \frac{1}{x}$ is known as the Langevin function and was originally developed in studying para-magnetic materials with statistical mechanics.[32] The inverse Langevin function $L^{-1}(x)$ is required to calculate the extension for a given applied force, x. Although no analytical solution for $L^{-1}(x)$ exists, many approximations have been proposed and I use:

$$L^{-1}(x) \approx x\frac{3 - x^2}{1 - x^2}, \tag{3.10}$$

which is simple enough to still be intuitive while having a maximum relative error of 4.9% near $x = 0.8$.[33] The key conclusion from Equations 3.9 and 3.10 is that as $< \overrightarrow{R} >$ approaches $R_{max} = NP$, the energy input required to continue increasing $< \overrightarrow{R} >$ increases dramatically.[31] Long polymer chains require more energy to bring to full extension and reach the finite extensibility regime than their short counterparts. The EC behavior, from which λ_E is calculated, ends at the onset of finite extensibility regime, explaining the increased λ_E seen in solutions of higher M_w polymer.

3.2 Elongational viscosity measurement and scaling

The quantity λ_E is of interest to polymer physicists as a measure of the time-scale of the polymer chain. In particular, the λ_E measured by the DoSER technique measures the longest relaxation time of the polymer, or the time it takes for the entire chain to react to a change in its environment. Another quantity, the elongational viscosity, η_E, is more practical. In general, viscosity describes how a fluid resists an applied strain rate:

$$\text{Stress} = \eta\dot{\epsilon},$$

where $\dot{\epsilon}$ is an applied strain rate and the stress is the force per area of fluid over which the strain rate is applied.[iii] The *elongational* viscosity, η_E, characterizes the fluid's resistance to extensional flow. The DoSER datasets can also be analyzed to

[iii] Alternatively, η can tell you what strain rate the fluid will reach for a given applied stress. Regardless, this is a gross oversimplification, as η can depend on the strain rate, the magnitude of strain, the type of flow, temperature, the fluid's history, and more.

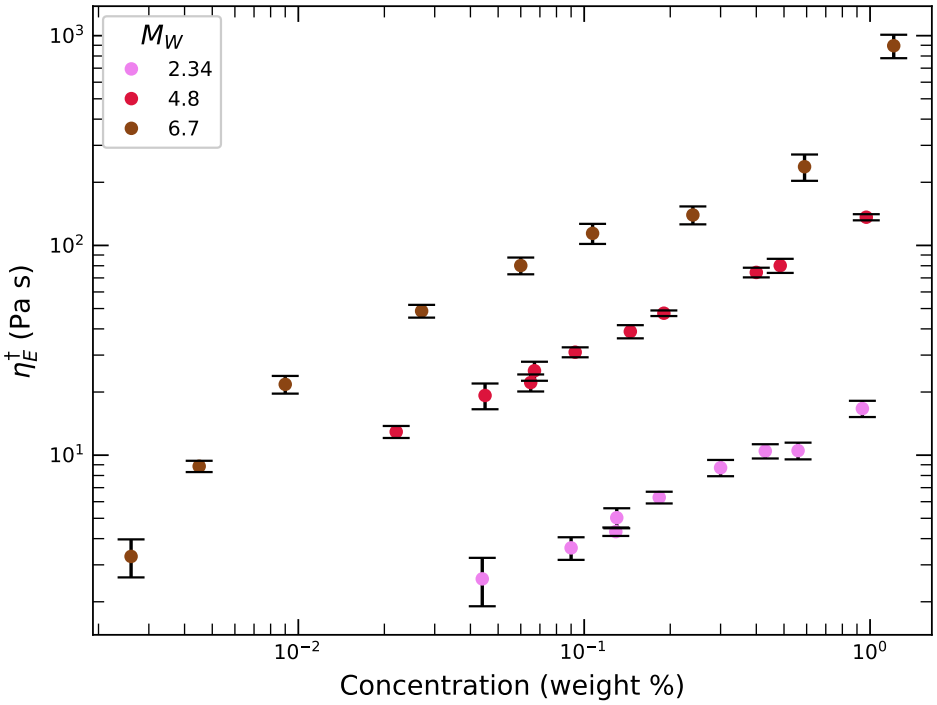

Figure 3.3: The estimated elongational viscosity ($\eta_E^\dagger$) measured by DoSER (mean of n = 5 trials) for covalent PAM with weight average molecular weight (M_w) from 2 Mg/mol to 7 Mg/mol and concentration from 0.01 weight % to 2 weight %. The error bars show ±1 standard deviation.

determine η_E with the use of λ_E, $D(t_c)$, and σ. I estimate η_E using:

$$\eta_E^\dagger = \frac{3\lambda_E\sigma}{D(t_c)\exp(-2)}, \tag{3.11}$$

using λ_E; the surface tension, σ; and the diameter at the critical time, $D(t_c)$. The details of this approximation are in Section 2.3. In aggregate, the observed η_E for the solutions tested in Section 3.1 behave similarly to λ_E (Figure 3.3).

Fitting η_E to a power law with M_w and c yields

$$\eta_E \sim M_w^{3.0} c^{0.5}. \tag{3.12}$$

The scaling result in Equation 3.12 shows that, like λ_E, η_E depends more strongly on M_w than c. Again, the experimentally observed behavior ($M_w^{3.0}$) is more sensitive to M_w than is predicted by theory: $M_w^{2(1-\nu)} = M_w^{0.8}$ for PAM in H_2O.[29] Here, ν is the Flory exponent which captures the strength of interactions between the polymer repeat units and the solvent, $\nu = 0.6$ for PAM in H_2O.[19] In literature reports of PEO solutions, $\eta_E \sim M_w^2$.[29] The exact value of the exponent from this article should be

viewed only as an estimate; the authors do not address this discrepancy or claim to fit $\eta_E \sim M_w^x$. Their dataset is limited to M_w = 1 and 2 Mg/mol, and the M_w was not verified by GPC or other analytical techniques prior to the DoSER experiments. Regardless, multiple independent experimental observations strongly disagree with the scaling predicted by theory. Similar to the arguments regarding the scaling for λ_E, η_E is explicitly calculated at the onset of the finite extensibility regime. The polymer chains have reached their full elongation near the moment the calculation is performed, and far exceeded the Gaussian limits of the Rouse model. Furthermore, the pendant amide groups may act as a parachute, creating drag with the H_2O as the polymer extends and diffuses through the solution. Another consideration is the ability of the amide pendant groups to engage in hydrogen bonding with one another or with the H_2O molecules. The summation of intermolecular forces such as hydrogen bonding is known to give rise to unexpected physical observations (such as the high boiling point of H_2O itself), and breaking these intermolecular attractions throughout extensional flow could explain the increased η_E.

Measuring the viscosity in shear (η_S) and extension (η_E) accentuates the difference between the fluids' responses in the different types of flow. The η_S measurements were performed by Dr. Red Lhota *via* traditional shear rheometry on a subset of the solutions I measured η_E *via* DoSER. In polymer solutions, η_S spans roughly one order of magnitude from 2 to 6 mPa s (0.002 to 0.006 Pa s). Even at the highest η_S, the PAM solutions only resist shear flow 10x as strongly as pure H_2O. The measured η_E spans from 3 Pa s to 130 Pa s; the lowest polymer concentration and M_w tested has 1000x the η_E of H_2O. These fluids exhibit two distinct behaviors: under shear flow they behave similarly to pure H_2O, while they strongly resist elongational motion. Furthermore, by changing the concentration and and M_w simultaneously, η_E and η_S can be changed independently. For example, lowering the concentration and increasing the M_w results in an increase in η_E and no change in η_S. In this system, observations of multiple solutions with the same η_S and different η_E further validates the necessity of measuring η_E of polymer solutions under elongational flow. η_E cannot be predicted from η_S, although both can be estimated from the M_w and c of the solution if the relationship is known.

Additionally, the distinct M_w scaling of η_E and λ_E yields the ability to estimate $\frac{D(t_c)}{D_0}$. I observed that $\lambda_E \sim M_w^{3.6}$ and $\eta_E \sim M_w^{3.0}$. Substituting those values into Equation 3.11 yields

$$M_w^{3.0} c^{0.5} \sim M_w^{3.6} c^{0.77} D(t_c)^{-1}.$$

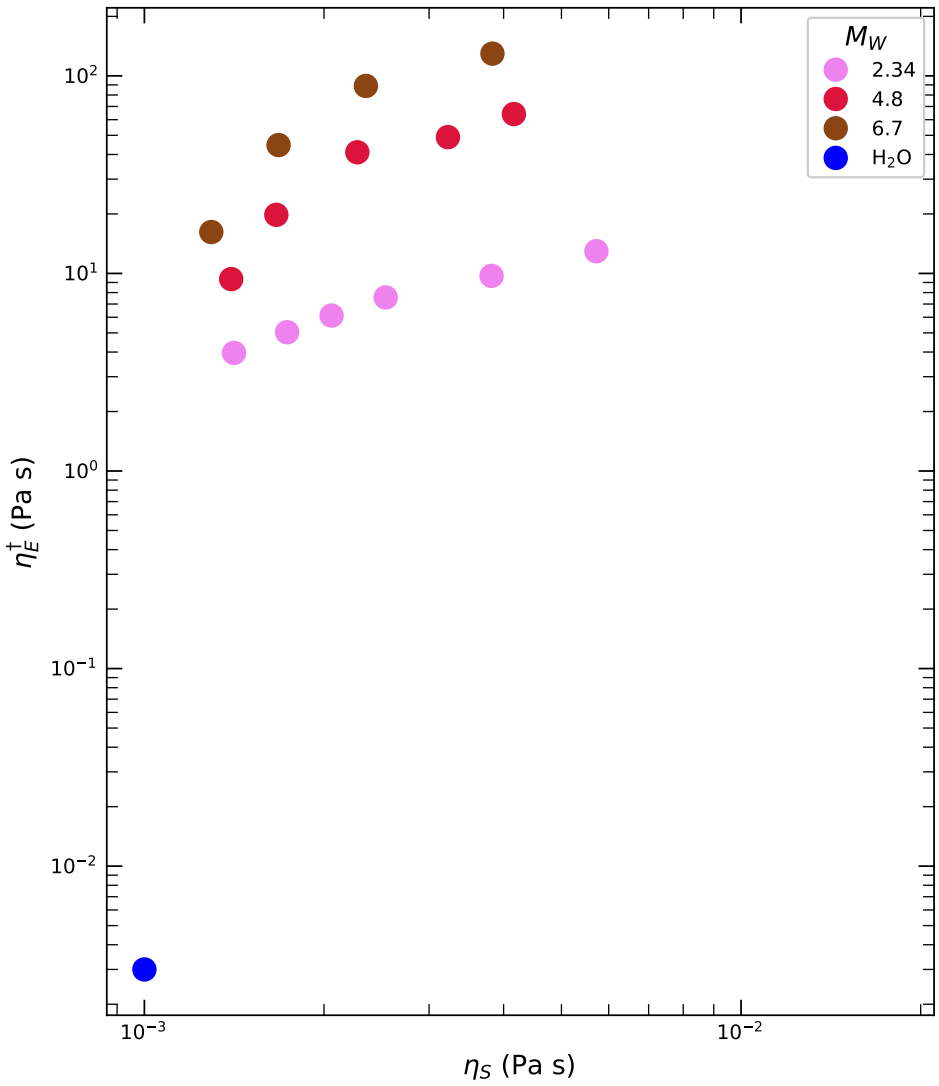

Figure 3.4: The shear viscosity, η_S, measured by low-amplitude oscillatory shear rheology, and the estimated extensional viscosity, $\eta_E^\dagger$, measured by DoSER (mean of n = 5 trials) of pure H_2O and PAM solutions of different concentrations and weight average molecular weight (M_w). The $\eta_E^\dagger$ of H_2O is calculated from Trouton's ratio.

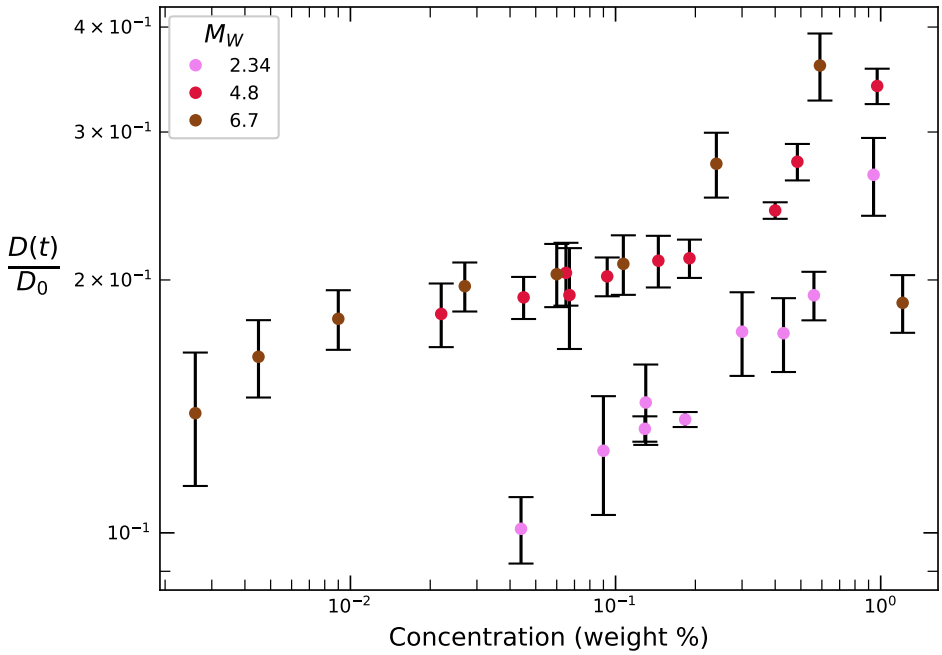

Figure 3.5: The mean minimum normalized diameter at the critical time ($D(t_c)/D_0$) of n = 5 trials, measured by DoSER, with error bars showing ± 1 standard deviation for covalent PAM with weight average molecular weight (M_w) from 2 Mg/mol to 7 Mg/mol and concentration from 0.01 weight % to 2 weight %.

This can be further reduced to

$$D(t_c) \sim M_w^{0.6} c^{0.27}, \tag{3.13}$$

revealing how $D(t_c)$ depends on the M_w and c of the solution. $\frac{D(t_c)}{D_0}$ is a constant fluid property and equivalent to:

$$\frac{D(t_c)}{D_0} = \left(\frac{G_E D_0}{4\sigma}\right)^{1/3}, \tag{3.14}$$

where G_E is the extensional elastic modulus of the fluid. Therefore, with a known value of σ, reasonable predictions of G_E can also be obtained from characterizing the polymer solutions with the DoSER experiment.

Indeed, $D(t_c)/D_0$ increases as concentration and M_w increase (Figure 3.5). In the EC regime ($t > t_c$), the strain rate ($\dot{\epsilon}$) is set by the λ_E of the solution:[29]

$$\dot{\epsilon} = \frac{2}{3\lambda_E} \sim \frac{1}{M_w^{3.5} c^{0.82}}. \tag{3.15}$$

The $\dot{\epsilon}$, prescribed by the polymers in solution, decreases as the concentration and M_w increase. Additionally, the $\dot{\epsilon}$ required to initiate the coil-stretch transition during

a DoSER experiment ($t = t_c$) decreases as the concentration and M_w increase. For low concentration (see Section 3.3) polymer solutions, the behavior preceding $t = t_c$ is independent of the M_w and c of the polymer present. The approach to $t = t_c$ is marked by rapid decrease in $D(t)/D_0$ and rapid increase in $\dot{\epsilon}$ (Figure 2.15). The onset of chain stretching at $\frac{D(t_c)}{D_0}$ halts the increase in $\dot{\epsilon}$, marks the beginning of the EC regime, and allows the polymers in solution to dictate the flow behavior for the filament.

$D(t_c)/D_0$ is measured precisely as the polymers' coiled configuration is giving way to chain extension.[30] The experimentally observed scaling of $D(t_c)/D_0$ shows two distinct slopes for each set of concentrations at the three M_w tested. This effect is more similar to η_S than η_E, as discussed in Section 3.3.

3.3 Concentration effects above and below c^*

The quantity c^* describes the overlap concentration for polymers in solution. This is the concentration where the random coils begin to interact with one another as the fluid deforms. The size of the coils depends on the M_w of the polymers, so c^* is a function of M_w as well as the solvent quality. The solvent quality captures the sum of the interactions between the repeat units of the polymer and the solvent in which it is dissolved. If the repeat units interact strongly with the solvent, a case of high solvent quality, polymer takes an extended conformation in solution to increase the amount of interaction between repeat unit and solvent. If the repeat units react unfavorably with the solvent, this is known as a poor solvent or low quality solvent, the polymer will assume a tightly coiled configuration to minimize the interaction between its repeat units and the solvent. Finally, the crossover between good and poor solvent, where the repeat units are exactly as comfortable being near other repeat units or solvent is referred to as a Θ solvent. This is complicated by the general increase in solubility with temperature, so most solvent-polymer pairs can exhibit a Θ-temperature, where the increase in solubility with temperature and the polymer-solvent interactions exactly balance, even if the solvent is not a Θ solvent at room temperature. At $c < c^*$, the shear viscosity, η_S, scales linearly with c. At $c > c^*$, the polymer-polymer interactions begin to contribute additional viscosity to the solution, so this exponent increases to > 1.[34]

The process to determine c^* from shear rheology is quite time consuming, and the c^* of these PAM-H_2O systems was painstakingly determined by Dr. Red Lhota.[2] However, the traditional c^* may not be as useful a quantity for elongational fluid prop-

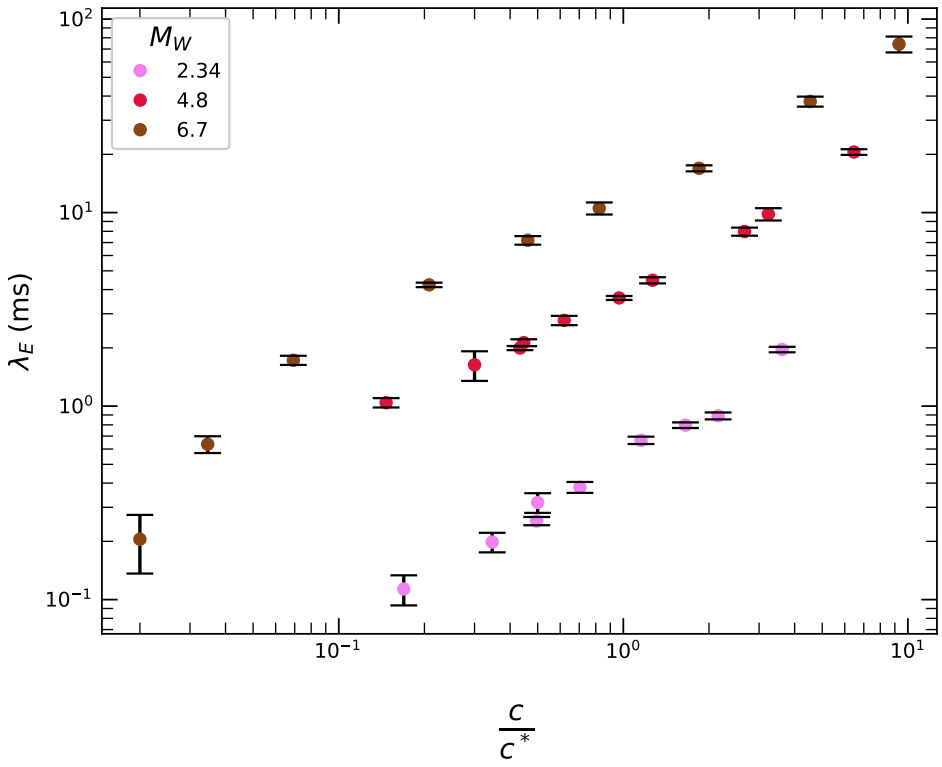

Figure 3.6: The elongational relaxation time (λ_E, mean of n = 5 trials) measured by DoSER for covalent PAM with weight average molecular weight (M_w) from 2 Mg/mol to 7 Mg/mol and concentration normalized by critical concentration for each M_w ($\frac{c}{c^*}$) ratio from 0.01 to 10. The error bars show ±1 standard deviation.

erties. Under small amplitude shear rheometry, the polymers are not disturbed very much from their coiled configuration. Elongational rheometry is a sharp contrast to that—the polymers reach their finite extensibility limit throughout the experiment. They also become highly aligned over the course of a DoSER experiment as the filament narrows simultaneously with the polymer extension. An extending, uncoiling polymer chain explores much more volume of solvent than the coiled configuration. Therefore the concentration at which a polymers will not interact with one another in solution is *much, much* lower in elongational flow than shear flow.[21,30]

The elongational fluid properties λ_E and η_E show no significant change in their behavior between $\frac{c}{c^*} < 1$ and $\frac{c}{c^*} > 1$ (Figures 3.6 and 3.7). This indicates that c^*, as determined by shear rheology, is an irrelevant quantity for the fluids' behavior under elongational flows. As seen previously,[21,27] this is consistent with the different molecular pictures of chain deformation under the different types of flow. In contrast, the quantity $\frac{D(t_c)}{D_0}$ scales differently above and below $\frac{c}{c^*} = 1$ (Figure 3.8). The distinct

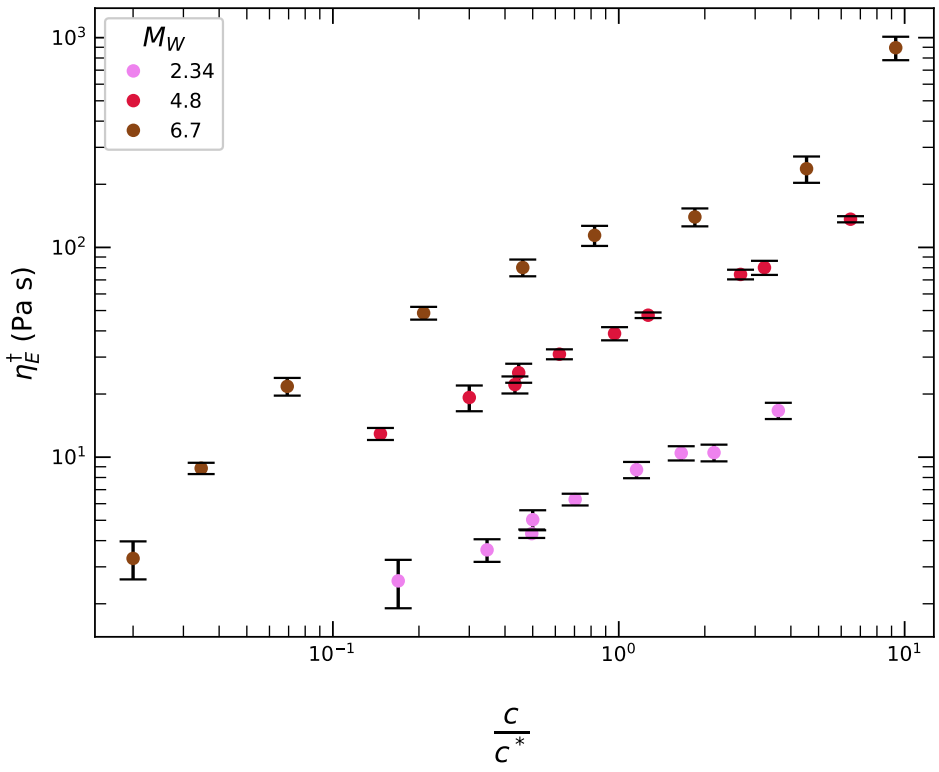

Figure 3.7: The estimated elongational viscosity ($\eta_E^\dagger$, mean of n = 5 trials) measured by DoSER for covalent PAM with weight average molecular weight (M_w) from 2 Mg/mol to 7 Mg/mol and concentration normalized by critical concentration for each M_w ($\frac{c}{c^*}$) from 0.01 to 10. The error bars show ±1 standard deviation.

scaling indicates that $\frac{D(t_c)}{D_0}$ depends on the volume pervaded by the polymer chains in their coiled state. Based on Equation 3.14, I conclude that the measured elongational elastic modulus, G_E, also depends on the interactions of polymer chains in their coiled state. In solutions where $c > c^*$, the polymer coils are overlapping with each other, reducing their mobility. The reduced mobility effectively diminishes the M_w that the polymers behave with, ultimately leading to a higher elastic modulus of the solutions. The $D(t_c)$ scaling in the two regimes ($c < c^*$ and $c > c^*$) exhibits very different dependence on concentrations. For $c < c^*$,

$$\frac{D(t_c)}{D_0} \sim c^{0.09} M_w^{0.44}, \tag{3.16}$$

while for $c > c^*$,

$$\frac{D(t_c)}{D_0} \sim c^{0.35} M_w^{0.52}. \tag{3.17}$$

The onset of EC behavior being determined by the solution's η_S, rather than η_E, is captured by the mathematical distinction expressed in Equations 3.16 and 3.17 for $\frac{D(t_c)}{D_0}$.

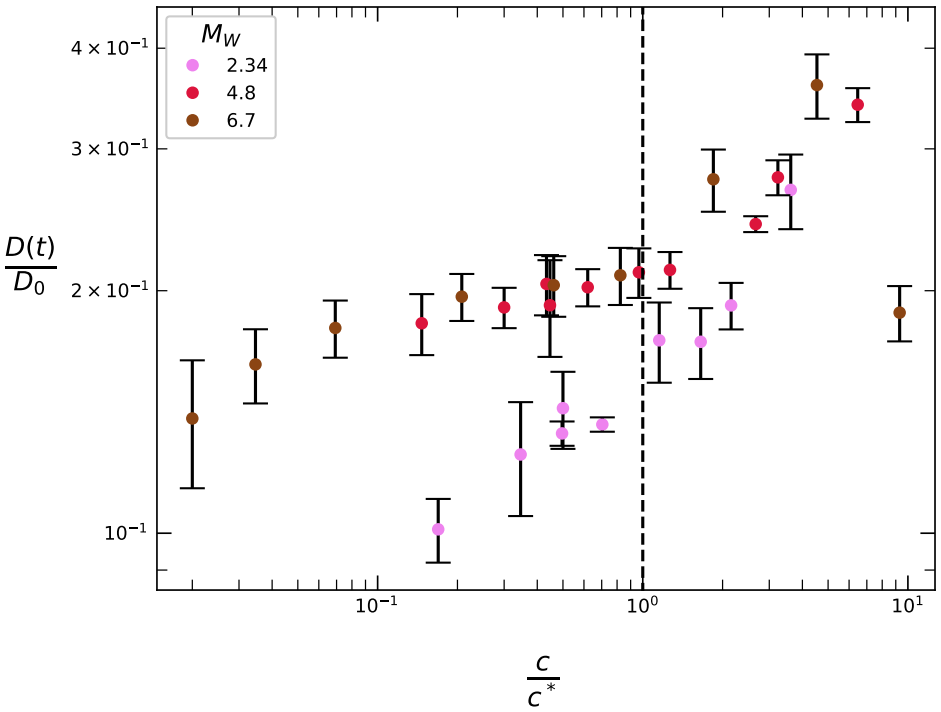

Figure 3.8: The minimum normalized diameter at the critical time ($D(t_c)D_0$, mean of n = 5 trials) measured by DoSER for covalent PAM with M_w from 2 Mg/mol to 7 Mg/mol and concentration normalized by critical concentration for each M_w ($\frac{c}{c^*}$) ratio from 0.01 to 10. The dashed line illustrates $c/c^* = 1$. The error bars show ±1 standard deviation.

The distinct c scaling behavior for η_E and η_S is well illustrated by calculating Trouton's ratio: $Tr = \frac{\eta_E}{\eta_S}$. For polymer solutions at any value of $\frac{c}{c*}$, Tr will be much larger than the value it takes for Newtonian fluids, 3. However, for all the M_w I tested, Tr takes a maximum at $\frac{c}{c*} < 1$ (Figure 3.9). At $\frac{c}{c*} > 1$, the η_S scaling has increased above linear and the effect of increasing the concentration is contributing more to increasing η_S than it is η_E. At $\frac{c}{c*} < 1$, the opposite is occurring. The effect of increasing c is still seen in rapid increase in η_E, while η_S is only growing linearly.

3.4 Bi-disperse PAM mixtures

In the physical system of the thinning filament, the exponential decay of $\frac{D_{EC}(t_c)}{D_0}$ is set by the sum:

$$\frac{D_{EC}(t)}{D_0} = \sum_i \left(\frac{g_i D_0}{4\sigma}\right)^{1/3} \exp\left(\frac{-t}{3\lambda_{E,i}}\right),$$

over all the relaxation modes in the solution, as shown in Equation 3.1. In practice, we assume that the single longest relaxation time dominates the response and assign

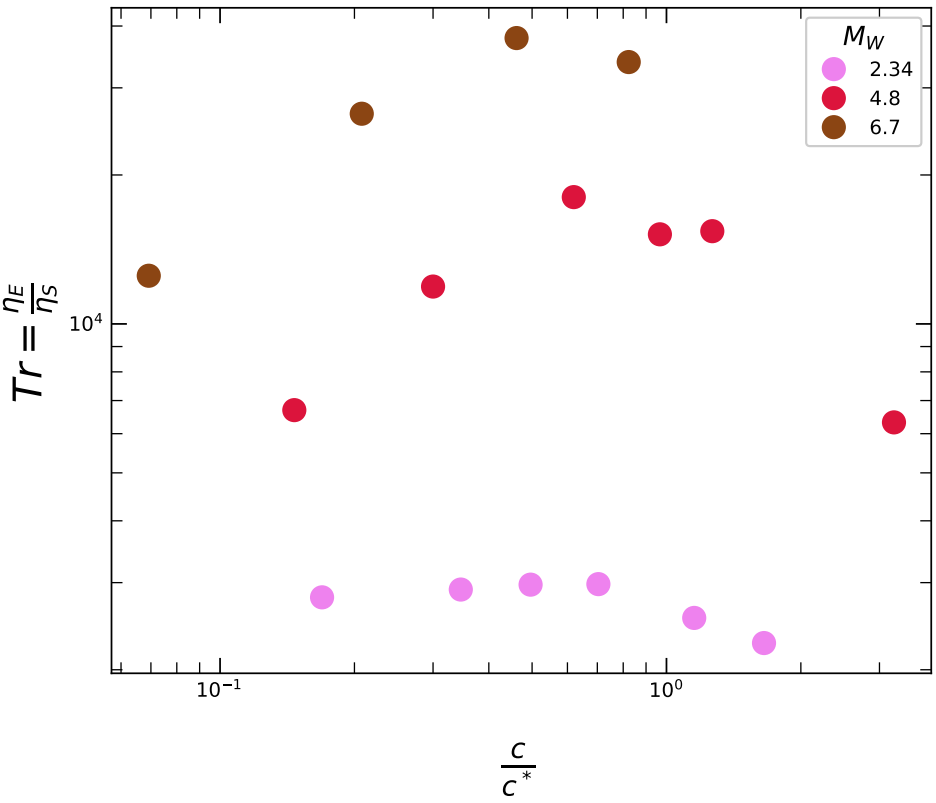

Figure 3.9: Trouton's ratio ($Tr = \eta_E/\eta_s$) measured by DoSER (mean of n = 5 trials) and low amplitude shear rheometry for covalent PAM with weight average molecular weight (M_w) from 2 Mg/mol to 7 Mg/mol and concentration normalized by critical concentration for each M_w ($\frac{c}{c^*}$) from 0.01 to 3.

it to the relaxation of the entire length of the polymer chain. This implicitly assigns the shorter relaxation times to subsections of the polymer backbone or relaxation of the polymer pendant groups.

However, even with the most careful chemical synthesis, real polymer solutions are statistical mixtures of individual molecules with many different lengths. The distribution of lengths is described by the *dispersity*, Đ= M_w/M_n. Controlled polymerizations can produce polymers with Đ< 1.1, however, the DoSER technique still over-represents the longest polymers within that narrow distribution. In the case of free radical polymerization, Đ ~ 1.5, and the polymer community still considers the DoSER analysis of λ_E to be valid.

To test the limits of the assumptions implicit in the measurement technique, I intentionally created polymer solutions with broad Đ. I made stock solutions of PAM with M_w of 1.6 Mg/mol and 6.7 Mg/mol with equal mass concentrations (0.08

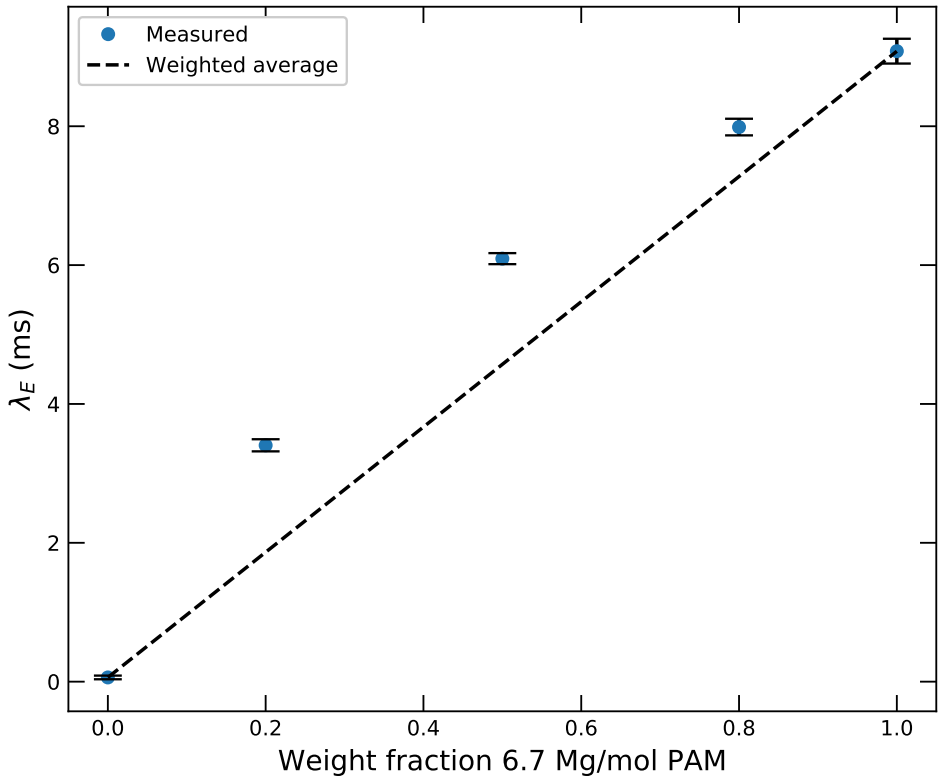

Figure 3.10: The measured elongational relaxation time (λ_E) for PAM solutions (mean of n = 5 trials) with different mass ratios of weight average molecular weight (M_w) = 1.6 Mg/mol and M_w = 6.7 Mg/mol. The dashed line shows the value of λ_E produced from the weighted means of the individual solutions λ_E. The error bars show ± one standard deviation.

weight %). I mixed these stock solutions in different ratios to create experimental solutions with mostly short chains, an even mix, and mostly long chains, and measured the solutions *via* DoSER (Figure 3.10 and Table 3.1).

For all mixtures of 1.6 and 6.7 Mg/mol PAM, the measured λ_E exceeds the value predicted by the weighted mean of the two solutions. The measured value always surpasses the predicted value; the presence of just 20 weight % 6.7 Mg/mol chains greatly increases the observed λ_E. Not only is the measurement biased towards higher M_w polymers, the lower the percentage of 6.7 Mg/mol polymer is in solution, the more the measured effective M_w deviates from the M_w of the weighted mean of the pure solutions (Figure 3.11).

The discrepancies in λ_E highlight a fundamental limitation of the DoSER technique: it cannot evaluate the distribution of molecular weights in a given solution. The best it can do, based on the experimental scaling relationships (Section 3.1), is

Table 3.1: Binary mixtures of PAM, their measured elongational relaxation time (λ_E), and effective weight average molecular weight (M_w).

$M_{w,1}$ (Mg/mol)	Mass fraction 1	$M_{w,2}$ (Mg/mol)	Mass fraction 2	Đ†	Weighted mean λ_E (ms)	Measured λ_E (ms)	Effective M_w^* (mg/mol)
	1.0		0	1	0.1	0.1 ± 0.0	1.58 ± 0.17
	0.8		0.2	1.61	1.9	3.4 ± 0.1	5.06 ± 0.03
1.6	0.5	6.7	0.5	1.38	4.6	6.1 ± 0.1	5.98 ± 0.02
	0.2		0.8	1.13	7.3	8.9 ± 0.1	6.46 ± 0.02
	0		1.0	1	9.1	9.1 ± 0.2	6.70 ± 0.03

†: Đ† in this table is relative to the Đ inherent to each polymer.
Đ† is assumed to be 1 for solutions of a single M_w polymer.
*: The effective M_w is calculated from the scaling laws in Section 3.1.
The measured values are the means of 5 experiments, ± one standard deviation.

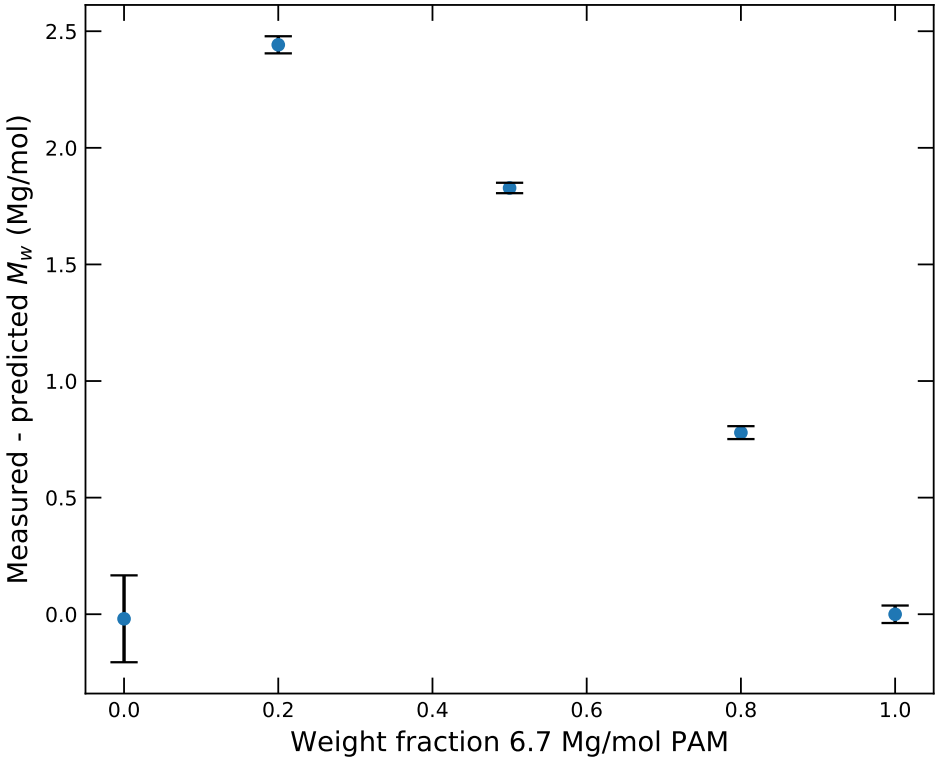

Figure 3.11: The difference between measured effective weight average molecular weight (M_w, mean of n = 5 trials) and weighted mean M_w of PAM solutions with different mass ratios of M_w = 1.6 Mg/mol and M_w = 6.7 Mg/mol. The error bars show ± one standard deviation.

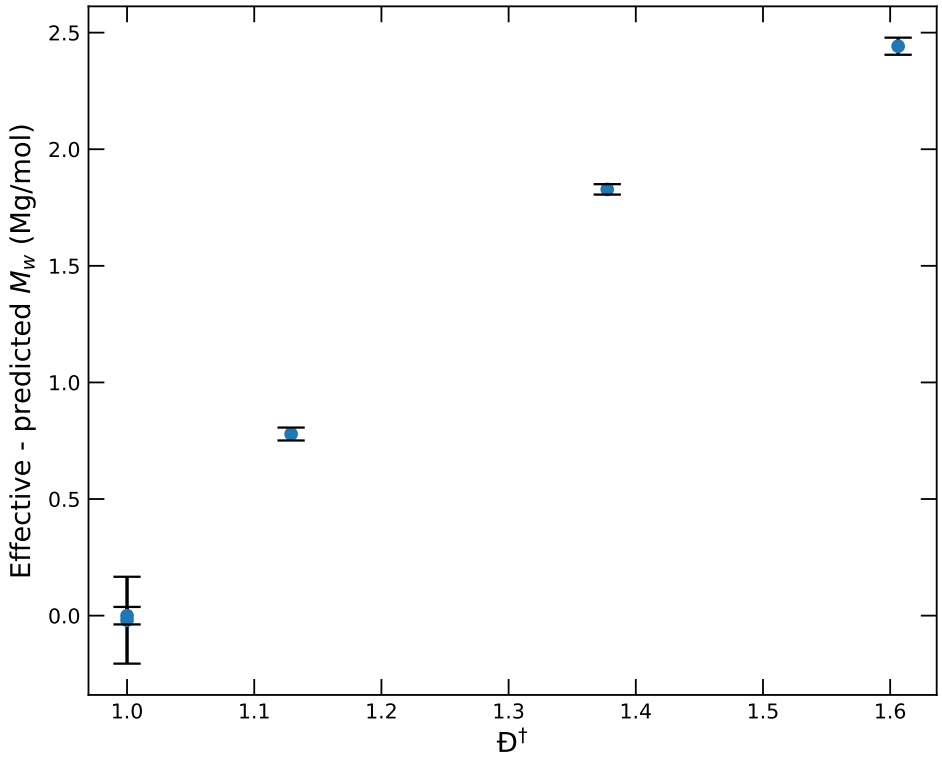

Figure 3.12: The difference between effective weight average molecular weight (M_w) and weighted mean M_w of PAM solutions with different mass ratios of M_w = 1.6 Mg/mol and M_w = 6.7 Mg/mol as a function of the dispersity ($Đ^{\dagger} = M_w/M_n$) of the solution. The $Đ^{\dagger}$ is calculated assuming the stock solutions have a Đ of 1, as illustrated in Table 3.1. The error bars show ± one standard deviation.

measure the *effective* M_w of the solution. The effective M_w is the M_w of polymer that a solution with the same mass concentration would require to produce the measured λ_E. Understanding this limitation is an important backdrop to the results with associative polymers because the distribution of associated species is unknown (Chapter 4). The broader the dispersity of the polymer solution, the more the measured λ_E exceeds the weighted mean of the solution, and similarly, the farther the calculated effective M_w is from its weighted average. For example, the Terpyridine-ended PAM used in those experiments has a M_w of 800 kg/mol, and if it formed a solution of 80% 2-mers (= 1.6 Mg/mol) and 20% 8-mers (= 6.4 Mg/mol), it would reproduce one the distribution I intentionally created in this study. This distribution evaluates to an effective M_w of 5 Mg/mol or, equivalently, a solution of 100% 6-mers.

3.5 Conclusions and future work

In this section, I share the first measurements of λ_E and η_E of aqueous polymer solutions with known M_w values. The M_w dependence of λ_E and η_E exceeds the relationship described by Rouse-Zimm theory. I propose that the discrepancy is due to the molecular structure of the PAM backbone and the experiment exceeding the small deformation limit within which the Rouse theory was derived.

To me, these scaling results in Section 3.2 directly reveal the alchemy of polymerization. To illustrate this, consider a solution of 1 kg of H_2O with 100 mg of acrylamide monomer dissolved (0.01 weight %). Our hypothetical solution will behave rheologically similar to pure water. If I arrange these acrylamides into the polymers with M_w = 3.4 Mg/mol, the solution's η_E increases to $\approx$ 37 mPa s, or 12x that of water. Doubling the M_w of these polymers to 6.7 Mg/mol, the longest polymers I tested, the η_E increases an additional 12x from the solution of 3.4 Mg/mol polymers to $\approx$ 0.45 Pa s. Finally, if instead I could stitch the same mass of acrylamides into a single 100 mg polymer chain, it would have an M_w of $6 * 10^{15}$ Mg/mol and a predicted η_E of 10^{64} Pa s, which is far beyond estimates for materials that are considered to be solids in a practical sense, e.g., Earth's mantle ($\eta_E \approx 10^{20}$ Pa s).[35]

Although the example in the paragraph above is exciting, it ignores the limitations of the observed scaling relationship. Based on the results with shorter PAM in Section 4.1, the exponential scaling with M_w does not hold down to polymers with $M_w \lesssim 0.8$ Mg/mol. Similarly, from the change in slope at $c \sim 10^{-2}$ in the M_w = 6.7 Mg/mol results in Figures 3.2 and 3.3, the scaling with concentration may change again and concentrations below 10^{-2}. Further study is needed to elucidate the upper bounds of the observed relationship as well. Because η_E and λ_E are intertwined, the observed scaling for η_E is subject to similar limitations.

To further explore the results in this chapter, in addition to determining the limits of the scaling relationship, I propose similar experiments on polymers with a modified backbone. Synthesizing water soluble polymers with larger pendant groups, with and without hydrogen bonding capability, would help to elucidate the effect of polymer mass away from the main backbone on η_E and λ_E.

References

[1] H. Kim. "New Long End-Associative Polymers for Mist Control in I. Aqueous Solutions and II. Hydrocarbon Solvents". California Institute of Technology, Aug. 26, 2022. DOI: 10.7907/RSX9-QT39. URL: https://resolver.caltech.edu/CaltechTHESIS:08252022-035254306 (visited on 09/30/2022).

[2] R. C. Lhota. "Rheological Characterization of Polymer Additives for Mist Control and Drag Reduction". California Institute of Technology, May 27, 2022. DOI: 10.7907/WAV1-4T47. URL: https://resolver.caltech.edu/CaltechTHESIS:05262022-231652129 (visited on 09/30/2022).

[3] M. H. Wei et al. "Megasupramolecules for Safer, Cleaner Fuel by End Association of Long Telechelic Polymers". In: *Science* 350.6256 (2015), pp. 72–75. ISSN: 10959203. DOI: 10.1126/science.aab0642.

[4] P. Munk et al. "Some Solution Properties of Polyacrylamide". In: *Macromolecules* 13.4 (July 1980), pp. 871–876. ISSN: 0024-9297, 1520-5835. DOI: 10.1021/ma60076a020. URL: https://pubs.acs.org/doi/abs/10.1021/ma60076a020 (visited on 02/04/2021).

[5] B. Xiong et al. "Polyacrylamide Degradation and Its Implications in Environmental Systems". In: *npj Clean Water* 1.1 (Dec. 2018), p. 17. ISSN: 2059-7037. DOI: 10.1038/s41545-018-0016-8. URL: http://www.nature.com/articles/s41545-018-0016-8 (visited on 09/01/2021).

[6] E. Sonker et al. "Preparation of Ultra-high-molecular-weight Polyacrylamide by Vertical Solution Polymerization Technique". In: *Polymer Engineering & Science* 59.6 (June 2019), pp. 1175–1181. ISSN: 0032-3888, 1548-2634. DOI: 10.1002/pen.25097. URL: https://onlinelibrary.wiley.com/doi/abs/10.1002/pen.25097 (visited on 07/02/2021).

[7] R. W. Lewis et al. "Ultra-High Molecular Weight Linear Coordination Polymers with Terpyridine Ligands". In: *Chemical Science* 10.24 (2019), pp. 6174–6183. ISSN: 2041-6520, 2041-6539. DOI: 10.1039/C9SC01115C. URL: http://xlink.rsc.org/?DOI=C9SC01115C (visited on 08/25/2021).

[8] E. A. Smith, S. L. Prues, and F. W. Oehme. "Environmental Degradation of Polyacrylamides". In: *Ecotoxicology and Environmental Safety* 37.1 (June 1997), pp. 76–91. ISSN: 01476513. DOI: 10.1006/eesa.1997.1527. URL: https://linkinghub.elsevier.com/retrieve/pii/S014765139791527X (visited on 03/30/2022).

[9] F. E. Bailey and R. W. Callard. "Some Properties of Poly(Ethylene Oxide)1 in Aqueous Solution". In: *Journal of Applied Polymer Science* 1.1 (Jan. 1959), pp. 56–62. ISSN: 00218995, 10974628. DOI: 10.1002/app.1959.070010110. URL: http://doi.wiley.com/10.1002/app.1959.070010110 (visited on 02/04/2021).

[10] F. E. Bailey, J. L. Kucera, and L. G. Imhof. "Molecular Weight Relations of Poly(Ethylene Oxide)". In: *Journal of Polymer Science* 32.125 (Nov. 1958), pp. 517–518. ISSN: 00223832, 15426238. DOI: 10.1002/pol.1958.1203212522. URL: http://doi.wiley.com/10.1002/pol.1958.1203212522 (visited on 02/04/2021).

[11] V. Bergeron et al. "Controlling Droplet Deposition with Polymer Additives". In: *Nature* 405.6788 (June 2000), pp. 772–775. ISSN: 0028-0836, 1476-4687. DOI: 10.1038/35015525. URL: http://www.nature.com/articles/35015525 (visited on 08/05/2020).

[12] B. A. Buchholz et al. "Flow-Induced Chain Scission as a Physical Route to Narrowly Distributed, High Molar Mass Polymers". In: *Polymer* 45.4 (Feb. 2004), pp. 1223–1234. ISSN: 00323861. DOI: 10.1016/j.polymer.2003.11.051. URL: https://linkinghub.elsevier.com/retrieve/pii/S0032386103011637 (visited on 01/24/2022).

[13] A. Dupas et al. "Mechanical Degradation Onset of Polyethylene Oxide Used as a Hydrosoluble Model Polymer for Enhanced Oil Recovery". In: *Oil & Gas Science and Technology – Revue d'IFP Energies nouvelles* 67.6 (Nov. 2012), pp. 931–940. ISSN: 1294-4475, 1953-8189. DOI: 10.2516/ogst/2012028. URL: http://ogst.ifpenergiesnouvelles.fr/10.2516/ogst/2012028 (visited on 10/06/2022).

[14] A.-L. Biance, C. Clanet, and D. Quéré. "Leidenfrost Drops". In: *Physics of Fluids* 15.6 (2003), p. 1632. ISSN: 10706631. DOI: 10.1063/1.1572161. URL: http://scitation.aip.org/content/aip/journal/pof2/15/6/10.1063/1.1572161 (visited on 09/03/2020).

[15] V. Bertola. "An Experimental Study of Bouncing Leidenfrost Drops: Comparison between Newtonian and Viscoelastic Liquids". In: *International Journal of Heat and Mass Transfer* 52.7-8 (Mar. 2009), pp. 1786–1793. ISSN: 00179310. DOI: 10.1016/j.ijheatmasstransfer.2008.09.028. URL: https://linkinghub.elsevier.com/retrieve/pii/S0017931008005875 (visited on 08/06/2020).

[16] D. Bartolo et al. "Dynamics of Non-Newtonian Droplets". In: *Physical Review Letters* 99.17 (Oct. 26, 2007), p. 174502. ISSN: 0031-9007, 1079-7114. DOI: 10.1103/PhysRevLett.99.174502. URL: https://link.aps.org/doi/10.1103/PhysRevLett.99.174502 (visited on 07/29/2020).

[17] V. Bertola. "Effect of Polymer Concentration on the Dynamics of Dilute Polymer Solution Drops Impacting on Heated Surfaces in the Leidenfrost Regime". In: *Experimental Thermal and Fluid Science* 52 (Jan. 2014), pp. 259–269. ISSN: 08941777. DOI: 10.1016/j.expthermflusci.2013.09.019. URL: https://linkinghub.elsevier.com/retrieve/pii/S0894177713002306 (visited on 09/02/2020).

[18] M. Xu et al. "Quantifying the Effect of Extensional Rheology on the Retention of Agricultural Sprays". In: *Physics of Fluids* 33.3 (Mar. 1, 2021), p. 032107. ISSN: 1070-6631, 1089-7666. DOI: 10.1063/5.0038391. URL: https://aip.scitation.org/doi/10.1063/5.0038391 (visited on 03/15/2021).

[19] M. Rubinstein and R. H. Colby. *Polymer Physics*. Oxford ; New York: Oxford University Press, 2003. 440 pp. ISBN: 978-0-19-852059-7.

[20] "Über Die Mechanische Bedeutung Des Zweiten Hauptsatzes Der Wärmetheorie". In: L. Boltzmann. *Wissenschaftliche Abhandlungen*. Ed. by F. Hasenöhrl. 1st ed. Cambridge University Press, Aug. 23, 2012, pp. 9–33. ISBN: 978-1-108-05279-5 978-1-139-38142-0. DOI: 10.1017/CBO9781139381420.003. URL: https://www.cambridge.org/core/product/identifier/CBO9781139381420A008/type/book_part (visited on 10/04/2022).

[21] C. Clasen et al. "How Dilute Are Dilute Solutions in Extensional Flows?" In: *Journal of Rheology* 50.6 (Nov. 2006), pp. 849–881. ISSN: 0148-6055, 1520-8516. DOI: 10.1122/1.2357595. URL: http://sor.scitation.org/doi/10.1122/1.2357595 (visited on 05/14/2021).

[22] J. Dinic and V. Sharma. "Power Laws Dominate Shear and Extensional Rheology Response and Capillarity-Driven Pinching Dynamics of Entangled Hydroxyethyl Cellulose (HEC) Solutions". In: *Macromolecules* 53.9 (May 12, 2020), pp. 3424–3437. ISSN: 0024-9297, 1520-5835. DOI: 10.1021/acs.macromol.0c00077. URL: https://pubs.acs.org/doi/10.1021/acs.macromol.0c00077 (visited on 05/05/2021).

[23] J. Wisniak. "Frederick Thomas Trouton: The Man, the Rule, and the Ratio". In: *The Chemical Educator* 6.1 (Feb. 2001), pp. 55–61. ISSN: 1430-4171. DOI: 10.1007/s00897000448a. URL: http://link.springer.com/10.1007/s00897000448a (visited on 10/04/2022).

[24] C. J. Petrie. "One Hundred Years of Extensional Flow". In: *Journal of Non-Newtonian Fluid Mechanics* 137.1-3 (Aug. 2006), pp. 1–14. ISSN: 03770257. DOI: 10.1016/j.jnnfm.2006.01.010. URL: https://linkinghub.elsevier.com/retrieve/pii/S037702570600036X (visited on 05/06/2020).

[25] V. Entov and E. Hinch. "Effect of a Spectrum of Relaxation Times on the Capillary Thinning of a Filament of Elastic Liquid". In: *Journal of Non-Newtonian Fluid Mechanics* 72.1 (Sept. 1997), pp. 31–53. ISSN: 03770257. DOI: 10.1016/S0377-0257(97)00022-0. URL: https://linkinghub.elsevier.com/retrieve/pii/S0377025797000220 (visited on 04/02/2021).

[26] J. Dinic, L. N. Jimenez, and V. Sharma. "Pinch-off Dynamics and Dripping-onto-Substrate (DoS) Rheometry of Complex Fluids". In: *Lab on a Chip* 17.3 (2017), pp. 460–473. ISSN: 1473-0197, 1473-0189. DOI: 10.1039/C6LC01155A. URL: http://xlink.rsc.org/?DOI=C6LC01155A (visited on 01/08/2020).

[27] J. Dinic et al. “Extensional Relaxation Times of Dilute, Aqueous Polymer Solutions”. In: *ACS Macro Letters* 4.7 (July 21, 2015), pp. 804–808. ISSN: 2161-1653, 2161-1653. DOI: 10.1021/acsmacrolett.5b00393. URL: https://pubs.acs.org/doi/10.1021/acsmacrolett.5b00393 (visited on 01/08/2020).

[28] J. Dinic, M. Biagioli, and V. Sharma. “Pinch-off Dynamics and Extensional Relaxation Times of Intrinsically Semi-Dilute Polymer Solutions Characterized by Dripping-onto-Substrate Rheometry”. In: *Journal of Polymer Science Part B: Polymer Physics* 55.22 (Nov. 15, 2017), pp. 1692–1704. ISSN: 08876266. DOI: 10.1002/polb.24388. URL: http://doi.wiley.com/10.1002/polb.24388 (visited on 01/08/2020).

[29] J. Dinic and V. Sharma. “Macromolecular Relaxation, Strain, and Extensibility Determine Elastocapillary Thinning and Extensional Viscosity of Polymer Solutions”. In: *Proceedings of the National Academy of Sciences* 116.18 (Apr. 30, 2019), pp. 8766–8774. ISSN: 0027-8424, 1091-6490. DOI: 10.1073/pnas.1820277116. URL: http://www.pnas.org/lookup/doi/10.1073/pnas.1820277116 (visited on 05/05/2021).

[30] J. Dinic and V. Sharma. “Flexibility, Extensibility, and Ratio of Kuhn Length to Packing Length Govern the Pinching Dynamics, Coil-Stretch Transition, and Rheology of Polymer Solutions”. In: *Macromolecules* 53.12 (June 23, 2020), pp. 4821–4835. ISSN: 0024-9297, 1520-5835. DOI: 10.1021/acs.macromol.0c00076. URL: https://pubs.acs.org/doi/10.1021/acs.macromol.0c00076 (visited on 05/05/2021).

[31] R. Petrosyan. “Improved Approximations for Some Polymer Extension Models”. In: *Rheologica Acta* 56.1 (Jan. 2017), pp. 21–26. ISSN: 0035-4511, 1435-1528. DOI: 10.1007/s00397-016-0977-9. URL: http://link.springer.com/10.1007/s00397-016-0977-9 (visited on 10/04/2022).

[32] C. Kittel. *Introduction to Solid State Physics*. 8th ed. Hoboken, NJ: Wiley, 2005. 680 pp. ISBN: 978-0-471-41526-8.

[33] A. Cohen. “A Pade Approximant to the Inverse Langevin Function”. In: *Rheologica Acta* 30.3 (1991), pp. 270–273. ISSN: 0035-4511, 1435-1528. DOI: 10.1007/BF00366640. URL: http://link.springer.com/10.1007/BF00366640 (visited on 10/01/2022).

[34] W. .-. Kulicke and R. Kniewske. “The Shear Viscosity Dependence on Concentration, Molecular Weight, and Shear Rate of Polystyrene Solutions”. In: *Rheologica Acta* 23.1 (Jan. 1984), pp. 75–83. ISSN: 0035-4511, 1435-1528. DOI: 10.1007/BF01333878. URL: http://link.springer.com/10.1007/BF01333878 (visited on 10/04/2022).

[35] H.-P. Bunge, M. A. Richards, and J. R. Baumgardner. “Effect of Depth-Dependent Viscosity on the Planform of Mantle Convection”. In: *Nature* 379.6564 (Feb. 1996), pp. 436–438. ISSN: 0028-0836, 1476-4687. DOI: 10.

1038/379436a0. URL: http://www.nature.com/articles/379436a0 (visited on 10/04/2022).

Chapter 4

ELONGATIONAL PROPERTIES OF END ASSOCIATIVE POLY(ACRYLAMIDE) SOLUTIONS

The associative PAMs in this section were synthesized by Dr. Hojin Kim. The synthetic details are available in the Methods section as well as his own thesis.[1] *Dr. Kim also performed proof of concept experiments* via *GPC to verify the associative nature of the terpyridine ended PAMs and their resistance to degradation by pumping.*

As highlighted in Section 3.4, the measurements in the DoSER technique weigh the longest relaxation times in solution the most heavily. Although I cannot assess the distribution of associative species formed from the DoSER measurements, I can confidently say "This solution of associative PAM *acts as* an equivalent solution of covalent PAM with the same concentration and this effective molecular weight."

All DoSER experiments in this chapter were performed with 22G (D_0 = 0.718 and D_{inner} = 0.413 mm) stainless steel needles, onto aluminum substrates with a gap height (H) of ~ 3.2 mm (H/D_0 = 4.5, $H/D_{pred}^{solvent}$ = 1.2), and at temperatures ranging from 15 to 17 ° C. The values of H and identity of the substrate was chosen to optimize the experimental conditions per the experiments in Chapter 2. With the exception of the experiment shown in Figures 4.11 and 4.12, all other mixtures of terpyridine-ended polymer and metal tested were created by adding metal ions to a polymer solution that was already at its target concentration.

4.1 Elongational relaxation time and elongational viscosity of terpyridine ended-poly(acrlyamides) with metal ions

As an associative PAM that forms megasupramolecules *via* metal-ligand associations, I tested solutions of terpyridine ended PAM with M_w of 800 kg/mol. With the addition of Ni^{2+} ions (1 mole of Ni^{2+} per 1 mole of polymer), the λ_E of the solution increased substantially (Figure 4.1). λ_E increases from 0.1 ms (Figure 4.1, yellow curve) to 7.1 ms (Figure 4.1, gray curve). The increased λ_E after adding the metal ions shows the formation of long, linear megasupramoecules in solution, enabled by the metal-ligand interactions between nickel and the terpyridine end groups. Based on the scaling for covalent PAM established in Equation 3.4, an λ_E

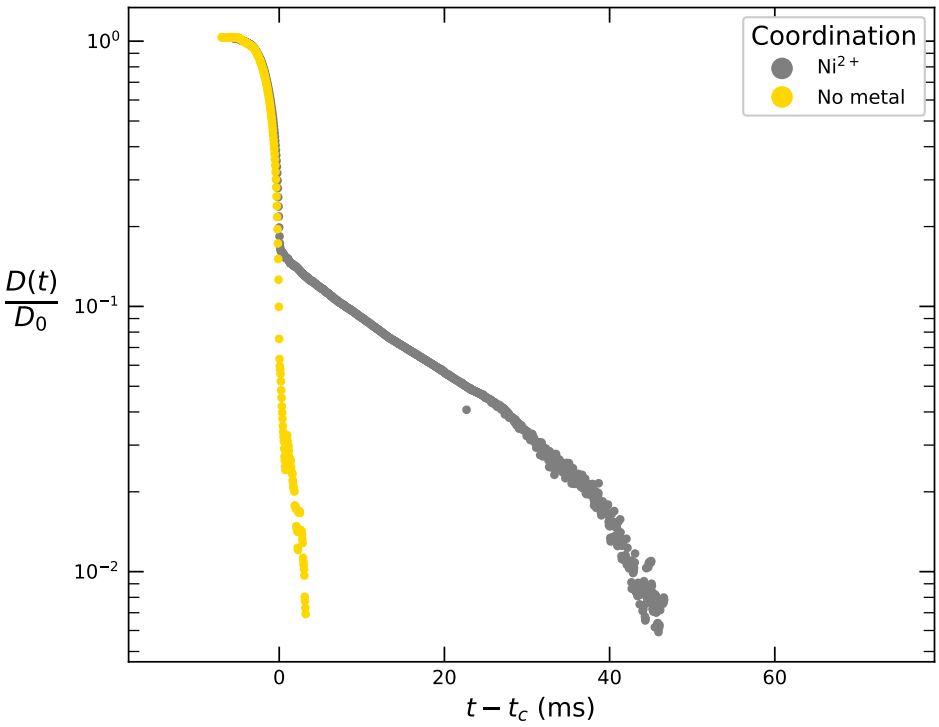

Figure 4.1: Minimum normalized diameter ($D(t)/D_0$) of n = 5 replicates of 800 kg/mol, terpyridine-ended PAM solutions at 0.1 weight % with no nickel (yellow) and 0.5 moles nickel / mole of terpyridine (1 mole nickel / mole polymer) (gray).

of 7.1 ms corresponds to an effective M_w of 5.5 Mg/mol at 0.1 weight %.

By comparison to covalent PAM solutions at the same concentration (0.1 weight %), I can see that the estimate of effective M_w is reasonable (Figure 4.2): the associative PAM solution with Ni^{2+}, determined to have an effective M_w of 5.5 Mg/mol, exhibits exponential decay of $\frac{D(t)}{D_0}$ with a slope between that of covalent PAM with M_w of 4.8 and 6.7 Mg/mol. The comparison with covalent PAM reveals another detail about the elongational behavior of the associative PAM solutions. It reaches the end of the EC regime (the beginning of the finite extensibility limit) sooner than expected.

Duration of EC regime

I use the slope of the EC regime to determine λ_E of the solution, but λ_E itself does not fully classify the fluid. Determining η_E from Equation 2.10 relies on the observation that the duration of the EC regime, Δt_{EC}, is consistently $6\lambda_E$.[2] The equation $\Delta t_{EC} = 6\lambda_E$ (Section 2.3) holds for both PEO and PAM solutions and is independent of the concentration and molecular weight. However, the shallow slope, with $\lambda_E = 7.1$ ms, of the PAM with nickle solution only persists for about

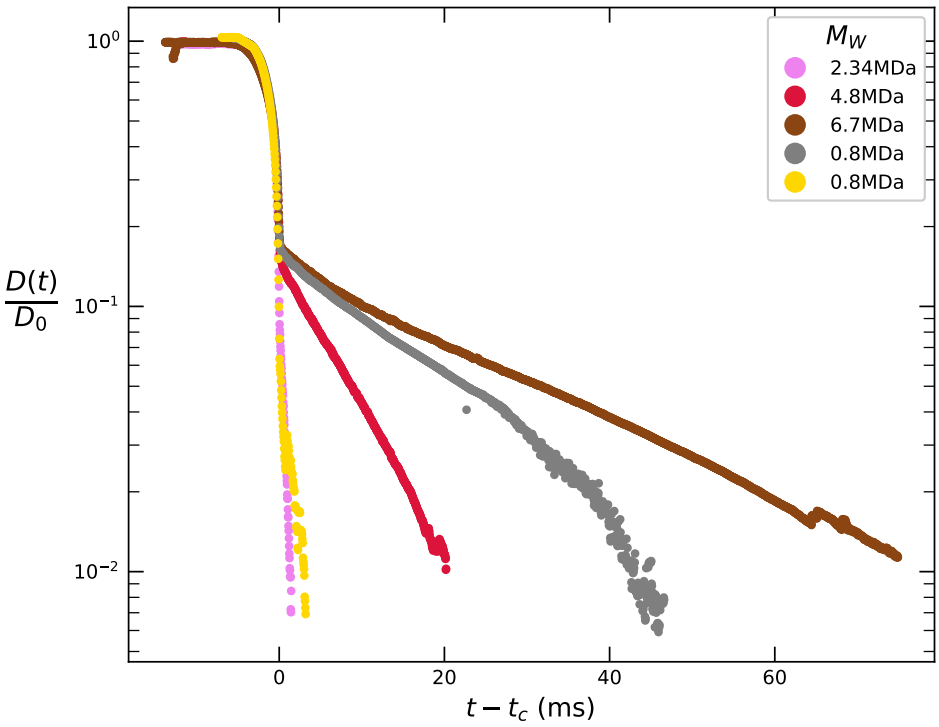

Figure 4.2: Minimum normalized diameter ($D(t)/D_0$) of n = 5 trials of terpyridine-ended PAM solutions with no nickel (yellow) and 0.5 moles nickel / mole of terpyridine (1 mole nickel / mole polymer) (gray), in comparison to covalent PAM solutions with weight-average molecular weight (M_w) of 2.3, 4.8, and 6.7 Mg/mol (pink, red, brown) at similar concentrations (0.1 weight %).

30 ms after t_c before giving way to the finite extension limit. For this solution, $\Delta t_{EC} = 4\lambda_E$ (Figure 4.3). The duration of the EC regime differs between associative and covalent PAMs that would otherwise have the same λ_E. In other words, the rate of exponential decay of the filament's diameter is the same but the lifetime of the filament is different.

The shorter duration of EC regime with an equivalent λ_E seen in associative PAM solutions means that these end-associated linear megasupramolecules are reaching their extensibility limit sooner than a covalent polymer with an equivalent length. The breaking of associative bonds occurs at a lower extension than the theoretical extension reached at a covalent polymer's finite extensibility limit, thus, the extensibility limit of the associated polymers is set by the strength of the non-covalent association. Non-covalent associations are weaker than a covalent chemical bond. As soon as the total configuration energy of the polymer can be reduced by relieving the tension of its uncoiled state by breaking the non-covalent association, it will

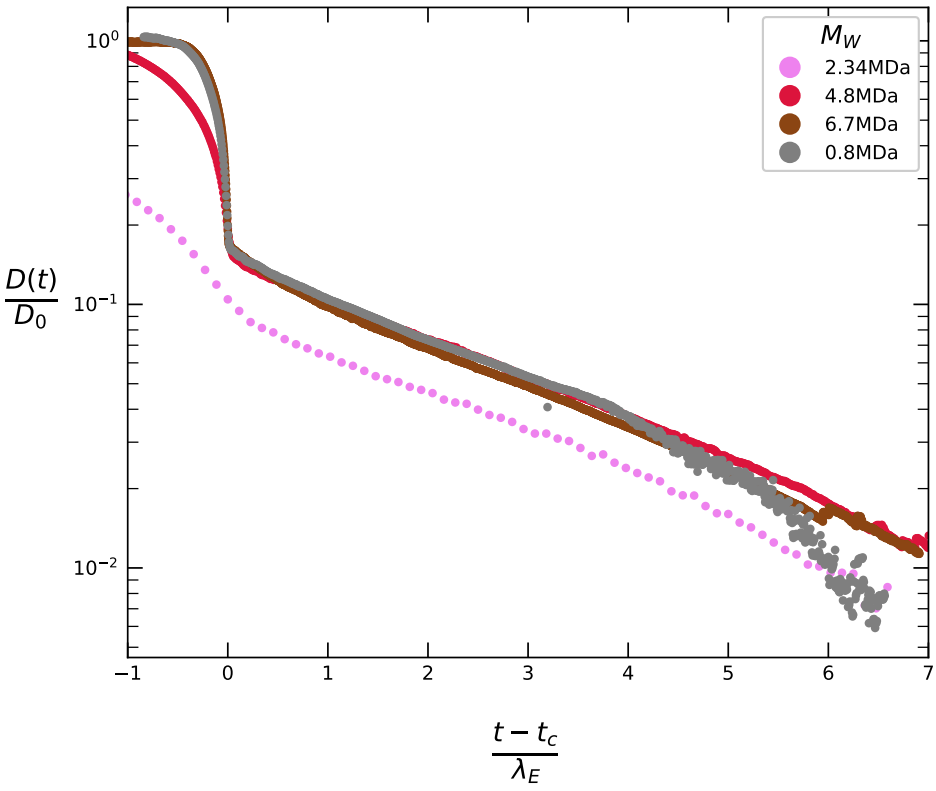

Figure 4.3: Minimum normalized diameter ($D(t)/D_0$) of n = 5 trials of terpyridine-ended PAM solution with 0.5 moles nickel / mole of terpyridine (1 mole nickel / mole polymer) (gray), in comparison to covalent PAM solutions with weight average molecular weight (M_w) of 2.3, 4.8, and 6.7 Mg/mol (pink, red, brown) at similar concentrations (0.1 weight %). The x-axis is normalized by each solution's elongational relaxation time (λ_E).

do so. Recall from Section 3.1 that for high elongation, the end-to-end distance is related to the force applied by the Langevin function,[3]

$$\frac{< R >}{NP} = \left(\coth\left(\frac{FP}{k_BT}\right) - \frac{k_BT}{FP}\right) = L\left(\frac{FP}{k_BT}\right), \tag{4.1}$$

and the end-to end distance can be calculated from the force applied *via* the inverse Langevin function,[4]

$$\frac{FP}{k_BT} = L^{-1}\left(\frac{< R >}{NP}\right) \approx \frac{< R >}{NP}\frac{3 - (< R > /NP)^2}{1 - (< R > /NP)^2}. \tag{4.2}$$

Using the association strength for formation of bis-terpyridine complexes with nickel, $FP = \Delta G = -2.3RT\log_{10}(K_2) = 61.1$ kJ/mol, the end-associated linear megasupramolecules can reach end-to-end distances $\approx 0.983R_{max}$ (Figure 4.10).[5] Covalent carbon-carbon single bonds, the covalent bonds in a traditional polymer

backbone, have a strength of approximately 420 kJ/mol and a corresponding maximum extension of $\approx 0.998 R_{max}$.[6]

The association rate depends on the identity of the specific metal and ligand pair, as well as the concentration of both. With the molecules and concentrations used here, it is feasible that the terpyridines could dis- and re-associate with metal ions on the time scale of the DoSER experiment, so I cannot be sure if the premature end of EC behavior is due to the *first* disassociation of metal-ligand pairs or rather marks a disassociation event which cannot be immediately proceeded by a re-association and regeneration of the long end associated polymer in solution. However, because Δt_{EC} is shorter for associative PAM than covalent PAM with equivalent M_w, I suspect the premature end of the EC behavior is in fact due to the first disassociation.

Effect on η_E

Because the instantaneous value of η_E increases throughout the experiment (Equation 2.9), the shorter Δt_{EC} observed in associative PAM solutions also results in decreased η_E. η_E is calculated from

$$\eta_E = \frac{3\lambda_E \sigma}{D(t_c)\exp(\frac{-(t-t_c)}{3\lambda_E})}, \tag{4.3}$$

with the elongation relaxation time, λ_E, the surface tension, σ, and the diameter at the critical time $D(t_c)$. Instead of using $t - t_c = 6\lambda_E$, as in Equation 2.10 for covalent PAM, approximating the end of the EC regime as $t - t_c = 4\lambda_E$ for associative PAM results in η_E decreased by $\exp(\frac{4}{3})/\exp(\frac{6}{3}) = .51$, with equivalent values of σ, λ_E, and $D(t_c)$. Although the terpyridine-Ni solution has λ_E equivalent to a solution of covalent PAM with $M_w = 5.5$ Mg/mol, its η_E^∞ is closer to that of covalent PAM with $M_w = 4.8$ Mg/mol (Figure 4.4).

4.2 Degradation of terpyridine-ended PAM

Further analysis of the terpyridine ended PAM is complicated due to the fact that the polymers slowly degrade in solution. I tested the same solutions of 0.1 weight % terpyridine-ended PAM with and without metal ions over the course of 65 days.

The results from the solution with no metal do not evolve in time (Figure 4.5, top), while the EC regime of the solution containing metal changes over time. Both λ_E and Δt_{EC} decrease as the solution ages (Figure 4.5, middle and bottom).

The degradation occurs because the terpyridine moieties on either end of the PAM chain are connected to the main chain via ester linkages. Esters are susceptible to

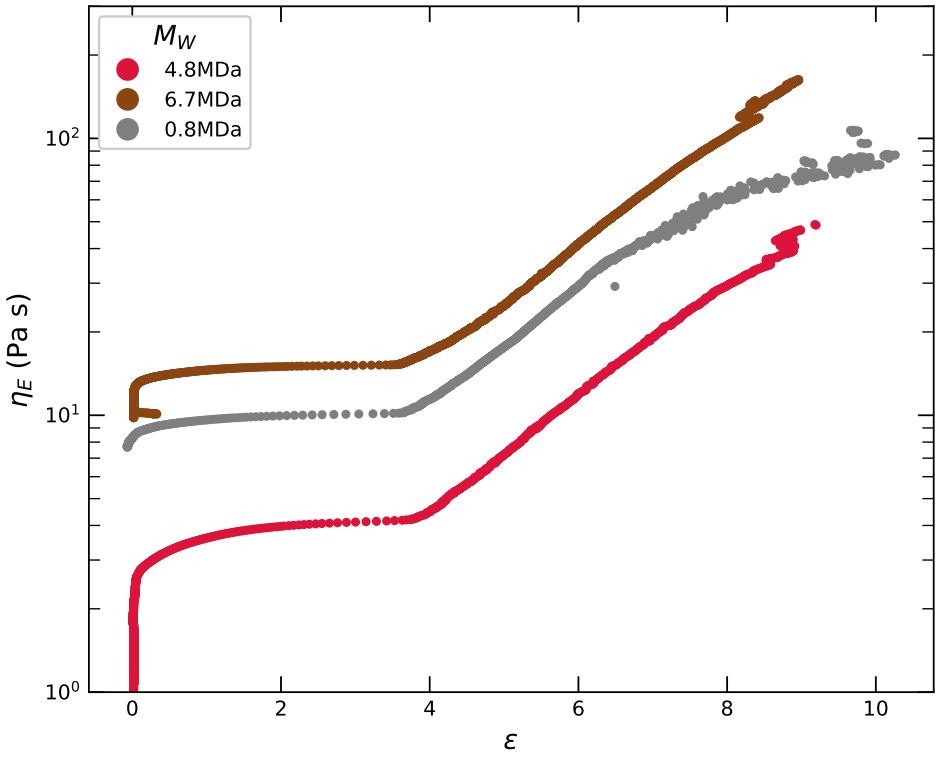

Figure 4.4: Elongational viscosity (η_E) against strain (ϵ) for n = 5 trials of covalent (red, brown) and 800 kg/mol terpyridine-Ni associated PAM with Ni^{2+} with 0.5 moles nickel / mole of terpyridine (gray) at 0.1 weight %.

hydrolytic degradation; they will decompose into an alcohol and a carboxylic acid (Figure 4.7). Because the only esters in the associative PAM are connecting the terpyridines to the main chain, the degradation only separates the terpyridine end groups from the polymer chain, which leaves the polymer chains 99+% intact. With no metal present, this degradation is virtually undetectable. However, it can be measured in the presence of metal because fewer polymer chains can associate to form megasupramolecues.

Despite the slow degradation of the terpyridine end groups, I can make comparisons between the solutions with different metal ions by making the solutions on the same day.

4.3 Effect of metal ions

The associations between divalent metal ions (M) and terpyridine ligands (L) have different bond strengths. The formation of the bis-complex (Ligand-Metal-Ligand, LML) from metal and unassociated ligands $M + 2\,L \overset{K_1}{\rightleftharpoons} LM + L \overset{K_2}{\rightleftharpoons} LML$ is

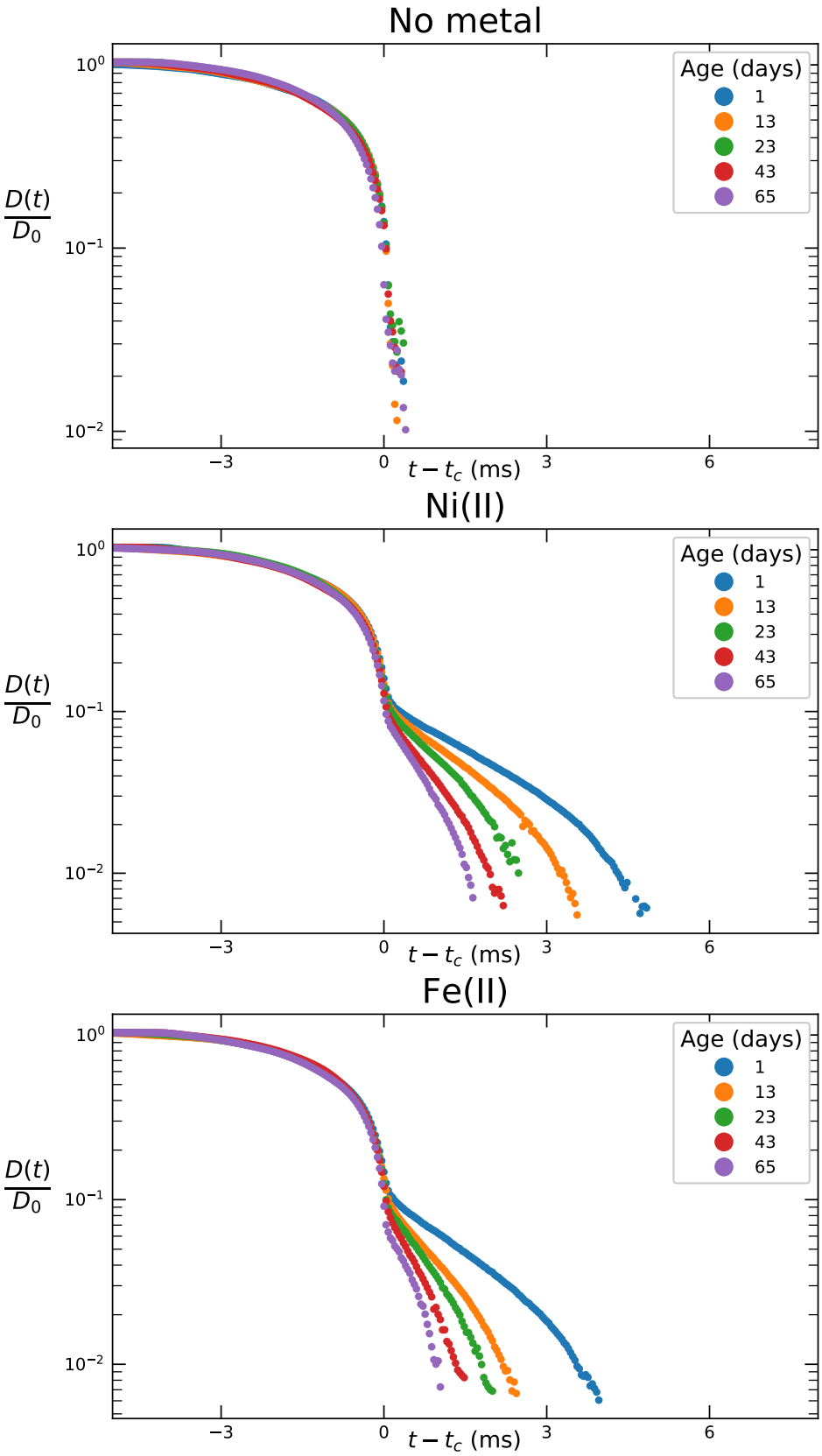

Figure 4.5: Minimum normalized diameter ($D(t)/D_0$, n = 5 trials for each day) of 0.04 weight % 800 kg/mol terpyridine-ended PAM solutions with no metal (top) and 1 mole nickel per 2 moles of terpyridine (1 mole nickel per 1 mole polymer) (bottom) as they evolve in time.

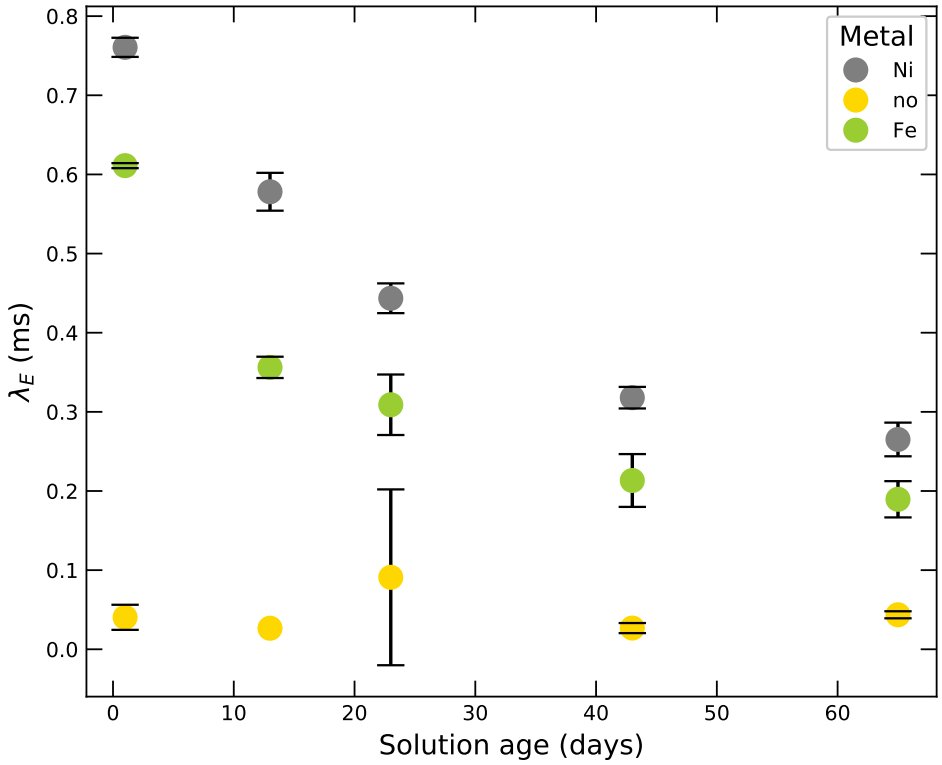

Figure 4.6: Elongational relaxation time (λ_E) of 800 kg/mol terpyridine-Ni associated PAM solutions at 0.04 weight % with no metal (yellow), 0.5 moles nickel / mole of terpyridine (1 mole nickel / mole polymer) (gray), and 0.5 moles iron / mole of terpyridine (1 mole iron / mole polymer) (green) as they evolve in time. Each λ_E is a mean of n = 5 replicates and the error bars show ± one standard deviation.

measured as the equilibrium constant $K_{eq} = K_1 K_2$. K_{eq} is related to the strength of the associative bond by,

$$\Delta G = -2.303 RT \log_{10} K_{eq}, \tag{4.4}$$

where T is the temperature and R is the universal gas constant.

The stability constants and formation rate constants are measured from free ligand and metal binding in solution; they do not account for the entropic penalty of joining polymer chains and the length of the backbone behind the ligands (Table 4.1). However, Fe and Ni have the highest affinity for bis-complexes and the highest overall K_{eq} and thus are the best candidates to form strong associations in solution. The chain-lengthening effect of association is only present with the formation of bis-complexes: a mono-complex of a single terpyridine and metal ion simply occupies the terpyridine end group and does not change the effective length of the polymer chain.

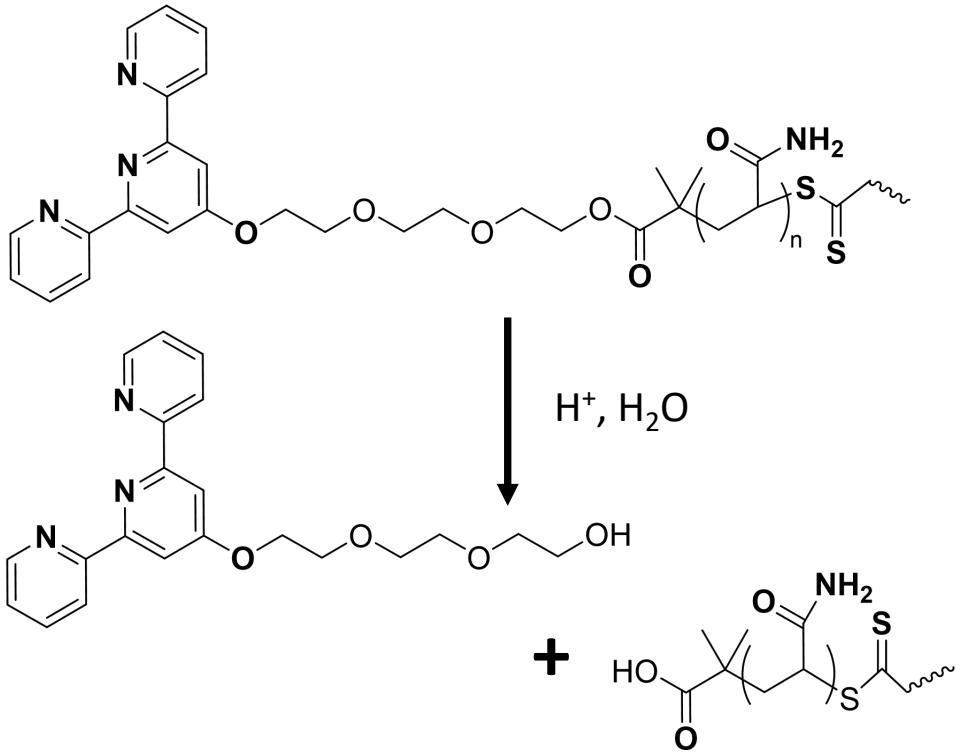

Figure 4.7: Proposed mechanism for hydrolytic degradation of the ester linkage connecting terpyridine end groups to the main PAM chain.

Table 4.1: Equilibrium constant of selected terpyridine-metal pair interactions, values from Lewis et al. [5]

Metal	$\log_{10} K_1$	$\log_{10} K_2$	$\log_{10} K_{eq}$
Ni	10.7	11.1	21.8
Fe	7.1	13.8	20.9
Cu	12.3	6.8	19.1
Co	9.5	9.1	18.6

The population of species formed is a mixture of polymer chains assembled into closed loops and long linear sequences, and the distribution of rings and linear sequences strongly affects the fluid properties. As exhibited in Section 3.4, λ_E and η_E are biased towards the longest linear polymer chains in solution. Additionally, the practical difference between loops and linear species is immense. Because the uncoiling of the polymer chain resists fluid flow and ultimately increases the viscosity of the solution, which linear megasupramolecules participate in much more than loops, a solution which forms primarily loops is not ideal.

Consider a solution entirely of two-polymer loops compared against a solution of two-polymers arranged linearly. The loops act as stiffer species of the same length

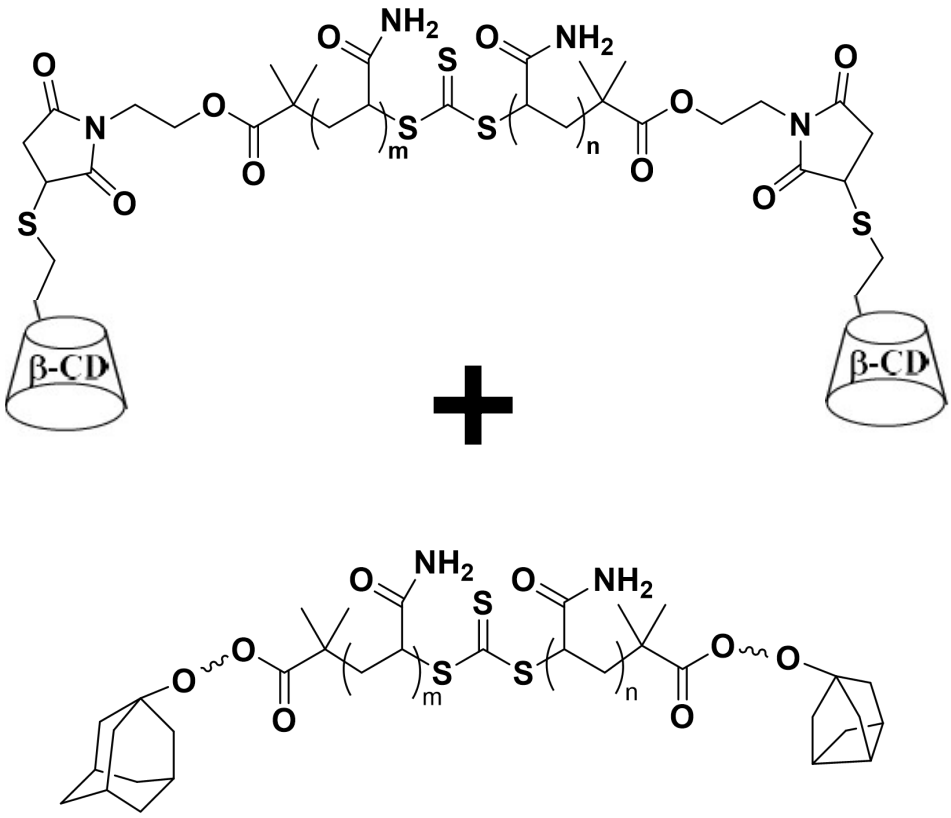

Figure 4.8: PAM synthesized via RAFT with β-cyclodextrin (top) and adamantane (bottom) end groups. Synthesis done by Dr. Hojin Kim.[1]

as a single chain while the linear confirmation acts a single linear polymer with twice the length. Because the λ_E and η_E scale with the chain length to 3.6 and 3.0 respectively, the increase in the effective length of a linearly arranged association increases λ_E by $2^{3.6} \sim 12$x and η_E by $2^{3.0} = 8$x. This effect is severely diminished in a solution of all loops, because the loops cannot uncoil and resist flow as dramatically as the linear arrangement.

4.4 Beta-cyclodextrin-adamantane associations

As an alternative to the metal-ligand associative chemistry accessed with terpyridine end groups, I investigated PAM with β-cyclodextrin (β-CD) and adamantane end groups (Figure 4.8). The β-CD and adamantane end groups are drawn to one another in solution due to guest-host interactions. β-CD forms a hydrophobic pocket through its chemical structure with which the adamantane will spontaneously associate (Figure 1.5).

When assessed by DoSER, the mixture of β-CD and adamantane ended PAM had a $\lambda_E = 0.05$ ms, near the detection limit of the hardware, at a concentration of 0.2

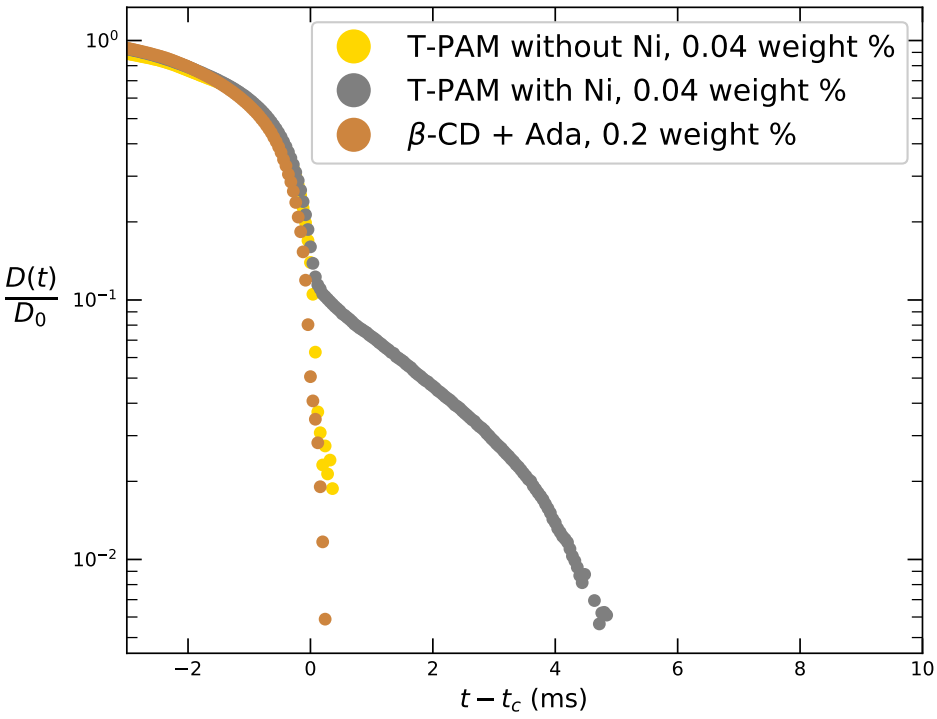

Figure 4.9: Normalized minimum diameter ($D(t)/D_0$) for n = 5 replicate experiments of a 1:1 mixture of 800 kg/mol β-cyclodextrin (β-CD) and adamantane (Ada) ended PAM at (0.2 weight % (brown), 800 kg/mol terpyridine ended PAM (T-PAM) with no metal in solution (yellow), and 800 kg/mol T-PAM with Ni at 0.04 weight % (gray).

Table 4.2: Molecular weights and Đ of associative PAMs studied

End group	M_n (kg/mol)	M_w (kg/mol)	Đ
Terpyridine	820	837	1.03
β-cyclodextrin	434	824	1.90
Adamantane	675	727	1.08

weight %.[i] The low λ_E of the β-CD and adamantane ended PAM solution shows that the associations are not forming to a high degree.

There are several possible reasons for the lower performance of the β-CD and adamantane. First, due to difficulty with the solubility of β-CD in H_2O, the synthesis is incredibly challenging and GPC analysis shows a high Đ for the β-CD ended polymers (Table 4.2). The high Đ indicates that the polymer chains are not fully telechelic:the synthesis did not produce polymers with *both* ends functionalized. A polymer chain with functional groups on only one end will act as a chain stopper,

[i]This value is based on a fit of only 6 data points.

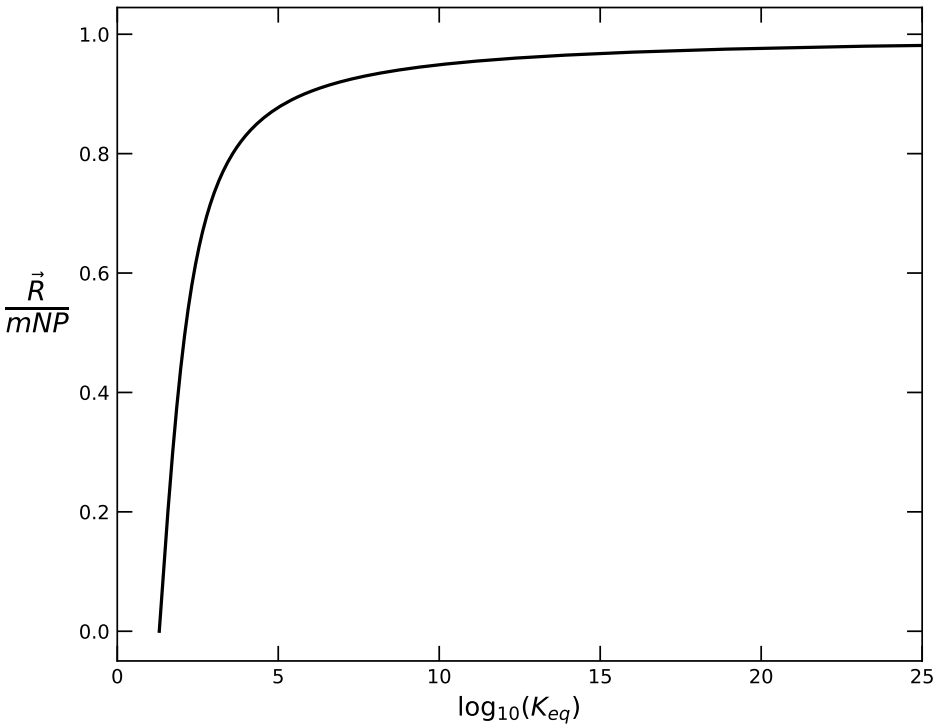

Figure 4.10: Normalized maximum extension $\frac{R}{R_{max}}$ ($R_{max} = mNP$, m is the number polymer repeat units, N is the number of monomer repeat units in a single polymer, and P is persistence length of a single repeat unit) as a function of association stability constant (K_{eq}). This model is based on the Padé approximation of the inverse Langevin function.[4]

preventing the megasupramolecules from growing with further associations. Furthermore, the association strength of the β-cyclodextrin and adamantane ($K_{eq} = 5$) is much weaker than the terpyridine-metal complexes ($K_{eq} = 21$) (Table 4.2). The lower K_{eq} has a compounding effect: first, it results in a lower number of associated species at thermodynamic equilibrium. Second, the maximum extension the megasupramolecule can reach is governed by the strength of the associative bond. The relationship between the bond strength and the maximum extension is expressed in Equation 4.2. For β-cyclodextrin and adamantane associations ($K_{eq} = 5$) the maximum extension is $R \approx 0.74R_{max}$, while for terpyridine-metal complexes ($K_{eq} = 21$) the maximum extension is $R \approx 0.98R_{max}$ (Figure 4.10). The decreased maximum extension with β-CD and adamantane associations leads to lower λ_E and η_E.

4.5 Conclusions and future work

The work in this chapter demonstrates the feasibility of using associative chemistry to create end associative megasupramolcules in aqueous solutions. These

megasupramolecules increase λ_E and survive pumping and reform associations in solution at equilibrium.

Based on the synthesis route to create the RAFT agents for telechelic polymerization, the terpyridine, β-cyclodextrin, and adamantane ended PAM all suffer from degradation of the ester linkage connecting the end group to the main polymer chain. If the degradation were solved, the metal-ligand interactions still suffer from a problem in their lack of specificity. Mixing terpyridine-ended PAM with nickel ions gives the largest increase in λ_E and η_E, but the terpyridines will form associations with many different metal ions.

When studying the terpyridine ended polymers in the lab, I dissolved them with high purity H_2O to prevent contamination of trace metal ions. The targeted application of the agricultural industry does not use H_2O with any degree of purity. For example, exposure to rust in any preceding steps after adding the polymer and Ni would disrupt the bis-terpyridine-Ni complexes and reduce the efficacy of the solution. Trace amounts of monovalent ions, such as Na^+, K^+, *etc*, could serve as chain capping ions, preventing further association.

Finally, although the targeted concentrations of polymer are low: $\lesssim 0.04$ weight %, with $N = 11,000$, the ideal concentration of metal is $0.25 * 10^{-4}$ weight % or 0.25 ppm. Despite the low magnitude of this value, 0.25 ppm Ni^{2+} exceeds the safe limit set by WHO for wastewater (0.02 ppm).[7,8]

Because of both problems with specificity and possible contaminants, further association chemistries should be explored. Ideally, these other associative groups would be specific so they are not disrupted by impurities in the water, and strongly interacting, with high K_{eq} to enable long associations and high extensibility. A good candidate for these requirements is cucurbit[n]uril inclusion complexes, which have K_{eq} up to 10^{15} and operate in a host-guest capacity similar to β-cyclodextrin.[9]

4.6 Supplemental information

Order of operations with metal ions (possibly move somewhere in the main)

The aggregate fluid properties depend on the identity of the metal which coordinates the terpyridine-ended poly(acrylamide) (T-PAM) together. The properties of the fluid also depend on the order in which the ingredients (polymer, water, metal) were added. To investigate this, I prepared a solution of T-PAM at a concentration of 0.1 weight %. I took an aliquot of this solution, added Ni^{2+} ions in a ratio of 1 Ni^{2+} to 2 terpyridine molecules and diluted the mixture of T-PAM and Ni^{2+} to the

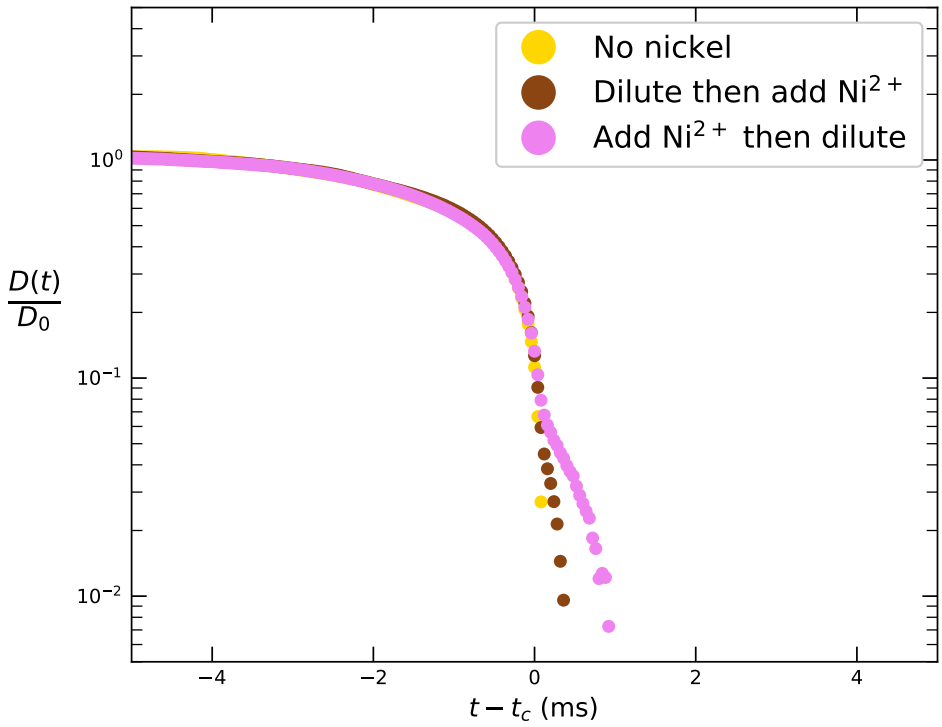

Figure 4.11: Normalized minimum diameter ($D(t)/D_0$) for n = 5 replicate experiments of 800 kg/mol terpyridine ended PAM (T-PAM) solutions with a concentration of 0.01 weight %. The solutions have no Ni^{2+} (yellow) or Ni^{2+} in a ratio of 0.5 moles nickel / mole of terpyridine, added either *after* (brown) or before (pink) dilution from 0.1 weight %, to 0.01 weight % T-PAM.

final concentration of 0.01 weight % (Figure 4.12, left). I diluted the stock T-PAM solution with no metal from 0.1 weight % to 0.01 weight %, and added Ni^{2+} ions in the same ratio of 1 Ni^{2+} to 2 terpyridine molecules *after* the dilution to 0.01 weight % (Figure 4.12, right). I also tested the 0.01 weight % T-PAM solution with no metal present. Each of these fluids behave distinctly from one another (Figure 4.11). The solution with Ni^{2+} added prior to dilution from 0.1 to 0.01 weight % has the largest λ_E, 0.12 ± 0.03 ms, while the solutions with no Ni^{2+} and Ni^{2+} added after dilution to 0.01 weight % have λ_E of 0.03 ± 0.00 ms. Although their λ_E are similar, the solutions with no Ni^{2+} and Ni^{2+} added after dilution can be distinguished by the lifetime of the filament. The solution with Ni^{2+} added after dilution has a longer-lived filament, which can be seen by the increased number of data points in which $t > t_c$. The similarity of the λ_E of these two solutions is presumably due to the low concentration these experiments were performed at which yields a brief elastocapillary regime and few data points with which to fit λ_E. In experiments at higher concentrations (e.g., Figure 4.5, performed at 0.04 weight %), solutions with

no metal and with Ni^{2+} ions added after dilution are statistically distinct.

The change in solution properties depending on the concentration *when the metal is added* further complicates the study and use of these associative polymers. These differences are due to the increased ease of association with higher concentrations of the terpyridine end groups. When the metal ions are added to a high concentration solution, more or longer megasupramolecules are formed. From the higher λ_E, these megasupramolecules appear to persist through the dilution to lower concentration. In contrast, when the metal ions are added to an already dilution solution, the T-PAM struggle to form associations with one another due to the low concentration of polymer making it difficult to find another T-PAM molecule to associate with.

With the exception of the experiment shown in Figures 4.11 and 4.12, all other mixtures of terpyridine-ended polymer and metal tested were created by adding metal ions to a polymer solution that was already at its target concentration.

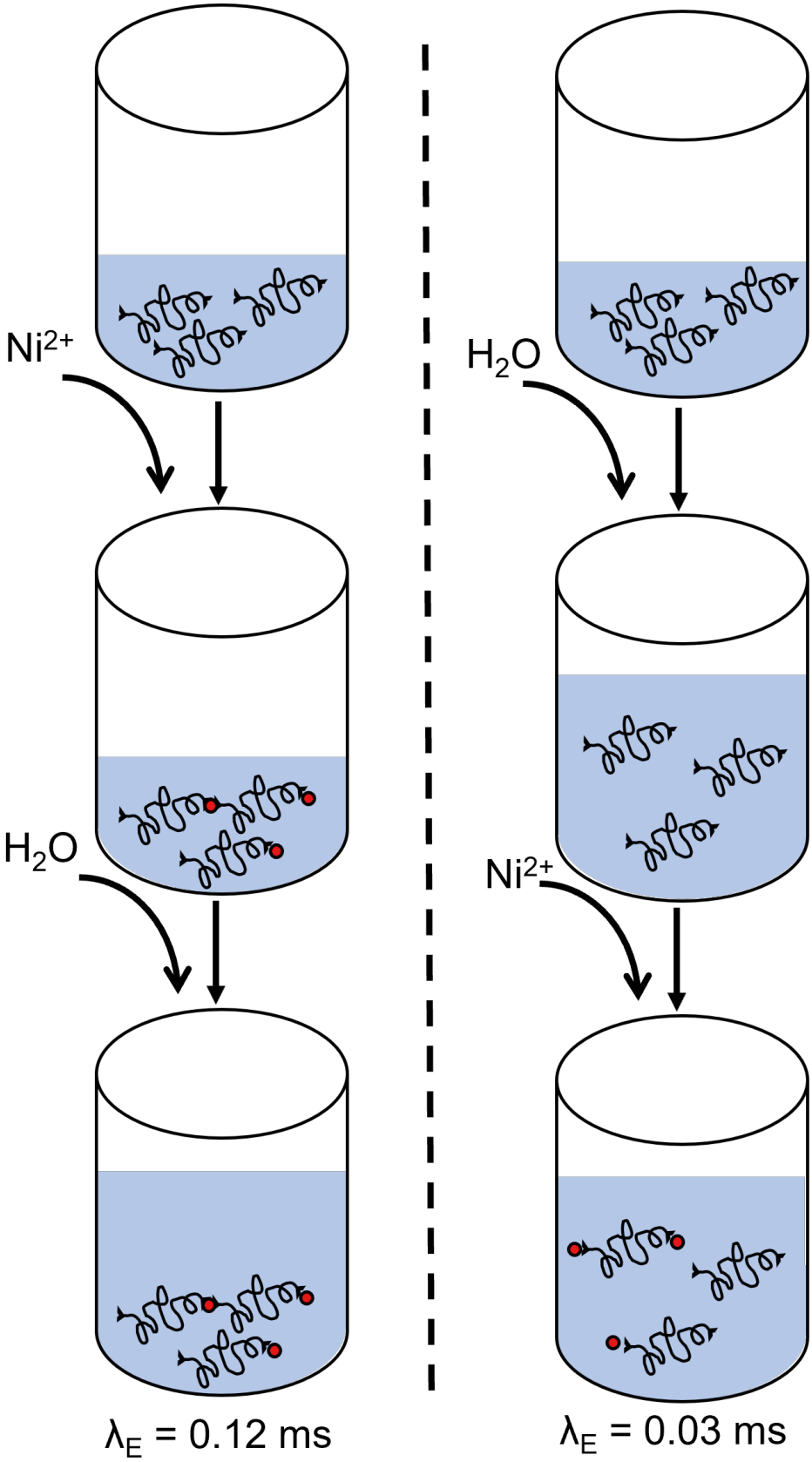

Figure 4.12: Cartoon showing the two different orders of operations to produce terpyridine-ended PAM (T-PAM) solutions with the same final concentration of polymer and Ni^{2+} ions. Left: Adding Ni^{2+} prior to dilution to the final polymer concentration resulting in higher elongational relaxation time (λ_E). Right: Adding Ni^{2+} after dilution to the final polymer concentration resulting in lower λ_E.

References

[1] H. Kim. "New Long End-Associative Polymers for Mist Control in I. Aqueous Solutions and II. Hydrocarbon Solvents". California Institute of Technology, Aug. 26, 2022. DOI: 10.7907/RSX9-QT39. URL: https://resolver.caltech.edu/CaltechTHESIS:08252022-035254306 (visited on 09/30/2022).

[2] J. Dinic and V. Sharma. "Macromolecular Relaxation, Strain, and Extensibility Determine Elastocapillary Thinning and Extensional Viscosity of Polymer Solutions". In: *Proceedings of the National Academy of Sciences* 116.18 (Apr. 30, 2019), pp. 8766–8774. ISSN: 0027-8424, 1091-6490. DOI: 10.1073/pnas.1820277116. URL: http://www.pnas.org/lookup/doi/10.1073/pnas.1820277116 (visited on 05/05/2021).

[3] M. Rubinstein and R. H. Colby. *Polymer Physics*. Oxford ; New York: Oxford University Press, 2003. 440 pp. ISBN: 978-0-19-852059-7.

[4] A. Cohen. "A Pade Approximant to the Inverse Langevin Function". In: *Rheologica Acta* 30.3 (1991), pp. 270–273. ISSN: 0035-4511, 1435-1528. DOI: 10.1007/BF00366640. URL: http://link.springer.com/10.1007/BF00366640 (visited on 10/01/2022).

[5] R. W. Lewis et al. "Ultra-High Molecular Weight Linear Coordination Polymers with Terpyridine Ligands". In: *Chemical Science* 10.24 (2019), pp. 6174–6183. ISSN: 2041-6520, 2041-6539. DOI: 10.1039/C9SC01115C. URL: http://xlink.rsc.org/?DOI=C9SC01115C (visited on 08/25/2021).

[6] W. M. Haynes, D. R. Lide, and T. J. Bruno, eds. *CRC Handbook of Chemistry and Physics*. 97th ed. CRC Press, June 24, 2016. ISBN: 978-1-315-38047-6. DOI: 10.1201/9781315380476. URL: https://www.taylorfrancis.com/books/9781498754293 (visited on 10/02/2022).

[7] I. A. Aneyo et al. "Biodegradation of Pollutants in Waste Water from Pharmaceutical, Textile and Local Dye Effluent in Lagos, Nigeria". In: *Journal of Health and Pollution* 6.12 (Dec. 1, 2016), pp. 34–42. ISSN: 2156-9614. DOI: 10.5696/2156-9614-6.12.34. URL: https://www.ncbi.nlm.nih.gov/pmc/articles/PMC6221506 (visited on 10/02/2022).

[8] G. K. Kinuthia et al. "Levels of Heavy Metals in Wastewater and Soil Samples from Open Drainage Channels in Nairobi, Kenya: Community Health Implication". In: *Scientific Reports* 10.1 (Dec. 2020), p. 8434. ISSN: 2045-2322. DOI: 10.1038/s41598-020-65359-5. URL: http://www.nature.com/articles/s41598-020-65359-5 (visited on 10/02/2022).

[9] E. A. Appel et al. "Supramolecular Polymeric Hydrogels". In: *Chemical Society Reviews* 41.18 (2012), p. 6195. ISSN: 0306-0012. DOI: 10.1039/c2cs35264h. URL: http://xlink.rsc.org/?DOI=c2cs35264h.

Chapter 5

DROPLET IMPACTS: POLYMER STRUCTURE, ELONGATIONAL PROPERTIES, AND SPRAY PERFORMANCE

The main experimental method used in this section was developed in collaboration with Dr. Chris Nelson at DOW. It was a priority that experiments could be replicated between the Kornfield laboratory at Caltech and DOW's laboratory in Michigan. Thus, we used the commonly available material of Laboratory Parafilm as our hydrophobic substrate to mimic impact onto plant leaves. Both of us were able to produce the same variety of outcomes with H_2O droplets onto pristine *parafilm sheets under the same experimental conditions of droplet diameter and height. The aqueous solutions of glycerol and PAM were prepared by RWL. η_S of PAM solutions was measured by Dr. Red Lhota, η_S of glycerol solutions was measured by RWL. All surface tensions were measured by RWL. The PAM was synthesized by Dr. Hojin Kim. All droplet impact experiments and analysis was done by RWL.*

5.1 Classifications of droplet outcomes

The droplet impact process comprises two main phases: expansion and retraction. They are marked by key moments: impact and maximum expansion (Figure 5.1).

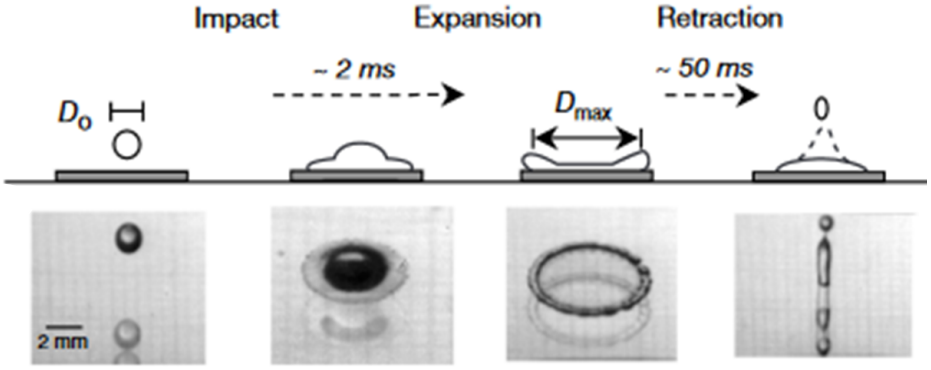

Figure 5.1: The phases of a droplet impact illustrated with a water droplet with diameter D_0 (Bergeron uses D_0 for droplet diameter, I use D) onto a hydrophobic substrate. Immediately after impact, the droplet enters the expansion phase until it reaches its maximum diameter, D_{max}. After which, it reverses direction and begins retraction. With enough energy, the droplet will rebound off the substrate after retraction phase. The dashed arrows indicate the passage of time in milliseconds (ms). Images modified from Bergeron et al. [1]. Reprinted with permission.

Regardless of the outcome, all droplets follow the same pattern. Starting from a spherical droplet falling towards the substrate, impact begins when the droplet makes contact with the target and begins expansion.[1–6] In the expansion phase, the momentum the droplet brings with impact causes the fluid to disrupt its spherical shape and flatten into a disc-like shape.[i] After some time ($\sim$ 5 ms), the droplet reaches its moment of maximum expansion where it momentarily has a velocity (v) and kinetic energy (KE) of 0 as it reverses direction. The retraction phase follows maximum expansion and is driven by surface tension. The fluid seeks to reduce the energy of its configuration by reducing the surface area exposed to both the atmosphere and the substrate and eventually reaches equilibrium.

The impact process can produce a several different experimental results which fall broadly into three categories: splash, rebound, and deposition.[9] Splash is categorized by the ejection of multiple small satellite droplets during the expansion phase of droplet impact. Prompt splash occurs at or shortly after the moment of impact, produces a fine mist of satellite droplets, and is attributed to surface roughness .[10] Corona splash and levitating lamella breakup occur in impacts with smooth surfaces. In low viscosity (η_S and η_E) fluids, a sheet of fluid equally expands in all directions in the expansion phase of the impact, creating a crown-like or *corona* appearance when viewed from the side.[7] Small droplets emerge from the edge of this sheet and eject from the fluid (Figure 5.2a). In higher η_S fluids, small volumes of fluid eject outwards and upwards from the expanding volume after impact, but are connected to the main droplet by filaments or lamella. If these lamella break up, they give way to a splash of the ejected droplets (Figure 5.2b).

If there is sufficient energy during the retraction, the fluid can rebound. In this case, rebound means some of all of the droplet disconnecting from the substrate upon which it impacted. A complete rebound occurs if the entire volume of fluid disconnects from the substrate (Figure 5.2c); a partial rebound occurs if less than the entire volume disconnects (Figure 5.2d). Finally, if the entirety of the droplet remains intact and on the substrate, the impact is classified as deposition (Figure 5.2e).

I performed impact experiments onto smooth surfaces and only encountered one set of conditions which produced prompt splash; the overwhelming majority of splash outcomes were corona or levitating lamellar breakup type splashes (Figure 5.4).

[i] Sometimes this moment will have a large gradient in the thickness, where the outer rim is the thickest part of the droplet and the inner volume is a very thin layer.

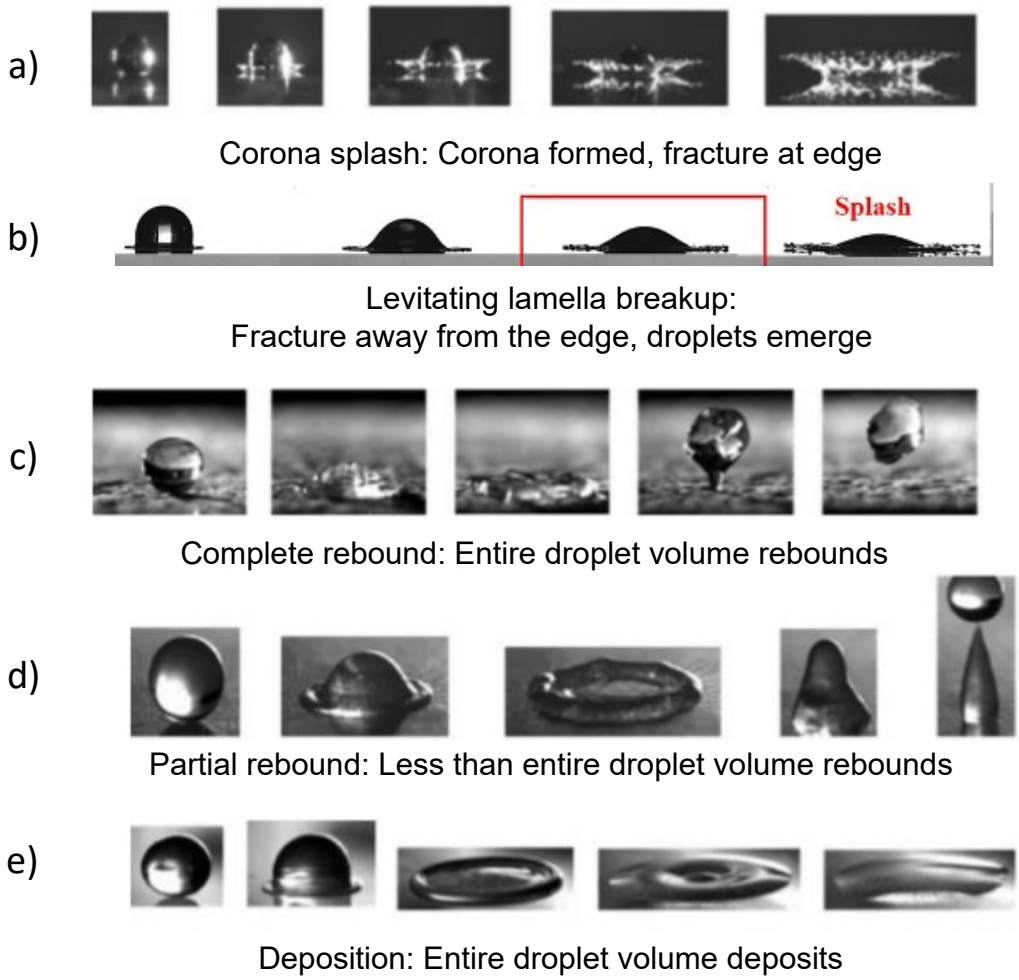

Figure 5.2: The categories of different droplet outcomes after impact: splashing, rebound, and deposition. a) Corona splash, where the fluid forms a sheet before releasing droplets; b) Levitating lamella breakup, where droplets emerge from the expanding fluid, image from Zhang et al. [7], reproduced with permission; c) Complete rebound, where the entire volume of fluid disconnects from the substrate; d) Partial rebound, where less than the entire volume disconnects from the substrate; and e) Deposition, where the entire volume of fluid remains intact and on the substrate. All images other than b) are from Rioboo, Tropea, and Marengo [8], reproduced with permission.

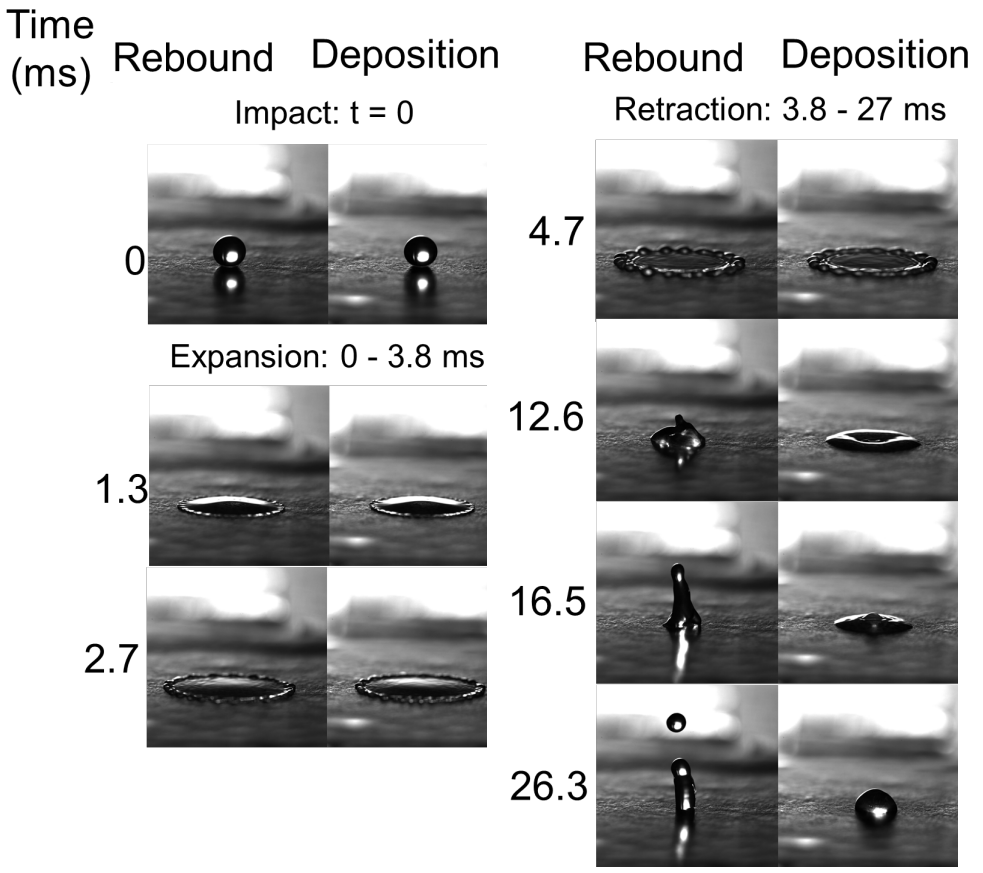

Figure 5.3: Timelapse of impacts with pure H_2O and 0.04 weight % 2.34 Mg/mol PAM solution onto parafilm. The H_2O (left) results in partial rebound, the PAM droplet (right) with the same velocity and diameter results in deposition. Time (t) is presented in milliseconds (ms).

Furthermore, I only observed partial rebounds, which require less energy to achieve than a complete rebound (Figure 5.3 left). I believe this is due to the limits on height and droplet diameter I could reach in our laboratory setup.

5.2 Experimental results: the relevant fluid properties and their effect on droplet fate

I tested the droplet impact behavior by dropping the fluids of interest from a given height H onto pristine parafilm substrates. I produced the droplets by ejecting fluid from a syringe via syringe pump. The pump was mounted on a vertical track and could be raised and lowered to change h and consequently the potential energy, PE, ($PE = mgH = \frac{4\pi}{3}(D/2)^3\rho gH$) of the droplets. By changing the needle diameter, I was able to change the droplet diameter which also changed the potential energy.

I tested pure H_2O, aqueous glycerol solutions, and aqueous PAM solutions. H_2O

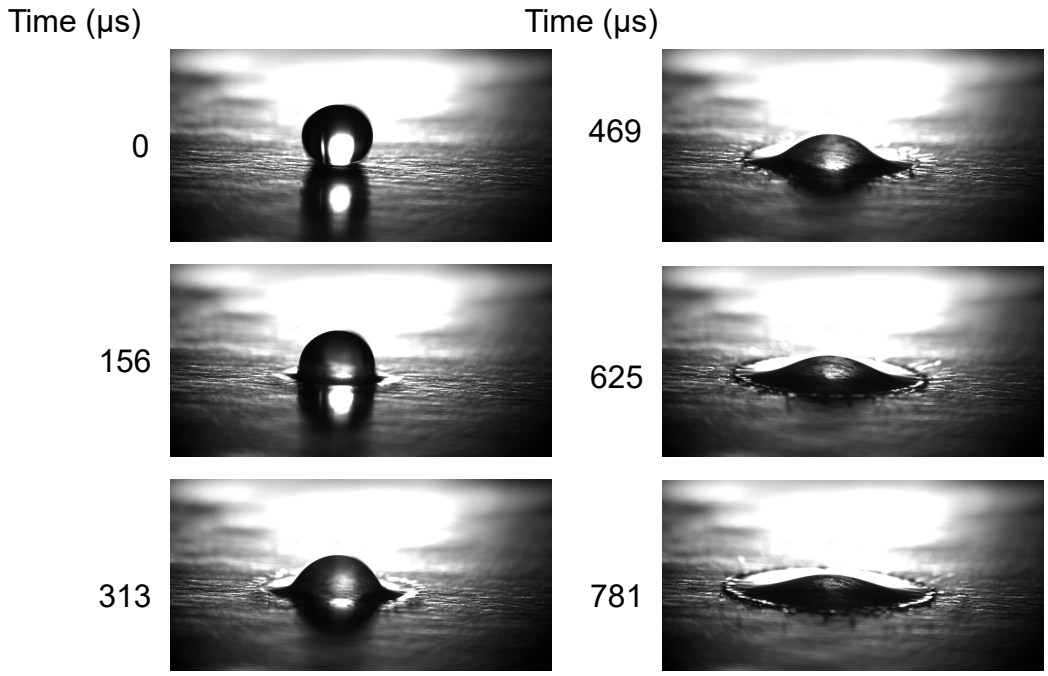

Figure 5.4: Timelapse images of a droplet impact that results in splash. This droplet is 0.1 weight %, 800 kg/mol terpyridine-ended PAM with no metal in solution. Time is presented in microseconds (μs).

itself has low η_S and high σ which classifies it as an inertio-capillary fluid ($Oh_S = \frac{\eta_S}{\sqrt{\sigma D \rho}} << 1$). Aqueous solutions of glycerol exhibit higher η_S, lower σ, but are still Newtonian fluids, whereas aqueous PAM solutions are low η_S, high η_E, and highly non-Newtonian. For Newtonian solutions, η_S can be converted to η_E by using Trouton's ratio, $Tr = \frac{\eta_E}{\eta_S} = 3$.[11–13]

On the droplet impact phase diagram (Figure 5.5), there are no obvious boundaries between the different regimes of behavior. I initially chose the axes as the dimensionless groups Weber number:

$$We = \frac{\rho v^2 D}{\sigma}, \tag{5.1}$$

and the elongational Ohnessorge number:

$$Oh_E = \frac{\eta_E}{\sqrt{\sigma D \rho}}, \tag{5.2}$$

as these are the most directly related the experimental variables: h, D, and η_E. We measures the relative strength of the droplet's inertia and surface tension. For impacts with pure H_2O, droplets with higher We rebound more readily than droplets with low We. Oh_E measures the relative strength of the droplet's extensional

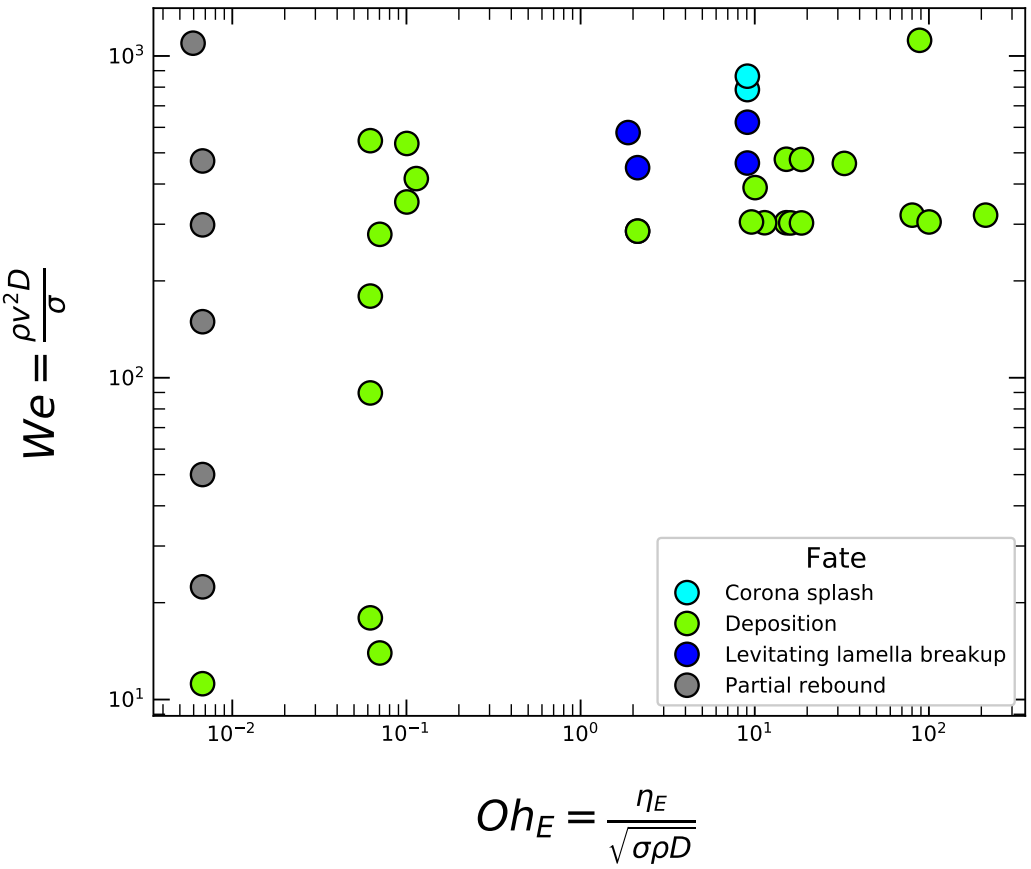

Figure 5.5: The outcome of droplet impact onto parafilm of pure H_2O , aqueous glycerol solutions, and aqueous PAM solutions. The phase diagram is presented in terms of the dimensionless Weber number, $We = \frac{\rho v^2 D}{\sigma}$ (ρ is the fluid's density, v is the droplet velocity, D is the droplet diameter, and σ is the fluid's surface tension), and the dimensionless elongational Ohnessorge number, $Oh_E = \frac{\eta_E}{\sqrt{\sigma D \rho}}$ (η_E is the fluid's elongational viscosity). Prompt splash, corona splash, levitating lamella breakup, partial rebound, and deposition are all observed. All data points are the result of $n \geq 3$ experimental replicates.

viscosity against the conservative forces of kinetic energy and surface tension. Droplets with high Oh_E dissipate more of their energy *via* viscous losses; the behavior of droplets with low Oh_E is determined by their surface tension and velocity.

Although Oh_E is defined as $Oh_E = \frac{\sqrt{We}}{Re_E}$, where Re_E is the elongational Reynolds number $Re_E = \frac{\rho v D}{\eta_E}$, Oh_E and We can be varied independently. I achieve this by increasing the height of the droplet, H, which increases velocity v, which is only present in We. Likewise, increasing the concentration or M_w of PAM in solution increases η_E and η_S. Only η_E is present in Oh_E, and η_S is absent from both We and Oh_E.

Although We and Oh_E can be varied independently, the results shown in Figure 5.5 are difficult to draw conclusions from. Changing the y-axis from We to the shear Reynolds number:

$$Re_S = \frac{\rho v D}{\eta_S}, \tag{5.3}$$

allows for clear boundaries to be drawn (Figure 5.6). Here, Re_S represents the fluids momentum under shear flow, and Oh_E captures the dissipation under elongational flow. With these dimensionless groups, we can draw a single boundary that separates the desired outcome of deposition from the splashing and rebound behavior.

5.3 Predicting splash behavior

The underlying mechanism of droplet impact is an ongoing area of academic research.[3,9,10,14–31] The fluid itself has constant properties of density (ρ), viscosity (η), and surface tension (σ) and the droplet's kinetic energy (diameter, D and velocity, v) can be varied without changing the fluid properties. Furthermore, the fluid's interactions with the substrate (the wettabillity), the substrate's morphology, and the properties of the atmosphere in which the experiment is conducted also affect the splashing behavior.

Numerous thresholds have been proposed, and generally they take the form of:

$$ReOh^x = A, \tag{5.4}$$

where $Re = \frac{\rho v D}{\eta}$, $Oh = \frac{\eta}{\sqrt{\sigma D \rho}}$, the constant A characterizes the substrate. If $ReOh^x > A$, the droplet is predicted to splash, and if $ReOh^x < A$, the droplet is predicted to not splash. The exponent x captures the effect of changes in η and different studies report $0.8 < x < 1.65$, including $x = 1$.[7,32–41] The affect of η on the droplet splashing behavior depends on the value of x, because $\eta^{x-1} \sim ReOh^x$.

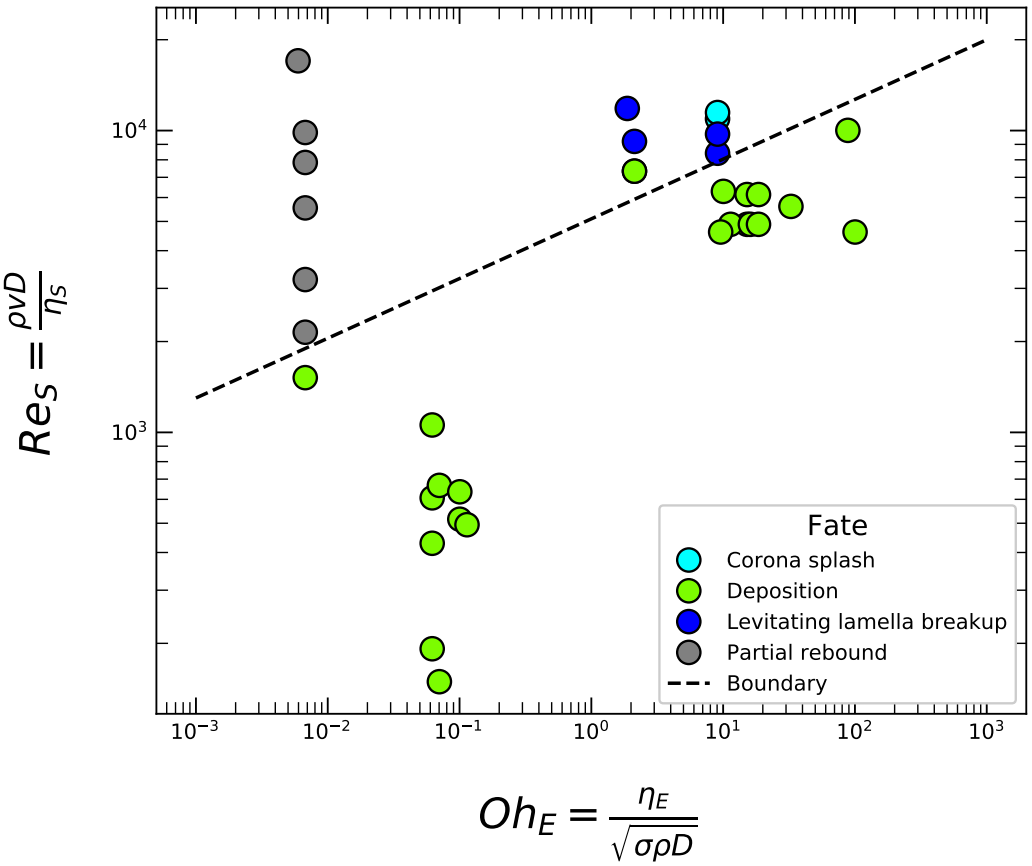

Figure 5.6: The outcome of droplet impact onto parafilm of pure H_2O, aqueous glycerol solutions, and aqueous PAM solutions. The phase diagram is presented in terms of the dimensionless shear Reynolds number, $Re_S = \frac{\rho v D}{\eta_S}$ (ρ is the fluid's density, v is the droplet velocity, D is the droplet diameter, and η_S is the fluid's shear viscosity), and the dimensionless elongational Ohnessorge number, $Oh_E = \frac{\eta_E}{\sqrt{\sigma D \rho}}$ (η_E is the fluid's elongational viscosity and σ is the fluid's surface tension). Prompt splash, corona splash, levitating lamella breakup, partial rebound, and deposition are all observed. All data points are the result of $n \geq 3$ experimental replicates.

If $x = 1$, the η terms from Re and Oh completely negate one another and produce a model which ignores η. If $x > 1$, then η appears in the numerator and increasing η raises $ReOh^x$ term, promoting splashing, and likewise if $x < 1$, η appears in the denominator and increasing η decreases the $ReOh^x$ term and inhibits splashing. The value of constant A depends on the surface the droplets impact onto and is determined experimentally. Its value depends on a myriad of factors including the compliance of the material and the surface energy between the droplet and the surface.

In my experiments, the phase diagram of droplet fate only shows distinct regions when viewed with the axes of Re_S, the *shear* Reynolds number and Oh_E, the *elongational* Ohnessorge number. The product of $Re_S Oh_E^x \sim \frac{\eta_E^x}{\eta_S}$, where now the effect of the exponent x is only modifying η_E. Essentially, increasing η_S while holding η_E constant always inhibits splashing. If $x = 0$, splashing behavior is independent of η_E, if $x > 0$, increasing η_E encourages splashing; and if $x < 0$, increasing η_E discourages splashing. The line that best separates the deposition regime from the splashing is defined as

$$Re_S Oh_E^{-0.21} = 4350. \tag{5.5}$$

The negative exponent in Equation 5.5 indicates that increasing η_E discourages splashing behavior. Regardless of η_E, high η_S inhibits splashing as small satellite droplets are not able to form upon impact with the substrate. In solutions with low η_S, the satellite droplets seen in levitating lamellar breakup form and begin to escape from the main volume; however, if η_E is sufficiently high, those droplets remain connected via their lamellar filaments and do not result in splashing behavior.

The other models for splash behavior do not account for η_E and instead only consider changes in η_S. The array of solutions tested in this work contains polymer solutions with the same η_S, different η_E, and different impact behavior. From this observation, it is clear that increased η_E must discourage splashing.

5.4 Predicting rebound behavior

After the expansion, the retraction phase of the droplet impact process can result in partial or complete droplet rebound. Rebound occurs if there is enough energy in the droplet to eject off the substrate after both the expansion and retraction phases. Consequently, the ability of a droplet to rebound can be predicted from an energy balance.[30] The energy balance begins at the moment of impact (Figure 5.7(a)) and includes the moments of maximum diameter (Figure 5.7(b)), the maximum

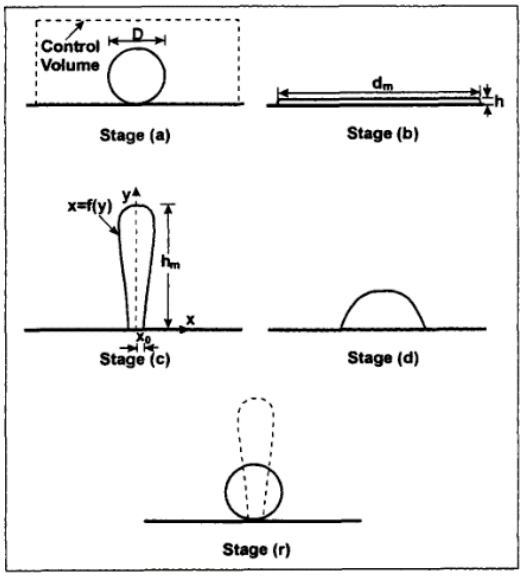

Figure 5.7: Select points in the impact process: Stage (a): the moment of impact of a droplet with diameter D, Stage (b): the end of the expansion phase, coinciding with the droplet reaching its maximum diameter (d_m), Stage (c): the droplet at its maximum separation from the substrate with height h_m, Stage (d): the final shape of the droplet at equilibrium, Stage (r): a hypothetical stage depicting the minimum rebound. Image from Mao, Kuhn, and Tran [30], reproduced with permission.

separation (Figure 5.7(c)), and the minimum energy rebound (Figure 5.7(r)). At stage (b), the droplet momentarily has 0 kinetic energy because it is changing direction. Thus, all of the energy is in the surface energy and can be captured as:

$$E_b = \sigma \left(\frac{\pi}{4} d_m^2 (1 - \cos\theta_c) + \pi \frac{2D^3}{3d_m} \right), \tag{5.6}$$

where D is the diameter of the spherical droplet, d_m is the diameter at stage (b), θ_c is the *equilibrium* contact angle between the fluid and the substrate, and σ is the surface tension. Stage (c) is highly variable depending on the outcome of the impact, so its energy cannot be written explicitly. Instead, it is defined as the energy at stage (b), E_b, minus the energy dissipated between stage (b) and (c), $Diss_{b-c}$. $Diss_{b-c}$ is evaluated via an empirical observation,

$$Diss_{b-c} = 0.12 \left(\frac{d_m}{D} \right)^{2.3} (1 - \cos\theta_c)^{0.63} \pi D^2 \sigma, \tag{5.7}$$

where the coefficients 0.12 and the exponents 2.3 and 0.63 are determined experimentally. The minimum energy for rebound is then described as:

$$E_r = \pi D^2 \sigma + \frac{\pi D^4 \rho g}{12}, \tag{5.8}$$

where ρ is the density, g is the acceleration due to gravity, and the second term captures the potential energy of a droplet with its center exactly one radius above the substrate. The first term captures the surface energy of a spherical droplet of fluid. Finally, an expression for the "excess rebound energy," or E_{ERE} can be defined as:

$$E_{ERE} = \frac{E_c - E_r}{E_r} = \frac{E_b - Diss_{b-c} - E_r}{E_r}, \tag{5.9}$$

where the energy terms are defined above. If $E_{ERE} > 0$, then a droplet is predicted to contain enough energy to rebound, and if $E_{ERE} < 0$, then the droplet does not have enough energy rebound from the substrate.

Other than ρ and σ, import quantities such as the impact velocity v and viscosity η, do not explicitly appear in any Equations 5.6, 5.7, or 5.8. Instead, they are used to determine the maximum spreading ratio, $\frac{d_m}{D}$. An energy balance between the σ, θ_c, D, and η is used to explicitly calculate $\frac{d_m}{D}$:

$$\left(\frac{1}{4}(1-\cos\theta_c) + 0.2\frac{We^{0.83}}{Re^{0.33}}\right)\left(\frac{d_m}{D}\right)^3 - \left(\frac{We}{12}+1\right)\left(\frac{d_m}{D}\right) + \frac{2}{3} = 0. \tag{5.10}$$

Here, We and Re are the Weber and Reynolds numbers, respectively, and the coefficient 0.2 and exponents 0.83 and 0.33 are determined experimentally. Equation 5.10 is a third-order polynomial, and its real root can be calculated for any values of Re, We, and θ_c:

$$\frac{d_m}{D} = \sqrt[3]{-\left(\frac{C_3}{2C_1}\right) + \sqrt{\left(\frac{C_3}{2C_1}\right)^2 + \left(\frac{C_2}{3C_1}\right)^3}} + \sqrt[3]{-\left(\frac{C_3}{2C_1}\right) - \sqrt{\left(\frac{C_3}{2C_1}\right)^2 + \left(\frac{C_2}{3C_1}\right)^3}}, \tag{5.11}$$

where C_1, C_2, and C_3 are the coefficients in the third order polynomial.

$$C_1 = \left(\frac{1}{4}(1-\cos\theta_c) + 0.2\frac{We^{0.83}}{Re^{0.33}}\right),$$

$$C_2 = -\left(\frac{We}{12}+1\right),$$

and

$$C_3 = \frac{2}{3}.$$

To test this, I calculated $\frac{d_m}{D}$ with both η_S and η_E in the Reynolds number, and used those values of $\frac{d_m}{D}$ to find calculate E_{ERE}. When η_S is used in Equation 5.11 to calculate E_{ERE} (Figure 5.8, left), the value of E_{ERE} is uncorrelated from the observed behavior. The calculated values of E_{ERE} predict most droplets to rebound,

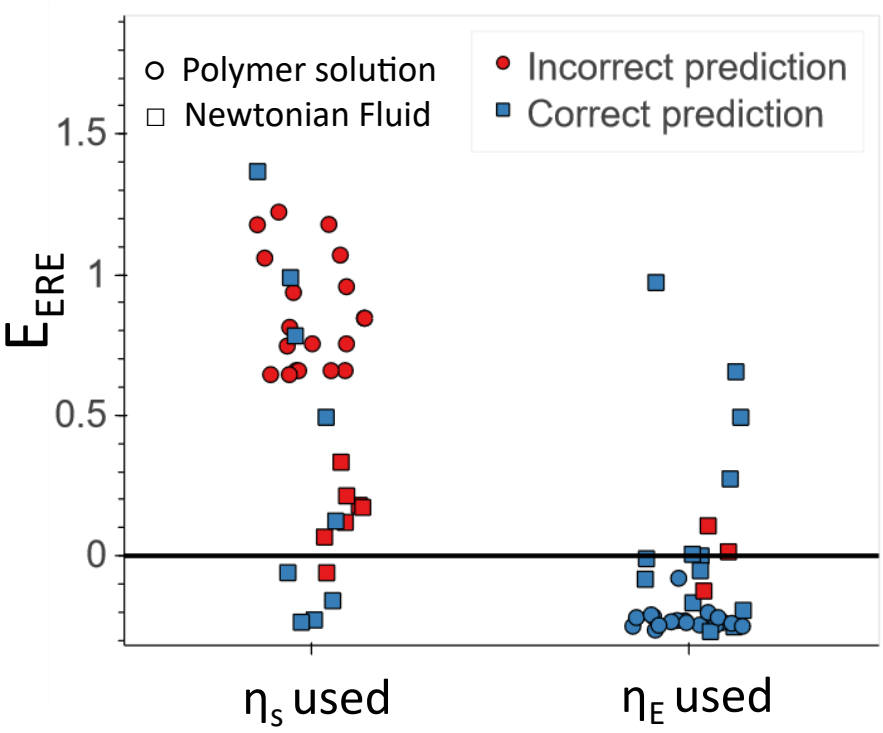

Figure 5.8: The value of excess rebound energy (E_{ERE}) for droplet impact experiments with a variety of fluids. If $E_{ERE} > 0$, the droplet is predicted to rebound; if $E_{ERE} < 0$, the droplet is predicted to deposit. The two categories are calculated using either the shear (η_S, left) or elongational (η_E, right) viscosity of the solutions. Within each grouping, the spread in the horizontal direction is meaningless and only present to allow the points to be viewed separately. The points colored blue represent correct predictions (e.g., rebound observed and $E_{ERE} > 0$) and the points colored red represent incorrect predictions. The circles are PAM solutions (polymer solutions) and the square symbols are H_2O or H_2O-glycerol solutions (Newtonian fluids).

but instead most of them deposit. This calculation is correct 26% of the time, correctly predicting outcomes for most of the H_2O and glycerol-H_2O solutions. None of the polymer solutions are predicted correctly when using η_S. When η_E is used (Figure 5.8, right), nearly every droplet (91%) is predicted correctly. With η_E, the incorrect predictions are with particular droplets of pure H_2O, and glycerol-H_2O solutions; the behavior of every PAM solution was predicted correctly.

These results highlight the importance of considering η_E when evaluating polymer solutions. The energy dissipation due to η_E dominates the dissipation from η_S and is responsible for rebound or lack-thereof in polymer solution impacts.

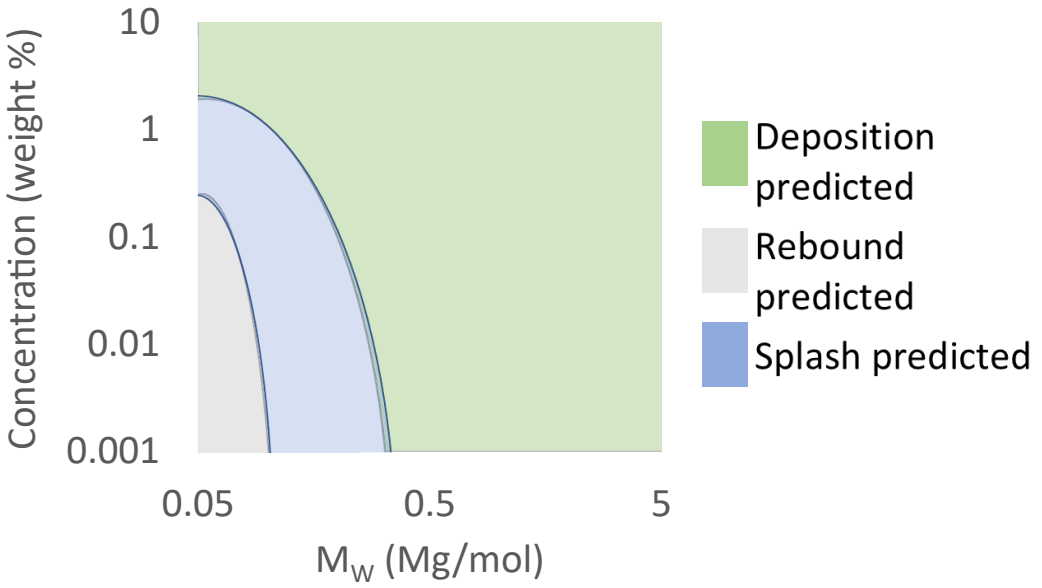

Figure 5.9: The phase diagram of simulated droplet impacts with fixed values of droplet diameter (D), fluid density (ρ), fluid surface tension (σ), and droplet velocity at impact (v) and changing weight average molecular weight (M_w) and weight % concentration of PAM in solution. As either the M_w or concentration of PAM increases, the droplet behavior moves from rebound, to splashing, to deposition.

5.5 Target molecular weight and concentration for field relevant droplets

Our collaborator, DOW Chemical, furnished us with reasonable values for D, ρ, σ, and v for droplets currently used in agricultural sprays. By assuming a value for θ_c and using the relationships discovered in Section 3.2 to estimate η_E and η_S, I was able to model the response of H_2O droplets in the expected range with different lengths (M_w) and concentrations (c, weight %) of PAM in solution.

To determine if a solution was expected to rebound, I calculated E_{ERE} with η_E. If $E_{ERE} > 0$, then the droplet is in the rebound region of the phase diagram. To determine if the droplet would splash, I calculated $\frac{Re_S}{Oh_E^{0.21}}$ and compared it to the experimentally determined threshold value for parafilm, 4350. If the droplet was predicted to both splash and rebound, I assigned its outcome to splash. Because the splashing event happens first, in the expansion phase, energy is dissipated by that splash that is not accounted for in the rebound model. Furthermore, in my experimental observations, I was unable to find conditions that resulted in splash, followed by rebound, so I am confident in allowing the splash criteria to overrule the rebound criteria.

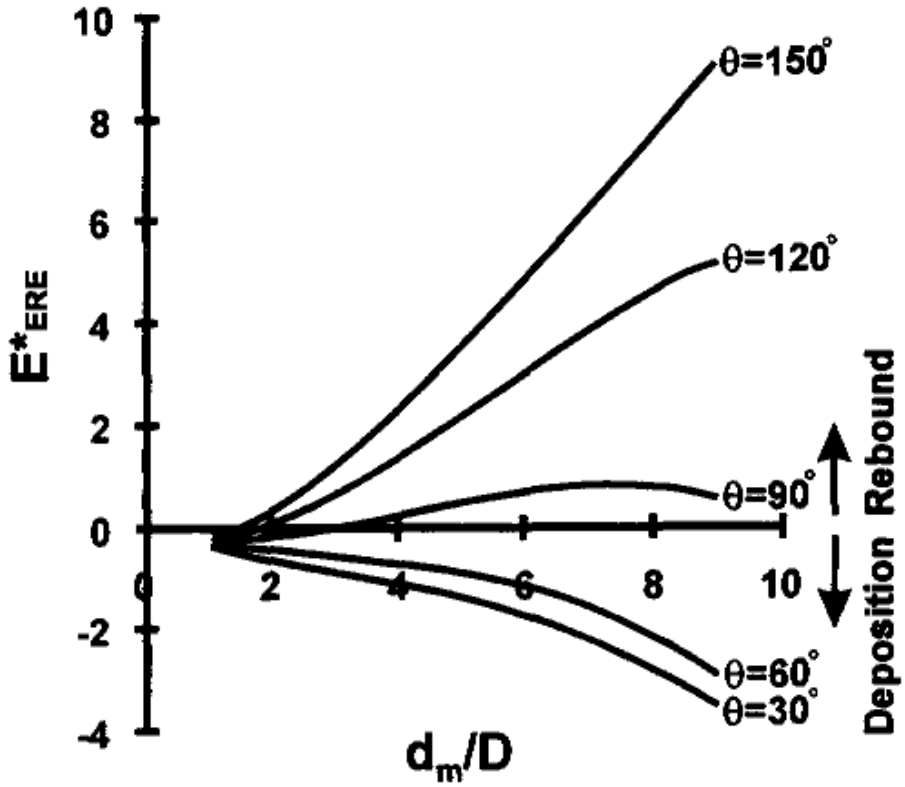

Figure 5.10: Excess rebound energy, E_{ERE}, as a function of maximum spreading diameter normalized by the droplet's diameter at impact ($\frac{d_m}{D}$) for different values of contact angle (θ in the figure shown, θ_c in my text). As θ_c increases, the value of E_{ERE} increases for a given $\frac{d_m}{D}$. Image from Mao, Kuhn, and Tran [30], reproduced with permission.

Combining these models reveals a gap: the θ_c term in my model doesn't depend on changes in σ, while in reality the to values are connected. In the mathematics used, changes in only σ have a minute outcome in terms of changing the outcome of droplets. However, in reality, a decrease in σ should be accompanied by an decrease in θ_c as the fluid is more willing to spread out over the substrate.

Increasing θ_c with other parameters staying constant results in higher E_{ERE} and increased likelihood of rebound (Figure 5.10). For example, impacting onto a more hydrophobic surface would result in more rebound.

Changes in θ_c due to the properties of the substrate alone, instead of the droplet, are well understood. In those cases, a decrease in θ_c results in less rebound and increased deposition. The surface tension is the driving force for the retraction phase and a decreased σ results in weaker retraction. The weaker and slower a droplet's retraction, the less likely it is to rebound from the substrate. Thus, the reduced

rebound from decreasing σ is compounded by the accompanying reduced rebound due to the decreased θ_c.

5.6 Droplet diameter distribution in sprays

Other observations in the literature support the hypothesis that the increased η_E found in polymer solutions leads to changes in the distribution of droplet sizes as fluid sprays from a nozzle or orifice.[42–50] After demonstrating the rebound and splash suppression of long polymers in aqueous solutions, we sent covalent and associative PAM to our collaborators at DOW to assess the change in droplet size distribution when the solutions are sprayed from an agricultural nozzle.[51]

These experiments have not been preformed yet; however, a general increase in the droplet size distribution would be beneficial for the target application. Other than losses due to splash and rebound, there significant losses from the fraction of droplets from the nozzle that are too *small*. These small droplets eventually drift off-target due to wind or other conditions and also contribute significantly to the increased need for pesticides. If the presence of polymers can simultaneously increase the average droplet size and ensure those larger droplets are depositing on target, that is an immense step towards reducing pesticide waste and drift onto neighboring farms and communities.

5.7 Conclusions and future work

The addition of covalent and associative PAM to H_2O suppress droplet rebound and splashing upon impact with hydrophobic surfaces. The results are promising for developing associative PAM into a agriculturally relevant additive. To fully realize this target, the spray studies in Section 5.6 must be completed.

A major benefit of adding polymer to the fluid is the increase in the droplet diameter sizes, which would reduce losses to drift of small droplets. The larger droplets are prevented from rebounding and splashing with sufficient length and concentration of PAM. Additionally, To fully model the retention of the PAM solutions, a relationship between the contact angle θ_c and surface tension σ needs to be implemented into the calculations demonstrated.

Finally, the specific associative chemistry of terpyridine and nickle or iron ions would prove challenging to implement in a practical sense. In our academic lab, I was able to dissolve the terpyridine ended polymers in high purity H_2O to prevent contamination of trace metal ions. The targeted application of the agricultural

industry does not use H_2O with any guaranteed degree of purity. For example, exposure to rust in any preceding steps after adding the polymer and Ni would disrupt the bis-terpyridine-Ni complexes and reduce the efficacy of the solution. Trace amounts of monovalent ions, such as Na^+, K^+, *etc*, could serve as chain capping ions, preventing further association. Other associative end groups that are more tolerant to contaminants should be implemented and investigated.

References

[1] V. Bergeron et al. “Controlling Droplet Deposition with Polymer Additives”. In: *Nature* 405.6788 (June 2000), pp. 772–775. ISSN: 0028-0836, 1476-4687. DOI: 10.1038/35015525. URL: http://www.nature.com/articles/35015525 (visited on 08/05/2020).

[2] B. V. Orme et al. “Droplet Retention and Shedding on Slippery Substrates”. In: *Langmuir* 35.28 (July 16, 2019), pp. 9146–9151. ISSN: 0743-7463, 1520-5827. DOI: 10.1021/acs.langmuir.9b00931. URL: https://pubs.acs.org/doi/10.1021/acs.langmuir.9b00931 (visited on 10/15/2020).

[3] E. Villermaux. “Fragmentation versus Cohesion”. In: *Journal of Fluid Mechanics* 898 (Sept. 10, 2020), P1. ISSN: 0022-1120, 1469-7645. DOI: 10.1017/jfm.2020.366. URL: https://www.cambridge.org/core/product/identifier/S0022112020003663/type/journal_article (visited on 03/24/2021).

[4] Y. Song et al. “The Use of Folate/Zinc Supramolecular Hydrogels to Increase Droplet Deposition on *Chenopodium Album* L. Leaves”. In: *ACS Sustainable Chemistry & Engineering* 8.34 (Aug. 31, 2020), pp. 12911–12919. ISSN: 2168-0485, 2168-0485. DOI: 10.1021/acssuschemeng.0c03396. URL: https://pubs.acs.org/doi/10.1021/acssuschemeng.0c03396 (visited on 09/17/2020).

[5] G. J. Dorr et al. “Spray Retention on Whole Plants: Modelling, Simulations and Experiments”. In: *Crop Protection* 88 (Oct. 2016), pp. 118–130. ISSN: 02612194. DOI: 10.1016/j.cropro.2016.06.003. URL: https://linkinghub.elsevier.com/retrieve/pii/S026121941630134X (visited on 03/25/2021).

[6] M. Qin et al. “On the Role of Liquid Viscosity in Affecting Droplet Spreading on a Smooth Solid Surface”. In: *International Journal of Multiphase Flow* 117 (Aug. 2019), pp. 53–63. ISSN: 03019322. DOI: 10.1016/j.ijmultiphaseflow.2019.05.002. URL: https://linkinghub.elsevier.com/retrieve/pii/S0301932218308772 (visited on 06/07/2022).

[7] H. Zhang et al. “Reversed Role of Liquid Viscosity on Drop Splash”. In: *Physics of Fluids* 33.5 (May 2021), p. 052103. ISSN: 1070-6631, 1089-7666. DOI: 10.1063/5.0048569. URL: https://aip.scitation.org/doi/10.1063/5.0048569 (visited on 06/07/2022).

[8] R. Rioboo, C. Tropea, and M. Marengo. “Outcomes from a Drop Impact on Solid Surfaces”. In: *Atomization and Sprays* 11.2 (2001), p. 12. ISSN: 1044-5110. DOI: 10.1615/AtomizSpr.v11.i2.40. URL: http://www.dl.begellhouse.com/journals/6a7c7e10642258cc,02b3b3196bd0e2a7,4224940d1f16de7f.html (visited on 08/23/2022).

[9] S. Moghtadernejad, C. Lee, and M. Jadidi. “An Introduction of Droplet Impact Dynamics to Engineering Students”. In: *Fluids* 5.3 (July 2, 2020), p. 107. ISSN: 2311-5521. DOI: 10.3390/fluids5030107. URL: https://www.mdpi.com/2311-5521/5/3/107 (visited on 12/01/2020).

[10] H. Zhang et al. “Effect of Wettability on Droplet Impact: Spreading and Splashing”. In: *Experimental Thermal and Fluid Science* 124 (June 2021), p. 110369. ISSN: 08941777. DOI: 10.1016/j.expthermflusci.2021.110369. URL: https://linkinghub.elsevier.com/retrieve/pii/S0894177721000224 (visited on 06/07/2022).

[11] J. Wisniak. “Frederick Thomas Trouton: The Man, the Rule, and the Ratio”. In: *The Chemical Educator* 6.1 (Feb. 2001), pp. 55–61. ISSN: 1430-4171. DOI: 10.1007/s00897000448a. URL: http://link.springer.com/10.1007/s00897000448a (visited on 10/04/2022).

[12] M. Rosello et al. “Dripping-onto-Substrate Capillary Breakup Extensional Rheometry of Low-Viscosity Printing Inks”. In: *Journal of Non-Newtonian Fluid Mechanics* 266 (Apr. 2019), pp. 160–170. ISSN: 03770257. DOI: 10.1016/j.jnnfm.2019.03.006. URL: https://linkinghub.elsevier.com/retrieve/pii/S0377025718302994 (visited on 03/05/2020).

[13] C. J. Petrie. “One Hundred Years of Extensional Flow”. In: *Journal of Non-Newtonian Fluid Mechanics* 137.1-3 (Aug. 2006), pp. 1–14. ISSN: 03770257. DOI: 10.1016/j.jnnfm.2006.01.010. URL: https://linkinghub.elsevier.com/retrieve/pii/S037702570600036X (visited on 05/06/2020).

[14] A.-L. Biance, C. Clanet, and D. Quéré. “Leidenfrost Drops”. In: *Physics of Fluids* 15.6 (2003), p. 1632. ISSN: 10706631. DOI: 10.1063/1.1572161. URL: http://scitation.aip.org/content/aip/journal/pof2/15/6/10.1063/1.1572161 (visited on 09/03/2020).

[15] N. Mourougou-Candoni et al. “Influence of Dynamic Surface Tension on the Spreading of Surfactant Solution Droplets Impacting onto a Low-Surface-Energy Solid Substrate”. In: *Journal of Colloid and Interface Science* 192.1 (Aug. 1997), pp. 129–141. ISSN: 00219797. DOI: 10.1006/jcis.1997.4989. URL: https://linkinghub.elsevier.com/retrieve/pii/S0021979797949894 (visited on 10/30/2020).

[16] D. Bartolo et al. “Dynamics of Non-Newtonian Droplets”. In: *Physical Review Letters* 99.17 (Oct. 26, 2007), p. 174502. ISSN: 0031-9007, 1079-7114. DOI: 10.1103/PhysRevLett.99.174502. URL: https://link.aps.org/doi/10.1103/PhysRevLett.99.174502 (visited on 07/29/2020).

[17] P. Dhar, S. R. Mishra, and D. Samanta. “Onset of Rebound Suppression in Non-Newtonian Droplets Post-Impact on Superhydrophobic Surfaces”. In: *Physical Review Fluids* 4.10 (Oct. 22, 2019). ISSN: 2469-990X. DOI: 10.1103/PhysRevFluids.4.103303. URL: https://link.aps.org/doi/10.1103/PhysRevFluids.4.103303 (visited on 06/11/2020).

[18] H. K. Huh et al. “Role of Polymer Concentration and Molecular Weight on the Rebounding Behaviors of Polymer Solution Droplet Impacting on Hydrophobic Surfaces”. In: *Microfluidics and Nanofluidics* 18.5-6 (May 2015), pp. 1221–1232. ISSN: 1613-4982, 1613-4990. DOI: 10.1007/s10404-014-1518-4. URL: http://link.springer.com/10.1007/s10404-014-1518-4 (visited on 12/16/2020).

[19] J. B. Lee et al. “Energy Budget of Liquid Drop Impact at Maximum Spreading: Numerical Simulations and Experiments”. In: *Langmuir* 32.5 (Feb. 9, 2016), pp. 1279–1288. ISSN: 0743-7463, 1520-5827. DOI: 10.1021/acs.langmuir.5b03848. URL: https://pubs.acs.org/doi/10.1021/acs.langmuir.5b03848 (visited on 12/16/2020).

[20] L. Xu. “Liquid Drop Splashing on Smooth, Rough, and Textured Surfaces”. In: *Physical Review E* 75.5 (May 31, 2007), p. 056316. ISSN: 1539-3755, 1550-2376. DOI: 10.1103/PhysRevE.75.056316. URL: https://link.aps.org/doi/10.1103/PhysRevE.75.056316 (visited on 07/10/2022).

[21] K. N. Prabhu, P. Fernades, and G. Kumar. “Effect of Substrate Surface Roughness on Wetting Behaviour of Vegetable Oils”. In: *Materials & Design* 30.2 (Feb. 2009), pp. 297–305. ISSN: 02613069. DOI: 10.1016/j.matdes.2008.04.067. URL: https://linkinghub.elsevier.com/retrieve/pii/S0261306908001659 (visited on 08/12/2022).

[22] E. Villermaux. “Fragmentation”. In: *Annual Review of Fluid Mechanics* 39.1 (Jan. 2007), pp. 419–446. ISSN: 0066-4189, 1545-4479. DOI: 10.1146/annurev.fluid.39.050905.110214. URL: http://www.annualreviews.org/doi/10.1146/annurev.fluid.39.050905.110214 (visited on 05/06/2020).

[23] S. Chen and V. Bertola. “The Impact of Viscoplastic Drops on a Heated Surface in the Leidenfrost Regime”. In: *Soft Matter* 12.36 (2016), pp. 7624–7631. ISSN: 1744-683X, 1744-6848. DOI: 10.1039/C6SM00893C. URL: http://xlink.rsc.org/?DOI=C6SM00893C (visited on 08/05/2020).

[24] H. Kim et al. “Drop Splashing on a Rough Surface: How Surface Morphology Affects Splashing Threshold”. In: *Applied Physics Letters* 104.16 (Apr. 21, 2014), p. 161608. ISSN: 0003-6951, 1077-3118. DOI: 10.1063/1.4873338. URL: http://aip.scitation.org/doi/10.1063/1.4873338 (visited on 07/10/2022).

[25] C. Josserand and S. Thoroddsen. “Drop Impact on a Solid Surface”. In: *Annual Review of Fluid Mechanics* 48.1 (Jan. 3, 2016), pp. 365–391. ISSN: 0066-4189, 1545-4479. DOI: 10.1146/annurev-fluid-122414-034401. URL: http://www.annualreviews.org/doi/10.1146/annurev-fluid-122414-034401 (visited on 08/05/2020).

[26] S. Chandra and C. T. Avedisian. “On the Collision of a Droplet with a Solid Surface”. In: *Proceedings: Mathematical and Physical Sciences* 432.1884 (Jan. 8, 1991), p. 30.

[27] V. Bertola. “An Experimental Study of Bouncing Leidenfrost Drops: Comparison between Newtonian and Viscoelastic Liquids”. In: *International Journal of Heat and Mass Transfer* 52.7-8 (Mar. 2009), pp. 1786–1793. ISSN: 00179310. DOI: 10.1016/j.ijheatmasstransfer.2008.09.028. URL: https://linkinghub.elsevier.com/retrieve/pii/S0017931008005875 (visited on 08/06/2020).

[28] J. Du et al. “Initial Spreading Dynamics of a Liquid Droplet: The Effects of Wettability, Liquid Properties, and Substrate Topography”. In: *Physics of Fluids* 33.4 (Apr. 2021), p. 042118. ISSN: 1070-6631, 1089-7666. DOI: 10.1063/5.0049409. URL: https://aip.scitation.org/doi/10.1063/5.0049409 (visited on 08/24/2022).

[29] M. Song et al. “Enhancing Droplet Deposition on Wired and Curved Superhydrophobic Leaves”. In: *ACS Nano* 13.7 (July 23, 2019), pp. 7966–7974. ISSN: 1936-0851, 1936-086X. DOI: 10.1021/acsnano.9b02457. URL: https://pubs.acs.org/doi/10.1021/acsnano.9b02457 (visited on 04/30/2022).

[30] T. Mao, D. C. S. Kuhn, and H. Tran. “Spread and Rebound of Liquid Droplets upon Impact on Flat Surfaces”. In: *AIChE Journal* 43.9 (Sept. 1997), pp. 2169–2179. ISSN: 0001-1541, 1547-5905. DOI: 10.1002/aic.690430903. URL: https://onlinelibrary.wiley.com/doi/10.1002/aic.690430903 (visited on 08/23/2022).

[31] D. A. Burzynski and S. E. Bansmer. “Droplet Splashing on Thin Moving Films at High Weber Numbers”. In: *International Journal of Multiphase Flow* 101 (Apr. 2018), pp. 202–211. ISSN: 03019322. DOI: 10.1016/j.ijmultiphaseflow.2018.01.015. URL: https://linkinghub.elsevier.com/retrieve/pii/S0301932217305153 (visited on 04/15/2022).

[32] G. Riboux and J. M. Gordillo. “Experiments of Drops Impacting a Smooth Solid Surface: A Model of the Critical Impact Speed for Drop Splashing”. In: *Physical Review Letters* 113.2 (July 11, 2014), p. 024507. ISSN: 0031-9007, 1079-7114. DOI: 10.1103/PhysRevLett.113.024507. URL: https://link.aps.org/doi/10.1103/PhysRevLett.113.024507 (visited on 10/05/2022).

[33] C. Mundo, M. Sommerfeld, and C. Tropea. “Droplet-Wall Collisions: Experimental Studies of the Deformation and Breakup Process”. In: *International Journal of Multiphase Flow* 21.2 (Apr. 1995), pp. 151–173. ISSN: 03019322. DOI: 10.1016/0301-9322(94)00069-V. URL: https://linkinghub.elsevier.com/retrieve/pii/030193229400069V (visited on 10/05/2022).

[34] T. Ashida et al. “Hidden Prompt Splashing by Corona Splashing at Drop Impact on a Smooth Dry Surface”. In: *Physical Review Fluids* 5.1 (Jan. 15, 2020), p. 011601. ISSN: 2469-990X. DOI: 10.1103/PhysRevFluids.5.011601. URL: https://link.aps.org/doi/10.1103/PhysRevFluids.5.011601 (visited on 10/05/2022).

[35] H. Almohammadi and A. Amirfazli. “Droplet Impact: Viscosity and Wettability Effects on Splashing”. In: *Journal of Colloid and Interface Science* 553 (Oct. 2019), pp. 22–30. ISSN: 00219797. DOI: 10.1016/j.jcis.2019.05.101. URL: https://linkinghub.elsevier.com/retrieve/pii/S0021979719306654 (visited on 10/05/2022).

[36] J. Palacios et al. “Experimental Study of Splashing Patterns and the Splashing/Deposition Threshold in Drop Impacts onto Dry Smooth Solid Surfaces”. In: *Experimental Thermal and Fluid Science* 44 (Jan. 2013), pp. 571–582. ISSN: 08941777. DOI: 10.1016/j.expthermflusci.2012.08.020. URL: https://linkinghub.elsevier.com/retrieve/pii/S089417771200235X (visited on 10/05/2022).

[37] C. S. Stevens, A. Latka, and S. R. Nagel. “Comparison of Splashing in High- and Low-Viscosity Liquids”. In: *Physical Review E* 89.6 (June 9, 2014), p. 063006. ISSN: 1539-3755, 1550-2376. DOI: 10.1103/PhysRevE.89.063006. URL: https://link.aps.org/doi/10.1103/PhysRevE.89.063006 (visited on 10/05/2022).

[38] H. Vu, D. Banks, and G. Aguilar. “Examining Viscosity and Surface Wettability on Lamella Lift Dynamics and Droplet Splashing”. In: *Atomization and Sprays* 21.4 (2011), pp. 303–315. ISSN: 1044-5110. DOI: 10.1615/AtomizSpr.2011002818. URL: http://www.dl.begellhouse.com/journals/6a7c7e10642258cc,4fa736af31a9c3d7,372150e6667fc6fd.html (visited on 10/05/2022).

[39] T. C. de Goede et al. “Effect of Wetting on Drop Splashing of Newtonian Fluids and Blood”. In: *Langmuir* 34.18 (May 8, 2018), pp. 5163–5168. ISSN: 0743-7463, 1520-5827. DOI: 10.1021/acs.langmuir.7b03355. URL: https://pubs.acs.org/doi/10.1021/acs.langmuir.7b03355 (visited on 10/05/2022).

[40] C. S. Stevens. “Scaling of the Splash Threshold for Low-Viscosity Fluids”. In: *EPL (Europhysics Letters)* 106.2 (Apr. 1, 2014), p. 24001. ISSN: 0295-5075, 1286-4854. DOI: 10.1209/0295-5075/106/24001. URL: https://iopscience.iop.org/article/10.1209/0295-5075/106/24001 (visited on 10/05/2022).

[41] R. L. V. Wal, G. M. Berger, and S. D. Mozes. “The Splash/Non-Splash Boundary upon a Dry Surface and Thin Fluid Film”. In: *Experiments in Fluids* 40.1 (Jan. 2006), pp. 53–59. ISSN: 0723-4864, 1432-1114. DOI: 10.1007/s00348-005-0045-1. URL: http://link.springer.com/10.1007/s00348-005-0045-1 (visited on 10/05/2022).

[42] M. H. Wei et al. “Megasupramolecules for Safer, Cleaner Fuel by End Association of Long Telechelic Polymers”. In: *Science* 350.6256 (2015), pp. 72–75. ISSN: 10959203. DOI: 10.1126/science.aab0642.

[43] R. W. Lewis et al. “Polymeric Drift Control Adjuvants for Agricultural Spraying”. In: *Macromolecular Chemistry and Physics* 217.20 (Oct. 2016), pp. 2223–2242. ISSN: 10221352. DOI: 10.1002/macp.201600139. URL: https://onlinelibrary.wiley.com/doi/10.1002/macp.201600139 (visited on 03/23/2022).

[44] D. J. Dijkstra et al. “The Relationship between Rheological Properties and Spraying Behavior of Polymer Dispersions”. In: *Macromolecular Symposia* 249–250.1 (Apr. 2007), pp. 647–653. ISSN: 10221360, 15213900. DOI: 10.1002/masy.200750450. URL: http://doi.wiley.com/10.1002/masy.200750450 (visited on 05/07/2021).

[45] B. Keshavarz et al. “Studying the Effects of Elongational Properties on Atomization of Weakly Viscoelastic Solutions Using Rayleigh Ohnesorge Jetting Extensional Rheometry (ROJER)”. In: *Journal of Non-Newtonian Fluid Mechanics* 222 (Aug. 2015), pp. 171–189. ISSN: 03770257. DOI: 10.1016/j.jnnfm.2014.11.004. URL: https://linkinghub.elsevier.com/retrieve/pii/S0377025714002055 (visited on 02/12/2020).

[46] E. Hilz. “Spray Drift Review: The Extent to Which a Formulation Can Contribute to Spray Drift Reduction”. In: *Crop Protection* (2013), p. 9.

[47] A. S. Felsot et al. “Agrochemical Spray Drift; Assessment and Mitigation—A Review*”. In: *Journal of Environmental Science and Health, Part B* 46.1 (Dec. 30, 2010), pp. 1–23. ISSN: 0360-1234, 1532-4109. DOI: 10.1080/03601234.2010.515161. URL: http://www.tandfonline.com/doi/abs/10.1080/03601234.2010.515161 (visited on 03/24/2022).

[48] S. Kooij et al. “What Determines the Drop Size in Sprays?” In: *Physical Review X* 8.3 (July 20, 2018). ISSN: 2160-3308. DOI: 10.1103/PhysRevX.8.031019. URL: https://link.aps.org/doi/10.1103/PhysRevX.8.031019 (visited on 06/11/2020).

[49] R. Wang et al. “Impacts of Polymer/Surfactant Interactions on Spray Drift”. In: *Colloids and Surfaces A: Physicochemical and Engineering Aspects* 500 (July 2016), pp. 88–97. ISSN: 09277757. DOI: 10.1016/j.colsurfa.2016.03.056. URL: https://linkinghub.elsevier.com/retrieve/pii/S0927775716301972 (visited on 07/26/2022).

[50] H. Zhu et al. “Effects of Polymer Composition and Viscosity on Droplet Size of Recirculated Spray Solutions”. In: *Journal of Agricultural Engineering Research* 67.1 (May 1997), pp. 35–45. ISSN: 00218634. DOI: 10.1006/jaer.1997.0151. URL: https://linkinghub.elsevier.com/retrieve/pii/S0021863497901517 (visited on 03/23/2022).

[51] M. Xu et al. “Quantifying the Effect of Extensional Rheology on the Retention of Agricultural Sprays”. In: *Physics of Fluids* 33.3 (Mar. 1, 2021), p. 032107. ISSN: 1070-6631, 1089-7666. DOI: 10.1063/5.0038391. URL: https://aip.scitation.org/doi/10.1063/5.0038391 (visited on 03/15/2021).

Chapter 6

ASSOCIATIVE POLY(CYCLOOCTADIENE) FOR FIRE SUPPRESSION IN ORGANIC LIQUIDS

The work in this chapter is in preparation for submission to peer-review, and I am one of many authors on that manuscript. The polymers in this section were synthesized by Dr. Hojin Kim following the work done in Wei et al. [1]. The shear rheology was performed by Dr. Red Lhota. Hojin and Red developed the method of dissolving the associative PCOD in PAO with the use of butylated hydroxytoluene (BHT). The difference between decalin and PAO as solvents is discussed extensively in both Kim [2] and Lhota [3]. The spray tests were done by Dr. Jacob Temme at ARL. The DoSER measurements, and analysis was done by RWL.

All DoSER experiments in this chapter were performed with 22G (D_0 = 1.016 and D_{inner} = 0.711 mm) PTFE needles, onto aluminum substrates with a gap height (H) of ~ 3.3 mm (H/D_0 = 3.2, $H/D_{pred}^{solvent}$ = 1.3), and at temperatures ranging from 15 to 17 ° C. The values of H and identity of the substrate was chosen to optimize the experimental conditions per the experiments in Chapter 2.

6.1 The benefit of polymers in organic liquids

In 2015, the Kornfield group showed that adding a specialty polymer, poly(cyclooctadiene) (PCOD) with associative end groups, to jet fuel reduces the likelihood and danger of explosive outcomes after an aviation accident.[1,4] We know that the presence of long polymers in solution act to resist elongational flows, and propose that the increased η_E shifts the size distribution of jet fuel droplets to larger droplets, and suppress the formation of small satellite droplets.[5–10] The larger droplets produced by polymer laden fluids, in turn, find their way out of the air and into a puddle more quickly than the same volume of smaller droplets. Removing flammable mist from the air substantially reduces fire risk.[11–14] Lubricating and heat transfer fluids, also found in avionic engines, pose a similar fire risk to untreated jet fuel. A broken fluid line, an accident, or other types of damage can create mists of these flammable fluids and expose them to ignition sources.[4,6] The compound commonly used in these fluids is poly(alphaolefin) (PAO) (Figure 6.1). Although PAO is chemically similar to jet fuel, it is substantially more viscous and the PCOD backbone is less soluble in PAO.[15]

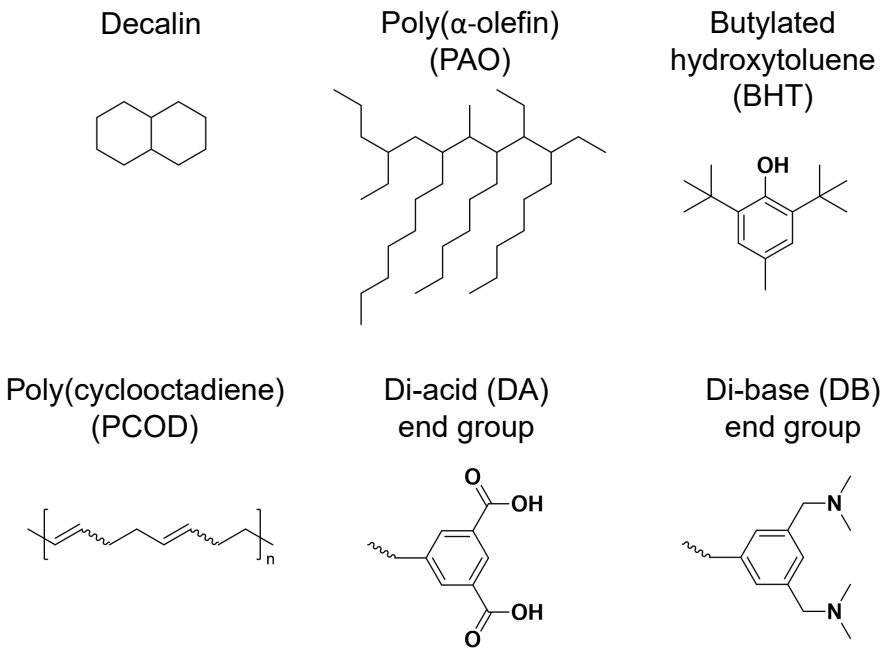

Figure 6.1: The structure of various chemical species in this section. Top: solvents decalin and an example of poly(α-olefin) (PAO). In practice, PAO is composed of a variety of branched alkyl structures. Bottom: polymers poly(cyclooctadiene) (PCOD) and the associative di-acid (DA) and di-base (DB) end groups.

Although the previous results demonstrated that mists of PCOD-jet fuel solutions are much harder to ignite than solutions without the polymer additives, the thresholds and mechanism of this benefit is unknown. Consequently, the technology is far from ready for deployment. Users would simply be guessing how much polymer additive to include to see the benefits, which would be further compounded by the relatively rarity of aircraft accidents. This disconnection between the solution structure and its performance as a fire safety tool presents an obvious opportunity to measure the fluid properties with DoSER and deepen the understanding of the technology, enabling further innovations without the difficult live-fire testing.[10,16–18]

With the DoSER technique, I studied the effects of the solvent quality on the non-associative and associative modified PCOD, and we correlate the fluid properties with their performance in jetting experiments. The associative-group end modified PCOD have di-acid (DA) and di-base (DB) end groups, which engage in hydrogen bonding with one another to form megasupramolecules in solution (Figure 6.1, bottom).

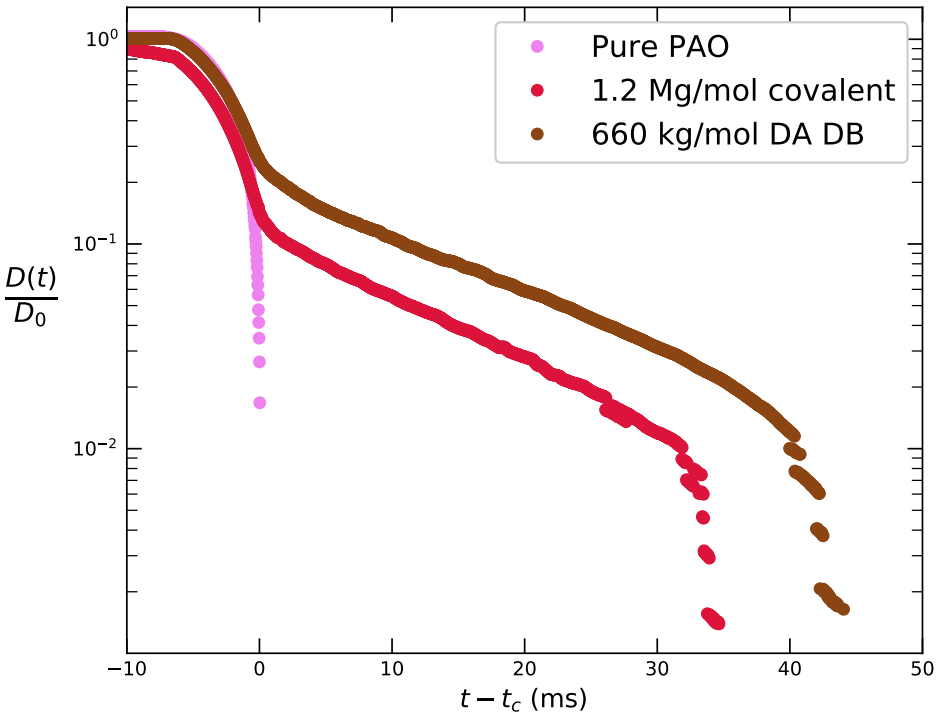

Figure 6.2: Normalized minimum diameter ($D(t)/D_0$) of n = 5 trials of pure solvent (PAO), 1.2 Mg/mol PCOD (covalent), and 660 kg/mol associative PCOD in a 1 to 1 ratio (DA DB). All polymer solutions are at a concentration of 0.5 weight %.

6.2 Covalent and associative poly(cyclooctadiene) in PAO

I measured the elongational fluid properties of both covalent and associative PCOD in PAO using DoSER. The solutions of pair-wise associative PCODs with both components have higher elongational relaxation time, λ_E, than their counterparts at high (0.5 weight %) concentration (Figure 6.2). It is possible for the DA end groups to weakly associate with one another, and the sample of pure DA has the lowest λ_E at both concentrations tested (Figure 6.3). The low λ_E relative to the other samples indicates that rings, enabled by DA-DA associations are forming in solution. As polymer rings do not resist elongational flow as strongly as linear polymers, their presence explains the decrease in the measured λ_E. The associative response of DA DB pairs depends on the concentration of polymers (Table 6.1). At high concentrations, 0.5 weight %, the solutions that contain both DA and DB have the highest λ_E (Table 6.1). At one tenth that concentration, 0.05 weight %, the solution with DA and DB is statistically indistinguishable from pure DB.

In this system of PAO and hydrogen bonding associations, the concentration of 0.5 weight % is required for the polymer end groups to locate each other in solution

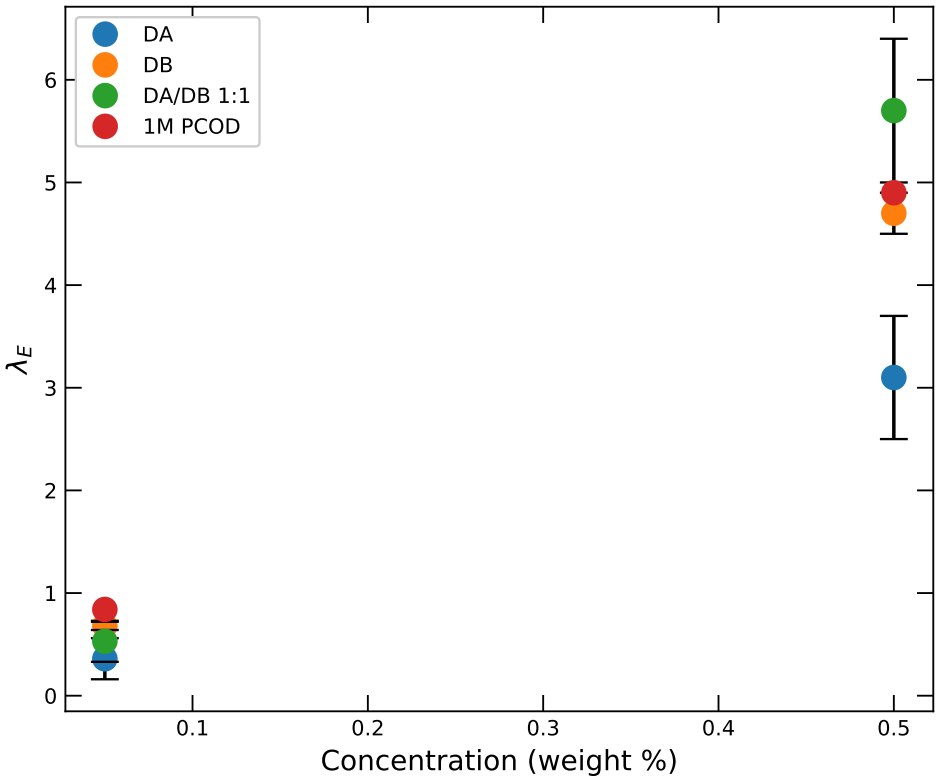

Figure 6.3: The measured elongational relaxation time (λ_E) as a function of concentration for solutions of of 660 kg/mol diacid-ended PCOD (DA), dibase-ended PCOD (DB), a 1 to 1 mixture of DA and DB (DA DB), and 1200 kg/mol PCOD (covalent) tested in decalin. The points are means of n = 5 trails and the error bars show ± 1 standard deviation.

and noticeably form linear megasupramolcules. The critical overlap concentration (c^*) of PCOD in PAO is 0.6 weight %, so at equilibrium the polymer chains are not likely to encounter one another.[3] At 0.05 weight % the thermodynamics of the associations are not strong enough to attract the polymers to one another, so they cannot associate into megasupramolecules and realize the λ_E increase.[1,19,20]

6.3 Solvent effects on association

To increase the signal from the assosciative groups, we tested the DA and DB ended polymers in decalin as well as PAO (Figure 6.1, top). The solvent plays an important role in the measured fluid properties. The solvents themselves also have different solvent shear viscosity (η_0): η_0 of PAO = 9.0 mPa s and η_0 of decalin = 2.9 mPa s. PCOD and its associative end groups, DA and DB, interact more favorable with decalin than PAO, leading to a larger coil size at equilibrium and a higher c^*. In decalin, PCOD has a c^* of 0.2 weight %.[3]

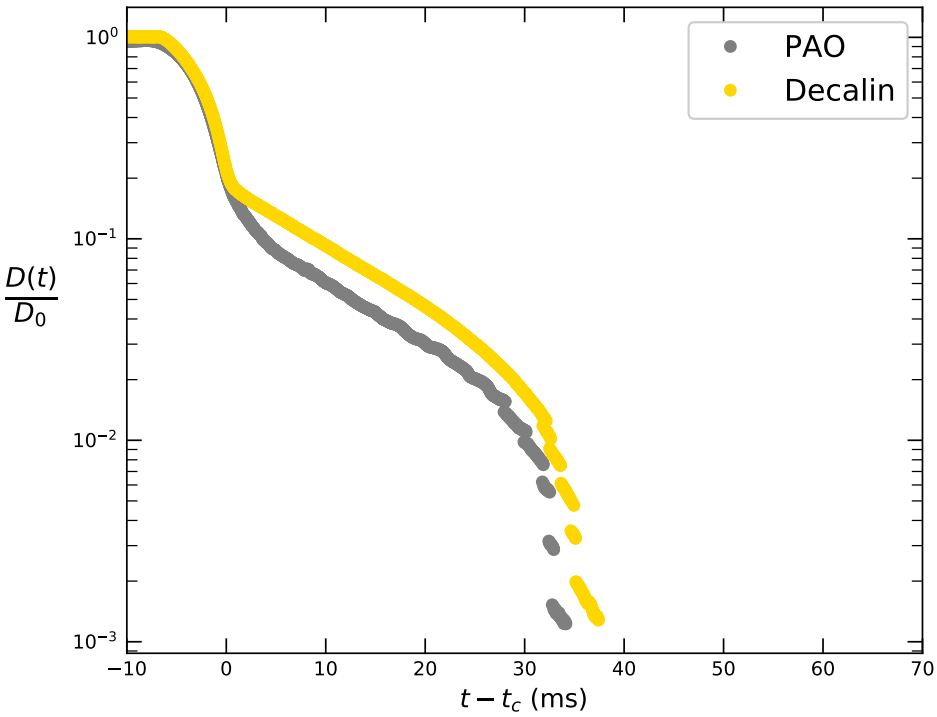

Figure 6.4: Normalized minimum diameter ($D(t)/D_0$) of n = 5 trials of 660 kg/mol dibase-ended PCOD (DB) at a concentration of 0.5 weight % in PAO and decalin.

Adding DB at 0.5 weight % to both solvents produces fluids with identical λ_E (Figure 6.4). Because λ_E depends only on the polymer concentration and conformation in solution, and not on the physical properties of the solution like η_0, we conclude that DB chains do not interact with one another from the identical values of λ_E in both solvents. The behavior at $t < t_c$ shows the difference in η_0 of the solvents: the transition to the elasto-capillary regime is much sharper and with higher $\frac{D(t_c)}{D_0}$ in decalin, the lower solvent with η_0.

The increased coil-size due to the due to more favorable interactions between the polymer backbone and decalin compared to PAO enhances the ability of the associative groups (DA and DB) to find one another in solution and form megasupramolecular structures.

The increased association effect is most noticeable in solutions of DA (Figure 6.5). The observed λ_E increases from 3.1 to 8.5, because the DA chains are now able to form end-associated linear chains instead of rings (Table 6.1). The solutions of DA DB pairs also benefit from increased concentration, similar to what I observed in PAO.

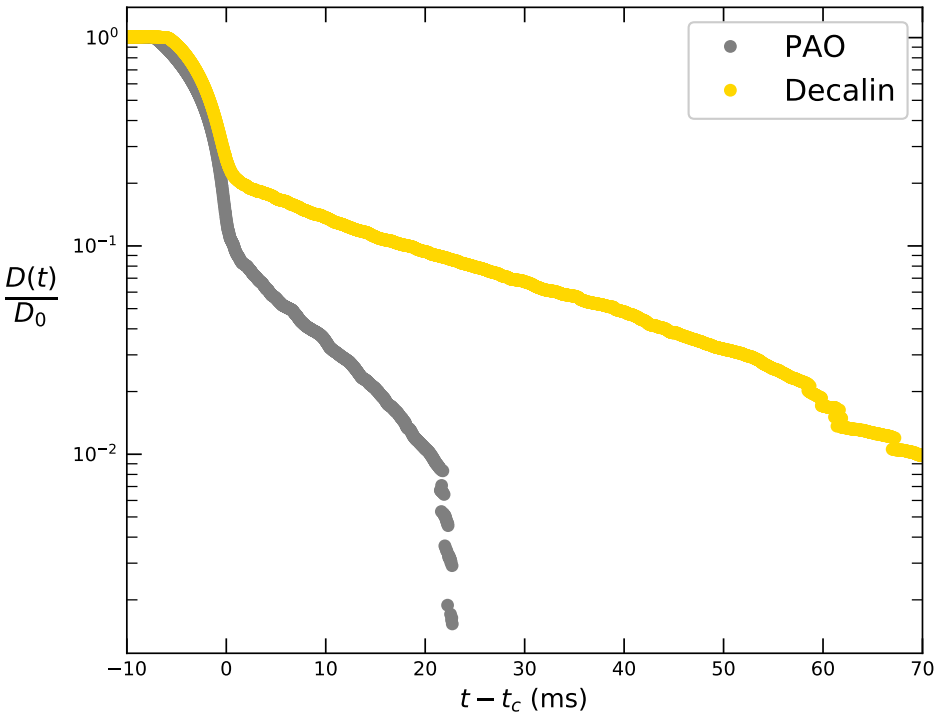

Figure 6.5: Normalized minimum diameter ($D(t)/D_0$) of n = 5 trials of 660 kg/mol diacid-ended PCOD (DA) at a concentration of 0.5 weight % in PAO and decalin.

Interestingly, there is evidence that decalin is drawing the DA end groups out to solution more strongly than the DB end groups. At 0.5 weight %, the solution of DA DB pairs and the solution of pure DA have similar λ_E, indicating they have similar length and concentration of long end associative polymers active. As the concentration decreases, λ_E of the DA DB solutions decreases more quickly than in pure DA solutions (Figure 6.6). The slower decrease in DA solution reveals a higher number of long, end associative polymers in solution. In other words, the presence of DB in the DA DB pair solution is actually impeding the formation of linear megasupramolecules. The most plausible explanation for this observation is that the solvent is attracting DA end groups more strongly than DB end groups, resulting in fewer DA-DB associations and more DA-DA associations.

6.4 Performance in spray testing

This section is not the first or only place the following spray testing results appear. It is included here to help bring context to the DoSER results in the preceding sections and the recommendations for future work. The spray testing was preformed by Dr. Jacob Temme at Army Research Labs; Dr. Temme, Dr. Lhota, RWL, and Professor Kornfield contributed to the data analysis.

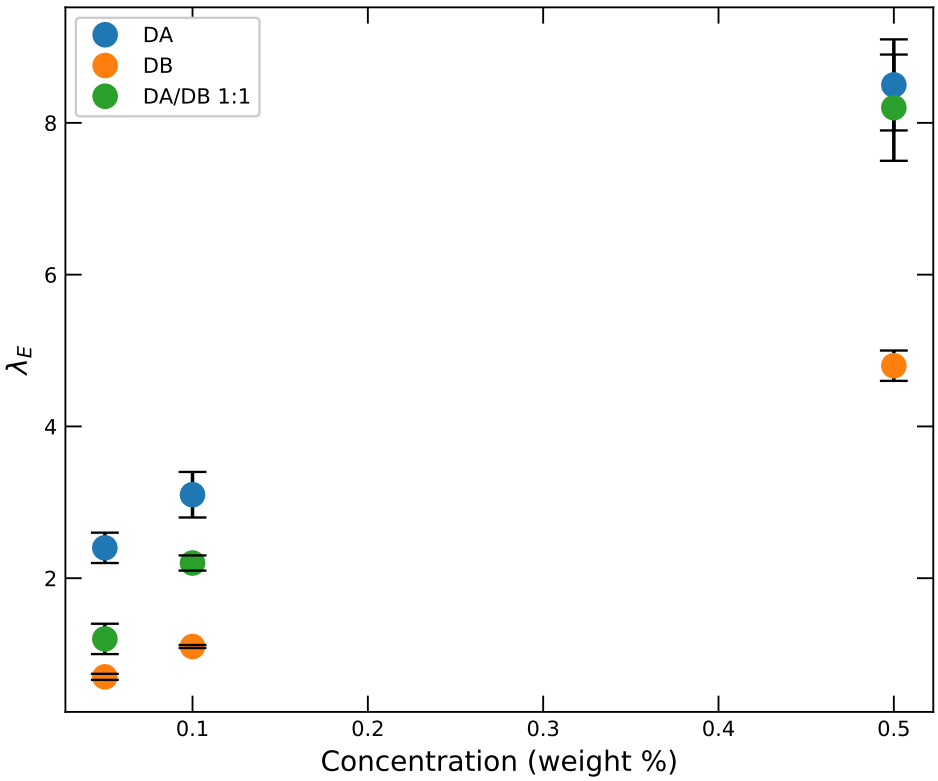

Figure 6.6: The measured elongational relaxation time (λ_E) as a function of concentration for solutions of 660 kg/mol diacid-ended PCOD (DA), dibase-ended PCOD (DB), a 1 to 1 mixture of DA and DB (DA DB). The points are means of n = 5 trails and the error bars show 1 standard deviation.

Table 6.1: Elongational relaxation time (λ_E) of of 660 kg/mol diacid-ended PCOD (DA), dibase-ended PCOD (DB), a 1 to 1 mixture of DA and DB (DA DB), and 1200 kg/mol PCOD (covalent) tested in PAO and decalin

Sample	Concentration (weight %)	λ_E (ms) PAO	λ_E (ms) Decalin
DA	0.5	3.1 ± 0.3	8.5 ± 0.6
DB	0.5	4.7 ± 0.3	4.8 ± 0.2
DA DB	0.5	5.7 ± 0.2	8.2 ± 0.7
Covalent	0.5	4.9 ± 0.2	-
DA	0.05	.36 ± .05	2.4 ± 0.2
DB	0.05	.68 ± .10	0.7 ± 0.0
DA DB	0.05	.53 ± .06	1.2 ± 0.2
Covalent	0.05	.84 ± .06	-

- indicates this value was not measured.

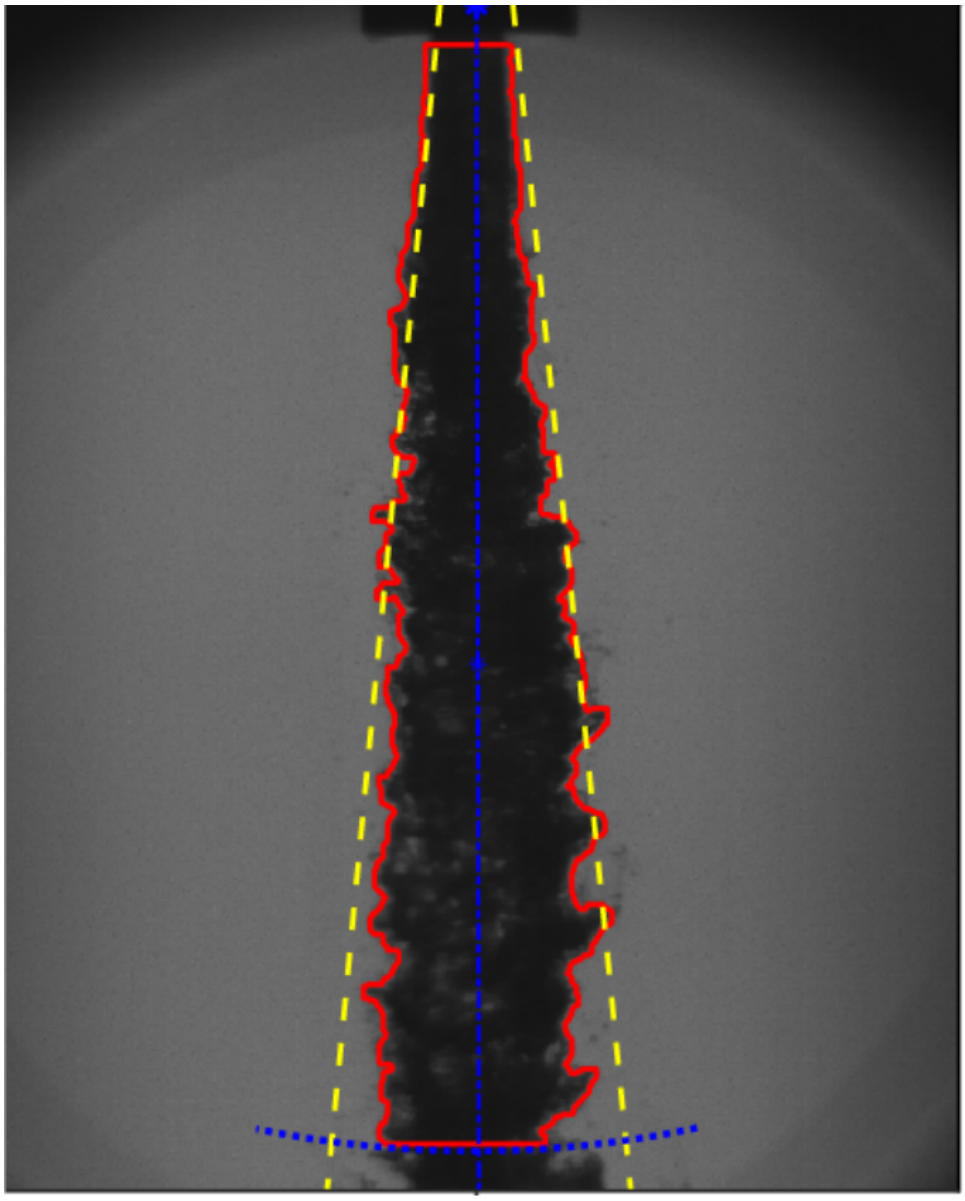

Figure 6.7: Example of PAO spray pattern and analysis to determine the spray angle. Red indicates edge of spray as determined by image analysis. Yellow indicates calculated spray angle. Image provided by Dr. Jacob Temme, ARL, reproduced from Lhota [3] with permission.

The performance of the polymer additive is ultimately determined by formation — or lack thereof — of streams of PAO producing flammable mists.[1] A proxy measurement for the live-fire testing shown in Figure 1.3 is done by analyzing the spray pattern of a jet of fluid (Figure 6.7). The spray pattern evolves over time and a smaller spray angle is indicative of smoother flow, fewer droplets, and less production of flammable mist. Adding either covalent or associative PCOD to the

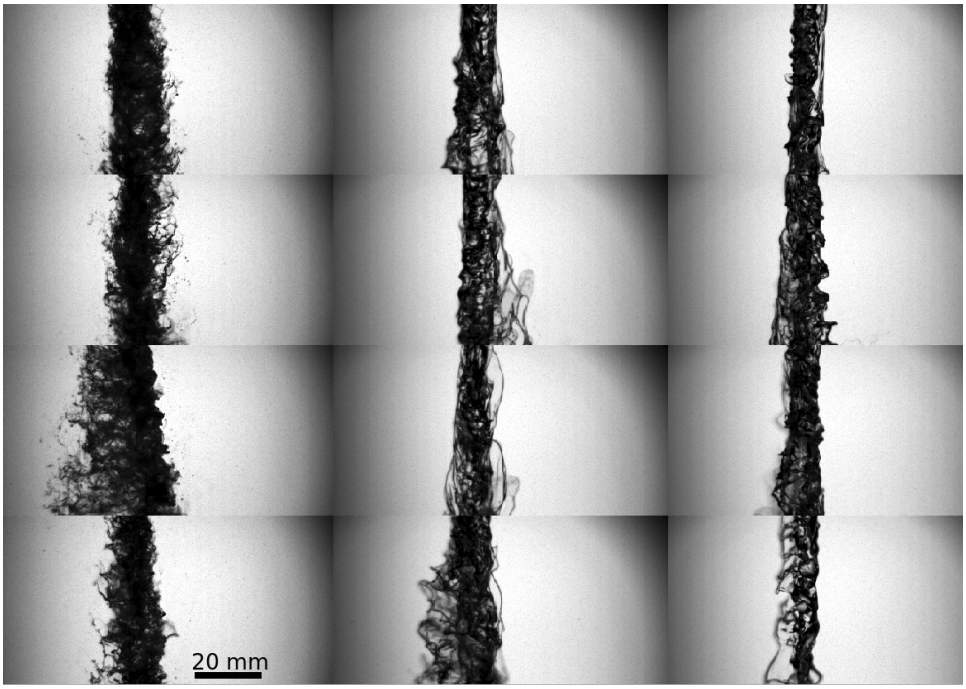

Figure 6.8: Representative spray images 30 to 35 mm downstream from the orifice for (left to right) PAO, 0.05 weight % 1.2 Mg/mol covalent PCOD in PAO, and 0.10 weight % 1.2 Mg/mol covalent PCOD in PAO. Images provided by Dr. Jacob Temme, ARL, and reproduced from Lhota [3] with permission.

PAO solution reduced the spray angle throughout the course of the experiment. The effect can be seen visually where streams of fluid containing PCOD maintain a more narrow angle and produce fewer filaments and droplets (Figure 6.8). The image analysis produces distinct spray angle behavior for the three solutions (Figure 6.9). The baseline PAO has a higher spray angle for almost the entire duration of the experiment, while the 0.1 weight % PCOD solution has the lowest. The lower concentration, 0.05 weight %, produces similar spray angles to 0.1 weight %, but has higher variance.

The associative PCODs produce similarly results, but exhibit much higher variance of spray angle throughout the course of the experiment (Table 6.2). First, at these low concentrations ($c < c^*$), the associations are suppressed due to the difficulty of finding another polymer chain to associate with (Table 6.1). I hypothesize that the shorter finite extensability observed in associative polymers compared to their covalent counterparts also contributes to the higher variance. As the spray evolves and filaments eject from the stream, the solution of associative polymers is not able to stretch to the same degree as a covalent PCOD and relinquish the droplet of fluid

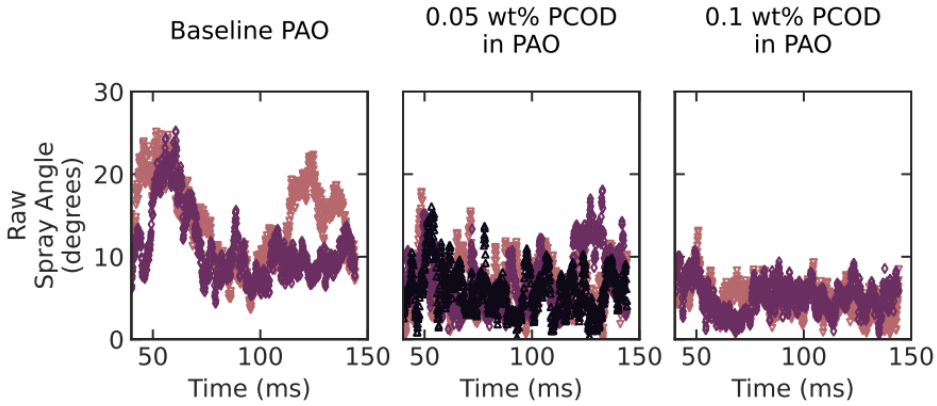

Figure 6.9: Spray angle in degrees as a function of time for (from left to right) pure PAO, 0.05 weight % 1.2 Mg/mol covalent PCOD in PAO, and 0.10 weight % 1.2 Mg/mol covalent PCOD in PAO. The colors indicate different experimental replicates. Images provided by Dr. Jacob Temme, ARL, and reproduced from Lhota [3] with permission.

Table 6.2: Spray angle of PAO solutions

Polymer	Concentration (weight %)	Spray angle (°)
PAO	-	12.7 ± 2.2
DA+DB	0.05	7.6 ± 5.2
Covalent	0.05	6.7 ± 0.7
DA+DB	0.10	4.9 ± 4.2
Covalent	0.10	5.0 ± 0.2

to the atmosphere more readily.

6.5 Conclusions and future work

The vast bulk of the chemicals industry is, in essence, the separation of crude oil into its useful parts. Some of it will become gasoline or jet fuel, some of it will be made into fluids that are not meant to be consumed as quickly, such as lubricants and coolants; and other fractions from the crude oil will serve some other fate. These fractions will be subject to a gauntlet of temperatures, gasses, solvents, other chemicals, separations, mechanical processes, *et cetera* all serving the higher purpose of refining them into some other molecule humans find useful. Outcomes of this multistage, tortuous process include pharmaceuticals, food additives, cosmetics, packaging, durable plastics, and specialty polymers such as associative PCOD. It seems almost cruel to then mix these specialty polymers back in with their less

refined cousins like fuels or lubricants, but the benefits are hard to ignore.

Adding associative PCOD to PAO does serve to control spray behavior and reduce droplet formation. However, due to the mediocre solvent quality, at low concentrations the associative versions of these polymers may not be optimal. Judging by the measured λ_E, spraying solutions of pure DB in PAO may have had better control over the spray behavior than solutions of DA and DB mixed. The DA DB pairs are short enough to survive the pumping and other events preceding spray, so a solution of only DB should also remain intact.

To alleviate this discrepancy, I propose changing the chemical identity of the polymer backbone. If polymers with the DA and DB associative end groups could be made with a backbone that more closely resembles the structure of PAO, then the associations would again become useful at low concentrations. I believe incorporating a long alkyl pendant group into the polymer backbone would help tremendously to accomplish this.

References

[1] M. H. Wei et al. "Megasupramolecules for Safer, Cleaner Fuel by End Association of Long Telechelic Polymers". In: *Science* 350.6256 (2015), pp. 72–75. ISSN: 10959203. DOI: 10.1126/science.aab0642.

[2] H. Kim. "New Long End-Associative Polymers for Mist Control in I. Aqueous Solutions and II. Hydrocarbon Solvents". California Institute of Technology, Aug. 26, 2022. DOI: 10.7907/RSX9-QT39. URL: https://resolver.caltech.edu/CaltechTHESIS:08252022-035254306 (visited on 09/30/2022).

[3] R. C. Lhota. "Rheological Characterization of Polymer Additives for Mist Control and Drag Reduction". California Institute of Technology, May 27, 2022. DOI: 10.7907/WAV1-4T47. URL: https://resolver.caltech.edu/CaltechTHESIS:05262022-231652129 (visited on 09/30/2022).

[4] R. L. A. David. "Associative Polymers as Antimisting Agents and Other Functional Materials via Thiol-Ene Coupling". Pasadena, California: California Institute of Technology, Mar. 7, 2008. 189 pp.

[5] R. S. Marano et al. "Polymer Additives as Mist Suppressants in Metalworking Fluids Part I: Laboratory and Plant Studies - Straight Mineral Oil Fluids". In: *S.A.E. Transactions* 104 (Section 5 1995), pp. 136–146.

[6] K. K. Chao et al. "Antimisting Action of Polymeric Additives in Jet Fuels". In: *AIChE Journal* 30.1 (Jan. 1984), pp. 111–120. ISSN: 0001-1541, 1547-5905. DOI: 10.1002/aic.690300116. URL: http://doi.wiley.com/10.1002/aic.690300116 (visited on 03/23/2016).

[7] R. W. Lewis et al. "Polymeric Drift Control Adjuvants for Agricultural Spraying". In: *Macromolecular Chemistry and Physics* 217.20 (Oct. 2016), pp. 2223–2242. ISSN: 10221352. DOI: 10.1002/macp.201600139. URL: https://onlinelibrary.wiley.com/doi/10.1002/macp.201600139 (visited on 03/23/2022).

[8] E. Hilz. "Spray Drift Review: The Extent to Which a Formulation Can Contribute to Spray Drift Reduction". In: *Crop Protection* (2013), p. 9.

[9] S. Kooij et al. "What Determines the Drop Size in Sprays?" In: *Physical Review X* 8.3 (July 20, 2018). ISSN: 2160-3308. DOI: 10.1103/PhysRevX.8.031019. URL: https://link.aps.org/doi/10.1103/PhysRevX.8.031019 (visited on 06/11/2020).

[10] B. Keshavarz et al. "Studying the Effects of Elongational Properties on Atomization of Weakly Viscoelastic Solutions Using Rayleigh Ohnesorge Jetting Extensional Rheometry (ROJER)". In: *Journal of Non-Newtonian Fluid Mechanics* 222 (Aug. 2015), pp. 171–189. ISSN: 03770257. DOI: 10.1016/j.jnnfm.2014.11.004. URL: https://linkinghub.elsevier.com/retrieve/pii/S0377025714002055 (visited on 02/12/2020).

[11] R. P. Mun, J. A. Byars, and D. V. Boger. "The Effects of Polymer Concentration and Molecular Weight on the Breakup of Laminar Capillary Jets". In: (1998), p. 13. DOI: 10.1016/S0377-0257(97)00074-8.

[12] A. N. Rozhkov. "Dynamics and Breakup of Viscoelastic Liquids (A Review)". In: *Fluid Dynamics* 40.6 (Nov. 2005), pp. 835–853. ISSN: 0015-4628, 1573-8507. DOI: 10.1007/s10697-006-0001-7. URL: http://link.springer.com/10.1007/s10697-006-0001-7 (visited on 09/30/2022).

[13] V. Tirtaatmadja, G. H. McKinley, and J. J. Cooper-White. "Drop Formation and Breakup of Low Viscosity Elastic Fluids: Effects of Molecular Weight and Concentration". In: *Physics of Fluids* 18.4 (Apr. 2006), p. 043101. ISSN: 1070-6631, 1089-7666. DOI: 10.1063/1.2190469. URL: http://aip.scitation.org/doi/10.1063/1.2190469 (visited on 02/12/2020).

[14] B. Keshavarz et al. "Ligament Mediated Fragmentation of Viscoelastic Liquids". In: *Physical Review Letters* 117.15 (Oct. 7, 2016), p. 154502. ISSN: 0031-9007, 1079-7114. DOI: 10.1103/PhysRevLett.117.154502. URL: https://link.aps.org/doi/10.1103/PhysRevLett.117.154502 (visited on 02/12/2020).

[15] Department of Defense. *Performance Specification Coolant Fluid, Hydrolytically Stable, Dielectric*. MIL-PRF-87252E. Department of Defense, Mar. 21, 2018. DOI: 10.1520/MNL10848M. URL: http://www.astm.org/doiLink.cgi?MNL10848M (visited on 08/01/2022).

[16] L. E. Rodd et al. "Capillary Break-up Rheometry of Low-Viscosity Elastic Fluids". In: *Applied Rheology* 15.1 (Feb. 1, 2005), pp. 12–27. ISSN: 1617-8106. DOI: 10.1515/arh-2005-0001. URL: https://www.degruyter.com/document/doi/10.1515/arh-2005-0001/html (visited on 08/04/2022).

[17] B. P. Robertson and M. A. Calabrese. *Volatile Dripping onto Substrate (vDoS) Extensional Rheology of Viscoelastic Polymer Solutions*. preprint. In Review, Nov. 8, 2021. DOI: 10.21203/rs.3.rs-964629/v1. URL: https://www.researchsquare.com/article/rs-964629/v1 (visited on 02/28/2022).

[18] G. H. McKinley. "Visco-Elasto-Capillary Thinning and Break-Up of Complex Fluids". In: (2005), p. 48.

[19] L. Sangroniz et al. "Effect of Hydrogen Bonding on the Physicochemical and Rheological Features of Chemically Modified Phenoxy". In: *Polymer* 159 (Dec. 2018), pp. 12–22. ISSN: 00323861. DOI: 10.1016/j.polymer.2018.11.002. URL: https://linkinghub.elsevier.com/retrieve/pii/S0032386118310206 (visited on 05/05/2021).

[20] E. Miller and J. Cooper-White. "The Effects of Chain Conformation in the Microfluidic Entry Flow of Polymer–Surfactant Systems". In: *Journal of Non-Newtonian Fluid Mechanics* 160.1 (July 2009), pp. 22–30. ISSN: 03770257. DOI: 10.1016/j.jnnfm.2009.02.009. URL: https://

linkinghub.elsevier.com/retrieve/pii/S0377025709000457 (visited on 05/05/2021).

Appendix A

MATHEMATICS, MEASUREMENTS, AND MOLECULES USED

A.1 Mathematics

Extensional properties

The EC regime (Equation 3.3) consists of the data after the critical time and before the finite-extensibility regime. To determine the extensional relaxation time (λ_E), a linear regression is performed on data recast as $\ln(D/D_0)$ versus $t - t_c$. The slope (m) obtained is thus used to calculate λ_E ($\lambda_E = \frac{-1}{3m}$).

Intra-frame t_c calculation

The intra-frame adjustments to t_c are performed as follows: The replicate with the lowest value of $\frac{D(t_c)}{D_0}$, determined by the frame with maximum strain rate is fixed as the reference replicate. We select a subset of the reference dataset consisting of the $t = t_c$ and the 9 frames prior to $t = t_c$. One at a time, the other replicates are compared to this subset of the reference data. The comparison is made between a subset of the 10 frames preceding $t = t_c$, (where $t < t_c$, excluding $t = t_c$) from the comparison datasets. To find the refined value of t_c, a constant is added to t_c which minimizes the euclidean distance (calculated with *scipy.spatial.distance.cdist*) between the $\frac{D(t)}{D_0}$ and $t - t_c$ pairs from the reference and replicate data. This unique value is determined by the iterative Broyden–Fletcher–Goldfarb–Shanno (BFGS) algorithm (implemented with *scipy.optimize.minimize*).[1–4] If the absolute value of the constant which minimizes the euclidean distance between these datasets is greater than 2/(frame rate), the constant is set to 2/(frame rate). The adjusted value (t_c from $\dot{\epsilon}$ plus the constant determined above) of t_c is propagated through the original time data and the relevant quantities (e.g., $D(t_c)$, η_E) are recalculated.

Modeling droplet behavior

To predict a rebound outcome, I followed the mathematics laid out in Mao, Kuhn, and Tran [5] with two key differences. I accounted for the potential energy of the droplet ($PE = \frac{\pi}{12}\rho g D^4$) in the (r) phase, which the authors intentionally neglected. I also calculated the quantity $\frac{d_m}{D}$ using η_E in the Re. Without both of these corrections, the predictions from the equations do not match my experimental observations. With them included, the predictions are highly ($\sim$ 91 %) accurate. Occasionally, for

solutions with very high values of η_E, the calculation of $\frac{d_m}{D}$ will result in a value < 1. Because that is a nonsensical result, I manually replaced those instances with $\frac{d_m}{D} = 1$ when calculating E_{ERE}.

To predict a splash outcome, the quantity $\frac{Re_S}{We_E^{0.21}}$ was calculated from the independently measured fluid properties and compared to the experimentally determined threshold of 4350. If $\frac{Re_S}{We_E^{0.21}} > 4350$, the droplet was predicted to splash.

If the droplet was predicted to both splash and rebound, the droplet was assigned to splash. I observed 0 occurrences of both splash and rebound under the same experimental conditions.

Calculating droplet velocity

The velocity v of the droplets was calculated from their potential energy (PE) using the conservation of energy. The height (H) between the needle and substrate, mass of the droplet (m), and acceleration due to gravity (g) are known. Setting $KE = \frac{1}{2}mv^2$ equal to $PE = mgH$. Thus, the velocity is calculated as:

$$v = \sqrt{2gH}. \tag{A.1}$$

The velocities resulting from this calculation range from 0.54 to 4.7 m/s, well below the terminal velocities of 9 m/s ($D = 2.8$ mm) or 12 m/s ($D = 3.6$ mm).

The calculated velocities were further verified by comparison to the velocity of the top and bottom points of the droplet using the high-speed videos with a known frame rate.

Spray angle calculations

The spray angle analysis was performed by MATLAB -based image analysis of spray videos, modified by ARL from Engine Combustion Tools.[6]

A.2 Measurements

Spray testing

Spray experiments were performed by Dr. Jacob Temme and coworkers at Army Research Laboratory (ARL). Methods, data, and figures included with permission of ARL. Further details are available in Lhota [7].

Fluid pressurized to 120 psi (0.83 MPa) was released through a 5 mm orifice into an atmospheric chamber. The spray was captured by two Phantom SA-X2 high-speed cameras paired with Zeiss 50mm lenses. Two fields of view were observed. The

first, a larger image from the nozzle tip to ~ 80 mm downstream, was recorded at 10,000 fps. The second, with high magnification, was centered on a 5 mm region from 30 to 35 mm downstream of the nozzle. This was recorded at 35,000 fps.

Droplet size measurements

Droplet diameter (D) was measured by capturing and weighing 10 droplets. The total mass was divided by 10 to find the mass of a single droplet (m), and D was calculated from the mass of a single droplet using the density (ρ):

$$D = \sqrt[3]{\frac{6m}{\pi\rho}}. \tag{A.2}$$

In this calculation, $\rho_{H_2O} = 0.99$ and $\rho_{PAO} = 0.85$ g/mL.

Droplet impact image and data analysis

Droplets were produced from needles with D_0 from 0.72 mm (22G) to 1.8 mm (15G) resulting in droplet diameters between 2.8 mm and 3.6 mm. The needle was positioned at heights from 2 cm to 118 cm, increasing the velocity with which the droplets struck the target. This set up produced droplets with KE from 2 μJ to 273 μJ and impact velocities between 0.5 and 4.7 m/s.

Droplet impacts were observed with the optical setup described in the DoSER materials section (Section A.2). The optical zoom was set to maximize the field of view, and the videos were recorded at 12,800 fps and a resolution of 1024x1024 pixels (1 Megapixel). For some impact experiments (Figures 5.3 and 5.4), the camera was placed on a custom designed and 3D printed wedge with an angle of 12° to visualize the entire impact event.

Gel-permeation chromatography

The molecular weights and dispersity index of the polymers in solution were determined on a GPC system with an Agilent PL Aquagel-OH Mixed-H 8μm 300 x 7.5mm column, Wyatt DAWN 8 multi-angle laser light scattering detector (λ=658.9nm), and a Waters Optilab differential refractometer (RI) (λ=658nm). Water with 200 ppm sodium azide and 8.5 g/L sodium nitrate was used as the eluent at the flow rate of 0.3mL/min with a temperature of 25°C. The data were analyzed using Wyatt Astra Software (version 7.3.2.19) using the Zimm fitting formula with $dn/dc = 0.159$ mL g^{-1} for PAM in water to obtain the weight-average molecular weight (M_w) for each polymer reported.

Surface tension measurements

Surface tension measurements were done by taking still images of pendant droplets of the fluid with the optical setup described in the DoSER materials section below. The images were converted from 16- to 8-bit, the scale was set from the known diameter of the needles, and the surface tension was determined using the PendantDrop plugin in ImageJ.[8]

Contact angle measurements

The contact angle measurements were performed using ImageJ on images taken with the optical setup described in the DoSER materials section below.

Shear rheometry

Shear rheometry was performed on an Anton Paar MCR 302 WESP rheometer using a cone-and-plate fixture with 50 mm diameter and 2.007° angle, with a truncation of 0.207 mm. The plate was cooled to 15 ± 0.1 °C using a Peltier plate to regulate temperature. Solutions were allowed to equilibrate for 5 minutes prior to testing. Shear rate sweeps were performed from 1 to 100 $\frac{1}{s}$. Glycerol solutions were tested by RWL. PAM solutions were tested by Dr. Lhota, more details can be found in their thesis.[7]

Dripping-onto-Substrate Extensional Rheometry (DoSER)

A dripping-onto-substrate extensional rheometry (DoSER) instrument was constructed from a 12000 lumen light source (GSVitec MultiLED G8 with QT lamp head operated in continuous mode), a syringe pump (Harvard Elite 11) on an adjustable track, a high-speed video camera (Photron FASTCAM Nova S12 type 1000K-M-32GB) equipped with an optical train as described below, and a custom holder for aluminum substrates (available in Supporting Information). The light passes through a diffuser before reaching the measurement plane. The platform the substrates sat on was mounted to a Thorlabs MT1 micrometer to manually adjust the gap distance. The optical train consisted of a Resolve4K 7:1 Zoom Video microscope lens, two rear projection lenses, a 1.0x objective lens, and a coupler, resulting in a resolution limit at full zoom of 3.5 μm. The camera was operated at 25,000 frames per second with a shutter speed of 70,000-90,000 Hz (i.e., ~12 μs exposure). Videos were recorded at spatial resolution of 1024x512 pixels and a 12-bit bit depth.

A 5 mL Luer lock syringe was used for each solution with various blunt tip needles, (Table A.1). For aqueous solutions, stainless steel needles were used; for PAO, PTFE

Table A.1: Blunt tip needles used and their dimensions.

Gauge	Inner diameter (D_{inner}) (mm)	Outer diameter (D_0) (mm)	Material	Supplier
18G	0.838	1.270	Stainless steel	VWR
22G	0.413	0.718	Stainless steel	VWR
22G	0.711	1.016	PTFE	Integrated Dispensing Solutions, Inc

Table A.2: Physical properties of the fluids tested

				θ_c (°)			
Fluid	σ (mN/m)	ρ (g/mL)	η (mPa s)	Glass	Al	Stainless steel[9,10]	Teflon[11]
PAO	30	0.85	3	30	19	37[#]	45[‡]
H_2O	73	0.99	1	33	71	62	120

[#]: Value from mineral oil[10]
[‡]: Value from hexadecane

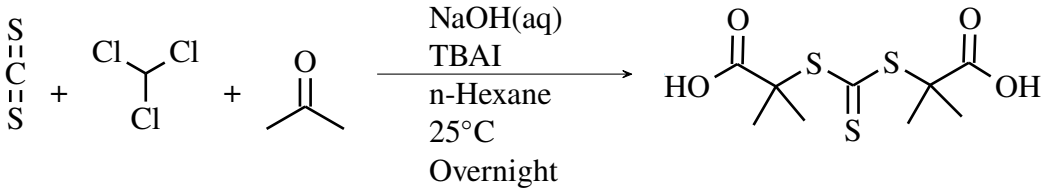

Scheme A.1: Reaction of carbon disulfide, chloroform, and acetone to form S,S-bis(α, α'-dimethyl-α"-acetic acid) trithiocarbonate (BDMAT)

needles were used to minimize the surface interactions between the fluid and the needle. The solutions were dispensed onto aluminum substrates (ThermalSupport, Aluminum 6.7mm Sample Pan, Part Number 5416717.2) and glass microscope slides (Corning, Micro Slides, Plain, Part Number 2947-75x25).

A.3 Molecules

All chemical reagents were obtained from Sigma Aldrich at 98% purity or higher unless otherwise stated. Deionized (DI) was used throughout. Polyalphaolefin (BRAYCO 889 MIC) was acquired from QC Lubricants (Table A.2).

Synthesis of S,S-bis(α, α'-dimethyl-α"-acetic acid) trithiocarbonate (BDMAT)
Procedure modified from Lai, et al.[12]

Carbon disulfide (4.4 g, 0.058 mol), chloroform (17.24 g, 0.144 mol), acetone (8.4g, 0.144 mol), and tetrabutylammonium iodide (0.43 g, 1.16 mmol) were mixed with 23 mL of n-hexane. The reaction flask was cooled with an ice bath. Aqueous sodium hydroxide solution (50%) was added slowly while keeping the temperature below 25 °C. The reaction mixture was removed from the ice bath after 2 hours and left to stir overnight. DI water (140mL) was added to dissolve the solid formed inside of the flask, and 12M $HCl_{(aq)}$ was added slowly and stirred for 30 mins. The mixture was filtered, and the solids were washed thoroughly with DI water. The crude product was recrystallized twice in a mixture of acetone and hexane (4:1, v/v) to give the product as yellow crystals. Yield 11%.

Poly(acrlyamide) synthesis

Acrylamide (1 g, 14 mmol) and BDMAT (appropriate amount from 1 mg/mL DMSO stock solution) were dissolved in water (7 mL, 2 M [acrylamide]) in a 50 mL round bottom flask. 0.1 N $HCl_{(aq)}$ (0.1mL) was added, the mixture was degassed by bubbling argon through the polymerization solution for 15 minutes, and the flask was placed inside of the LED reactor and irradiated for 8 hours (Figure A.1). The polymers were transferred to a 250 mL beaker, dissolved in approximately 100 mL of DI water, and precipitated in acetone (500 mL) to remove excess acrylamide and dried under vacuum before use.

Table A.3 includes weight-average molecular weight (M_w), number-average molecular weight (M_n), and dispersity index (Đ) for each polymer used in this work.

Visible light LED reactor

Visible light LED reactor was used for PAM synthesis (Figure A.1).[13] A custom photo-reactor was constructed using a Chanzon 30W LED (λ_{peak}= 440 nm-450 nm) powered by a Chanzon 900 mA constant current LED driver. The LED chip was attached to an aluminum heatsink (10.9cm x 5.8cm x 8.9cm) using thermally conductive adhesive (MG Chemicals). A 7cm computer CPU cooler fan (AMD) was attached to the back side of the aluminum heatsink, and the fan was connected to a 12V 2A DC power supply. The LED and the cooling unit were housed in a rectangular plastic box with a cover (27.9cm x 17.8cm x 12.7cm). The interior of the plastic box was lined with aluminum foil and the box was placed on top of a stir plate. The LED reactor is shown in Figure A.1.

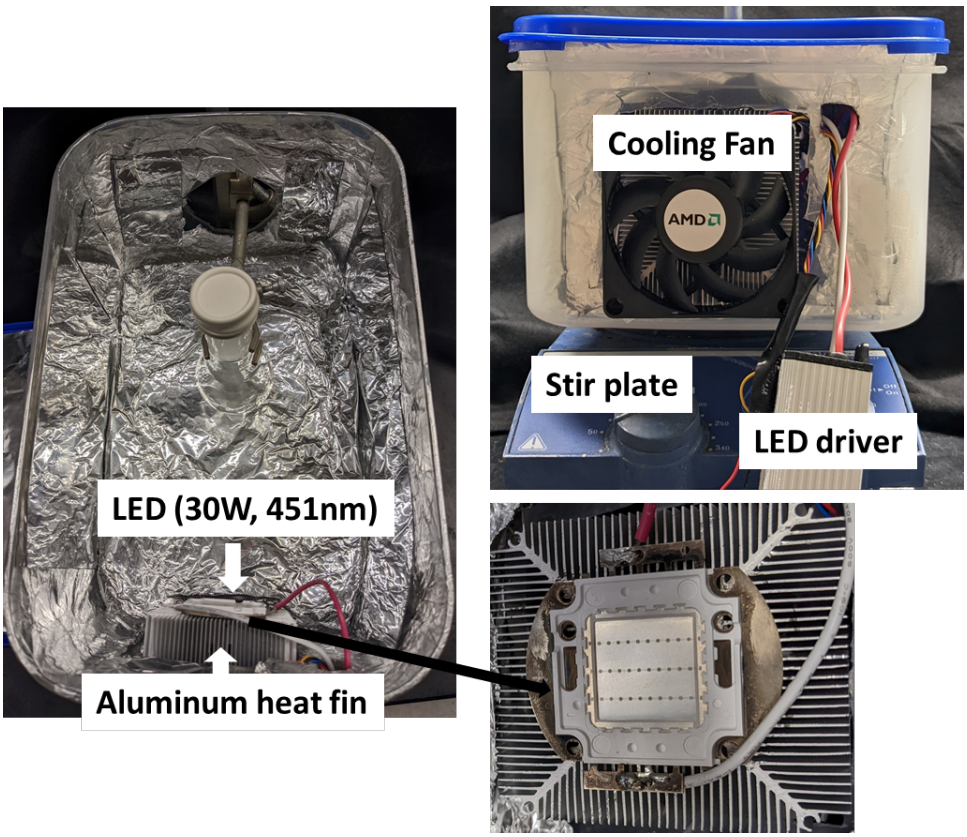

Figure A.1: Visible light LED reactor

Table A.3: Covalent and associative polyacrylamide (PAM) molecular weights and dispersities used in this work.

End group	M_n (Mg/mol)	M_w (Mg/mol)	Đ
Covalent	1.50	1.65	1.10
Covalent	1.40	2.34	1.67
Covalent	3.00	4.80	1.60
Covalent	5.00	6.70	1.34
Terpyridine	0.82	0.84	1.03
β-cyclodextrin	0.43	0.82	1.90
Adamantane	0.68	0.73	1.08

M_w: Weight-average molecular weight
M_n: Number-average molecular weight
Đ: Dispersity index (M_w/M_n)

Table A.4: Covalent and associative polycyclooctadiene (PCOD) molecular weights and dispersities used in this work.

End group	M_n (Mg/mol)	M_w (Mg/mol)	Đ
Covalent[#]	0.70	1.26	1.80
DA	0.44	0.66	1.49
DB	0.47	0.67	1.44

[#]: Polyisobutylene (purchased from Sigma Aldrich)
M_w: Weight-average molecular weight
M_n: Number-average molecular weight
Đ: Dispersity index (M_w/M_n)

Glycerol solution preparation

Pure glycerol was mixed with molecular biology grade H_2O in a glass vial. The solution was left overnight and used without further modification.

PAM solution preparation

Stock solutions of 1 weight % covalent PAM were prepared by dissolving polymer in molecular biology grade H_2O in a glass vial. The polymer was left on overnight on a wrist-action shaker (Burrell Scientific). The polymer solutions were further diluted to their final concentration and used without further modification.

Terpyridine-ended PAM solution preparation

Stock solutions of 1 weight % terpyridine-ended PAM were prepared by dissolving polymer in molecular biology grade H_2O in a glass vial. The polymer was left on overnight on a wrist-action shaker (Burrell Scientific). The polymer solutions were further diluted to their final concentration, and then a the metal solution was added. The metal stock solutions (1 mM) were prepared from chloride salts of each metal (e.g., $FeCl_2$, $NiCl_2$) and 10 mM HCl to prevent oxidation of Fe^{2+} to Fe^{3+}. After the addition of the metal ions, the solutions were allowed to equilibrate for 12 hours before testing.

Note: the order of operations is paramount when dealing with terpyridine ended PAM. Adding an equivalent amount of metal ions *prior* to dilute to the final concentration and adding metal ions *after* dilution result in different properties.

β-cyclodextrin- and adamantane-ended PAM solution preparation

Stock solutions of 1 weight % associative-ended PAM were prepared by dissolving polymer in molecular biology grade H_2O in a glass vial. The polymer was left on

overnight on a wrist-action shaker (Burrell Scientific). The polymer solutions were further diluted to their final concentration, 0.2 weight %. Aliquots from each vial were taken and mixed together in equal volumes to produce the 1:1 mixture for testing.

PCOD Synthesis

The details of PCOD synthesis and solution preparation are available in Kim [13]. The polymers and solutions were used without further modification.

References

[1] C. G. Broyden. "The Convergence of a Class of Double-rank Minimization Algorithms 1. General Considerations". In: *IMA Journal of Applied Mathematics* 6.1 (1970), pp. 76–90. ISSN: 0272-4960, 1464-3634. DOI: 10.1093/imamat/6.1.76. URL: https://academic.oup.com/imamat/article-lookup/doi/10.1093/imamat/6.1.76 (visited on 08/05/2022).

[2] R. Fletcher. "A New Approach to Variable Metric Algorithms". In: *The Computer Journal* 13.3 (Mar. 1, 1970), pp. 317–322. ISSN: 0010-4620, 1460-2067. DOI: 10.1093/comjnl/13.3.317. URL: https://academic.oup.com/comjnl/article-lookup/doi/10.1093/comjnl/13.3.317 (visited on 08/05/2022).

[3] D. Goldfarb. "A Family of Variable-Metric Methods Derived by Variational Means". In: *Mathematics of Computation* 24.109 (1970), pp. 23–26. ISSN: 0025-5718, 1088-6842. DOI: 10.1090/S0025-5718-1970-0258249-6. URL: https://www.ams.org/mcom/1970-24-109/S0025-5718-1970-0258249-6/ (visited on 08/05/2022).

[4] D. F. Shanno. "Conditioning of Quasi-Newton Methods for Function Minimization". In: *Mathematics of Computation* 24.111 (1970), pp. 647–656. ISSN: 0025-5718, 1088-6842. DOI: 10.1090/S0025-5718-1970-0274029-X. URL: https://www.ams.org/mcom/1970-24-111/S0025-5718-1970-0274029-X/ (visited on 08/05/2022).

[5] T. Mao, D. C. S. Kuhn, and H. Tran. "Spread and Rebound of Liquid Droplets upon Impact on Flat Surfaces". In: *AIChE Journal* 43.9 (Sept. 1997), pp. 2169–2179. ISSN: 0001-1541, 1547-5905. DOI: 10.1002/aic.690430903. URL: https://onlinelibrary.wiley.com/doi/10.1002/aic.690430903 (visited on 08/23/2022).

[6] M. Bardi et al. "Engine Combustion Network: Comparison of Spray Development, Vaporization, and Combustion in Different Combustion Vessels". In: *Atomization and Sprays* 22.10 (2012), pp. 807–842. ISSN: 1044-5110. DOI: 10.1615/AtomizSpr.2013005837. URL: http://www.dl.begellhouse.com/journals/6a7c7e10642258cc,5b18f0e860ebc687,20adc8ff175d5f43.html (visited on 10/04/2022).

[7] R. C. Lhota. "Rheological Characterization of Polymer Additives for Mist Control and Drag Reduction". California Institute of Technology, May 27, 2022. DOI: 10.7907/WAV1-4T47. URL: https://resolver.caltech.edu/CaltechTHESIS:05262022-231652129 (visited on 09/30/2022).

[8] A. Daerr and A. Mogne. "Pendent_Drop: An ImageJ Plugin to Measure the Surface Tension from an Image of a Pendent Drop". In: *Journal of Open Research Software* 4.1 (Jan. 28, 2016), p. 3. ISSN: 2049-9647. DOI: 10.5334/jors.97. URL: https://openresearchsoftware.metajnl.com/article/10.5334/jors.97/ (visited on 07/29/2022).

[9] A. Martinez-Urrutia et al. “Contact Angle Measurement for LiBr Aqueous Solutions on Different Surface Materials Used in Absorption Systems”. In: *International Journal of Refrigeration* 95 (Nov. 2018), pp. 182–188. ISSN: 01407007. DOI: 10.1016/j.ijrefrig.2018.05.041. URL: https://linkinghub.elsevier.com/retrieve/pii/S0140700718302044 (visited on 08/12/2022).

[10] K. N. Prabhu, P. Fernades, and G. Kumar. “Effect of Substrate Surface Roughness on Wetting Behaviour of Vegetable Oils”. In: *Materials & Design* 30.2 (Feb. 2009), pp. 297–305. ISSN: 02613069. DOI: 10.1016/j.matdes.2008.04.067. URL: https://linkinghub.elsevier.com/retrieve/pii/S0261306908001659 (visited on 08/12/2022).

[11] S. Lee, J.-S. Park, and T. R. Lee. “The Wettability of Fluoropolymer Surfaces: Influence of Surface Dipoles”. In: *Langmuir* 24.9 (May 1, 2008), pp. 4817–4826. ISSN: 0743-7463, 1520-5827. DOI: 10.1021/la700902h. URL: https://pubs.acs.org/doi/10.1021/la700902h (visited on 08/12/2022).

[12] J. T. Lai, D. Filla, and R. Shea. “Functional Polymers from Novel Carboxyl-Terminated Trithiocarbonates as Highly Efficient RAFT Agents”. In: *Macromolecules* 35.18 (Aug. 1, 2002), pp. 6754–6756. ISSN: 0024-9297, 1520-5835. DOI: 10.1021/ma020362m. URL: https://pubs.acs.org/doi/10.1021/ma020362m (visited on 07/14/2022).

[13] H. Kim. “New Long End-Associative Polymers for Mist Control in I. Aqueous Solutions and II. Hydrocarbon Solvents”. California Institute of Technology, Aug. 26, 2022. DOI: 10.7907/RSX9-QT39. URL: https://resolver.caltech.edu/CaltechTHESIS:08252022-035254306 (visited on 09/30/2022).